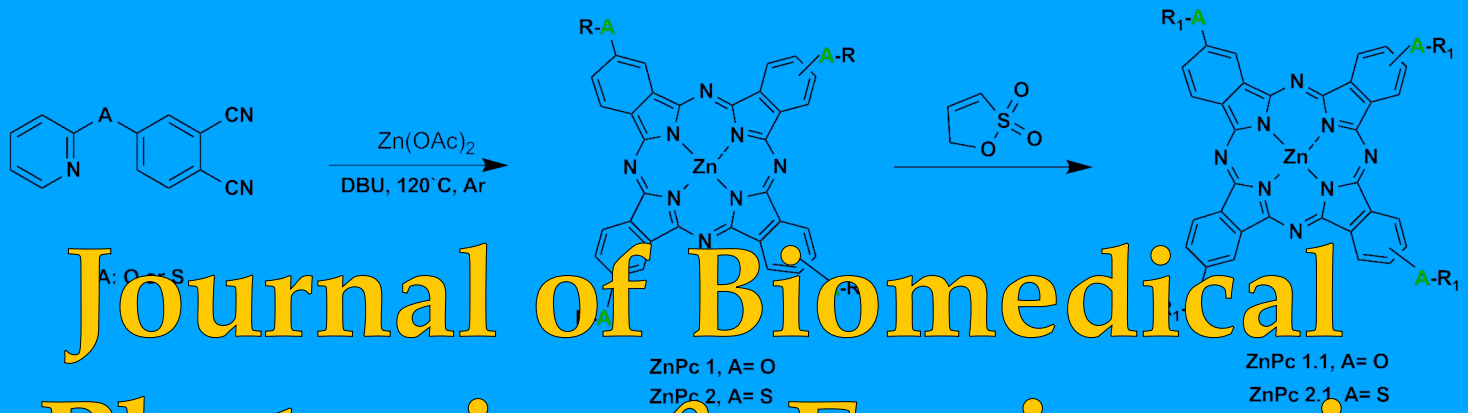
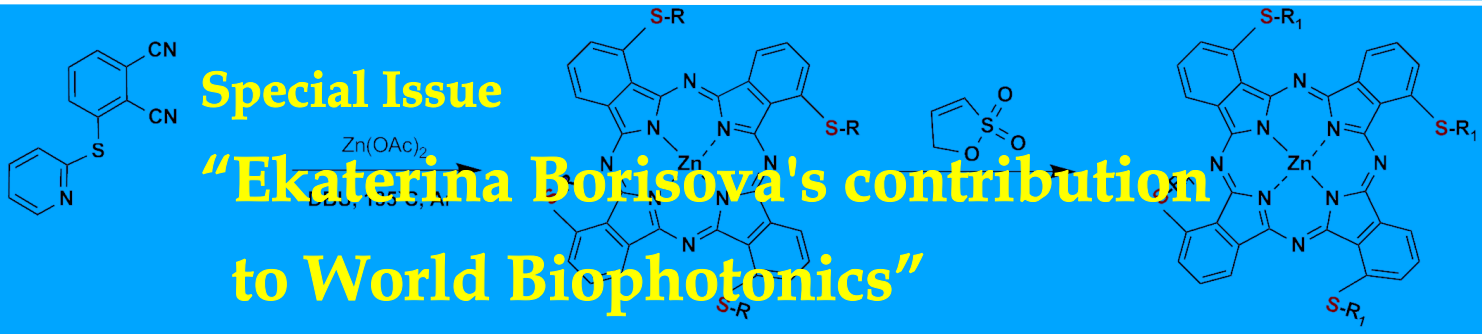
Volume 7, Issue 4, 2021

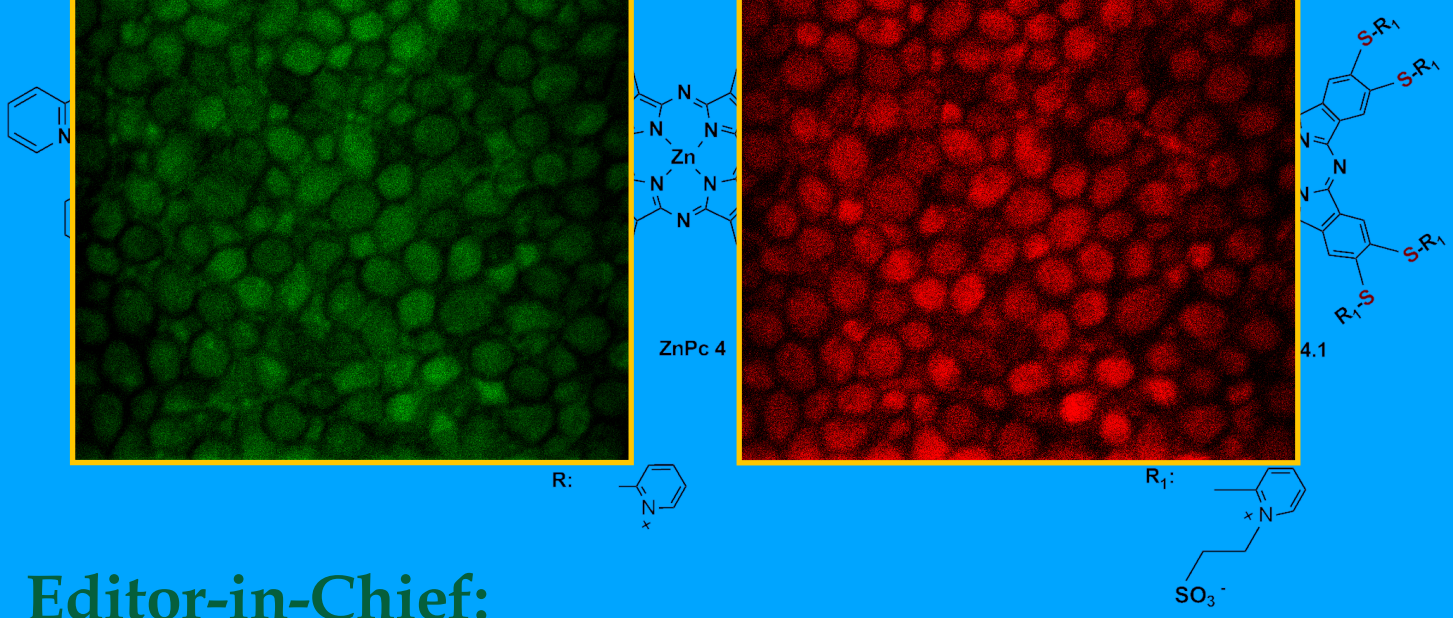


Journal of Biomedical Photonics & Engineering



Special Issue

"Ekaterina Borisova's contribution to World Biophotonics"



Editor-in-Chief:
Valery V. Tuchin

© 2021 J-BPE

Journal of Biomedical Photonics & Engineering
by Samara National Research University

Volume 7, Issue 4 (December 2021)

Special Issue
“Ekaterina Borisova's contribution to World Biophotonics”

Special Issue Editors

Latchezar Avramov, DSc
Institute of Electronics, Bulgarian Academy of Sciences, Sofia, Bulgaria

Alla B. Bucharskaya, PhD
Saratov State Medical University, Russia

Tatiana Novikova, PhD
Razvigor M. Ossikovski, PhD
LPICM, CNRS, Ecole polytechnique, IP Paris, Palaiseau, France

Valery P. Zakharov, DSc
Samara National Research University, Russia

Elina A. Genina, DSc
Oxana Semyachkina-Glushkovskaya, PhD
Saratov State University, Russia

Valery V. Tuchin, DSc, corr.-member of the RAS
Saratov State University, Russia
National Research Tomsk State University, Russia
Institute of Precision Mechanics and Control of the RAS, Saratov, Russia

© 2021 J-BPE

Editor-In-Chief

Valery V. Tuchin - Saratov National Research State University, Russian Federation;
Institute of Precision Mechanics and Control RAS, Russian Federation; a corr.-member of RAS

Deputy Editor-In-Chief

Valery P. Zakharov - Samara National Research University, Russian Federation

Postal address:
39B Lukacheva st., room #301
Samara 443086, Russian Federation

Used Figures from this issue on the Cover

Vanya Mantareva et al. Phthalocyanines Structure Versus Photodynamic Effectiveness towards Pathogenic Microorganisms: Our Recent Experience, 040202, Fig. 6 (background, edited), Fig. 7.

© 2021 J-BPE

Contents

Introduction

A review of career devoted to Biophotonics – In memoriam to Ekaterina Borisova (1978–2021) 040101
Tsanislava Genova, Latchezar Avramov, Boyko Kolev, Alexander Gisbrecht, Irina Bliznakova, Lidiya Zaharieva, Victoria Mircheva, Stoyan Ilyov, Ivan Angelov, Vanya Mantareva, Petranka Troyanova, Petya Pavlova, Tatiana Novikova, Razvigor Ossikovski, Deyan Ivanov, Viktor Dremin, Edik U. Rafailov, Sergey G. Sokolovsky, Alexander Bykov, Igor V. Meglinski, Ivan Bratchenko, Oxana Semyachkina-Glushkovskaya, Elina Genina, Alexey N. Bashkatov, Alla B. Bucharskaya, Valery Zakharov, Janis Spigulis, Sindhoora Kaniyala Melanthota, Spandana K. U., Nirmal Mazumder, Shama Prasada K., Peter Townsend, Luís Oliveira, Alexander V. Priezzhev, Dick (H.J.C.M.) Sterenborg, and Valery V. Tuchin

Review

Phthalocyanines Structure Versus Photodynamic Effectiveness towards Pathogenic Microorganisms: Our Recent Experience 040202
Vanya Mantareva, Ivan Angelov, Meliha Syuleyman, Veselin Kussovski, Ivelina Eneva, Latchezar Avramov, and Ekaterina Borisova

Articles

Photodynamic Action in Thin Sensitized Layers: Estimating the Utilization of Light Energy 040301
Gennady Meerovich, Igor Romanishkin, Ekaterina Akhlyustina, Marina Strakhovskaya, Evgeniya Kogan, Ivan Angelov, Victor Loschenov, and Ekaterina Borisova

Tissue Spectroscopy and Optical Clearing of Colorectal Mucosa in the Pursuit of New Cancer Diagnostic Approaches 040302
Luís Fernandes, Hugo Silva, Inês Martins, Sónia Carvalho, Isa Carneiro, Rui Henrique, Valery V. Tuchin, and Luís M. Oliveira

Accuracy of Common Motion Estimators in Wave-Based Optical Coherence Elastography 040303
Justin R. Rippy, Manmohan Singh, Salavat Aglyamov, and Kirill V. Larin

Assessing Porcine Iris Elasticity and Mechanical Anisotropy with Optical Coherence Elastography 040304
Christian Zevallos-Delgado, Taye T. Mekonnen, Fernando Zvietcovich, Manmohan Singh, Salavat Aglyamov, and Kirill Larin

Laser Applications for Estimation of Microbial Activity and Investigation of NIR Skin Autofluorescence 040305
Alexey Lihachev, Dmitrijs Bļizņuks, Jānis Liepiņš, and Ilze Lihacova

Influence of Melanin Content on Laser Doppler Flowmetry and Tissue Reflectance Oximetry Signal Formation 040306
Viktor Dremin, Nadezhda Golubova, Elena Potapova, and Andrey Dunaev

Activation of Apoptosis and Autophagy by Gratiola Officinalis Extract in Human Tumor Cell Lines 040307
Natal'ya V. Polukonova, Maria A. Baryshnikova, Dmitry A. Khochankov, Evgeniya V. Stepanova, Eliso S. Solomko, Anna V. Polukonova, Dmitrij A. Mudrak, Artem M. Mylnikov, Alla B. Bucharskaya, Galina N. Maslyakova, and Nikita A. Navolokin

Devices for Photodynamic Studies Based on Light-Emitting Diodes 040308
Gennady A. Meerovich, Kirill G. Linkov, Alexei V. Nekhoroshev, Alexander V. Borodkin, Ekaterina V. Akhlyustina, Ivan P. Angelov, Denis A. Glechik, and Victor B. Loschenov

 © 2021 J-BPE

Review (outside the Special Issue)

A Review of EEG Signal Analysis for Diagnosis of Neurological Disorders using Machine Learning 040201
Vandana Joshi and Nirali Nanavati

Articles (outside the Special Issue)

The Sedimentation Rate of Free Erythrocytes and Their Associates, the Influence of a Standing Ultrasonic Wave 040501
Valeri A. Doubrovski, Sergey V. Markov, Stanislav O. Torbin, and Elena P. Karpocheva

Visualization and Spectral Analysis of Pubic Periosteum Atrophy 040502
Vladimir I. Belokonev, Valery P. Zakharov, Sergey Y. Pushkin, Zinaida V. Kovaleva, Andrey V. Zharov, Natalya S. Burnaeva, Elizaveta V. Zakharova, and Yulia A. Khristoforova

 © 2021 J-BPE

 doi: 10.18287/JBPE21.07.040101

A review of career devoted to Biophotonics – In memoriam to Ekaterina Borisova (1978–2021)

Tsanislava Genova[1*], Latchezar Avramov[1], Boyko Kolev[1], Alexander Gisbrecht[1], Irina Bliznakova[1], Lidiya Zaharieva[1], Victoria Mircheva[1], Stoyan Ilyov[1], Ivan Angelov[1], Vanya Mantareva[2], Petranka Troyanova[3], Petya Pavlova[4], Tatiana Novikova[5], Razvigor Ossikovski[5], Deyan Ivanov[5], Viktor Dremin[6,7], Edik U. Rafailov[7], Sergey G. Sokolovsky[7], Alexander Bykov[8], Igor V. Meglinski[7,8,9], Ivan Bratchenko[10], Oxana Semyachkina-Glushkovskaya[11,12], Elina Genina[11,13], Alexey N. Bashkatov[11,13], Alla B. Bucharskaya[11,13,14], Valery Zakharov[10], Janis Spigulis[15], Sindhoora Kaniyala Melanthota[16], Spandana K. U.[16], Nirmal Mazumder[16], Shama Prasada K.[17], Peter Townsend[18], Luís Oliveira[19,20], Alexander V. Priezzhev[21], Dick (H.J.C.M.) Sterenborg[22,23], and Valery V. Tuchin[11,13,24,25]

[1] Institute of Electronics, Bulgarian Academy of Sciences, Sofia, Bulgaria

[2] Institute of Organic Chemistry with Centre of Phytochemistry, Bulgarian Academy of Sciences, Sofia, Bulgaria

[3] Tsaritsa Yoanna-ISUL University Hospital, Sofia, Bulgaria

[4] Technical University Sofia, Branch Plovdiv, Plovdiv, Bulgaria

[5] LPICM, CNRS, Ecole Polytechnique, Institut Polytechnique de Paris, Palaiseau, France

[6] Research and Development Center of Biomedical Photonics, Orel State University, Orel, Russia

[7] College of Engineering and Physical Sciences, Aston University, Birmingham, UK

[8] Optoelectronics and Measurement Techniques Unit, University of Oulu, Oulu, Finland

[9] Institute of Clinical Medicine N.V. Sklifosovsky, I.M. Sechenov First Moscow State Medical University, Moscow, Russia

[10] Department of Laser and Biotechnical Systems, Samara National Research University, Samara, Russia

[11] Science Medical Center, Saratov State University, Saratov, Russia

[12] Physics Department, Humboldt University, Berlin, Germany

[13] Laboratory of Laser Molecular Imaging and Machine Learning, National Research Tomsk State University, Tomsk, Russia

[14] Saratov State Medical University, Saratov, Russia

[15] Biophotonics Laboratory, Institute of Atomic Physics and Spectroscopy, University of Latvia, Riga, Latvia

[16] Department of Biophysics, Manipal School of Life Sciences, Manipal Academy of Higher Education, Manipal, Karnataka, India

[17] Department of Cell and Molecular Biology, Manipal School of Life Sciences, Manipal Academy of Higher Education, Manipal, Karnataka, India

[18] University of Sussex, UK

[19] Physics Department, School of Engineering, Polytechnic Institute of Porto, Porto, Portugal

[20] Center of Innovation in Engineering and Industrial Technology, ISEP, Porto, Portugal

[21] Faculty of Physics, M.V. Lomonosov Moscow State University, Moscow, Russia

[22] Department of Biomedical Engineering and Physics of the Academic Medical Centre in Amsterdam, Amsterdam, the Netherlands

[23] Surgical Innovations Group at the Netherlands Cancer Institute, Amsterdam, the Netherlands

[24] Laboratory of Laser Diagnostics of Technical and Living Systems, Precision Mechanics and Control Institute of the Russian Academy of Sciences, Saratov, Russia

 doi: 10.18287/JBPE21.07.040101

[25] A.N. Bach Institute of Biochemistry, Research Center of Biotechnology of the Russian Academy of Sciences, Moscow, Russia

*** e-mail:** ts.genova@gmail.com

1 Introduction

Regretfully, because of her sudden demise, Assoc. Prof. Ekaterina Borisova is no longer amongst us. COVID-19 pulled away a brilliant scientist during the peak of her scientific career (see Fig. 1). All authors would like to express deepest condolences and sincere support to her family, friends, relatives and colleagues! We, therefore, rightfully commemorate her dedicated and devoted contribution to biophotonics, her readiness to always support, help, motivate and inspire all her colleagues and collaborators.

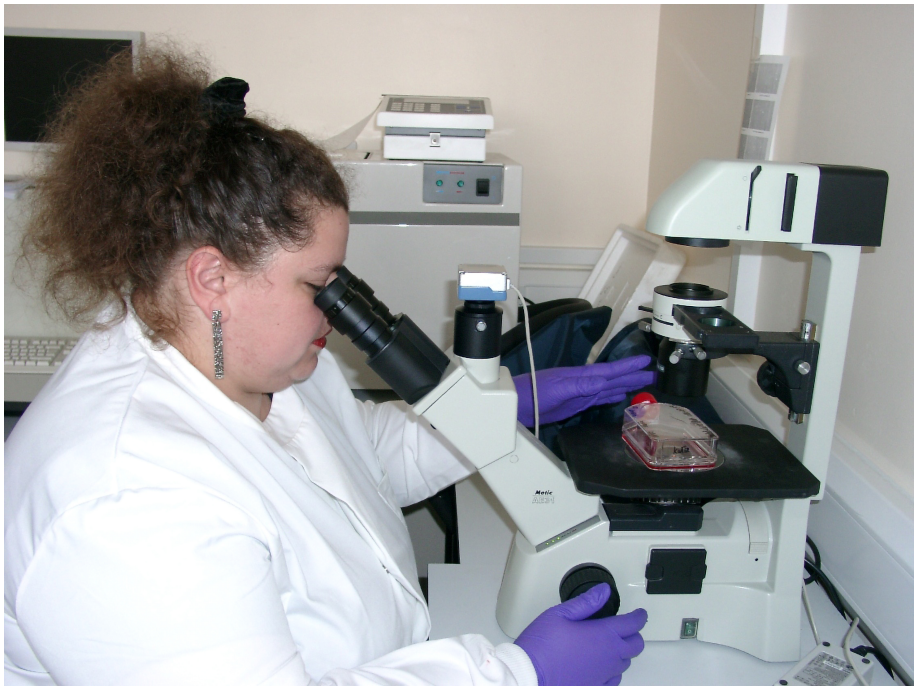


Fig. 1 Assoc. Prof. Ekaterina Borisova examining samples under microscope.

2 Biography

Ekaterina Borisova was an alumna in Medical Physics and Laser Physics from Faculty of Physics, Sofia University, Bulgaria. Her PhD degree in Physics was obtained from the Institute of Electronics – Bulgarian Academy of Sciences (IE-BAS) in 2005. At the age of 29 she was one of the youngest researchers in Bulgaria to reach the academic position of Associate Professor. In 2012 she became a Scientific Secretary of IE-BAS, in 2014 – Member of the Academic Council in the BAS and in March 2016 she was elected as a member of the Executive Council of the BAS. She has a great publication impact as author/co-author of six book chapters, more than 120 articles in peer-review journals and full texts conference reports, five national and European patents in the field of biophotonics.

 doi: 10.18287/JBPE21.07.040101

Assoc. Prof. Ekaterina Borisova's scientific contribution was recognized with senior membership of SPIE (2015), SPIE community champion award (2021). She was also the member of the European Physics Society, European Society of Photobiology, European Platform of Photodynamic Medicine and Union of Physicists in Bulgaria. In 2019 she was elected to the class of OSA Senior members. The research of Assoc. Prof. Ekaterina Borisova in the field of optical spectroscopy of human tissues for oncologic applications was honored with the BAS Prize for best young scientist in the field of Physics (2004), Prize "Pythagoras" of the Ministry of Education and Sciences for the Best Young Scientist in Bulgaria in the year 2012. She was one of the winners to receive an UNESCO / L'Oreal fellowship "For Women in Science" for Bulgaria in 2014.

Her professionalism and devotion to science was recognized with inclusion in the editorial board of the Journal of Biomedical Photonics & Engineering. A large amount of the duly efforts of Dr. Ekaterina Borisova were focused on the clinical implementation of spectroscopy methods for cancer detection, so called optical biopsy in the University Hospital "Tsaritsa Yoanna – ISUL", Sofia, Bulgaria. She started and took an active part in the foundations of the Biophotonics laboratory and the National Center of Biomedical photonics in the Institute of Electronics, Bulgarian Academy of Sciences. Assoc. Prof. Borisova was a supervisor of numerous undergraduate students who finished their academic education and many of them pursued a carrier of researchers with her guidance and support.

3 Scope of Research

The primary scientific topic of Assoc. Prof. Ekaterina Borisova was the optical techniques for diagnostics and development of laser and optical systems for biomedical and clinical application. The scope of her research included fluorescence and diffuse optical spectroscopy (DOS), application of novel photosensitizers and photodiagnosis, photodynamic therapy, opening of the blood brain-barrier, Raman spectroscopy of biological tissues, photoinactivation of pathogens, application of polarized light techniques in fluorescence spectroscopy and in tissue polarimetry for cancer detection.

3.1 Skin optical biopsy

In the last 10 years she worked persistently on one of her ultimate research goals – the development of a clinical device for objective diagnosis of cutaneous lesions. Her pioneering work was focused on detailed investigations of the fluorescence and DOS optical properties of skin *ex vivo* and *in vivo* [1–22]. The main fluorophores and chromophores, as well as their diagnostic value for differentiation of skin lesions versus normal tissue have been evaluated [23, 24]. The applicability of different approaches for data processing was also investigated [25–28]. From then on, she had been patiently gathering spectral data for the development of a robust algorithm for tissue classification [26, 28]. These studies resulted in the creation of a prototype device for diagnosis of cutaneous lesions that goes now through the clinical trials stage. She further focused on optical biopsy of skin with the study of new

 doi: 10.18287/JBPE21.07.040101

optical modalities and combinations of complementary techniques for the diagnosis of pathological tissue alterations [29–35].

A cooperative work between Assoc. Prof. Ekaterina Borisova and Prof. Petya Pavlova from Technical University Sofia, branch Plovdiv, started in 2004, when significant efforts were spent to find suitable method for automated classification of skin diseases using spectra and extracting some etalon distributions. The first result was presented at IX national conference of "Biomedical physics and engineering", Sofia, 2004. Assoc. Prof. Ekaterina Borisova showed a part of this work at Conference on Lasers and Electro-Optics Europe (2007) [25]. Non-traditional techniques were used for testing similarity by applying mathematical transformations from colorimetry. This method provided options to connect the spectrums with the digital images of lesions. The results were presented at XVII International Laser Physics Workshop, (LPHYS'09) in Barcelona [19] and were included in the specialized book "Melanoma in the Clinic – Diagnostics, Management and Complications of Malignancy" [36]. We also tried to involve scientists from other areas expanding the comparative analysis with use of neural networks and presenting the results at technical conference of IFAC "Technology, culture and international stability" [28].

Assoc. Prof. Ekaterina Borisova was always ready to embrace new ideas and scientific horizons, for instance, by adopting multimodal techniques, including multispectral, fluorescence lifetime and Raman imaging/spectroscopy for skin diagnosis/analysis [37–38] and autofluorescence spectroscopy of cutaneous neoplasia under different spectral domain excitation wavelengths [39].

3.2 Autofluorescence and photodiagnosis, photodynamic therapy of gastrointestinal tract

Assoc. Prof. Ekaterina Borisova was also directing her efforts to the improvement of gastrointestinal cancer diagnostics by using endogenous and exogenous fluorescence imaging and spectroscopy. A detailed study on the endogenous fluorophores in the lower part of the gastrointestinal tract investigated with the fluorescence spectroscopy was carried out in the framework of this topic [40–42]. The implementation of a novel technique for tissue investigation – synchronous fluorescence spectroscopy, resulted in better addressing of the endogenous fluorophores observed in tissues [43–46]. The biological origin of the fluorescence contrast between cancerous and healthy gastrointestinal tissue was one of the main investigated areas [47], to determine more sensitive and specific optical markers for tissue differentiation and early detection of gastrointestinal cancer with autofluorescence diagnostics.

Moreover, Assoc. Prof. Ekaterina Borisova also worked on photodiagnosis and photodynamic therapy of gastrointestinal tract. Her work included the investigation of novel photosensitizers and the optimal parameters for their irradiation and photodynamic activation [48–57]. As a result, significant amount of her work was dedicated to the photodynamic diagnosis [48, 58], photodynamic efficacy [59] and therapy as well [60–63].

 doi: 10.18287/JBPE21.07.040101

3.3 Photodynamic opening of blood-brain barrier

Another significant scientific scope of research was extensively studied by Assoc. Prof. Ekaterina Borisova and colleagues – the photodynamic opening of the blood-brain barrier [64] and evaluation of pathways for brain clearing [65], also including the use of different photosensitizers [66], optimizing laser technologies for targeted opening of the blood-brain barrier and targeted drug brain delivery [67, 68].

3.4 Polarization-sensitive optical techniques

Additionally, polarized light-based techniques were also implemented as label-free diagnostic modalities for biomedical applications. Firstly, the polarization effects in autofluorescence spectra were reported [69], later on this work was extended to obtain polarization sensitive excitation-emission matrices for colorectal tumor detection [70]. In 2017 an international scientific "POLHIS" project was initiated with the LPICM, Ecole Polytechnique, France, for digital histology of tissues with Mueller matrix microscopy. Thereafter, the polarimetric diagnosis of tissues became a focus of another cooperation with the Institute of Optical Materials and Technologies, "Acad. J. Malinowski" – Bulgarian Academy of Sciences, yielding several proceedings papers [71–73], one of which was recognized with Best Student Paper Award from the SPIE [74]. Further, a memorandum for cooperation between the IE-BAS and the University of Oulu, Finland, was useful to produce other prolific results in the field of tissue polarimetry [75–77], where one of the manuscripts was awarded with a Cover Page in the Journal of Biophotonics [75]. A currently ongoing project between the IE-BAS and the Department of Biophysics from Manipal School of Life Sciences and Manipal Academy of Higher Education, India, has also demonstrated the important scientific findings on polarimetric detection of the malignant lesions of the digestive system [78] within the framework of the Machine-Learning approach [79]. Also, a review article is submitted and entitled as "Types of spectroscopy and microscopy techniques for cancer diagnosis: a review" to Lasers in Medical Sciences [80]. In memory of Assoc. Prof. Ekaterina Borisova, we are editing a book entitled "Optical Polarimetric Modalities for Biomedical Research" in Springer-Nature [81].

3.5 Modelling and Monte Carlo simulations

During the last few years, in a collaboration with Prof. Igor Meglinski (Oulu, Finland) and Dr. Tatiana Novikova (CRNS, France), Assoc. Prof. Ekaterina Borisova expressed her interest to their pioneering studies dedicated to propagation of cylindrical vector laser beams through turbid tissue-like scattering medium [82–84]. Assoc. Prof. Ekaterina Borisova provided tissue samples to the team and, therefore, the ground-breaking experiments of transferring shaped light carrying orbital angular momentum through the cancerous and non-cancerous tissues [84–86] became possible. Thus, with Katia's input we expect further revolutionary developments in Biomedical Optics and Biophotonics with so-called twisted light.

 doi: 10.18287/JBPE21.07.040101

4 Prolific international collaborations

For many years, together with Alexander Priezzhev and Valery Tuchin, Assoc. Prof. Ekaterina Borisova led the Biophotonics section at the world-famous International Conference Laser Optics (ICLO) in St. Petersburg, was the editor of special issues of the world's leading journals in the field of biophotonics and biomedical optics, collaborated with many scientific groups, including several groups at Saratov State University (in addition to the already mentioned joint publications see more [65, 68, 87–98]), Moscow State University and the Polytechnic of Porto.

In a very prolific way, Ekaterina Borisova had been successfully gathering scientists from different countries and institutions to work together. Recently, in Saratov through the efforts of the Institute of Electronics, Bulgarian Academy of Sciences, together with SSU, SSMU, Institute of Biochemistry and Physiology of Plants and Microorganisms and Precision Mechanics and Control Institute of the Russian Academy of Sciences, the development of a new strategy for the combined treatment of a tumor has begun, namely, the plasmon photothermal and photodynamic anticancer therapies using nanocomposites of gold nanoparticles with a novel type photosensitizer. The first results showed the effectiveness of the approach [98], but unfortunately, they were suspended. Ekaterina was the link between scientific groups from Bulgaria and Russia that synthesized agents and nanocomposites and conducted animal tests. For all of us, the loss of Assoc. Prof. Ekaterina Borisova is very painful. We hope to be able to continue research in memory of her.

Furthermore, Ekaterina Borisova had good collaboration with many Russian groups. During 3 years she has joint projects with Oxana Semyachkina-Glushkovskaya's team in Saratov State University. Assoc. Prof. Ekaterina Borisova was PI of the project from Russian Foundation of Basic Research (2017–2018) "Development of new optical technologies for improvement of diagnostics quality of gastric cancer". The aim of the project was to develop innovative technologies for sensitive diagnosis of the initial stages of gastric cancer and ways to prevent the development of metastases, as well as preventive methods to reduce the incidence of this pathology in risk groups. In 2021, Ekaterina received the grant from Russian Science Foundation. The idea of this project was to develop the specific antibodies for fluorescent gastroscopy and detection of malignant changes in stomach. Assoc. Prof. Ekaterina Borisova was also co-PI of project "Development of a pilot technology for early diagnosis of gastric cancer based on fluorescent gastroscopy using immune antibodies to PD-L1". The project solves the urgent and complex problem of early diagnosis of gastric cancer based on the application of pioneering discoveries in the field of immunology of malignant tumors and the development of a new direction in the molecular diagnosis of cancer based on the use of antibodies to PD-L1 – the ligand of programmed death. Russian-Bulgarian collaboration was very productive, including organization of exchange of students, training courses and publication more than 30 articles in the peer review journals (see Refs. [64–68, 87–99]) as well as preparation of several thesis of candidate of science. She kindly allowed us to publish for the first time the maps of autofluorescence emission of normal skin *in vivo* measured by her in the monograph (Fig. 5.5) [93] and was very proud

about that. The ideas of Ekaterina will be continued in further research at Saratov State University with the sunny memory about the best friend and bright scientist.

In 2019, Luís Oliveira invited Ekaterina Borisova and Irina Larina from the Baylor College of Medicine in Texas, USA, to organize a biophotonics session in the PHOTOPTICS conference, which was held in Malta on February 2020 [100]. Although COVID-19 was starting to spread by that time, their joint efforts brought many worldwide known speakers to Malta to participate in this session, turning it a success. Also, in mid-2019, Ekaterina Borisova invited Luís Oliveira, so that they could both serve as co-editors of a special issue of the Journal Electronics (MDPI), with the title "Advanced Laser Technologies for Biophotonics", which was open for submissions until June 2021 [102].

Another close collaboration between Assoc. Prof. Ekaterina Borisova and Samara National Research University started in 2019 with a joint project "Multivariative Raman and fluorescence diagnosis of cutaneous tumors". Within this project, scientists from Sofia and Samara tried to combine optical techniques in order to increase the efficiency of skin cancer diagnosis. This collaboration provided an opportunity to perform joint studies of *ex vivo* tumors [102] and analyze the *in vivo* data collected both in Sofia and Samara [32], including data that helped to detect such rare tumor as amelanotic melanoma [103]. During her short visit to Samara (November 2019) Assoc. Prof. Ekaterina Borisova presented a number of lectures in Samara State Medical University and in Samara National Research University devoted to fluorescent diagnosis of tumors. One of Ekaterina's lectures was prepared for the junior scientists in the course of XVII Conference on optics and laser physics (run by Samara branch of Lebedev Physical institute of RAS). Collaborators from Sofia and Samara have extensive plans to continue the joint research and experimental work together.

Over the last decade, a number of Assoc. Prof. Ekaterina Borisova's activities involved collaboration with researchers of the Biophotonics Laboratory at University of Latvia led by J. Spigulis. After meetings and discussions at several international conferences (including SFM–2012 in Saratov), Ekaterina's PhD student Alexandra Zhelyazkova participated at the first Biophotonics-Riga conference in August 2013. Good working contacts were established, and next year both Bulgarian ladies came to Riga, this time to the AOMD–8 conference where Ekaterina Borisova presented an invited talk [27]. This conference involved also a working group's meeting of the COST BM1205 action "European network for skin cancer detection using laser imaging" where both Riga and Sofia groups were represented. Regular meetings of this action took place at various European cities (Brussels, Leeds, Sheffield, Floriana, Amsterdam, Porto, Split, Angers, Bari), which made possible to meet Assoc. Prof. Ekaterina Borisova several times a year and to exchange the latest research news of Riga and Sofia groups. Personal exchanges have started (Alexandra to Riga and Dr. Ilona Kuzmina to Sofia) which resulted in a joint paper [29] presented in Ekaterina's invited talk at the Biophotonics Riga – 2017 conference. The next, maybe most important step in our collaboration was the joint Bulgarian-Latvian research project "Multispectral and fluorescent imaging of skin tumours" initiated by Katia late 2017 in the frame of collaboration agreement between Bulgarian and Latvian Academies of Sciences. It included personal exchanges, so opening a

 doi: 10.18287/JBPE21.07.040101

possibility for J. Spigulis to present results of the Riga group at the ICSQE–20 conference in Nessebar [104] and to visit Katia's lab in September 2018. In summer 2019 two researchers from Riga (I. Lihacova and A. Lihacev) visited the colleagues in Sofia, and Katia paid a return visit to Riga in frame of this project in November 2019. Soon after that her student Deyan Ivanov visited Riga where joint measurements of the *ex vivo* skin lesion samples (brought from Sofia) were taken; the results were reported in the SPIE BIOS'2020 conference [37]. After the Covid–19 pandemic started in March 2020, only virtual meetings were allowed; two of them included the Ekaterina's invited talk at the Biophotonics Riga – 2020 conference in August [33] and the invited talk of J. Spigulis at the ICSQE–21 conference [105] in September, 2020. Assoc. Prof. Ekaterina Borisova chaired the virtual session in this conference, full of optimism as usually.

"I have always admired Katia's energy and optimism, as well as the fact that the difficult position in which she had to compete with the rest of the world did not stop her from doing it anyway," writes Dick Sterenborg from the Academic Medical Centre in Amsterdam and the Netherlands Cancer Institute. At her invitation, I twice traveled to Nessebar, next to the Burgas, Bulgaria, where she created a pleasant and comfortable atmosphere at the conference, and together we tried to get a grant, but it never came to real cooperation, her passing away prevented.



Fig. 2 Assoc. Prof. Ekaterina Borisova at the VII International Symposium "TOPICAL PROBLEMS OF BIOPHOTONICS – 2019" (TPB-2019) held on board of a river ship cruising along the Volga river (Russia) from July 27 through July 31, 2019, organized by the Institute of Applied Physics of the Russian Academy of Sciences and the Privolzhskiy Research Medical University as a continuation of the previous TPB symposia held biannually from 2007 through 2017 that attracted leading experts in the field of biophotonics from around the world.

Ekaterina Borisova's capability to organize and host scientific events has resulted in the completion of numerous international meetings in Bulgaria and all over the world. She gained experience in hosting international scientific events being the chair of the 15th International School on Quantum Electronics which took place from 15 to 19 September 2008 in Bourgas, Bulgaria, established by Institute of Electronics, Bulgarian Academy of Sciences [106]. For the 23th Annual International Laser Physics Workshop (LPHYS'14) held from July 14 to July 18, 2014 in the city of

 doi: 10.18287/JBPE21.07.040101

Sofia, Bulgaria [107] and hosted by IE-BAS Assoc. Prof. Ekaterina Borisova was leading the local organizing committee. She was in Advisory & Program Committee of the 26th Annual International Laser Physics Workshop [108]. In 2010, she won the invitation to hold in Bulgaria in 2011 the 19th meeting of the famous annual International Conference on Advanced Laser Technologies (ALT'11). Her brilliantly prepared proposal successfully competed with that prepared by the Italian colleagues. The ALT'11 meeting was held in Golden Sands resort from 3 to 8 September 2011. On institutional level, it was co-organized by the Institute of Electronics, Bulgarian Academy of Sciences; Prokhorov General Physics Institute, Russian Academy of Sciences; International Laser Center of M.V. Lomonosov Moscow State University and the Center for Laser Technology and Materials, Russian Academy of Sciences. As the Chair-person of the local organizing committee Ekaterina Borisova succeeded in holding a very successful conference. According to general opinion of the participants (see photo in Fig. 3) the ALT'11 meeting was among the best ones held in previous years. Selected papers presented at the conference were published in the Special Section on Laser Technologies for Biomedical Applications of the high-ranking Journal of Biomedical Optics [109].



Fig. 3 Group photo of attendees of the ALT'11 meeting (Golden Sands resort, Bulgaria, from 3 to 8 September 2011), organized by Ekaterina Borisova (first on the left).

5 Conclusion

In a recent interview to the OSA journal Optics & Photonics News [110] Assoc. Prof. Ekaterina Borisova said: "I am already the head of the "Biophotonics" laboratory at the IE-BAS. I do have a plenty of research plans – to raise the number of optical spectroscopic techniques and instruments that we use now for biological tissue investigations; to train new junior scientists and students in the field of biophotonics; to work for an enlargement of the role of spectroscopic techniques for early detection of cancer as primary and add-on tools in clinical diagnostics." Those words embodied her lively plans for the future, a future she was robbed of.

All those who had the privilege to know, study, work and interact with Assoc. Prof. Ekaterina Borisova feel the immense pain of the huge loss imposed, hence, being deprived of a wonderful colleague, teacher, leader, supervisor, friend with smart sense of humor and competency in all aspects of life, prolific scientist, bright and unique person (see Fig. 2). Assoc. Prof. Ekaterina Borisova's

great legacy is to continue the work on her ideas, reach the goals she had set and follow her inspiration.

We are grateful for the given opportunity to knew Katia, to work with her and to be her friends! You will stay always in our hearts, Katia…

Acknowledgements

We would like to acknowledge the support from the National Science Fund of the Bulgarian Ministry of Education and Science (NSFB-MES) under all current projects involving Assoc. Prof. Ekaterina Borisova, which are grant numbers: #DN 18-8; #KP06-N29/11/18.12.18; #KP06-N28/11/14.12.2018; #KP06-Russia-9/2020; #KP-06-N23/8; #KP-06/N38/13; #KP06-India-8/07.08.2019; #KP-06-KOST-6. Also, projects under NRRI #DO1-401/18.12.2020 and #D01-392/18.12.2020.

References

1. E. G. Borisova, L. A. Avramov, "Laser system for optical biopsy and in vivo study of the human skin," Proceedings of SPIE 4397, 405–409 (2001).
2. P. Djorev, E. Borisova, and L. Avramov, "Interaction of the IR laser radiation with human skin - Monte-Carlo simulation," Proceedings of SPIE 5226, 403–407 (2003).
3. E. G. Borisova, P. P. Troyanova, V. P. Stoyanova, and L. A. Avramov, "Laser-induced fluorescence spectroscopy of benign and malignant cutaneous lesions," Proceedings of SPIE 5830, 394–398 (2005).
4. L. Avramaov, E. Borisova, P. D. Townsend, and L. A. Valberg, "Potential and Current Uses Of Luminescence In Medical Diagnosis," Materials Science Forum 480–481, 411–416 (2005).
5. E. Borisova, I. Angelov, V. Mantareva, D. Petrova, P. Townsend, L. Valberg, and L. Avramov, "Tumour detection by exogenous fluorescent dyes using new generation photomultiplier tubes," Proceedings of SPIE 5830, 399–403 (2005).
6. E. Borisova, P. Trojanova, and L. Avramov, "Reflectance measurements of skin lesions – Noninvasive method for diagnostic evaluation of pigmented neoplasia," Proceedings of SPIE 5862, 58620A (2005).
7. E. Borisova, L. Avramov, and P. Troyanova, "Light-induced fluorescence spectroscopy and optical coherence tomography of basal cell carcinoma," Journal of Innovative Optical Health Sciences 2(03), 261–268 (2009).
8. E. Borisova, P. Troyanova, and L. Avramov, "Optical biopsy of non-melanin pigmented cutaneous benign and malignant lesions," Proceedings of SPIE 6257, 62570U (2006).
9. E. Borisova, I. Bliznakova, N. Momchilov, P. Troyanova, and L. Avramov, "Fluorescence spectroscopy investigations of cutaneous tissues," AIP Conference Proceedings 899, 465–466 (2007).
10. I. Bliznakova, E. Borisova, and L. Avramov, "Laser- and light-induced autofluorescence spectroscopy of human skin in dependence on excitation wavelengths," Acta Physica Polonica A 112(5), 1131–1136 (2007).
11. E. Borisova, I. Bliznakova, P. Troyanova, and L. Avramov, "Light-induced autofluorescence of animal skin used in tissue optical modeling," Optics InfoBase Conference Papers 6628, 60 (2007).
12. E. G. Borisova, E. Nikolova, P. P. Troyanova, and L. A. Avramov, "Autofluorescence and diffuse reflectance spectroscopy of pigment disorders in human skin," Journal of Optoelectronics and Advanced Materials 10(3), 717–722 (2008). ISSN: 14544164.
13. P. Troyanova, E. Borisova, and L. Avramov, "Fluorescence and reflectance properties of hemoglobin-pigmented skin disorders," Proceedings of SPIE 6734, 673415 (2007).
14. E. Borisova, P. Troyanova, and L. Avramov, "Influence of measurement geometry on the human skin reflectance spectra detection," Proceedings of SPIE 6734, 673416 (2007).
15. E. Borisova, P. Troyanova, P. Pavlova, and L. Avramov, "Diagnostics of pigmented skin tumors based on laser-induced autofluorescence and diffuse reflectance spectroscopy," Quantum Electronics 38(6), 597–605 (2008).
16. E. Borisova, P. Troyanova, E. Nikolova, and L. Avramov, "Cutaneous tumors in vivo investigations using fluorescence and diffuse reflectance techniques," Proceedings of SPIE 6791, 679105 (2008).
17. E. Borisova, D. Dogandjiiska, I. Bliznakova, L. Avramov, E. Pavlova, and P. Troyanova, "Multispectral autofluorescence diagnosis of non-melanoma cutaneous tumors," Proceedings of SPIE 7368, 736823 (2009).
18. E. Borisova, L. Avramov, P. Pavlova, E. Pavlova, and P. Troyanova, "Qualitative optical evaluation of malignancies related to cutaneous phototype," Proceedings of SPIE 7563, 75630X (2010).

19. P. Pavlova, E. Borisova, L. Avramov, E. Petkova, and P. Troyanova, "Investigation of Relations between Skin Cancer Lesions' Images and Their Fluorescent Spectra," Laser Physics 20(3), 596–603 (2010).
20. E. Borisova, P. Pavlova, E. Pavlova, P. Troyanova, and L. Avramov, "Optical biopsy of human skin – A tool for cutaneous tumours' diagnosis," International Journal Bioautomation 16 (1), 53–72 (2012).
21. V. Mantareva, D. Petrova, L. Avramov, I. Angelov, E. Borisova, M. Peeva, and D. Wöhrle, "Long wavelength absorbing cationic Zn(II)-phthalocyanines as fluorescent contrast agents for B16 pigmented melanoma," Journal of Porphyrins and Phthalocyanines 9(1), 47–53 (2005).
22. E. Drakaki, E. Borisova, M. Makropoulou, L. Avramov, A. A. Serafetinides, and I. Angelov, "Laser induced autofluorescence studies of animal skin used in modeling of human cutaneous tissue spectroscopic measurements," Skin Research and Technology 13(4), 350–359 (2007).
23. A. Zhelyazkova, E. Borisova, L. Angelova, E. Pavlova, and M. Keremedchiev "Excitation-emission matrices measurements of human cutaneous lesions – Tool for evaluation of fluorescence origin," Proceedings of SPIE 9032, 90320A (2013).
24. G. Borisova, P. Angelova, and P. Pavlova, "Endogenous and exogenous fluorescence skin cancer diagnostics for clinical applications," IEEE Journal of Selected Topics in Quantum Electronics 20(2), 6606819 (2014).
25. E. Borisova, P. Pavlova, P. Troyanova, and L. Avramov, "Automation of cancer diagnosis based on colorimetric transformation of cutaneous reflectance spectra," Optics InfoBase Conference Papers 4386657, 73192 (2007).
26. E. Borisova, E. Pavlova, T. Kundurjiev, P. Troyanova, T. Genova, and L. Avramov, "Light-induced autofluorescence and diffuse reflectance spectroscopy in clinical diagnosis of skin cancer," Proceedings of SPIE 9129, 91291O (2014).
27. E. Borisova, Al. Jeliazkova, E. Pavlova, P. Troyanova, T. Kundurdjiev, P. Pavlova, and L. Avramov, "Reflectance spectroscopy of pigmented cutaneous benign and malignant lesions," Proceedings of SPIE 9421, 94210I (2014).
28. Pavlova P., N. Shakev, and E. Borisova, "Comparative analysis of methods for ascertainment the similarity between reflected spectra obtained from skin lesions," IFAC PapersOnLine 52(25), 365–369 (2019).
29. E. Borisova, T. Genova, P. Troyanova, I. Terziev, V. Zakharov, I. Bratchenko, M. Lomova, D. Gorin, and L. Avramov, "Microscopic and macroscopic spectral peculiarities of cutaneous tumours," Proceedings of SPIE 10592, 1059202 (2017).
30. E. Borisova, T. Genova-Hristova, P. Troyanova, I. Terziev, E. A. Genina, A. N. Bashkatov, O. Semyachkina-Glushkovskaya, V. Tuchin, and L. Avramov, "Optical UV-VIS-NIR spectroscopy of benign, dysplastic and malignant cutaneous lesions ex vivo," Proceedings of SPIE 10685, 106853T (2018).
31. E. Borisova, T. Genova-Hristova, P. Troyanova, E. Pavlova, I. Terziev, O. Semyachkina-Glushkovskaya, M. Lomova, E. Genina, G. Stanciu, D. Tranca, and L. Avramov, "Multispectral detection of cutaneous lesions using spectroscopy and microscopy approaches," Proceedings of SPIE 10467, 104670M (2018).
32. E. Borisova, A. Gisbrecht, T. Genova-Hristova, P. Troyanova, E. Pavlova, N. Penkov, I. Bratchenko, V. Zakharov, I. Lihachova, I. Kuzmina, and J. Spigulis, "Multispectral autoflourescence detection of skin neoplasia using steady-state techniques," Proceedings of SPIE 11047, 1104704 (2019).
33. E. Borisova, T. Genova, V. Mircheva, P. Troyanova, I. Bratchenko, L. Bratchenko, Y. Khristoforova, V. Zakharov, I. Lihacova, A. Lihacovs, and J. Spigulis, "Multispectral fluorescence detection of pigmented cutaneous tumours," Proceedings of SPIE 11585, 1158504 (2020).
34. Y. A. Khristoforova, I. A. Bratchenko, L. A. Bratchenko, O. O. Myakinin, D. N. Artemyev, A. A. Moryatov, S. V. Kozlov, E. G. Borisova, T. I. Genova, P. P. Troyanova, and V. P. Zakharov, "Optical biopsy of skin cancer based on Raman and fluorescence spectroscopy," Proceedings of SPIE 11582, 115821K (2020).
35. V. Mircheva, L. Zaharieva, S. Ilyov, P. Troyanova, I. Lihacova, A. Lihacovs, I. Bratchenko, L. Bratchenko, Y. Khristoforova, and V. Zakharov, "Near-infrared autofluorescence spectroscopy and photobleaching detection of melanin-pigmented cutaneous neoplasia," Journal of Physics: Conference Series 1859 (1), 012044 (2021).
36. P. Pavlova, E. Borisova, L. Avramov, E. Petkova, and P. Trotanova, "Investigation of Relations between Skin Cancer Lesions' Images and Their Reflectance and Fluorescent Spectra," Chapter 6 In Melanoma in the Clinic – Diagnostics, Management and Complications of Malignancy, M. Murph (Ed.), InTech Open Access Publisher, 87–104 (2011). ISBN: 978-953-307-571-6.
37. J. Spigulis, I. Kuzmina, V. Lukinsone, M. Tamošiūnas, I. Oshina, L. Ozolina, A. Maslobojeva, M. Kuzminskis, D. Ivanov, and E. Borisova, "Towards combined multispectral, FLIM and Raman imaging for skin diagnostics," Proceedings of SPIE 11232, 112320N (2020).
38. L. Bratchenko, E. Abrosimova, S. Stafeev, E. Tupikova, E. Borisova, and I. Bratchenko, "Conventional Raman and surface-enhanced Raman spectroscopy for human skin components analysis," In 2020 International Conference on Information Technology and Nanotechnology (ITNT), 26–29 May, Samara, Russia (2020).
39. E. Borisova, D. Ivanov, B. Kolev, T. Genova, V. Mircheva, S. Ilyov, L. Zaharieva, I. Lihachova, A. Lihachovs, J. Spigulis, and P. Troyanova, "Autofluorescence spectroscopy of cutaneous neoplasia under ultraviolet, visible and near infrared excitation," Proceedings of SPIE 11363, 113630Z (2020).
40. E. Borisova, L. Plamenova, M. Keremedchiev, B. Vladimirov, and L. Avramov, "Endogenous and exogenous fluorescence of gastrointestinal tumors-initial clinical observations," Proceedings of SPIE 8770, 87701C (2013).

41. E. Borisova, L. Angelova, A. Zhelyakova, T. Genova, O. Semyachkina-Glushkovskaya, M. Keremedchiev, N. Penkov, B. Vladimirov, and L. Avramov, "Endogenous and exogenous fluorescence spectroscopy of gastrointestinal tumours – In vitro studies," Journal of Optoelectronics and Advanced Materials 16(9–10), 1196–1205 (2014). ISSN: 1454-4164.
42. E. Borisova, Ts. Genova, O. Semyachkina-Glushkovskaya, N. Penkov, I. Terziev, and B. Vladimirov, "Excitation-emission matrices (EEMs) of colorectal tumors — tool for spectroscopic diagnostics of gastrointestinal neoplasia," Frontiers of Optoelectronics 10(3), 292–298 (2017).
43. E. Borisova, T. Genova, A. Zhelyazkova, L. Angelova, M. Keremedchiev, N. Penkov, I. Terziev, B. Vladimirov, O. Semyachkina-Glukhovskaya, and L. Avramov, "Synchronous autofluorescence spectroscopy of gastrointestinal tumours – Tool for endogenous fluorophores evaluation," Optoelectronics and Advanced Materials, Rapid Communications 9(9–10), 1234–1238 (2015).
44. T. Genova, E. Borisova, A. Zhelyazkova, N. Penkov, B. Vladimirov, I. Terziev, O. Semyachkina-Glushkovskaya, and L. Avramov, "Colorectal cancer stage evaluation using synchronous fluorescence spectroscopy technique," Optical and Quantum Electronics 48(8), 378 (2016).
45. E. Borisova, O. Semyachkina-Glushkovskaya, T. Genova, N. Penkov, I. Terziev, B. Vladimirov, and L. Avramov, "Synchronous fluorescence spectroscopy of colon neoplasia," Proceedings of SPIE 10336, 1033602 (2017).
46. E. Borisova, T. Genova-Hristova, N. Penkov, I. Terziev, P. Troyanova, B. Vladimirov, and L. Avramov, "Synchronous fluorescence spectroscopy of soft tissues – Tool for diagnostics of malignant lesions," Proceedings of 2018 International Conference Laser Optics 8435383, 493 (2018).
47. T. Genova, E. Borisova, N. Penkov, B. Vladimirov, A. Zhelyazkova, and L. Avramov, "Excitation-emission matrices and synchronous fluorescence spectroscopy for cancer diagnostics in gastrointestinal tract," Quantum Electronics 46(6), 510–514 (2016).
48. E. Borisova, O. Semyachkina-Glushkovskaya, N. Navolokin, V. Mantareva, I. Angelov, I. Agranovich, A. Khorovodov, N. Shushunova, A. Bodrova, I. Fedosov, A. Namykin, A. Abdurashitov, and L. Avramov, "Photodynamic diagnostics of stress-induced gastrointestinal neoplasia in laboratory animals using 5-Aminolevulinic acid and Al-phthalocyanine," Proceedings of SPIE 10501, 105011E (2018).
49. I. Agranovich, A. Khorovodov, M. Kanevsky, T. Genova-Hristova, A. Gisbrecht, I. Angelov, V. Mantareva, N. Navolokin, O. Semyachkina-Glushkovskaya, and E. Borisova, "Detection of stress-induced gastrointestinal lesions using Al-phythalocynanines in experimental animals," Proceedings of SPIE 11047, 1104709 (2019).
50. T. Genova, A. Khorovodov, A. Terskov, M. Kanevsky, A. Gisbrecht, L. Avramov, and O. Semyachkina-Glushkovskaya, "Stomach and intestine neoplasia fluorescence detection using 5-ALA/PpIX photosensitization," Proceedings of SPIE 11047, 1104708 (2019).
51. E. Borisova, T. Genova, A. Khorovodov, I. Agranovich, M. Kanevskiy, S. Konnova, I. Angelov, V. Mantareva, N. Navolokin, and O. Semyachkina-Glushkovskaya, "ALA/PpIX photodiagnosis of stress-induced gastrointestinal primary tumors and metastases in experimental animals," Proceedings of SPIE 11079, 110790N (2019).
52. I. Agranovich, E. Borisova, N. Navolokin, A. Bucharskaya, G. Maslyakova, A. Shirokov, A. Abdurashitov, I. Angelov, A. Khorovodov, A. Terskov, A. Mamedova, M. Klimova, and O. Semyachkina-Glushkovskaya, "Phenomenon of atypical vascular effects of epinephrine and an increase of photodynamic response by nitroglycerin in rats with colon adenocarcinoma: adrenergic and nitrergic mechanisms and novel applied aspects," Biomedical Optics Express 10(8), 4115–4125 (2019).
53. E. Borisova, T. Genova, A. Yakimansky, V. Mantareva, I. Angelov, A. Gisbrecht, Al. Khorovodov, I. Agranovich, M. Klimova, and O. Semyachkina-Glushkovskaya, "Conjugation of Zn (II) phthalocyanine with polymeric brushes for improved photodiagnostics and photodynamic therapy of gastric tumours," Proceedings of SPIE 11457, 114570R (2020).
54. E. Borisova, M. Kanevskiy, S. Konnova, A. Khorovodov, I. Agranovich, T. Genova, L. Avramov, N. Navolokin, and O. Semyachkina-Glushkovskaya, "5-ALA/PpIX photodiagnosis of stress-induced gastrointestinal metastatic tumours in laboratorial animals," Proceedings of SPIE 11363, 113630U (2020).
55. I. Agranovich, A. Khorovodov, M. Kanevsky, T. Genova, A. Gisbrecht, I. Angelov, V. Mantareva, N. Navolokin, O. Semyachkina-Glushkovskaya, and E. Borisova, "Stress-induced neoplasia detection in the lower part of gastrointestinal tract of rats using phthalocyanines," Journal of Physics: Conference Series 1859(1), 012038 (2021).
56. V. Mantareva, V. Kussovski, I. Angelov, E. Borisova, L. Avramov, G. Schnurpfeil, and D. Wöhrle, "Photodynamic activity of water-soluble phthalocyanine zinc(II) complexes against pathogenic microorganisms," Bioorganic & Medicinal Chemistry 15(14), 4829–4835 (2007).
57. V. Kussovski, V. Mantareva, I. Angelov, P. Orozova, D. Wöhrle, G. Schnurpfeil, E. Borisova, and L. Avramov, "Photodynamic inactivation of aeromonas hydrophila by cationic phthalocyanines with different hydrophobicity," FEMS Microbiology Letters 294(2), 133–140 (2009).
58. A. Pavlov, E. Borisova, O. Pavlova, I. Agranovich, A. Khorovodov, A. Terskov, A. Mamedova, M. Klimova, L. Avramov, and O. Semyachkina-Glushkovskaya, "Photodynamic diagnostics of early gastric cancer: Complexity measures of gastric microcirculation and new model of metastatic adenocarcinoma of rat stomach," Journal of Innovative Optical Health Sciences 12(2), 1950007 (2019).

59. V. Mantareva, A. Kril, I. Angelov, R. Dimitrov, E. Borisova, and L. Avramov, "Effects of the position of galactose units to Zn(II) phthalocyanine on the uptake and photodynamic activity towards breast cancer cells," Proceedings of SPIE 8427, 842743 (2012).
60. I. Angelov, V. Mantareva, V. Kussovski, D. Woehrle, E. Borisova, and L. Avramov, "Improved antimicrobial therapy with cationic tetra- and octa-substituted phthalocyanines," Proceedings of SPIE 7027, 702717 (2008).
61. V. N. Mantareva, I. Angelov, D. Wöhrle, E. Borisova, and V. Kussovski, "Metallophthalocyanines for antimicrobial photodynamic therapy," Journal of Porphyrins and Phthalocyanines 17(6–7), 399–416 (2013).
62. N. Momchilov, I. Bliznakova, E. Borisova, P. Troyanova, and L. Avramov, "Development of low-cost photodynamic therapy device," Acta Physica Polonica Series A 112(5), 1125–1130 (2007).
63. E. Borisova, D. Kyurkchiev, K. Tumangelova-Yuzeir, I. Angelov, T. Genova-Hristova, O. Semyachkina-Glushkovskaya, and K. Minkin, "Evaluation of photodynamic treatment efficiency on glioblastoma cells received from malignant lesions: Initial studies," Proceedings of SPIE 10716, 1071602 (2017).
64. O. Semyachkina-Glushkovskaya, J. Kurths, E. Borisova, S. Sokolovski, V. Mantareva, I. Angelov, A. Shirokov, N. Navolokin, N. Shushunova, A. Khorovodov, M. Ulanova, M. Sagatova, I. Agranivich, O. Sindeeva, A. Gekalyuk, A. Bodrova, and E. Rafailov, "Photodynamic opening of blood-brain barrier," Biomedical Optics Express 8(11), 5040–5048 (2017).
65. O. Semyachkina-Glushkovskaya, V. Chehonin, E. Borisova, I. Fedosov, A. Namykin, A. Abdurashitov, A. Shirokov, B. Khlebtsov, Y. Lyubun, N. Navolokin, M. Ulanova, N. Shushunova, A. Khorovodov, I. Agranovich, A. Bodrova, M. Sagatova, A. E. Shareef, E. Saranceva, T. Iskra, M. Dvoryatkina, E. Zhinchenko, O. Sindeeva, V. Tuchin, and J. Kurths, "Photodynamic opening of the blood-brain barrier and pathways of brain clearing," Journal of Biophotonics 11(8), e201700287 (2018).
66. O. Semyachkina-Glushkovskaya, E. Borisova, V. Mantareva, I. Angelov, I. Eneva, A. Terskov, A. Mamedova, A. Shirokov, A. Khorovodov, M. Klimova, I. Agranovich, I. Blokhina, N. Lezhnev, and J. Kurths, "Photodynamic opening of the blood-brain barrier using different photosensitizers in mice," Applied Sciences (Switzerland) 10(11), 33 (2020).
67. O. V. Semyachkina-Glushkovskaya, A. S. Abdurashitov, E. I. Saranceva, E. G. Borisova, A. A. Shirokov, and N. V. Navolokin, "Blood-brain barrier and laser technology for drug brain delivery," Journal of Innovative Optical Health Sciences 10(51), 1730011 (2017).
68. O. V. Semyachkina-Glushkovskaya, E. U. Rafailov, S. G. Sokolovsky, E. G. Borisova, V. Mantareva, I. Angelov, A. Shirokov, N. Navolokin, N. A. Shushunova, A. P. Khorovodov, A. V. Terskov, A. A. Bodrova, M. V. Ulanova, E. Shrif, V. V. Tuchin, and J. Kurths, "The laser technologies of targeted opening of blood-brain barrier for drug brain delivery," Proceedings of 2018 International Conference Laser Optics (ICLO) 8435846, 501 (2018).
69. E. Borisova, L. Angelova, Al. Jeliazkova, Ts. Genova, E. Pavlova, P. Troyanova, and L. Avramov, "Polarization effects in cutaneous autofluorescent spectra," Proceedings of SPIE 9129, 91292G (2014).
70. E. Borisova, T. Genova, A. Zhelyazkova, L. Angelova, M. Keremedchiev, N. Penkov, and L. Avramov, "Polarization sensitive excitation-emission matrices for detection of colorectal tumours – initial investigations," Journal of Physics: Conference Series 594, 012031 (2015).
71. D. Ivanov, E. Borisova, T. Genova, L. Nedelchev, and D. Nazarova, "Tissue polarimetric discrimination analysis of skin and colon histological samples," AIP Conference Proceedings 2075, 170017 (2019).
72. D. Ivanov, V. Strijkova, L. Nedelchev, D. Nazarova, and E. Borisova, "Visualizing Healthy and Malignant Tissues via Polarized Light Imaging and Chemical Staining," Journal of Physics and Technology 3(1), 14–17 (2019).
73. D. Ivanov, R. Ossikovski, T. Novikova, P. Li, E. Borisova, T. Genova, L. Nedelchev, and D. Nazarova, "Tissue polarimetric study I: In search of reference parameters and depolarizing Mueller matrix model of ex vivo colon samples," Proceedings of SPIE 11075, 1107514 (2019).
74. D. Ivanov, T. Genova-Hristova, E. Borisova, L. Nedelchev, and D. Nazarova, "Multiwavelength polarimetry of gastrointestinal ex vivo tissues for tumor diagnostic improvement," Proceedings of SPIE 11047, 1104707 (2019).
75. D. Ivanov, V. Dremin, A. Bykov, E. Borisova, T. Genova, A. Popov, R. Ossikovski, T. Novikova, and I. Meglinski, "Colon cancer detection by using Poincaré sphere and 2D polarimetric mapping of ex vivo colon samples," Journal of Biophotonics 13(8), e202000082 (2020).
76. D. Ivanov, V. Dremin, E. Borisova, A. Bykov, T. Novikova, I. Meglinski, and R. Ossikovski, "Polarization and depolarization metrics as optical markers in support to histopathology of ex vivo colon tissue," Biomedical Optics Express 12(7), 4560–4572 (2021).
77. D. Ivanov, V. Dremin, E. Borisova, A. Bykov, I. Meglinski, T. Novikova, and R. Ossikovski, "Symmetric decomposition of Mueller matrices reveals a new parametric space for polarimetric assistance in colon cancer histopathology," Proceedings of SPIE 11646, 1164614 (2021).
78. S. Ilyov, D. Ivanov, Ts. Genova, V. Mircheva, L. Zaharieva, B. Kolev, B. Vladimirov, H. Valkov, N. Mazumder, K. Sindhoora, O. Semyachkina-Glushkovskaya, L. Avramov, and E. Borisova, "Reflectance polarization ex vivo measurements of gastrointestinal carcinoma lesions for cancer diagnostics," Journal of Physics: Conference Series 1859, 012041 (2021).

79. K. M. Sindhoora, K. U. Spandana, D. Ivanov, E. Borisova, U. Raghavendra, S. Rai, S. P. Kabekkodu, K. K. Mahato, and N. Mazumder, "Machine-learning-based classification of Stokes-Mueller polarization images for tissue characterization," Journal of Physics: Conference Series 1859, 012045 (2021).
80. K. M. Sindhoora, Y. Kistenev, E. Borisova, D. Ivanov, O. Zakharova, A. Boyko, D. Vrazhnov, D. Gopal, S. Chakrabarti, S. Prasada K, and N. Mazumder "Types of spectroscopy and microscopy techniques for cancer diagnosis: a review," Lasers in Medical Sciences [to be published].
81. N. Mazumder, Y. Kistenev, E. Borisova and S. Prasada K. (Eds.), "Optical Polarimetric Modalities for Biomedical Research," Springer-Nature [to be published].
82. A. Doronin, N. Vera, J. P. Staforelli, P. Coelho, and I. Meglinski, "Propagation of cylindrical vector laser beams in turbid tissue-like scattering medium," Photonics 6(2), 56 (2019).
83. A. Doronin, N. Vera, J. Staforelli, T. Novikova, and I. Meglinski, "Perspectives of optical diagnosis with vector light beams," Proceedings of SPIE 10873, 108730K (2019).
84. I. Meglinski, "Spin Angular Momentum of Light in Digital Histopathology," In International Webinar Conference on Lasers, Optics, Photonics & Sensors (LOPS 2021), 12–13 June, Virtual Conference (2021).
85. I. Meglinski, "Vector Light in Biomedical Diagnosis," Horizons of Optics, Photonics and Emerging Sciences (HOPES), IEEE Webinar series (2020).
86. I. Meglinski, N. Vera, J. P. Staforelli, and A. Doronin, "Twisted structured light for tissue diagnosis," In 8th International Conference on Photonics, Optics and Laser Technology – PHOTOPTICS 2020, 27–29 February, Valletta, Malta (2020).
87. O. Semyachkina-Glushkovskaya, A. Pavlov, J. Kurths, E. Borisova, A. Gisbrecht, O. Sindeeva, A. Abdurashitov, A. Shirokov, N. Navolokin, E. Zinchenko, A. Gekalyuk, M. Ulanova, D. Zhu, Q. Luo, and V. Tuchin, "Optical monitoring of stress-related changes in the brain tissues and vessels associated with hemorrhagic stroke in newborn rats," Biomedical Optics Express 6(10), 4088–4097 (2015).
88. O. Sindeeva, E. Borisova, A. Abdurashitov, E. Zhinchenko, A. Gekalyuk, M. Ulanova, A. E. Sharif, V. Razubaeva, S. Serov, L. Yankovskaya, V. V. Tuchin, and O. Semyachkina-Glushkovskaya, "The stress-related changes in the cerebral blood flow in newborn rats with intracranial hemorrhage: metabolic and endothelial mechanisms," Journal of Biomedical Photonics & Engineering 1(4), 248–254 (2016).
89. O. Semyachkina-Glushkovskaya, J. Kurths, A. N. Pavlov, E. G. Borisova, A. S. Abdurashitov, D. Zhu, P. Li, Q. Luo, and V. V. Tuchin, "Silent Vascular Catastrophes in the Brain in Term Newborns: Strategies for Optical Imaging," IEEE Journal of Selected Topics in Quantum Electronics 22(3), 88–101 (2016).
90. O. Semyachkina-Glushkovskaya, E. Borisova, A. Namikin, I. Fedosov, A. Abdurashitov, E. Zhinchenko, A. Gekalyuk, M. Ulanova, V. Rezunbaeva, L. Avramov, D. Zhu, Q. Luo, and V. Tuchin, "Hypoxia and Neonatal Haemorrhagic Stroke: Experimental Study of Mechanisms," Advances in Experimental Medicine and Biology 923, Oxygen Transport to Tissue XXXVIII, Springer International Publishing Switzerland, 173–179 (2016).
91. O. Semyachkina-Glushkovskaya, E. Borisova, M. Abakumov, D. Gorin, L. Avramov, I. Fedosov, A. Namykin, A Abdurashitov, A. Serov, A. Pavlov, E. Zinchenko, V. Lychagov, N. Navolokin, A. Shirokov, G. Maslyakova, D. Zhu, Q. Luo, V. Chekhonin, V. Tuchin and J. Kurths, "The Stress and Vascular Catastrophes in Newborn Rats: Mechanisms Preceding and Accompanying the Brain Hemorrhages," Frontiers in Physiology 7, 210 (2016).
92. V. V. Tuchin, E. Borisova, M. Jędrzejewska-Szczerska, M. J. Leahy, F. S. Pavone, J. Popp, and J. Pozo, "A special issue on Biophotonics in Europe," Frontiers of Optoelectronics 10(3), 203–210 (2017).
93. V. V. Tuchin, Tissue Optics: Light Scattering Methods and Instruments for Medical Diagnostics, 3rd ed., SPIE Press, Bellingham, WA (2015).
94. O. Semyachkina-Glushkovskaya, E. Borisova, S. Sokolovski, V. Mantareva, I. Angelov, A. Shirokov, N. Navolokin, N. Shushunova, A. Khorovodov, M. Ulanova, M. Sagatova, I. Agranivich, A. Bodrova, E. Rafailov, and V. Tuchin, "Laser-induced generation of singlet oxygen: new strategies in the treatment of brain tumor," In International Conference on Photonics and Imaging in Biology and Medicine, 26–28 September, Suzhou, China (2017). ISBN: 978-1-943580-35-4.
95. O. Semyachkina-Glushkovskaya, E. U. Rafailov, S. G. Sokolovsky, E. G. Borisova, V. Mantareva, I. Angelov, A. Shirokov, N. Navolokin, N. A. Shushunova, A. P. Khorovodov, A. V. Terskov, A. A. Bodrova, M. V. Ulanova, E. Shrif, V. V. Tuchin, and J. Kurths, "The Laser Technologies of Targeted Opening of Blood-Brain Barrier for Drug Brain Delivery," In IEEE Conference Proceedings: International Conference Laser Optics, 4–8 June, Saint Petersburg, Russia (2018). ISBN: 978-1-5386-3612-1.
96. O. Semyachkina-Glushkovskaya, J. Kurths, E. Borisova, S. Sokolovski, V. Mantareva, I. Angelov, A. Shirokov, N. Navolokin, N. Shushunova, A. Khorovodov, M. Ulanova, M. Sagatova, I. Agranivich, O. Sindeeva, A. Gekalyuk, A. Bodrova, and E. Rafailov, "Photodynamic opening of blood-brain barrier: non-invasive approaches and age differences," In the 26th International Conference on Advanced Laser Technologies, 9–14 September, Tarragona, Spain (2018).
97. A. N. Bashkatov, V. P. Zakharov, A. B. Bucharskaya, E. G. Borisova, Y. A. Khristoforova, E. A. Genina, and V. V. Tuchin, "Malignant Tissue Optical Properties," Chapter 1 in Multimodal Optical Diagnostics of Cancer, V. V.

Tuchin, J. Popp, and V. Zakharov (Eds.), Springer Nature Switzerland AG, Cham, Switzerland, 3–106 (2020). ISBN 978-3-030-44593-5.
98. O. Semyachkina-Glushkovskaya, D. Postnov, A. Lavrova, I. Fedosov, E. Borisova, V. Nikolenko, T. Penzel, and V. V. Tuchin, "Biophotonic Strategies of Measurement and Stimulation of the Cranial and the Extracranial Lymphatic Drainage Function," IEEE Journal of Selected Topics in Quantum Electronics 27(4), 7400313 (2021).
99. A. Bucharskaya, G. Maslyakova, M. Chekhonatskaya, S. Pakhomy, D. Mudrak, N. Navolokin, G. Terentyuk, E. Borisova, V. Mantareva, I. Angelov, B. Khlebtsov, N. Khlebtsov, V. Genin, A. Bashkatov, E. Genina, and V. Tuchin, "The assessment of tumor vascularization degree for predicting the effectiveness of plasmonic photothermal and photodynamic therapy," Proceedings of SPIE 11845, 1184508 (2021).
100. Photoptics 2020, 8th International Conference on Photonics, Optics and Laser Technology [https://photoptics.scitevents.org/?y=2020].
101. E. Borisova, and L. Oliveira (Eds.), "Special Issue "Advanced Laser Technologies for Biophotonics," Electronics (2021).
102. E. Borisova, I. Bratchenko, Y. Khristoforova, L. Bratchenko, T. I. Genova, A. I. Gisbrecht, A. A. Moryatov, S. V. Kozlov, P. P. Troyanova, and V. P. Zakharov, "Near-infrared autofluorescence spectroscopy of pigmented benign and malignant skin lesions," Optical Engineering 59(6), 061616 (2020).
103. I. Bratchenko, Y. Khristoforova, L. Bratchenko, A. Moryatov, S. Kozlov, E. Borisova, and V. Zakharov, "Optical Biopsy of Amelanotic Melanoma with Raman and Autofluorescence Spectra Stimulated by 785 nm Laser Excitation," Journal of Biomedical Photonics & Engineering 7(2), 020308 (2021).
104. J. Spigulis, A. Lihachev, V. Lukinsone, M. Osis, and I. Oshina, "Lasers for in-vivo skin diagnostics: some recent developments," Proceedings of SPIE 11047, 1104703 (2019).
105. J. Spigulis, V. Lukinsone, I. Oshina, E. Kviesis-Kipge, M. Tamosiunas, and A. Lihachev, "Riga Group's recent results on laser applications for skin diagnostics," Journal of Physics: Conference Series 1859, 012033 (2021).
106. The 15th International School on Quantum Electronics "Laser physics and applications", 2008 (accessed 21 Nov 2021) [http://www.icsqe2020.ie-bas.org/sqe2008/index.htm].
107. 23rd Annual International Laser Physics Workshop – LPHYS'2014. Local Organizing Committee, 2014 (accessed 21 Nov 2021) [https://www.lasphys.com/workshops/lasphys14/local-organizing-committee].
108. 26rd Annual International Laser Physics Workshop – LPHYS'2017. Advisory and Program Committee, 2017. (accessed 21 Nov 2021) [https://www.lasphys.com/workshops/lasphys17/advisory-program-committee].
109. E. Borisova, H. Schneckenburger, and A. Priezzhev, "Special Section on Laser Technologies for Biomedical Applications," Journal of Biomedical Optics 17 (10), 101501 (2012).
110. R. Robinson, "Ekaterina Borisova on Creativity," Optics & Photonics News, 28 January 2020 (accessed 21 Nov 2021) [https://www.optica-opn.org/home/career/2020/january/ekaterina_borisova_on_creativity/].

Phthalocyanines Structure Versus Photodynamic Effectiveness towards Pathogenic Microorganisms: Our Recent Experience

Vanya Mantareva[1*], Ivan Angelov[1,3+], Meliha Syuleyman[1], Vesselin Kussovski[2], Ivelina Eneva[1], Latchezar Avramov[3], and Ekaterina Borisova[3]

[1] Institute of Organic Chemistry with Centre of Phytochemistry, Bulgarian Academy of Sciences, 9 Acad. Georgi Bonchev st., Sofia 1113, Bulgaria

[2] The Stephan Angeloff Institute of Microbiology, Bulgarian Academy of Sciences, 26 Acad. Georgi Bonchev st., Sofia 1113, Bulgaria

[3] Institute of Electronics, Bulgarian Academy of Sciences, 72 Tzarigradsko shose blvrd., Sofia 1784, Bulgaria

e-mail: * mantareva@yahoo.com, + ipangelov@gmail.com

Abstract. The present review paper aims to summarize our recent experience in research and development of new phthalocyanine complexes and investigations of the main photophysical, photochemical and photobiological properties which are related to antimicrobial photodynamic therapy (aPDT) as alternative method for inactivation of the resistant pathogens. The effect of functionalization of Zn(II) phthalocyanine (ZnPc) with biologically-active natural substances such as amino acids, sugars and steroids was studied in comparison to the basic ZnPc ring molecule. The structural features of the substitution groups were chosen to facilitate the main properties responsible for PDT outcome. For example, the linkage groups of amino acids tyrosine, phenylalanine, lysine and arginine have positive charge in physiological media to the better attachment to bacterial wall and some of them have a good fluorescence for a contribution to the visualization of the infected area. Also, ZnPcs linked to sugars and steroids was expecting to possess receptor specific selectivity. The physicochemical properties of the novel functionalized ZnPcs are presented in respect to their efficiency for a number of pathogenic bacterial and fungal species. Additionally, the complexes of two heavy metal ions such as lutetium(III) (Lu(III)) and tin(IV) (Sn(IV)) were synthesized and evaluated for antimicrobial PDT. These complexes were designed with the same structural skeleton as our previous water-soluble methylpiridyloxy-substituted phthalocyanine complexes with zinc (II), silicon (IV), germanium (IV), indium (III) and gallium (III), all with relatively promising antibacterial efficiency. © 2021 Journal of Biomedical Photonics & Engineering.

Keywords: Photosensitizers; Phthalocyanines; PDT; Photochemistry; Antibacterial photodynamic therapy; aPDT.

Paper #3445 received 28 Jul 2021; revised manuscript received 10 Sep 2021; accepted for publication 12 Sep 2021; published online 25 Sep 2021. doi: 10.18287/JBPE21.07.040202.

1 Introduction

Photodynamic therapy (PDT) is well-accepted curative modality with fast outcome after treatment, which is applicable on different acute disorders including infections [1, 2]. The method is based on a local irradiation of the target spot of the problematic area associated with pathogens where the photosensitizer (PS) is preferably accumulated. The efficacy of PDT action depends on the saturation with molecular oxygen but usually the

atmosphere surrounding is adequate for the process. The procedure starts with a light absorption within visible or near infrared spectra, which initiates a physical conversion of generation of first singlet excited state PS^1. The absorbed energy of PS^1 may relax by radiative and non-radiative conversions with high input of the intersystem crossing transition which leads to production of the triplet excited state PS^3 [3]. The molecules in their triplet excited state can take part in the photochemical reactions with participation of the molecular oxygen placed in the vicinity of PS^3 as well as with the surrounded bioorganic molecules as part of the structure of pathogens. The progress of the photosensitization includes different reactive oxygen species (ROS) such as singlet oxygen ($^1O_2$), superoxide anion ($O^{2\bullet-}$), hydroxyl radical (•OH) and hydrogen peroxide, all causing the irreversible oxidative damage of membranes so that the development of drug resistance is not yet observed for photodynamic inactivation [4].

It is believed that the fast development of drug- and multi-drug resistance is associated with the over-use and often abuse to the presently available chemotherapeutic drugs [5]. The knowledge about the efficacy of compounds absorbing in the far-red spectral region on the local infections has more than hundred years' historical timeline. Though, the "Golden era" of discovery and common usage of antibiotics has limited the progress of development of PDT method towards pathogenic microorganisms. Since the time when the resistance problem was announced as a high social health problem, the PDT topic together with many other approaches are under consideration as alternative methods to the antibiotics treatment [6].

The structure of a PS has to be capable to accumulate in high amounts into pathogens to result in the pathogens inactivation after light irradiation with a specific wavelength [7, 8]. The research and development of new generation PS, which are especially designed for pathogenic microbes, have been under intensive research consideration [9, 10]. The interaction of a PS with the pathogenic microbial species depends on their morphological characteristics, which have the well-defined difference for both bacterial species. For example, the bacterial wall of Gram (−) bacteria is more complicated having an additional layer than that in Gram (+) bacteria, which can act as a permeability barrier to limit the drug penetration and the further inactivation. The most involved mechanisms of drug uptake are known to happen by the physical uptake of PS molecules to the membranes due to hydrophobic and charge interactions [11]. These mechanisms can act together with the membrane's receptors-interactions, which are likely delivered the sufficient amount of PS to the target cells. The studies also present the selectivity of the uptakes in randomly arranged pathogens over the surrounding organized mammalian cells [12–14]. The specific structural characteristics of the particular pathogenic specie of one group of pathogens with common features need to be considered in strength designed PS's. The focus in investigations is made on the biologically-active functional groups for substitution of PS with a goal for improvement of the chemical, physicochemical and photoinactivation PS properties [15].

For these reasons, the new generation photosensitive drugs used for antimicrobial PDT (aPDT) or photodynamic inactivation (PDI), as well as the photodisinfection of medical devices related to human activity and treatment, have a well-defined chemical structure, cationic charge and hydrophilic or amphiphilic nature [16]. Nowadays only few numbers of metal coordinated phthalocyanine complexes (MPcs) of zinc (ZnPc), aluminum ($AlPcS_n$) and silicon (Pc4) are clinically approved for PDT of different tumor localization [17]. However, the knowledge about these drugs suggested the low uptake capacity and non-selective efficiency on pathogenic bacteria and fungi [18]. On the other hand, taking into account the structural flexibility and the advanced optical properties of MPcs, such as the long wavelength of absorption (> 680 nm), the high molar absorptivity (> 10^5 $M^{-1}\cdot cm^{-1}$), lack of dark toxicity and relatively high photocytotoxicity, the promising MPcs with advanced properties towards pathogenic species are under development [19, 20].

The review presents new research studies, together with already published results, in order to give a general picture of the effects that functionalizing biocompatible groups have on the overall properties of MPcs photosensitizers when used against pathogens.

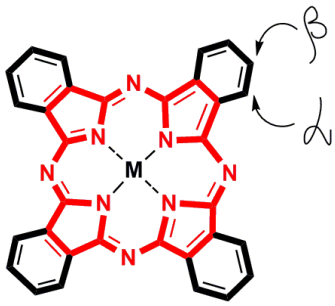


Fig. 1 Chemical structure of phthalocyanine complex (MPc) with the positions for conjugation.

2 Biologically-active groups to Zn(II)-phthalocyanines towards pathogens

The phthalocyanine molecule possess structural characteristics of symmetrical planar skeleton with sixteen positions for substitutions on the ring macrocycle and one or two axial positions for substitutions to the coordinated metal ions (M) (Fig. 1).

The peripherally substituted MPcs are assumed as more likely to interact with the target cells because of the extent area of these groups as well as the axial substitutions with bulky groups, which influence on the aggregation behaviour and arrangement of photo-inactive molecular associates [21].

2.1 Amino acids substituted Zn(II)-phthalocyanines

The chemical conjugates of phthalocyanines (Pc) with amino acids have been of research interest during more

than two decades [22–24]. The intention in the beginning was the improvement of solubility of highly hydrophobic Pc molecule. The further studies aim modifications of properties of absorption, fluorescence and singlet oxygen generation [25, 26]. In addition, some new essential biological properties appear related to the cell-specificity, the uptake and the photocytotoxicity. In our studies, four amino acids tyrosine, phenylalanine, lysine and arginine were selected to advance the properties of ZnPcs as photosensitizers [27]. The non-essential amino acids phenylalanine, lysine and arginine (for adolescent) are well documented with their positive physiological effects, curative action and the wide usage in medicine as prodrugs [28]. Next to their biological functions, they also have some specific properties as, for example, is the detectable fluorescence of tyrosine and phenylalanine [29]. Other selected amino acids are lysine and arginine, which are well documented with their ability of excellent penetration and interaction with cell membranes [30, 31]. These properties were expected to affect the physicochemical properties and the easy localization of ZnPc's functionalized with amino acids in sufficient amount for an effective pathogen's photo-inactivation. Ultimately the conjugation of two biologically-active molecules was expected to lead to a photosensitive compound with synergistic action on the target. Presently, treatments of acute infections related to pathogenic species have been settled with the chemotherapy with conventional and newly developed antibiotics [32]. Even so they are known to induce several side effects due to non-selectivity of uptakes, which can lead to harmful toxicity in healthy host tissues and the fast development of drug resistance to the treatment regime [33].

2.1.1 Synthesis of ZnPcs linked to amino acids

New bioconjugates of Zn(II) phthalocyanine with four and eight amino acids were synthesized. Two molecules of different origin were connected by amide bond between carboxyl groups of tyrosine, phenylalanine, lysine and arginine, and amino (aminophenoxy) group of phthalocyanine placed on four and eight peripheral positions to the Pc ring in the presence of coupling agents (Fig. 2).

The conjugation was performed using multi-step procedure to prepare two starting tetra- and octa-aminophenoxy- substituted Zn(II) phthalocyanines. Briefly, the used synthetic pathway presented in Fig. 3 starts with synthesis of dinitriles with nitrophenoxy group by following the reaction step of cyclotetramerization in the presence of zinc salt, the next step by reaction of reduction of nitro groups to amino groups were carried out according to the literature [34–36].

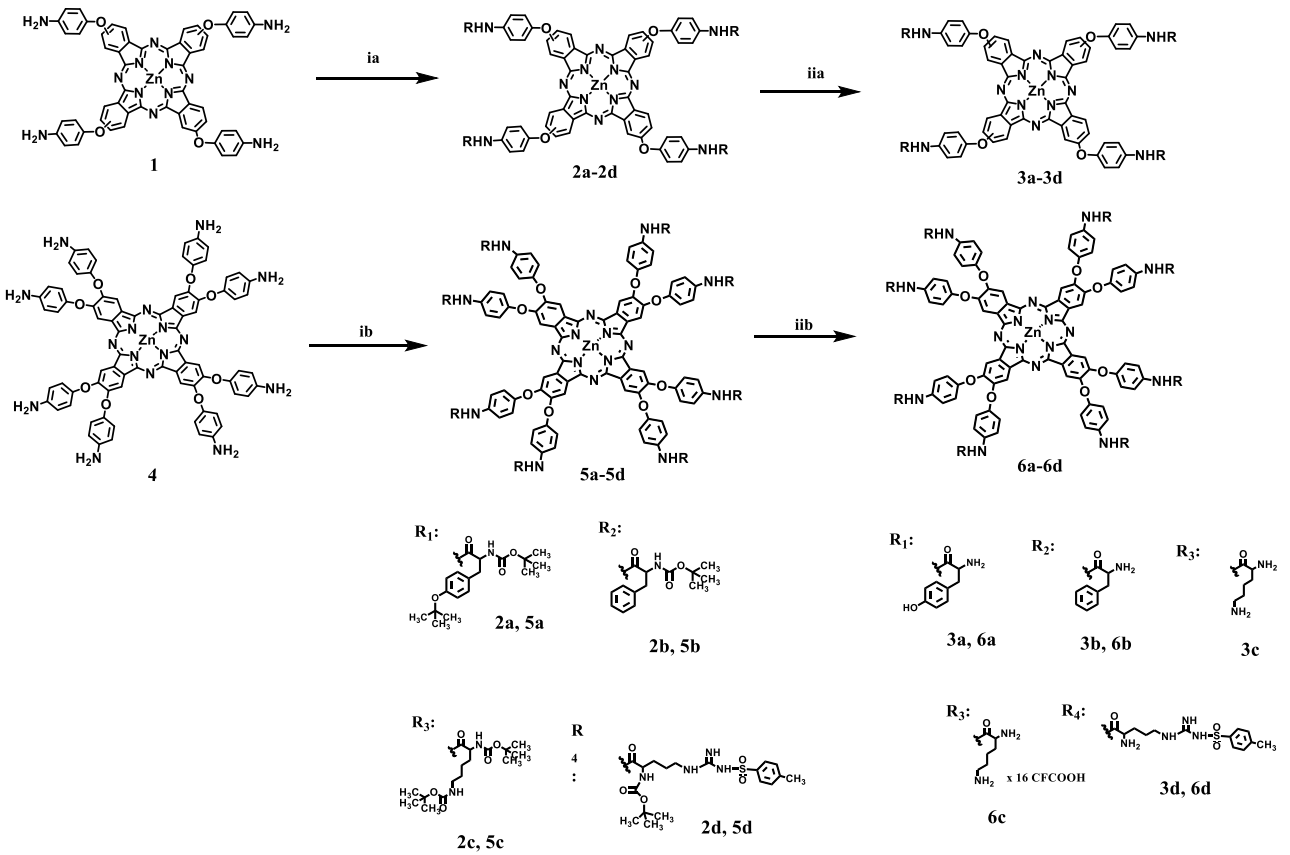


Fig. 2 Synthesis of Zn(II) phthalocyanines linked to amino acids (tyrosine, phenylalanine, arginine and lysine). Reactions and conditions: (ia) protected amino acid-OH, DMTMM, NMM, THF, ice bath, rt; (ib) protected amino acid-OH, DMTMM, NMM, DMF, ice bath, rt; (iia) TFA, THF, rt; (iib) TFA, DMF, rt.

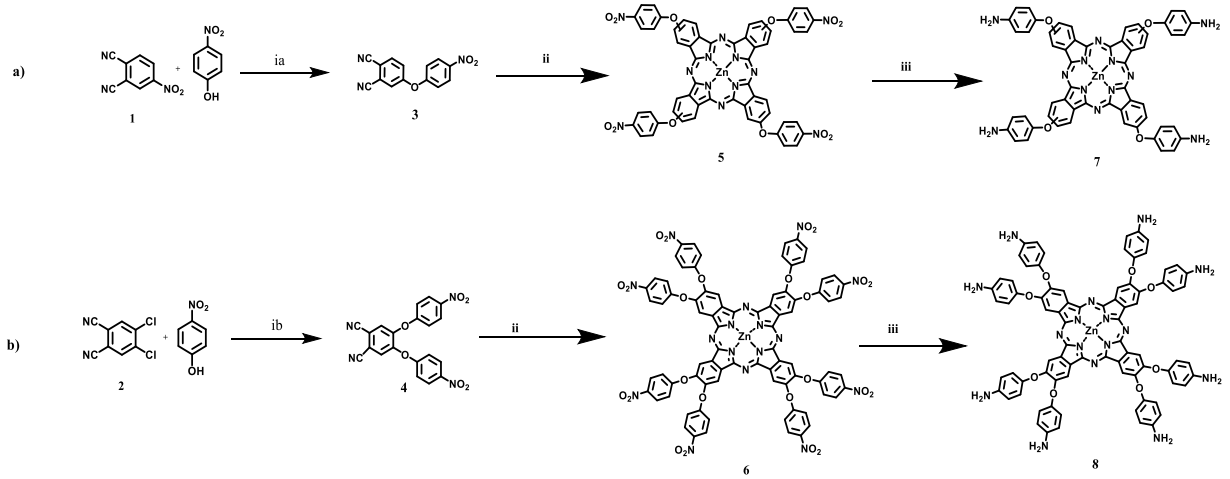


Fig. 3 Synthesis Zn(II) phthalocyanines for conjugation: (ia) K2CO3, dry DMF, RT, Ar; (ib) K2CO3, dry DMF, 90 °C, Ar; (ii) $Zn(OAc)_2$, DBU, 1-pentanol; (iii) dry DMF, Na_2Sx9H_2O.

Zn(II) conjugates with the selected amino acids were obtained with a relative yield: 44% for lysine conjugates to 87% for phenylalanine and tyrosine derivatives. The conjugates ZnPc with selected amino acids were analysed, with such known spectroscopic techniques as IR, ^{1}HNMR, MS and UV–Vis spectroscopy. They showed excellent solubility in most organic solvents. The aimed high solubility was observed for two ZnPc conjugates with lysine and arginine (Fig. 2-6a and 6c) showing water solubility.

2.1.2 Physicochemical properties

Electronic absorption spectra of the conjugates with amino acids and basic photophysicochemical properties were measured in Dimethyl Sulfoxide (DMSO) and data are collected in Table 1. The absorption spectra were all similar, which is characteristic for non-aggregated metalphthalocyanines. They showed a B band at 352 to 366 nm, a band at 617 nm and intensive sharp Q-band at 680 to 683 nm, which strictly followed the Lambert–Beer law. The amino acids lead to red shifts of the absorption maxima with 10 to 12 nm compared to unsubstituted ZnPc but the type of the amino acids less influence the position of the absorption maxima of the compounds. Upon excitation at 360 nm, 610 nm and 660 nm they showed relatively high fluorescence emissions at 690 to 694 nm but with low fluorescence quantum yield (Φ_F) from 0.018 – 0.069 except for tetra tyrosine substituted Zn(II) phthalocyanine ($\Phi_F = 0.12$). The lower values of the fluorescence quantum yield of the phthalocyanines may be due to the physical quenching by the bulky substituents on the amino acids in addition to the influence of free amino groups on peripheral positions of the ZnPc ring. The high values of the fluorescence quantum yield of the tetra tyrosine substituted ZnPc, which is comparable with the fluorescence quantum yield of unsubstituted ZnPc, is may be due to the contribution in the total fluorescence of the phthalocyanine and tyrosine molecules. Recently Zhang et al. [37] showed that the introduction of NH_2- groups to ZnPc may have different effects than the other studied substituents (−$OCH(CH_3)_2$, H, NO_2). This group can incite numerous roles: a good electron donor, a strong proton acceptor, a hydrogen bonding formation ability and a good ligand for coordination of metal ions. Moreover, the amino-substituted ZnPc may show very low fluorescence quantum yield as the new Zn(II) phthalocyanines with tyrosine, arginine, lysine and phenylalanine except tetra tyrosine substituted Zn(II) phthalocyanine on symmetrical peripheral positions presented but the fluorescence lifetime does not decrease significantly.

The lifetime of the bio-conjugates is comparable with lifetime of the unsubstituted ZnPc. The lower values of the fluorescence quantum yield and not so significant lowering of the lifetimes of new compounds compared to unsubstituted ZnPc can be explained by the effect of quenching of the unprotected NH_2-groups, which is in contribution to a high electron density of the molecules. Therefore, it is more likely to occur the photo-induced electron transfer (PET) and as a consequence is decrease of fluorescence yields. The protection with tetra-butoxycarbonyl group (Boc), which is electron withdrawing group can reduce the electron density of nitrogen atom and this leads to less effective quenching of the singlet excited state of the conjugates through PET [37]. This observation supports the reductive quenching of amino groups, which disfavour the intersystem crossing based on the intramolecular PET effect.

The efficiency of the Zn(II) conjugates with amino acids in generating singlet oxygen, as reflected by the rate of decay of the singlet oxygen quencher 1,3 - diphenylisobenzofuran (DPBF) in DMSO, was also examined. Tetra conjugates showed higher values according to their octa analogues as tetra tyrosine and phenyalanine conjugates ($\Phi_\Delta = 0.63$ and 0.71), with exception of tetra lysine conjugates, which has lower value of singlet oxygen ($\Phi_\Delta = 0.36$) than its octa analogue ($\Phi_\Delta = 0.57$) and almost same values with arginine compounds – ($\Phi_\Delta = 0.39$) for tetra compound and ($\Phi_\Delta = 0.40$) for octa- substituted ZnPc derivatives.

Table 1 Physicochemical properties of Zn(II) phthalocyanines linked to amino acids in DMSO.

PS	λ_{abs} (nm), (log ε)	Emission λ_{em} (nm)	Φ_F	τ_F (ns)	Φ_Δ	dC/dt (M/s)
3a	680 (3.02), 352 (–)	692	0.12	2.91	0.63	3.1×10^{-10}
6a	680 (4.36), 364 (3.94)	689	0.04	2.03	0.38	32×10^{-10}
3b	682 (4.23), 353 (3.93)	693	0.069	2.82	0.71	5.63×10^{-10}
6b	683 (4.17), 357 (3.88)	690	0.018	2.67	0.23	3.5×10^{-10}
3c	683 (3.63), 356 (3.38)	693	0.047	2.85	0.36	13.5×10^{-10}
6c	681 (5.28), 360 (4.86)	690	0.03	–	0.57	2.20×10^{-10}
3d	682 (4.27), 352 (3.97)	694	0.055	2.89	0.39	1.53×10^{-10}
6d	682 (4.02), 355 (3.73)	690	0.038	2.56	0.40	7.89×10^{-10}
ZnPc*	672 (5.21), 341 (2.61)	679	0.20	3.99	0.67	0.94×10^{-10}

The formation of molecular singlet oxygen does not affect the intensity of the Q-band of the conjugates, which suggests that there is no photooxidative effect on the phthalocyanine molecules during their irradiation. The option of singlet oxygen physical quenching is more probable by the eight peripheral substituents than four groups on ZnPc ring molecule. The physical quenching by bulky substituents was known to diminish the singlet oxygen quantum yields of some other substituted phthalocyanines [38]. The low values of the conjugates (0.23–0.40) correlate to the quenching of excited state due to PET effect of the amino groups closed to ZnPc (phenylamine and benzylamine groups) resulting in the lower singlet oxygen generation. This effect can be inhibited by the distance of NH_2 to the Pc-molecule, acidity of media and protonation of amino groups [39].

The photostability study of the tetra and octa Zn(II) phthalocyanines with the amino acids tyrosine, phenylalanine, lysine and arginine was carried out by following the absorption spectra during irradiation (60 mW·cm^{-2} at 665 nm wavelength). All studied compounds were as effective as unsubstituted ZnPc which showed relatively high stability at the applied light. The results are summarized in Table 1 showing the rates (dC/dt) in one of the same order of magnitude. The obtained rates suggested an optimal photostability without formation of the by-products due to irradiation. The collapse of the absorption spectra without any distortion of the shape which suggested the lack of structural alteration of phthalocyanine molecules in the spectra of irradiation was observed for all studied phthalocyanines.

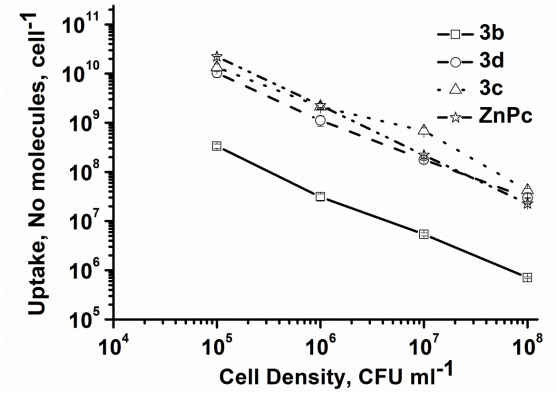
2.1.3 Uptake and photoinactivation efficacy

Uptake of the Zn(II) conjugates with phenylalanine, lysine and arginine (Fig. 2–3b–3d and 6b–6d) on fungal cells *C. albicans* were studied by using chemical extraction method which included incubation of the studied conjugates in the cellular suspensions with different cell density (10^5–10^8 Colony-forming units/mL (CFU/mL)). The collected supernatants with the extraction mixtures were measured the fluorescence between 650–800 nm with λ_{ex} = 637 nm. The results obtained are presented as number of molecules (No), uptake in a one bacterial cell (No / cell). Fig. 4 shows that Zn(II)Pc linked to amino acids have relatively high uptakes with values two order of magnitute higher for 3c and 3d (10^{11}) than for 3b (10^9). This low uptake of 3b is probably due to its low solubility at the extraction mixture (THF / SDS). The octa- compounds showed similar values (10^{11} No / cell). The compound 6b showed the highest level of uptake among the octa- compounds. The typical inverse behaviour of decreasing of the accumulation of the studied conjugates with increasing of the cell density (10^5–10^8 CFU / mL) of suspensions was observed as in for the other pathogens. The obtained results are in agreement with the observation that the cellular accumulation depends on the cell density of suspension [40].

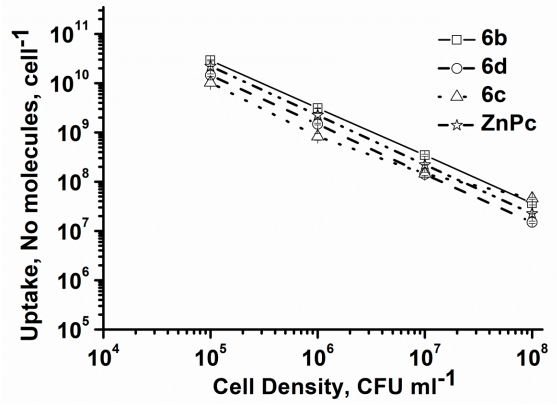
It is well studied that the cell membrane can bind more effectively the cationic compounds [41]. According to the obtained results with ZnPcs with phenylalanine, lysine and arginine the relatively high level of binding is a result of the amino groups which facilitate the binding to cell membrane of *C. albicans*. The interactions can occur by the hydrophobic nature of ZnPc or some physical force. On the other side lysine and arginine are able at physiological pH to act as cationic ZnPcs with higher accumulation and retention time of these compounds in membranes.

The photoinactivation study with Zn(II)Pcs with amino acids showed the lack of dark toxicity and low

photocytotoxicity (~2log) for *Candida albicans* (Fig. 5). The study was carried out at concentration of 10 μM and irradiation on 665 nm wavelength by Light emitted diode (LED) (light dose 50 J·cm^{-2} at 60 mW·cm^{-2} light intensity). Only both arginine substituted compounds (3b, 3d and 6d) showed complete photoinactivation, followed from lysine substituted 3c. These results are supported by the properties of singlet oxygen generation and the uptakes.



(a)



(b)

Fig. 4 Uptake of a) 3b, 3c, 3d; b) 6b, 6c, 6d (5.5 μM) in dependence on the cell density of *Candida albicans* in suspension with incubation time 20 min. The data are presented as means ±SD (n=3).

The carbohydrates such as galactosa and furanosa chemically linked to ZnPc were studied with low efficiency towards pathogenic microorganisms [42]. The low efficiency was also obtained with ZnPc conjugated with steroid [43].

2.1.4 In vitro photocytotoxicity

Photocytotoxicity assays were carried out with new conjugates (Fig.2–3a, 6a and 3c) in comparison with unsubstituted ZnPc and tetra aminophenoxy Zn(II) phthalocyanine (TZnPcNH$_2$) on two human breast cancer cells lines (MDA-MB-321 and MCF-7) and normal human cell line (MCF-10A). All of the studied conjugates (3a, 6a and 3c) showed no dark toxicity in a wide concentration range (0.15–20 μM) at irradiation with LED 665 nm and light parameters used in PDT study (50 J·cm^{-2} and 60 mW·cm^{-2}) [44]. Both tyrosine conjugates (tetra- and octa-) showed similar photocytotoxicity for concentrations up to 10 μM and with moderate photocytotoxicity at concentrations over 10 μM (37% viability for MCF-7 and 50% for MDA-MB-231). The healthy cell line (MCF - 10A) were not affected by irradiation for concentration between 1–10 μM from both tyrosine conjugates. Only unsubstituted ZnPc showed strong photocytotoxic effect towards tested cell lines. The amino acids – conjugates (3a and 6a) and ZnPc showed negligible photocytotoxic effect on normal cells (~80% viable cells) at concentrations bellow 10 μM and significant photocytotoxicity for concentrations over 10 μM for tumour cell lines (MDA-MB-231 and MCF-7). The interesting result is that the both aminophenoxy Zn(II) phthalocyanines used for conjugation showed very low phototoxic potential towards MDA-MB-231 tumour cells even at high dye concentrations and a lack of photocytotoxicity towards the cell lines MCF-7 and MCF- 10A.

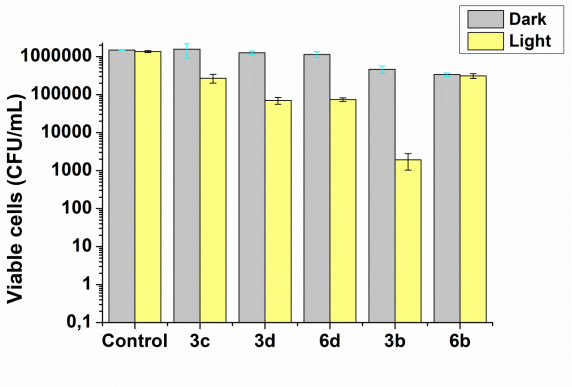


Fig. 5 Photocytotoxicity of 3b, 6b, 3c, 3d, 6d on *Candida albicans*.

3 Zn(II) phthalocyanines bearing both charges towards pathogens

The present knowledge about the influence of charge on the properties related to PDT efficacy is that the cationic photosensitizers including phthalocyanine complexes (MPcs) are better than anionic and neutral MPcs [45]. An interesting group of charged compounds which appears promising as photoantimicrobials are zwitterionic photosensitizers. They have the advantage of water solubility and low aggregation capability. Typical examples of zwitterions are amino acids with one amine and one carboxylic group where the basic NH$_2$- group is strong enough to deprotonate acidic-COOH group in solution [46]. These substituents have characteristic of a dipolar ion with positive and negative parts so that the net charge of the molecule is zero.

The zwitterionic Zn(II) phthalocyanines were synthesized by the treatment with 1,3-propanesultone at nitrogen of pyridiloxy group by following the well-known procedure [47]. Briefly, the reaction starts from dinitriles prepared from commercially available 4- and 3- nitrophthalonitrile in reaction with 3-hydroxypyridine in DMSO using potassium carbonate as a base. The both

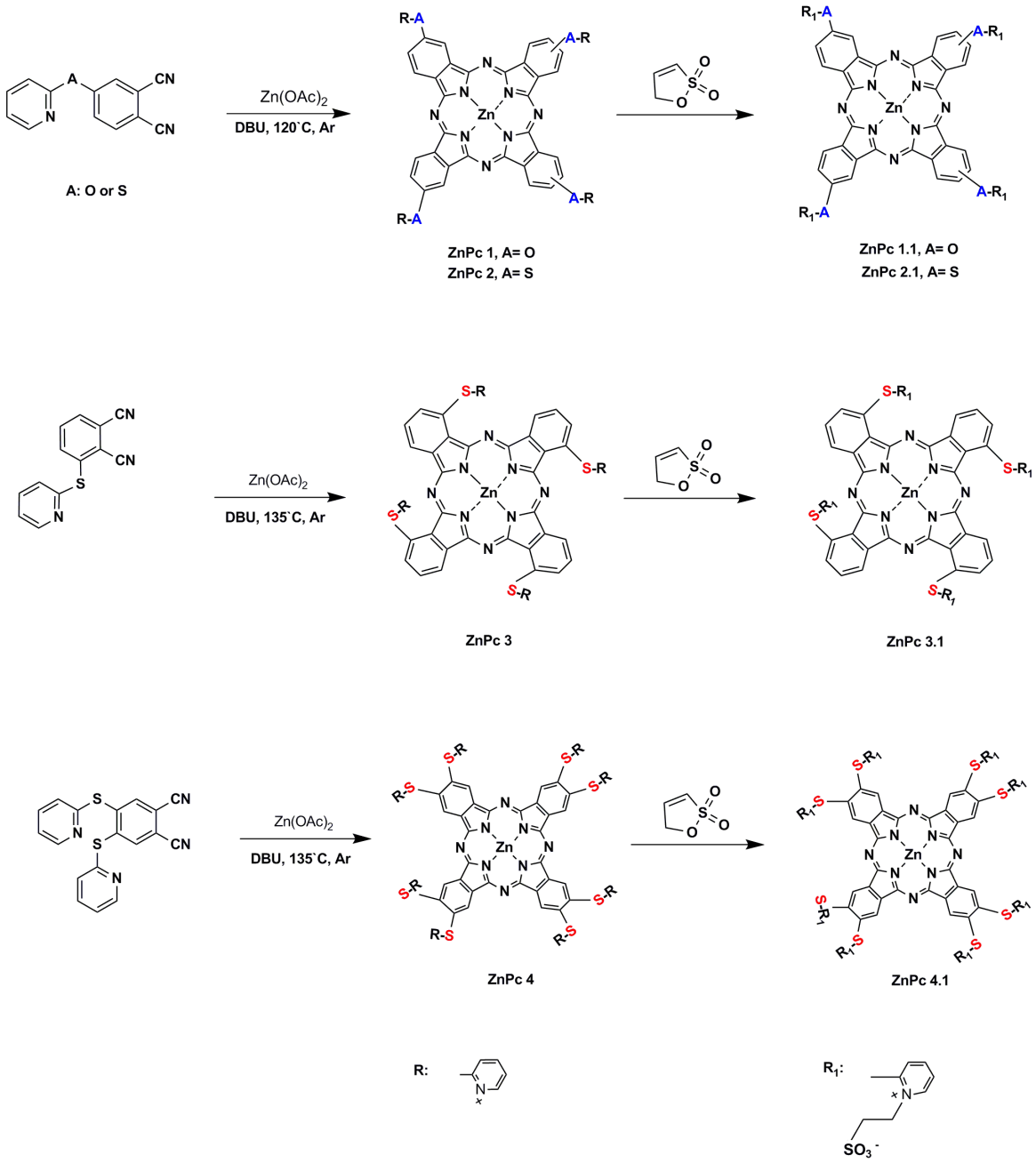


Fig. 6 Synthesis tetra-(3-/ 4-) pyridiloxy and pyridilsulfur Zn(II) phthalocyanines (ZnPc 1-4). Conditions: Zn(OAc)2, DBU, 1-pentanol and the derivatives ZnPc 1.1 – 4.1 after propanesulton in dry DMF.

reactions are productive for the chosen conditions (48 h, room temperature (RT)) and give the high purity products with approximately 80% yields. The physicochemical studies of differing in the positions zwitterionic ZnPcs suggested that they have promising photoproperties for biomedicine [48]. Nowadays together with different zwitterionic compounds such as carboxybetaine, phosphocholine, sulfobetaine also many phthalocyanines bearing selected as useful substituents have been synthesized and studied for PDT efficacy [37].

Our studies with the structurally different ZnPcs namely as the numbers of substituents (four and eight), the bridging atoms (sulfur or oxygen) and the positions of the substitution groups (Fig. 6). The peripherally substituted ZnPcs are as followed: tetra- 2-(N-propanesulfonic acid) oxypyridine (ZnPc1.1); tetra- 2-(N-propanesulfonic acid) mercaptopyridine (ZnPc2.1) and non-peripherally substituted compound is tetra- 2-(N-propanesulfonic acid) mercaptopyridine (ZnPc3.1), and octa- 2-(N-propanesulfonic acid) mercaptopyridine (ZnPc4.1). The bridging atom of sulfur add to absorption a red shift of approximately 10 nm (684 nm) as compared to the oxygen bridging atom in ZnPc1.1 (674 nm).

Two model pathogenic bacterial strains were tested, the both associated with the acute infections to humans namely a Gram (+) pathogenic bacterium *Enterococcus faecalis (E. faecalis)* and the Gram (–) bacterium *Pseudomonas aeruginosa* (*P. aeruginosa*), which is

known as a hardest to the inactivate, due to bacterial wall consisting of one additional layer of phosphatidyl-ethanolamines [49]. However, the Gram (–) species are also known with low susceptibility to the conventional therapy and with fast development of resistance to the treatment [50].

3.1 Uptake and localization study

The studied zwitterionic ZnPcs showed relatively high uptakes on resistant pathogenic bacterial strains of Gram (+) *E. faecalis* and Gram (–) *P. aeruginosa* as suspensions with different cell densities and as early stage biofilms formation [51]. It is assumed that the uptakes occur by a non-chemical attachment to the bacterial species in suspension or organized as biofilms. These compounds showed a high tendency of aggregation in water and buffered solution which can lead to ineffective photodynamic process. A Gram (–) *P. aeruginosa* was observed with less amount of the tested ZnPc1.1-4.1 with approximately one order of magnitude that the Gram (+) specie. The typical inversely proportional behaviour for the uptake values at the increasing cell densities was observed. This phenomenon is typical for any suspensions and repeated independently on the applied PS and type of treated bacteria since the first report for the Gram-negative *Escherichia coli* [52]. Many different pathogens and photosensitizing compounds were studied with similar accumulation behaviour [53, 54]. This may occur due to higher competition between the ZnPc molecules to bind to one bacterial cell with increasement of the bacterial density and as a consequence with the fewer available binding sites. The knowledge that the binding ability of the incubated ZnPcs can occur by hydrophobic or electrostatic interactions, or hydrogen bounding is valid also for zwitterionic ZnPcs, which possess the both charges in one substitution group. Obviously, this characteristic tends to improve the uptakes showing the almost equal values for octa-substituted ZnPc 4.1 for the both bacterial species.

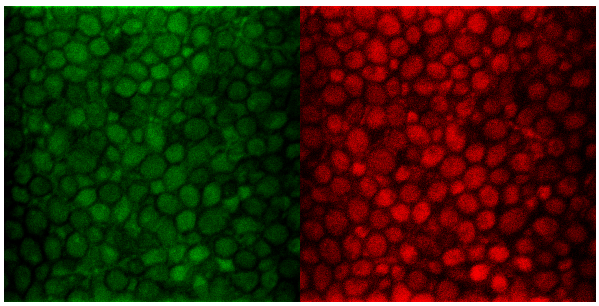


Fig. 7 The typical fluorescence confocal images of the slice of *C. albicans* biofilm (excitation 488 nm; emission 530–580 nm for the native fluorescence and excitation 635 nm; emission 660–720 nm for ZnPc1.1).

The biofilm's penetration and localization of zwitterionic ZnPcs in the fungal biofilms were evaluated by means of confocal laser scanning fluorescence microscopy (Fig. 7). The study is based on the fluorescence difference between the natural chromophores of cells which can be visualized by excitation with lasers 365 nm and 488 nm to image the typical green fluorescence in the region of emission 520–580 nm. The red fluorescence of ZnPc1.1-4.1 was observed at excitation with laser 635 nm for the emission spectra 660–740 nm as previously observed for bacterial biofilms [55, 56]. By the overlapping of the green channel and red channel of fluorescence signals was observed the significant ZnPc1.1 spreading throughout the biofilms. This was shown by two modes of observation, namely the fluorescence and transmittance. Among the studied ZnPcs, only non-peripheral ZnPc3.1 was observed with limited penetration in biofilms. The observed sufficient accumulation of ZnPc1.1, 2.1 and 4.1 into pathogenic bacterial biofilms suggested their potential for sufficient photodynamic inactivation. The different structures of the photoactive compounds influence the membrane permeability and on the uptakes [57].

3.2 Photoinactivation and dark cytotoxicity study

The cells were evaluated with saturation enough to expect the high generation of ROS products, which affect easily the membranes in the close vicinity of ZnPc4.1 with eight substitution groups was studied to have higher inactivation of planktonic and biofilm cultured. The photodynamic inactivation studies with zwitterionic ZnPc1.1-4.1 suggested different effectiveness of these compounds towards pathogenic bacteria, namely a complete photoinactivation with 6 μM ZnPc4.1 for the tested model strains (*E. faecalis* and *P. aeruginosa*). There was observed a difference in the activity of the tetra-substituted ZnPc1.1-3.1 with the lack of any effect of non-peripheral ZnPc3.1. The Gram (–) bacterium *P. aeruginosa* was not inactivated even at high drug concentration such as 30 μM ZnPcs. Two peripherally substituted ZnPc1.1 and ZnPc2.1 were evaluated with significant inactivations (> 3logs). The studies on normal cell line suggested the lack of dark toxicity but after irradiation the phototoxicity occurred. The irradiation was carried out with light source LED 665-nm on normal cells (Balb / c, 3T3) incubated with ZnPc1.1-4.1. The promising features of the zwitterionic ZnPcs are the lack of dark toxicity and a high phototoxicity at therapeutic light exposure on the normal cells.

In conclusion, the zwitterionic ZnPcs have charges influence on the uptakes and localization in an advanced way than the cationic ZnPcs derivatives [39, 58]. Moreover, the resistant Gram (–) *P. aeruginosa* showed promising results with the octa-substituted ZnPc4.1 as a result of the optimal physicochemical properties of singlet oxygen generation. It was still low-effective to inactivate an early-stage biofilm even at high doses of ZnPcs with the response below 3logs. The problem with pathogens resistance and not so efficient treatment of biofilms with PDT approach features the needs for improvement of the applied procedure in order to have better PS distribution on the grown biofilms and the effective inactivation of the resistant pathogens.

4 Lu^{3+} and Sn^{4+} phthalocyanines towards pathogenic species

The insertion of non-transition metal or semi-metal diamagnetic closed shell ions in the phthalocyanine core is well documented way for improvement of the main physicochemical properties associated with the excited states of the molecules [59]. The knowledge about the effect of the large atoms in regards to the photophysical properties of the phthalocyanine complexes (MPcs) is also well documented [60]. However, there are limited studies about the impact of the large metal ions (Lu^{3+} and Sn^{4+}) on the PDI efficiency. On one side, there is a steric hindrance effect due to the physical placement of large atoms out of the plane of macrocycle, which tends to lower the aggregation capacity of MPcs. On the other hand, the high coordination number of these metals permits attachment of one or more axial bulky groups of substituents, which also can decrease the aggregation behavior of the complexes.

Phthalocyanine complexes of lutetium ion (Lu^{3+}) have been of research interest due to their unique physicochemical properties and the ability for coordination of two or more Pc molecules [61, 62]. In regards to biomedical application, there is only one known Lu(III) complex, namely Lu(III)-texapyrine (Lu-tex^{TM}), which after many years of investigations, was considered for PDT and for diagnosis of cancer [63]. Nowadays the Lu(III)Pcs which are designed for PDT should be monomolecular and with cationic charge [64]. In our recent studies, two new water-soluble cationic lutetium (III) phthalocyanines (LuPcs) were synthesized and were investigated as effective towards fungus *Candida albicans* [65]. These are peripheral and non-peripheral Lu(III) phthalocyanines with four pyridyloxy groups which after methylation were converted to their water-soluble derivatives LuPc 1.1 and 1.2 (Fig. 6) [66].

The existing studies with tin (Sn(IV)) complexes for PDT are with purpurins, which were reported with an excellent PDT efficacy more than the related zinc complexes [70]. During 90s years this research resulted in a new PDT drug ($SnEt_2$) with very high potential to replace the originally clinically accepted porphyrin derivatives [67]. The known Sn(II/ IV) phthalocyanine complexes were explored with relatively high quantum yield of the triplet excited state and the favourable photo-physicochemical properties [68, 69]. In the similar way, two new Sn(IV) phthalocyanines (Sn4+Pcs) with hydroxyl groups on axial positions were synthesized. The obtained water-soluble Sn(IV)Pcs are the corresponding compounds to Lu(III)Pcs, which are differing in the positions of methylpyridyloxy groups in non-peripheral (SnPc 2.1) and peripheral (SnPc 2.2) positions (Fig. 8).

4.1 Synthesis of LuPcs and SnPcs

The dinitriles, which are differed in the position of pyridyloxy- group namely 4-(3-pyridiloxy) nitrophthalonitrile (1) and 3-(3-pyridiloxy) phthalonitrile (2) were used as monomers for cyclotetramerization [70]. The synthetic procedure was previously applied for synthesis of other complexes of MPcs with N- quaternized atom. The CN group was confirmed with the sharp narrow band at 2228 cm^{-1} and the aromatic ether group with vibrations at 1280 and 1253 cm^{-1} in the IR spectrum.

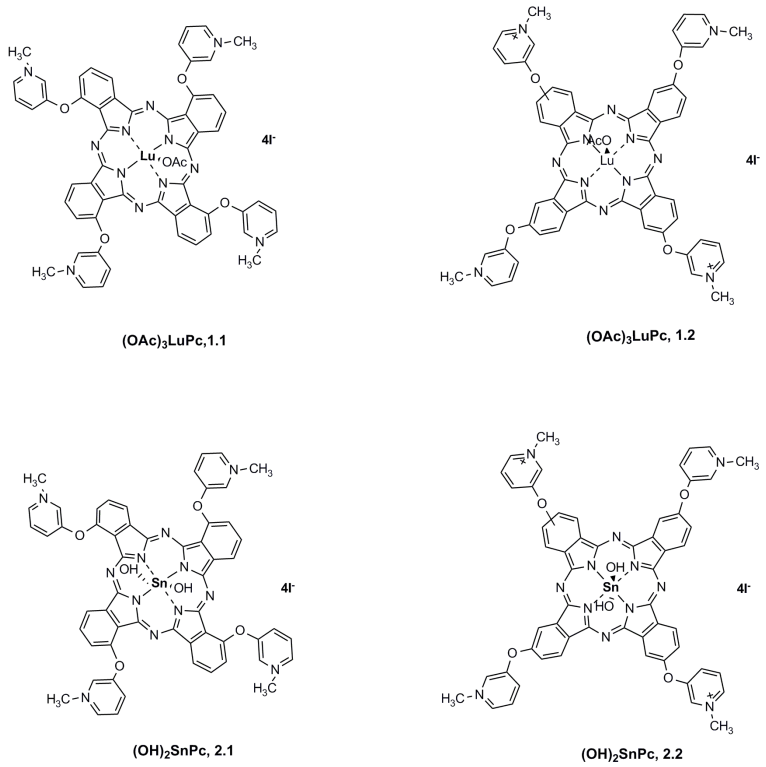


Fig. 8 Chemical structures of the studied MPcs coordinated with heavy metal ions of Lu(III) and Sn(IV).

The molecular ion peak at *m/z* 221 $[M]^+$ and two fragmentation ions peaks at *m/z* 127 $[M\text{-}C_5H_4NO^-]^+$ and at *m/z* 78 $[C_5H_4N]^+$ were obtained by means of MS spectroscopy. The cyclotetramerization reactions were carried out by addition of anhydrous salt of lutetium acetate and tin chloride by reflux in freshly distilled 1-pentanol, DBU in argon atmosphere. Another route involves Pc ring formation by the initial step of dissolved lithium pieces in n-pentanol. It was noticed the precipitation of the green product in 1-pentanol at the time of exchange of metal ions. The characteristic for the synthesis of Lu(III)Pcs is that the product was obtained as a mixture of three products, namely Li_2Pc, double-decker $LuPc_2$ and the mono-molecular LuPc (~60%) plus other impurities. The purification by column flash chromatography resulted in positional (region) isomers of desired product. The chemical characterization performed by the routine analyses showed ^1H NMR spectra with shifting of the signals depending to the position of the substituents and for CH_3 groups the recorded signals corresponded to the structures. IR spectra showed intense bands at 1237 cm^{-1} due to the presence of aromatic ether bonds (Ar-O-Ar). The mass spectra (MALDI-TOF) is characterized with a molecular peak *m/z* 1214.718 [M-OAc+DHB] for 1 and *m/z* 1214.398 [M-OAc+DHB] for 2. The final step of alkylation reaction was carried out with an excess of dimethyl sulphide or methyl iodide in DMF, which converted LuPcs into water-soluble derivatives 1.1 and 1.2. in relatively high yields (79–93%) and purity [71].

The similar synthetic procedure was followed to prepare the water-soluble SnPcs (Fig. 6). The specificity in the synthesis of tin complexes is that two different complexes Sn(II)Pcs or Sn(IV)Pcs can be obtained in dependence on the molar ratio between the starting monomer (dinitriles) and the used salt ($SnCl_4$). The complex Sn(IV)Pc was prepared by using an equal ratio between both mixed solids. By addition of an excess of tin salt, Sn(II)Pc was synthesized. Taking into account our further experiments, we have prepared Sn(IV)Pcs, which are assumed to be more capable to limit the aggregation due to axial substituents of chlorine converted to hydroxyl group by pyridine in ammonium hydroxide treatment. The reactions were carried out in 1-pentanol for 5 h with lithium granules to facilitate the formation of Pc ring and then the tin metalation was performed with the same equivalent of SnCl4 as for the starting dinitrile at reflux for one additional hour. The purification of SnPcs 1 and 2 was carried out with dichloromethane (DCM) and methanol (MeOH) in increasing of gradient of MeOH. The water-soluble SnPcs 3 and 4 were washed in a series of solvents with different polarity and then dried on glass oven overnight. Four new Sn(IV)Pcs were chemically characterized with the routine analytical techniques. 1H NMR spectra corresponded to the predicted structures with a typical shifting of the signals depending to the position of the substituents. The signals of CH_3 groups in the investigated compounds are well corresponding to the protons of four methyl groups. IR spectra showed the lack of the peak around 2230 cm^{-1} (C≡N) and the appearance of new peak at 3304 cm^{-1} for the complex. The aliphatic hydrocarbons showed stretching at 2910–2985 cm^{-1} and for aromatic C–H at 3015 to 3035 cm^{-1}. The mass spectra were obtained with the signals of M+ (1382) for SnPc2.1 and (1225) for SnPc2.2 which are *m/z* of these compounds.

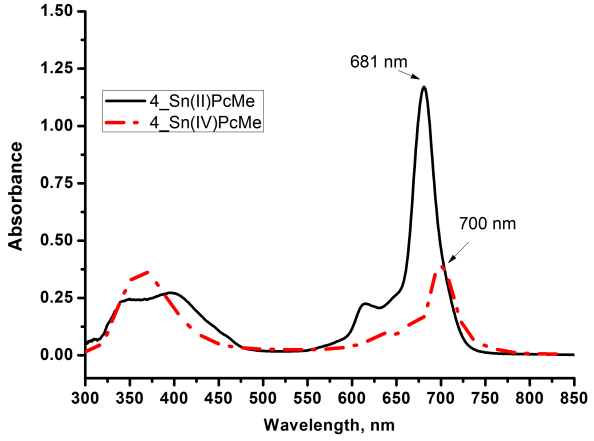
4.2 Physicochemical properties

Lutetium (Lu(III)) and Sn(IV) phthalocyanine complexes, which are differing only in the inserted metal ions were characterized with similar photo-physicochemical properties. Both complexes have red shifted absorption Q-band as compared to the same MPc with zinc metal ion (ZnPcMe). The absorption maxima were determined for the peripheral LuPc2 and SnPc2 at 675 nm and 678 nm in dimethylsulphoxide (DMSO) and even more shifted to 684 nm and 687 nm for non-peripheral LuPc4 and SnPc4 together with the low intensity peaks around 610 nm and the low-intensity B-bands between 360–367 nm. The quaternization of pyridyloxy-group leads to compounds with increased solubility but also to formation of the photo- inactive aggregates. For example, the absorption spectra of LuPcs (2 and 4) in water or buffer showed aggregation with a low intensity splitted Q-bands with appearance of the second band (681 nm for 2 and 692 nm for 4). Thus was previously observed with the other studies by us Mpcs (M: Zn, Al, In, Si, and Ge) with an exception of Ga(IV) Pcs, which exist as monomeric molecules in water [72]. The limitation of the formation of non-photoactive aggregates is possible by addition of an anionic detergent or some hydrophobic vehicle molecules [73]. The undesirable tendencies of formation of photo- inactive associates in water are also minimal for experimental studies in buffered media of the fungal cell suspensions.

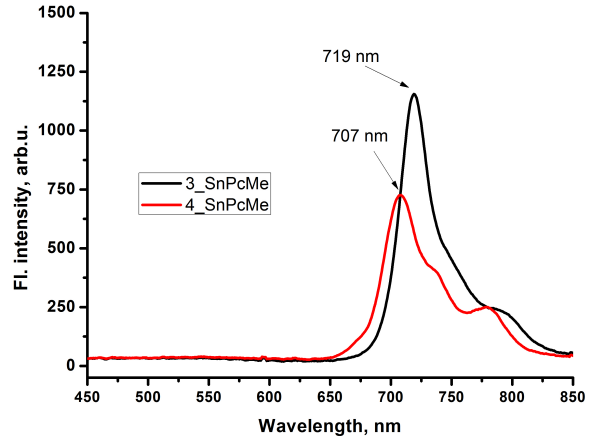
The fluorescence emission maxima were recorded at 704 nm and 721 nm for LuPcs and at 707 nm and 719 nm for SnPcs in DMSO (Fig. 9). The fluorescence spectra of Lu(III) Pcs and Sn(IV) Pcs showed a long red shift of the emission maximum (29–36 nm) as compared to the absorption maxima of Q-bands. The proximity of the wavelength in absorption and excitation spectra is indicative for the nuclear configurations of the ground and excited states, which are not affected by the excitation wavelength (365 nm, 635 nm, and 660 nm).

The fluorescence lifetime (τ_F) of a compound suggests the time interval, in which it can participates in photosensitization process. The fluorescence decay curves were mono-exponential and typical for non-aggregated molecular species. The fluorescence properties of quantum yield and lifetime of the complexes with the both metals (Lu^{3+} and Sn^{4+}) and the same substituted zinc complex (ZnPcMe) showed that the heavy atom ions complexes have relatively low quantum yields (0.01–0.08) and also lifetimes (2.24 ns for LuPc1.2 and 3.27 ns for LuPc1.1) as compared to the same properties of ZnPcMe, which have higher values (respectively 0.2; 3.99 ns). The very fast quenching of the fluorescence can be explained also by the presence of bulky substituents as well as the differences in the location of substitution groups so that the non-peripheral complexes underwent a faster quenching of the

fluorescence signal showing the shorter life-time than the peripheral derivatives.



(a)



(b)

Fig. 9 (a) Absorption spectra of Sn(II) vs Sn(IV) phthalocyanines, 2.2 and (b) fluorescence spectra of both new Sn(IV) phthalocyanines (2.1 and 2.2).

The capability of the both complexes of Lu(III) and Sn(IV) to produce singlet oxygen was measured in DMSO solutions in order to avoid some aggregation. The used indirect photochemical method is based on the oxidation of a chemical substrate 1,3-Diphenylisobenzofuran (DPBF) from the generated in the reaction vesicle molecular singlet oxygen during specific light irradiation. The calculations were performed referred to the quantum yield of the standard compound (ZnPc, 0.67 in DMSO) [74]). The values of singlet oxygen quantum yield were similar, namely 0.32 and 0.35 for LuPcs (1.1 and 1.2). In conclusion there is no significant difference in the singlet oxygen quantum yields by the replacement of Zn(II) and Al(III) with the large atom ions of Lu(III) and Sn(IV). The studies showed that there was significant decrease in the fluorescence quantum yields of Lu(III)- and Sn(IV) Pcs but not so much in their singlet oxygen quantum yields of importance for PDI efficacy.

4.3 Uptake and localization of Lu(III) phthalocyanines

The promising physicochemical properties of the water-soluble cationic Lu(III)- and Sn(IV)- phthalocyanines are the base for their photobiological investigations on pathogenic species. The expansion of the sensitiser uptake is known to depend on the structural modifications, one of which is the lack of symmetry in large atom's coordinated MPc molecules. *Candida albicans* is the most prevalent pathogen representing about 60% of all yeasts isolated in clinical samples. The uptake and localization studies were performed on the suspensions of following the fluorescence. The molecules attached to *C. albicans* cells were calculated on the basis of the fluorescence intensity of the spectra taken from extracted samples and referring to the calibration curves recorded for the same compound in the extraction mixture [74, 75]. The uptakes of LuPcs (3 μM) for different cellular suspensions (10^5 – 10^8 CFU mL^{-1}) followed the typical decrease of uptake with increase of the cell density. The samples were taken from the supernatant (1) in Phosphate-buffered saline (PBS) after incubation, (2) in PBS after 1st and 2nd cell wash, and (3) after cell extraction with a mixture of 2% Sodium dodecyl sulphate (SDS): Tetrahydrofuran (THF) or Dimethylformamide (DMF) (9 : 1) depends on the solubility of the studied compound. The obtained line dependence suggests that both Lu(III)Pcs and Sn(IV)Pcs are reliable to uptake into fungal cells and in amounts, which are not in a dependence on the coordinated metal ions. The typical inverse dependence of the decrease of the number of molecules accumulated into fungal cells with increase of the cell density was observed with a steep slope for the both LuPcs.

It is well accepted that cationic dyes are more likely to taken up by the bacterial and fungal species as a result of the nature of the cell wall and the binding process tend to occur via an electrostatic mechanism of interactions [76, 77]. The fluorescence confocal microscopy studies showed that the water-soluble cationic LuPcs have the surface localization in fungal cells with relatively high amount and in biofilms with extension inside the fungal cells. The full penetration into 48-h developed fungal biofilm occurred preferably on the cell wall and in the cytoplasm. The green fluorescence taken at excitation 488 nm and emission 500–580 nm shows the native fluorescence of the biofilm. The typical red fluorescence was observed for excitation with laser 635 nm and emission 660–740 nm. The formed *C. albicans* biofilms were determined with thicknesses between 17 and 23 μm and the scans on the slices showed the fluorescence within the whole biomass suggesting the full penetration of LuPcs.

The confocal fluorescence study of biofilms with Sn(IV) Pcs was not possible perhaps of the poor fluorescence intensity of the tin containing photosensitizers. The reason may be due to an improper excitation spectrum, which has limited light penetration and in case of fungal cells the cells inactivation may have happened layer by layer till the whole biofilm destruction

in a single step of irradiation. The phthalocyanine complexes with the same substituents but with different metal ions (ZnPcMe, SiPc1, GePc1, GaPc1 and GaPc2) were with approximately 2/3 limited penetration on the basis of the entire biofilm [66, 74]. The observation that Lu (III)Pcs completely penetrate into 48-h fungal biofilm can be explained with the cationic charge of the methylpyridyloxy groups as well as with some loss of planarity of the Pc ring due to large size of Lu atom. Even so the fungal biofilms incubated with LuPcs demonstrated the full penetration depth after the proper light excitation (635 nm) but very low photodynamic response (< 3 log) on the studied biofilms. [74]. The uptake and localization behaviour of Lu(III)Pcs seems to be in advance to their application in optical diagnosis. The complexes with large atom ions such as lutetium and tin together with the charge feature are an effective structure approach for improvement of the photosensitizer's penetration and selectivity for better photodynamic inactivation.

4.4 In vitro study on C. albicans

The phthalocyanine complexes with large atoms of Lu(III) and Sn(IV) were studied for their antimicrobial photodynamic efficacy on the pathogenic fungus *C. albicans* as suspension with density of approximately 10^7 CFU·mL^{-1} [78]. The studies were carried out with a wide concentration range of Lu(III)- and Sn(IV)-Pcs (1 μM – 30 μM). The photodynamic response towards *C. albicans* was lower than 3 log for 1–20 μM MPcs. The photoinactivation studies suggested that despite the significant uptake of both kinds of MPcs tested in these concentrations, the complete photo-inactivation was observed over 20 μM at the optimal tested light parameters (50 J·cm^{-2} and 60 mW·cm^{-2}). Lu(III)Pcs as well as Sn(IV)Pcs showed lack of dark toxicity for the studied concentrations. Considering the impact of the coordinated metal ion, the PDT effect of water-soluble LuPcs was studied in comparison to Zn(II) phthalocyanine with the same functional groups as substituents (ZnPcMe). At as low concentration as 3 μM MPcs the lower uptake was determined for the both LuPcs as compared to the uptake of ZnPcMe for *C. albicans* within a range of cell density (10^5–10^8 CFU / mL). Zn(II) and Si(IV) coordinated complexes were studied with higher phototoxic effects towards *C. albicans* for lower concentrations than that needed with LuPcs and SnPcs. All PDT studies were performed without cell washing after incubation followed by exposure with mild light dose (50 J·cm^{-2}) from a specific light source (LEDs emitted at 635 or 665 nm). The relatively high singlet oxygen quantum yields and high uptake in cells resulted in low PDI effect which can be explained with the lower cell susceptibility to singlet oxygen and another ROS.

The comparisons of the PDT responses of Lu(III)Pcs versus Sn(IV)Pcs on *C. albicans* planktonic and biofilm showed that ZnPcMe, which has the same substituents and differs only with Zn(II) coordination showed the photoinactivation with higher activity towards pathogens in suspension as well as biofilms. The molecular electronic structure due to replacement of Zn(II) with Lu(III) or Sn(IV) has changed the photophysical parameters but doesn't influence in a positive way on the photodynamic efficiency. The much harsh photodynamic conditions are needed together with repetitive application of the procedure in order to be effective the treatment of pathogens biofilms.

5 Conclusions

The knowledge of the structural characteristics, composition, location and nature of the substituents, the charge of the molecules and the effect these features have on the pharmacokinetic characteristics of phthalocyanine complexes used as photosensitive compounds for PDT of tumour cells and PDI of pathogenic microorganisms are essential.

The biologically active substituents used to increase selectivity of phthalocyanine complexes with respect to the treated objects give specific characteristics to these compounds both in terms of accumulation and in terms of localization in cellular structures and in the ways of treating the objects in order to increase the efficiency of light-activated photodynamic reactions.

The coordination of the phthalocyanine complex by means of large metal ions provides additional opportunities both for optimizing the physicochemical and pharmacokinetic characteristics of these complexes and for realizing compounds with different hydrophobicity. It is also a promising method for increasing their efficiency and reducing the toxicity of phthalocyanine complexes in their functionalization with bioactive conjugates such as sugars, sterols and amino acids.

In the use of phthalocyanine complexes for PDI of pathogenic microorganisms, the realization of compounds with affinity to the potential of bacteria membrane is of extremely importance for efficiency.

In conclusion, in terms of the realization of even more effective phthalocyanine photosensitizers, in-depth additional and appropriate studies are necessary to link the effectiveness of PDT with the structure of the compounds.

Disclosures

All authors declare that there is no conflict of interests in this paper.

Acknowledgments

The authors of this review thanks the Bulgarian National Science Fund for support with the project KP-06-H29/11/2018, KP-06-H23/8/2018 and KP-06-H38/13/2019.

References

1. N. Moldonado-Carmona, T.-S. Ouk, M. J. F. Calvete, M. M. Pereira, N. Villandier, and S. Leroy-Lhez, "Conjugating biomaterials with photosensitizers: advances and perspectives for photodynamic antimicrobial chemotherapy," Photochemical & Photobiological Sciences 19(4), 445–461 (2020).
2. P.-C. Lo, M. S. Rodriges-Morgade, R. K. Pandey, D. K. P. Ng, T. Torres, and F. Dumoulin, "The unique features and promises of phthalocyanines as advanced photosensitisers for photodynamic therapy of cancer," Chemical Society Reviews 49(4), 1041–1056 (2020).
3. X. Li, B.-D. Zheng, X.-H. Peng, S.-Z. Li, J.-W. Ying, Y. Zhao, J.-D. Huang, and J. Yoon, "Phthalocyanines as medicinal photosensitizers: Developments in the last five years," Coordination Chemistry Review 379, 147–160 (2019).
4. N. Sekkat, H. van der Bergh, T. Nyokong, and N. Lange, "Like a Bolt from the Blue: Phthalocyanines in Biomedical Optics," Molecules 17(1), 98–144 (2012).
5. A. Segalla, C. D. Borsarelli, S. E. Braslavsky, J. D. Spikes, G. Roncucci, D. Dei, G. Chiti, G. Jori, and E. Reddi, "Photophysical, photochemical and antibacterial photosensitizing properties of a novel octacationic Zn(ii)-phthalocyanine," Photochemical & Photobiological Sciences 1(9), 641–648 (2002).
6. T. C. White, K. A. Marr, and R. A. Bowden, "Clinical, cellular, and molecular factors that contribute to antifungal drug resistance," Clinical Microbiology Reviews 11(2), 382–402 (1998).
7. J. M. Dabrowski, B. Pucelik, A. Regiel-Futyra, M. Brindell, O. Mazuryk, A. Kyzioł, G. Stochel, W. Macyk, and L. G. Arnaut, "Engineering of relevant photodynamic processes through structural modifications of metallotetrapyrrolic photosensitizers," Coordination Chemistry Reviews 325, 67–101 (2016).
8. L. Sobotta, P. Skupin-Mrugalska, J. Piskorz, and J. Mielcarek, "Porphyrinoid photosensitizers mediated photodynamic inactivation against bacteria," European Journal of Medicinal Chemistry 175, 72–106 (2019).
9. V. Almeida-Marrero, J. A. Gonzales-Delgado, and T. Torres, "Emerging Perspectives on Applications of Porphyrinoids for Photodynamic Therapy and Photoinactivation of Microorganisms," Macroheterocycles 12(1), 8–16 (2019).
10. V. Mantareva, I. Angelov, D. Wöhrle, E. Borisova, and V. Kussovski, "Metallophthalocyanines for antimicrobial photodynamic therapy: an overview of our experience," Journal of Porphyrins and Phthalocyanines 17(6–7), 399–416 (2013).
11. F. M. Lauro, P. Pretto, L. Covolo, G. Jori, and G. Bertoloni, "Photoinactivation of bacterial strains involved in periodontal diseases sensitized by porphycene-polylysine conjugates," Photochemical & Photobiological Sciences 1(7), 468–470 (2002).
12. T. N. Demidova, M. R. Hamblin, "Effect of cell-photosensitizer binding and cell density on microbial photoinactivation," Antimicrobial Agents and Chemotherapy 49(6), 2329–2335 (2005).
13. C. A. Pereira, R. L. Romeiro, A. C. B. P. Costa, A. K. S. MacHado, J. C. Junqueira, and A. O. C. Jorge, "Susceptibility of Candida albicans, Staphylococcus aureus, and Streptococcus mutans biofilms to photodynamic inactivation: an in vitro study," Lasers in Medical Science 26(3), 341–348 (2011).
14. M. A. DiPalma, M. G. Alvarez, A. L. Ochoa, M. E. Milanesio, and E. N. Durantini, "Optimization of cellular uptake of zinc(II) 2,9,16,23-tetrakis[4-(N-methylpyridyloxy)] phthalocyanine for maximal photoinactivation of Candida albicans," Fungal Biology 117(11–12), 744–751 (2013).
15. B. S. Vig, K. M. Huttunen, K. Laine, and J. Rautio, "Amino acids as promoieties in prodrug design and development," Advanced Drug Delivery Reviews 65(10), 1370-1385 (2013).
16. L. S. Li, Z. P. Luo, Z. Chen, J. C. Chen, S. Y. Zhou, P. Xu, P. Hu, J. D. Wang, N. S. Chen, J. L. Huang, and M. D. Huang, "Enhanced Photodynamic Efficacy of Zinc Phthalocyanine by Conjugating to Heptalysine," Bioconjugate Chemistry 23(11), 2168–2172 (2012).
17. T. Dougherty, "An update on photodynamic therapy applications," Journal of Clinical Laser Medicine & Surgery 20(1), 3–7 (2002).
18. R. Malik, A. Manocha, and D. K. Suresh, "Photodynamic therapy – A strategic review," Indian Journal of Dental Research 21(2), 285–291 (2010).
19. V. Mantareva, V. Kussovski, and I. Angelov, "Cationic Metal Phthalocyanines as Effective Photosensitizers Towards Pathogenic Microorganisms," Chapter 5 in Photosensitizers: Types, Uses and selected Research, C. Withmire (Ed.), Nova Science Publishers, New York (2016).
20. M. Garcia-Iglesias, E. Huerta, "Towards new multivalent supramolecular helical structures based on phthalocyanines for PDT applications," Journal of Porphyrins and Phthalocyanines 21(11), 745–750 (2017).
21. M. Wainwright, Photosensitizers in Biomedicine, John Wiley and Sons, Chichester, UK (2009). ISBN: 978-0-470-74494-9.
22. M.-R. Ke, J. M. Eastel, K. L. K. Ngai, Y.-Y. Cheung, P. K. S. Chan, M. Hui, D. K. P. Ng, and P.-C. Lo, "Photodynamic inactivation of bacteria and viruses using two monosubstituted zinc(II) phthalocyanines," European Journal of Medicinal Chemistry 84, 278–283 (2014).

23. J. D. Miller, E. D. Baron, H. Scull, A. Hsia, J. C. Berlin, T. Mc Cormick, V. Colussi, M. E. Kenney, K. D. Cooper, and N. L. Oleinick, "Photodynamic therapy with the phthalocyanine photosensitizer Pc 4: the case experience with preclinical mechanistic and early clinical-translational studies," Toxicology and Applied Pharmacology 224(3), 290–299 (2007).
24. F. Dumoulin, M. Durmus, V. Ahsen, and T. Nyokong, "Synthetic pathways to water-soluble phthalocyanines and close analogs," Coordination Chemistry Reviews 254(23–24), 2792–2847 (2010).
25. N. Kuznetsova, N. Gretsova, E. Kalmykova, E. Makarova, S. Dashkevich, V. Negrimovskii, O. Kaliya, and E. Lukyanets, "Relationship between the photochemical properties and structure of pophyrins and related compounds," Russian Journal of General Chemistry 70(1), 133–140 (2000) [in Russian].
26. A. V. Ziminov, Y. A. Sidunets, V. S. Fundamensky, V. V. Gurzhiy, and S. M. Rams, "Synthesis, characterization, and investigation of photochemical properties of tetra-substituted zinc phthalocyanines bearing 4-(3,5-dimethyl-1H-pyrazol-1-yl)phenyl moiety with different linker heteroatoms," Inorganica Chimica Acta 501, 119306 (2020).
27. E. Guzel, A. Gunsel, B. Tuzun, G. Y. Atmaca, A. T. Bilgicli, A. Erdogmus, and M. N. Yarasir, "Synthesis of tetra-substituted metallophthalocyanines: Spectral, structural, computational studies and investigation of their photophysical and photochemical properties," Polyhedron 158, 316–324 (2019).
28. S. A. Mikhalenko, L. I. Soloveela, and E. A. Lukyanetz, "Phthalocyanines and Related Compounds: XXXVII. Synthesis of Covalent Conjugates of Carboxy-substituted Phthalocyanines with α-Amino Acids," Russian Journal of General Chemistry 74(3), 451–459 (2004).
29. E. A. Lukyanetz, V. N. Nemykin, "The key role of peripheral substituents in the chemistry of phthalocyanines and their analogs," Journal of Porphyrins and Phthalocyanines 14(01), 1–40 (2010).
30. Ao Wang, R. Zhou, L. Zhou, K. Sun, J. Jiang, and S. Wei, Positively charged phthalocyanine-arginine conjugates as efficient photosensitizer for photodynamic therapy, Bioorganic & Medicinal Chemistry 25(1), 1643–1651 (2017).
31. N. Nombona, E. Antunes, W. Chidawanyika, P. Kleyi, Z. Tshentu, and T. Nyokong, "Synthesis, photophysics and photochemistry of phthalocyanine-ε-polylysine conjugates in the presence of metal nanoparticles against Staphylococcus aureus," Journal of Photochemistry and Photobiology A: Chemistry 233, 24–33 (2012).
32. Q. Sun, B.-Y. Zheng, Y.-H. Zhang, J.-J. Zhuang, M.-R. Ke, and J. D. Huang, "Highly photocytotoxic silicon(IV) phthalocyanines axially modified with l-tyrosine derivatives: Effects of mode of axial substituent connection and of formulation on photodynamic activity," Dyes and Pigments 141, 521–529 (2017).
33. M. R. Ke, J. M. Eastel, K. L. K. Ngai, Y. Y. Cheung, P. K. S. Chan, M. Hui, D. K. P. Ng and P. C. Lo, "Oligolysine-conjugated zinc(II) phthalocyanines as efficient photosensitizers for antimicrobial photodynamic therapy," Chemistry–An Asian Journal 9(7), 1868–1875 (2014).
34. D. Wöhrle, M. Eskes, K. Shigehara, and A. Yamada, "A Simple Synthesis of 4, 5-Disubstituted 1, 2-Dicyanobenzenes and 2, 3, 9, 10, 16, 17, 23, 24-Octasubstituted Phthalocyanines," Synthesis 1993(02), 194–196 (1993).
35. S. E. Maree, T. Nyokong, "Syntheses and photochemical properties of octasubstituted phthalocyaninato zinc complexes," Journal of Porphyrins and Phthalocyanines 5(11), 782–792 (2001).
36. M. B. Aliosman, I. Z. Eneva, I. B. Stoineva, M. Durmus, and V. N. Mantareva, "Aminophenoxy-substituted zinc (II) phthalocyanines as basic photosensitizers for conjugation with biologically active moieties via amide bond," Bulgarian Chemical Communications 49, (2017), 79-85.
37. X.-F. Zhang, X. Li, L. Niu, L. Sun, and L. Liu, "Charge Transfer Photophysics of Tetra(α-amino) Zinc Phthalocyanine," Journal of Fluorescence 19(6), 947–954 (2009).
38. L. Sobotta, S. Lijewski, J. Dlugaszewska, J. Nowicka, J. Mielcarek, and T. Goslinski, "Photodynamic inactivation of Enterococcus faecalis by conjugates of zinc (II) phthalocyanines with thymol and carvacrol loaded into lipid vesicles," Inorganica Chimica Acta 489, 180–190 (2019).
39. D. Lin, Y. Wang, Q. Zhan, J. Zhou, L. Zhou, and S. Wei, "The substituted amino group type dependent sensitivity enhancing of cationic phthalocyanine derivatives for photodynamic activity," Journal of Photochemistry and Photobiology A: Chemistry 315, 107–120 (2016).
40. A. Shrestha, A. Kishen, "Polycationic Chitosan-Conjugated Photosensitizer for Antibacterial Photodynamic Therapy," Photochemistry and Photobiology 88(3), 577–583 (2012).
41. V. Mantareva, I. Angelov, V. Kussovski, R. Dimitrov, L. Lapok, and D. Wörhle, "Photodynamic efficacy of water-soluble Si(IV) and Ge(IV) phthalocyanines towards Candida albicans planktonic and biofilm cultures," European Journal of Medicinal Chemistry 46(9), 4430–4440 (2011).
42. I. Angelov, A. Kril, R. Dimitrov, E. Borisova, L. Avramov, and V. Mantareva, "Light enhancement of in vitro antitumor activity of galactosylated phthalocyanines," Photonics & Lasers in Medicine 5(2), 123–140 (2016).
43. V. Mantareva, M. Syuleyman, A. Slavova-Kazakova, I. Angelov, and M. Durmus, "Mestranol moieties clicked to Zn(II)phthalocyanine for controllable photosensitized oxidation of cholesterol," Archives of Biotechnology and Biomedicine, 041–048 (2021).
44. M. Aliosman, I. Angelov, Y. Mitrev, I. Iliev, M. Durmuş, and V. Mamtareva, "Novel Zn(II) phthalocyanine with tyrosine moieties for photodynamic therapy: Synthesis and comparative study of light-associated properties," Polyhedron 162, 121–128 (2019).

45. V. Mantareva, M. Aliosman, M. Durmuş, and I. Angelov, "Amino acids substituted phthalocyanine complexes: an overview on the synthetic approaches and UV-vis properties related to photodynamic applications," Bulgarian Chemical Communications 50, 185–192 (2018).
46. S. Hermann, A. H. Wagenknecht, "Synthesis of N,N-dimethylaminopyrene-modified short peptides for chemical photocatalysis," Journal of Peptide Science 23(7–8), 563-566 (2017).
47. B. Kiyak, A. A. Esenpinar, and M. Balut, "Synthesis, characterization, photophysical and photochemical properties of zinc and indium phthalocyanines bearing a vanillylacetone moiety known as an anticarcinogenic agent," Polyhedron 90, 183–196 (2015).
48. A. Ogunsipe, D. Maree, and T. Nyokong, "Solvent effects on the photochemical and fluorescence properties of zinc phthalocyanine derivatives," Journal of Molecular Structure 650(1–3), 131–140 (2003).
49. S. K. Sharma, T. Dai, G. B. Kharkwal, Y.-Y. Huang, L. Huang, V. J. B. de Arce, G. P. Tegos, and M. R. Hamblin, "Drug discovery of antimicrobial photosensitizers using animal models," Current Pharmaceutical Design 17(13), 1303–1319 (2011).
50. W. C. M. A. Melo, L. F. Castro, and R. M. M. T. S. Dal'Mas, "Effectiveness of photodynamic therapy on gram-negative bacteria," in Science Against Microbial Pathogens: Communicating Current Researchand Technological Advances 3, Badajos, Spain, 662–667 (2011).
51. V. Kussovski, V. Mantareva, I. Angelov, P. Orozova, D. Wohrle, G. Schnurpfeil, E. Borisova, and L. Avramov, "Photodynamic inactivation of Aeromonas hydrophila by cationic phthalocyanines with different hydrophobicity," FEMS Microbiology Letters 294(2), 133–140 (2009).
52. V. Mantareva, I. Angelov, V. Kussovski, D. Woehrle, and S. Dimitrov, "Metallophthalocyanines as photodynamic sensitizers for treatment of pathogenic bacteria. Uptake and photoinactivation properties," Comptes Rendus de l'Acade'mie Bulgare des Sciences 63(1), 77–84 (2010).
53. V. Mantareva, I. Angelov, D. Wohrle, V. Dogandhiyska, S. Dimitrov, and V. Kussovski, "Water-soluble phthalocyanine complexes of Ga(III) and In(III) in the photodynamic inactivation of pathogenic fungus," Proceedings of SPIE 7747, 774712 (2011).
54. V. Mantareva, I. Angelov, V. Kussovski, and S. Dimitrov, "Advanced photodynamic inactivation of dental pathogenic microorganisms with water-soluble and cationic phthalocyanines," in Science Against Microbial Pathogens: Communicating Current Research and Technological Advances 1(11), FORMATEX Research Centre, Badajos, Spain, 650-661 (2011).
55. I. Angelov, V. Mantareva, V. Kussovski, D. Woehrle, H. Kisov, M. Belcheva, T. Georgieva, and S. Dimitrov, "Susceptibility of representative Dental Pathogens to inactivation by the PDT with water-soluble photosensitizers," Proceedings of SPIE 7994, 79941A (2011).
56. R. Gergova, T. Georgieva, I. Angelov, V. Mantareva, S. Valkanov, I. Mitov, and S. Dimitrov, "Photodynamic therapy with water-soluble phtalocyanines against bacterial biofilms in teeth root canals," Proceedings of SPIE 8427, 842744 (2012).
57. V. Kussovski, V. Mantareva, I. Angelov, L. Avramov, E. Popova, and S. Dimitrov, "Al(III), Pd(II) and Zn(II) phthalocyanines for inactivation of dental pathogen Aggregatibacter actinomycetemcomitans as planktonic and biofilm-cultures," Proceedings of SPIE 8427, 84273X (2012).
58. C. Gol, M. Durmus, "Investigation of photophysical, photochemical and bovine serum albumin binding properties of novel water-soluble zwitterionic zinc phthalocyanine complexes," Synthetic Metals 162(7–8), 605-613 (2012).
59. G. Dilber, M. Durmus, and H. Kantekin, "Non-aggregated zwitterionic Zinc (II) phthalocyanine complexes in water with high singlet oxygen quantum yield," Dyes and Pigments 160, 267–284 (2019).
60. S. Colak, M. Durmus, and S. Z. Yildiz, "Investigation of the photophysical and photochemical properties of peripherally tetra-substituted water-soluble zwitterionic and cationic zinc (II) phthalocyanines," Dalton Transactions 45(25), 10402–10410 (2016).
61. V. N. Nemykin, E. A. Luk'yanets, "11 The Key Role of Peripheral Substituents in Chemistry of Phthalocyanines," in Handbook of Porphyrin Science vol. 3, K. Kadish, K. M. Smith, and R. Guilard (Eds.), Word Scientific Publishing, Singapore, 1–323 (2010).
62. F. Foschi, C. R. Fontana, K. Ruggiero, R. Riahi, A. Vera, A. G. Doukas, T.C. Pagonis, R. Kent, P. P. Stashenko, and N. S. Soukos, "Photodynamic inactivation of Enterococcus faecalis in dental root canals in vitro," Lasers in Surgery and Medicine: The Official Journal of the American Society for Laser Medicine and Surgery 39(10), 782–787 (2007).
63. E. P. Prochnow, M. R. Martins, C. B. Campagnolo, R. C. Vianna, M. A. Villetti, and K. Z. Kantorski, "Antimicrobial photodynamic effect of phenothiazinic photosensitizers in formulations with ethanol on Pseudomonas aeruginosa biofilms," Photodiagnosis and Photodynamic Therapy 13, 291–296 (2016).
64. V. Mantareva, C. Gol, V. Kussovski, M. Durmus, and I. Angelov, "Impact of water-soluble zwitterionic Zn(II) phthalocyanines against pathogenic bacteria," Zeitschrift für Naturforschung C 74(7–8), 183–191 (2019).
65. V. Mantareva, V. Kussovski, I. Angelov, D. Wöhrle, R. Dimitrov, E. Popova, and S. Dimitrov, "Non-aggregated Ga (III)-phthalocyanines in the photodynamic inactivatio planktonic and biofilm cultures of pathogenic microorganisms," Photochemical & Photobiological Sciences 10(1), 92–102 (2011).

66. V. Mantareva, V. Kussovski, I. Angelov, E. Borisova, L. Avramov, G. Schnurpfeil, and D. Wöhrle, "Photodynamic activity of water-soluble phthalocyanine zinc (II) complexes against pathogenic microorganisms," Bioorganic & Medicinal Chemistry 15(14), 4829–4835 (2007).
67. M. Wainwrigh, T. Maisch, S. Nonell, K. Plaetzer, A. Almeida, G. P. Tegos, and M. R. Hamblin, "Photoantimicrobials–are we afraid of the light?" The Lancet Infectious Diseases 17(2), e49–e55 (2017).
68. V. Kussovski, V. Mantareva, M. Durmus, and I. Angelov, "Quaternized Zn (II) phthalocyanines for photodynamic strategy against resistant periodontal bacteria," Zeitschrift für Naturforschung C 73(5–6), 221–228 (2018).
69. T. Nyokong, "Effects of substituents on the photochemical and photophysical properties of main group metal phthalocyanines," Coordination Chemistry Reviews 251(13–14), 1707–1722 (2007).
70. M. Durmus, S. Yeslot, B. Cosut, A. Gul Gurek, A. Kilic, and V. Ahsen, "Comparison of photophysicochemical properties of hexaphenoxycyclotriphosphazenyl-substituted metal-free, mono-and bis-lutetium phthalocyanines," Synthetic metals 160(5–6), 436–444 (2010).
71. R. Zugle, C. Litwinski, and T. Nyokong, "Photophysical characterization of dysprosium, erbium and lutetium phthalocyanines tetrasubstituted with phenoxy groups at non-peripheral positions," Polyhedron 30(9), 1612–1619 (2011).
72. F. L. Lu, "The effects of substituents, molecular symmetry, ionic radius of the rare earth metal, and macrocycle on the electronic absorption spectra characteristics of sandwich-type bis(phthalocyaninato) and mixed (phthalocyaninato)(porphyrinato) rare earth complexes," Polyhedron 26(14), 3939–3946 (2007).
73. J. L. Sessler, G. Hemmi, T. D. Mody, T. Murai, A. K. Burrell, and S. W. Young, "Texaphyrins: synthesis and applications," Accounts of Chemical Research 27(2), 43–50 (1994).
74. V. Mantareva, M. Durmus, M. Aliosman, I. Stoineva, and I. Angelov, "Lutetium(III) acetate phthalocyanines for photodynamic therapy applications: Synthesis and photophysicochemical properties," Photodiagnosis and Photodynamic Therapy 14, 98–103 (2016).
75. V. Mantareva, V. Kussovski, M. Durmus, E. Borisova, and I. Angelov, "Photodynamic inactivation of pathogenic species Pseudomonas aeruginosa and Candida albicans with lutetium (III) acetate phthalocyanines and specific light irradiation," Lasers in Medical Science 31(8), 1591–1598 (2016).
76. N. Masilela, T. Nyokong, "The synthesis and photophysical properties of novel cationic tetra pyridyloxy substituted aluminium, silicon and titanium phthalocyanines in water," Journal of Luminescence 130(10), 1787–1793 (2010).
77. D. Wöhrle, N. Iskander, G. Graschew, H. Sinn, E. Friedrich, W. Maier-Borst, J. Stern, and P. Schlag, "Synthesis of positively charged phthalocyanines and their activity in the photodynamic therapy of cancer cells," Photochemistry and Photobiology 51(3), 351–356 (1990).
78. I. Eneva, M. Aliosman, I. Angelov, K. Popov, and V. Mantareva, "Mono-ring phthalocyanine complexes of large ions Lu3+ and Sn4+: synthesis and comparison of photophysical properties," Bulgarian Chemical Communications 49(D), 246–252 (2017).

Photodynamic Action in Thin Sensitized Layers: Estimating the Utilization of Light Energy

Gennady Meerovich[1]*, Igor Romanishkin[1], Ekaterina Akhlyustina[2], Marina Strakhovskaya[3,4], Evgeniya Kogan[5], Ivan Angelov[6,7], Victor Loschenov[1,2], and Ekaterina Borisova[7]

[1] Prokhorov General Physics Institute of the Russian Academy of Sciences, 38 Vavilova str., Moscow 119991, Russia
[2] National Research Nuclear University 'MEPHI', 31 Kashirskoe shosse, Moscow 115409, Russia
[3] Department of Biology, Lomonosov Moscow State University, 1–12 Leninskie Gory, Moscow, 119234, Russia
[4] Federal Research and Clinical Center of Specialized Medical Care and Medical Technologies of the Federal Medical and Biological Agency of Russia, 28 Orekhovyy Bul'var, Moscow 115682, Russia
[5] I. M. Sechenov First Moscow State Medical University, 2–4 Bolshaya Pirogovskaya str., Moscow 119991, Russia
[6] Institute of Organic Chemistry with Centre of Phytochemistry, Bulgarian Academy of Sciences, 9 acad. Georgi Bonchev str., Sofia 1113, Bulgaria
[7] Institute of Electronics, Bulgarian Academy of Sciences, 72 Boulevard Tzarigradsko shose, Sofia 1784, Bulgaria

*** e-mail:** meerovich@mail.ru

Abstract. The result of photodynamic action significantly depends on the density of the light dose absorbed by the photosensitizer. The efficiency of using light to excite photosensitizer molecules and minimization of its loss plays an important role in ensuring the overall success of the process. When carrying out photodynamic treatment of thin sensitized layers (such as inactivation of surface pathogens or *in vitro* screening studies of photosensitizers), only a part of the light dose is absorbed in the layer, while a significant part is lost, especially at low concentrations of the photosensitizer. In this work, we evaluate the decrease in absorbed light dose depending on the extinction and concentration of the photosensitizer in a thin sensitized layer, the shape of its absorption spectrum, and the shape of the excitation light source spectrum. It was found out that a significant loss of the absorbed dose occurs upon excitation of photosensitizers, especially with low extinction, when using light sources with a broad emission spectrum. This loss must be taken into consideration when predicting the results of photodynamic exposure and optimizing its tactics. © 2021 Journal of Biomedical Photonics & Engineering.

Keywords: photodynamic action; relative absorbed photodynamic dose; laser diode; photosensitizer.

Paper #3436 received 24 May 2021; revised manuscript received 11 Jun 2021; accepted for publication 11 Jun 2021; published online 28 Jul 2021. doi: 10.18287/JBPE21.07.040301 [Special issue on Ekaterina Borisova's contribution to World Biophotonics].

1 Introduction

Photodynamic action (PDA) is widely used for the therapy of neoplasms [1, 2], infected wounds and other pathological foci of various etiologies [3–5], disinfection of biological fluids, blood components, and water [6]. The photodynamic effect is the photooxidative destruction of molecular structures that ensure the functioning of tumor cells and pathogens (bacteria, viruses) by reactive oxygen species (ROS). Molecules of a photosensitizer (PS) that sensitize the environment in the affected area catalyze the generation of ROS in their vicinity upon excitation with light. The light transfers the energy necessary for this process to the medium containing the photosensitizer. The effect of PDA increases with the volume density of the energy absorbed by PS, which depends on the light intensity, the concentration and extinction of PS.

Light-emitting diodes (LED) and lasers, primarily on laser diodes (LD), are widely used as light sources for PDA. These light sources provide radiation with high intensity, and their emission spectrum is narrower ($\Delta\lambda_{LED}$ = 20 – 30 nm, $\Delta\lambda_{LD}$ = 4 nm) than the absorption bands of PS. Such light sources can be created, in general, with practically any wavelength (at least in the red and near-infrared spectral ranges) suitable for the excitation of PS. Broadband light sources with a spectral band selected by a bandpass filter in the PS absorption region can also be used for the excitation of PSs [7]. However, only the part of the light energy that lies in the spectral region of the PS absorption band is absorbed. The rest of the light passes through the sensitized medium.

Many PDA problems require the PS excitation in thin (≤ 5 mm) layers of sensitized aqueous compositions. Such problems include photodynamic inactivation of pathogens – viruses or bacteria, on various surfaces [8, 9], *in vitro* screening studies of PS properties [10, 11]. For small layer thicknesses and low (less than 10 μM) PS concentrations used for such a PDA, a significant part of the light in the spectral range of the PS absorption band can pass through the layer without participating in the PDA process. This loss, which can be described as a decrease of relative absorbed photodynamic dose (RAPD) [12], results in decreased PDA efficiency. It can also lead to errors in screening studies of PSs with various extinction and concentration since both the losses and the amount of the absorbed energy in the sensitized medium for different PSs will be different.

2 Materials and Methods

In this work, such an assessment was carried out for aqueous solutions of cationic PS, which are distinguished by high values of extinction and quantum yield of ROS generation: methylene blue, $C_{16}H_{18}ClN_3S$ (ε_{664} = 0.61 × 10^5 $M^{-1}cm^{-1}$);
zinc octakis(cholinyl)phthalocyanine, $ZnPcChol_8$ (ε_{682} = 1.7 × 10^5 $M^{-1}cm^{-1}$); meso-tetrakis[1-(2'-bromoethyl)-3-pyridyl]-bacteriochlorin tetra-bromide, $(3\text{-PyBrE})_4BCBr_4$ (ε_{762} = 1 × 10^5 $M^{-1}cm^{-1}$). These PS do not aggregate in a wide range of concentrations and are promising both for photodynamic inactivation of pathogens [6, 8, 9, 13] and for antitumor photodynamic therapy [10, 14, 15]. Fig. 1 shows the normalized spectral contours $A(\lambda)$ of the absorption bands of these PSs (the absorption spectrum at low concentration divided by its maximum value) and the normalized emission spectra $I_{norm}(\lambda)$ of LEDs (mLED-664, mLED-684, mLED-763, Biospec, Russia), which can be used to excite these PSs (light intensity spectral density divided by the integral intensity).

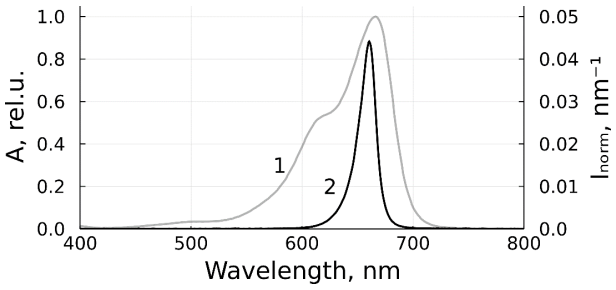
The estimates of the RAPD in a non-scattering layer with the thickness L, obtained in the approximation that the spectral characteristics of PS absorption are independent of its concentration, lead to the following relation characterizing RAPD parameter η, equal to a ratio between the light energy absorbed in the layer and total light energy illuminating the layer during the PDA process:

$$\eta = 1 - \frac{\int_{\lambda_1}^{\lambda_2} I(\lambda) \times e^{-2.3\,D(\lambda)} d\lambda}{\int_{\lambda_1}^{\lambda_2} I(\lambda)\, d\lambda}, \quad (1)$$

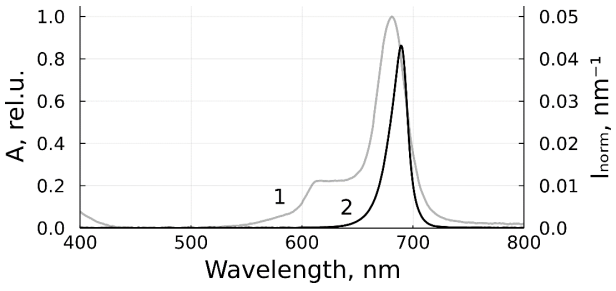
where

$$D(\lambda) = \varepsilon A(\lambda) C L. \quad (2)$$

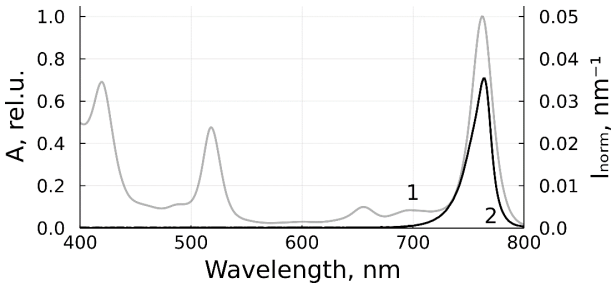
Here $D(\lambda)$ is the optical density of the layer containing PS, ε and C – extinction and molar concentration of PS, λ_1 and λ_2 are the boundaries of the spectral range in which the spectrum of the radiation source lies, $I(\lambda)$ is the spectral density of the light intensity.



(a)



(b)



(c)

Fig. 1 Normalized spectral contours (1) of the absorption bands of photosensitizers (a – $C_{16}H_{18}ClN_3S$, b – $ZnPcChol_8$, c – $(3\text{-PyBrE})_4BCBr_4$) and normalized emission spectra (2) of LEDs for their excitation.

For a broadband light source with a bandpass filter that illuminates in the range from λ_1 to λ_2, the Eq. (1) becomes

$$\eta = 1 - \frac{\int_{\lambda_1}^{\lambda_2} e^{-2.3\,D(\lambda)}\,d\lambda}{\lambda_2 - \lambda_1}. \qquad (3)$$

For a monochromatic or narrow-band source, the spectral half-width of which is much smaller than the absorption spectrum half-width, the Eq. (1) is simplified to

$$\eta = 1 - e^{-2.3\,D(\lambda)}. \qquad (4)$$

3 Results

The estimates obtained using these formulas show that when thin layers of the studied PS with a concentration below 10 μM are irradiated, a significant part of the light energy is not absorbed. Instead, it passes through the sensitized layer. RAPD depends on the PS's extinction, its concentration, the spectral shapes of the PS's absorption and the source emission (Figs. 2, 3). The highest values of RAPD are achieved upon monochromatic excitation at a wavelength coinciding with the spectral absorption maximum of the PS. When using LEDs with optimally selected radiation wavelengths, the difference in the value of RAPD is small. However, when using a source whose radiation wavelength is noticeably different from the wavelength of the spectral maximum of the absorption band of the PS (even within the boundaries of the band), RAPD decreases significantly, especially for PS with a narrow absorption band. RAPD of broadband sources with transmission bandpass filters in thin layers is much lower. The values of RAPD for light from such sources can be 1.5–2 times lower than from narrow-band sources.

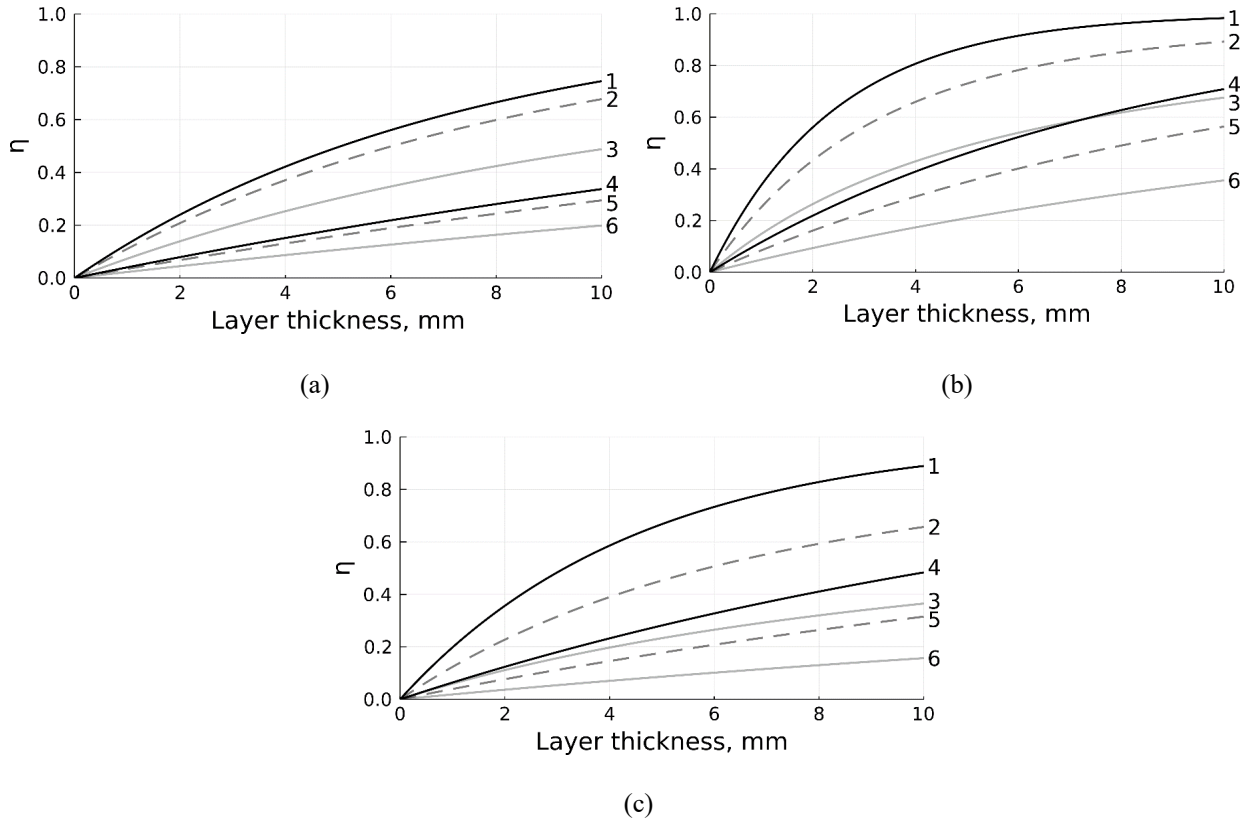


Fig. 2 Dependence on the layer thickness of RAPD for sources with the wavelength of the maximum radiation coinciding with the wavelength of the spectral maximum of absorption of PS with two concentrations: (a) $C_{16}H_{18}ClN_3S$, (b) $ZnPcChol_8$; (c) $(3\text{-}PyBrE)_4BCBr_4$; 1, 2, 3 – concentration of 10 μM, 4, 5, 6 – concentration of 3 μM; 1, 4 – laser; 2, 5 – LED; 3, 6 – broadband radiation source with a bandwidth of 100 nm.

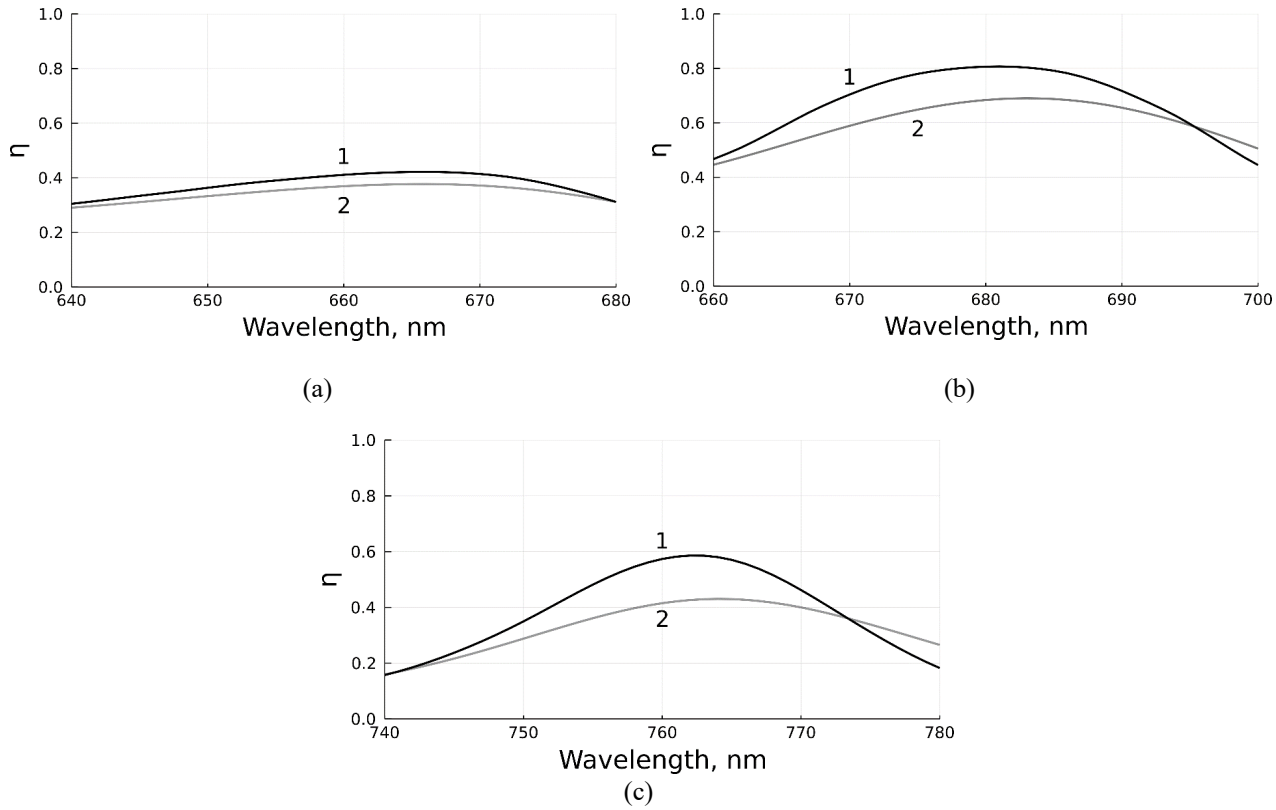


Fig. 3 RAPD of the sensitized PS layer with a thickness of 5 mm depending on the wavelength of the spectral maximum of the light source (1 – laser, 2 – LED). PS concentration is 10 μM: (a) $C_{16}H_{18}ClN_3S$, (b) $ZnPcChol_8$; (c) $(3\text{-}PyBrE)_4BCBr_4$.

4 Conclusions

The estimates demonstrate that during PDA in thin sensitized layers, a significant part of the exciting light leaves the layer without being absorbed, and RAPD depends on the layer thickness, PS extinction and concentration, as well as the shape of the exciting light and absorption spectral bands of PS. The loss of a part of the light energy reduces the efficiency of the PDT as a whole. This loss must be taken into account when predicting PDA results and optimizing its tactics, particularly when choosing light sources and parameters of irradiation for photodynamic disinfection of surfaces from viral and bacterial infections [2, 5], or clinical photodynamic treatment to local virus-infected foci [5, 6]. The obtained results are also important for *in vitro* studies and comparing the photodynamic efficiency of PSs [10, 14] since the values of RAPD are very different for PSs with different extinction, especially when using broadband light sources. However, it should be noted that for in vivo studies of antitumor PDA, it becomes necessary to consider the scattering properties of the medium for evaluating RAPD. Photodynamic effectiveness also becomes more dependent not only on RAPD but on photochemical and photobiological factors as well. High absorption and scattering would also result in greater depth inhomogeneity of PDA in thick sensitized layers or solid tumors, reducing the overall effectiveness of the treatment.

Disclosures

All authors declare that there is no conflict of interests in this paper.

Acknowledgements

The research of M. Strakhovskaya, G. Meerovich was funded by RFBR according to the project #20-04-60084.

The research of E. Akhlyustina, E. Kogan, I. Angelov, E. Borisova was funded by RFBR and BNSF according to the bilateral project (RFBR #20-52-18008, BNSF #KP-06-Russia/9-2020).

References

1. J. Usuda, T. Inoue, T. Tsuchida, K. Ohtani, S. Maehara, N. Ikeda, Y. Ohsaki, T. Sasaki, and K. Oka, "Clinical trial of photodynamic therapy for peripheral-type lung cancers using a new laser device in a pilot study," Photodiagnosis and Photodynamic Therapy 30, 101698 (2020).
2. H. Abrahamse, M. R. Hamblin, "New photosensitizers for photodynamic therapy," Biochemical Journal 473(4), 347–364 (2016).
3. G. A. Meerovich, E. V. Akhlyustina, I. G. Tiganova, E. A. Lukyanets, E. A. Makarova, E. R. Tolordava, O. A. Yuzhakova, I. D. Romanishkin, N. I. Philipova, Yu. S. Zhizhimova, Yu. M. Romanova, V. B. Loschenov, and A. L. Gintsburg, "Novel Polycationic Photosensitizers for Antibacterial Photodynamic Therapy," in Advances in Experimental Medicine and Biology, Springer, New York, 1–19 (2019).
4. M. C. Geralde, I. S. Leite, N. M. Inada, A. C. G. Salina, A. I. Medeiros, W. M. Kuebler, C. Kurachi, and V. S. Bagnato, "Pneumonia treatment by photodynamic therapy with extracorporeal illumination - an experimental model," Physiological Reports 5(5), e13190 (2017).
5. L. D. Dias, V. S. Bagnato, "An update on clinical photodynamic therapy for fighting respiratory tract infections: a promising tool against COVID-19 and its co-infections," Laser Physics Letters 17(8), 083001 (2020).
6. E. Ben-Hur, A. C. E. Moor, H. Margolis-Nunno, P. Gottlieb, M. M. Zuk, S. Lustigman, B. Horowitz, A. Brand, J. Van Steveninck, and T. M. A. R. Dubbelman, "The photodecontamination of cellular blood components: mechanisms and use of photosensitization in transfusion medicine," Transfusion Medicine Reviews 10(1), 15–22 (1996).
7. D. Korneev, O. Kurskaya, K. Sharshov, J. Eastwood, and M. Strakhovskaya, "Ultrastructural Aspects of Photodynamic Inactivation of Highly Pathogenic Avian H5N8 Influenza Virus," Viruses 11(10), 955 (2019).
8. K. Sharshov, M. Solomatina, O. Kurskaya, I. Kovalenko, E. Kholina, V. Fedorov, G. Meerovich, A. Rubin, and M. Strakhovskaya, "The Photosensitizer Octakis(cholinyl)zinc Phthalocyanine with Ability to Bind to a Model Spike Protein Leads to a Loss of SARS-CoV-2 Infectivity In Vitro When Exposed to Far-Red LED," Viruses 13(4), 643 (2021).
9. M. G. Strakhovskaya, G. A. Meerovich, A. N. Kuskov, S. A. Gonchukov, and V. B. Loschenov, "Photoinactivation of coronaviruses: going along the optical spectrum," Laser Physics Letters 17(9), 093001 (2020).
10. R. I. Yakubovskaya, A. D. Plyutinskaya, E. A. Plotnikova, M. A. Grin, and A. F. Mironov, "Comparative in vitro study of different classes of photosensitizers. Pyropheophorbides and chlorines," Russian Journal of Biotherapy 14(1), 43–51 (2015) [in Russian].
11. G. A. Meerovich, E. V. Akhlyustina, I. G. Tiganova, E. A. Lukyanets, E. A. Makarova, E. R. Tolordava, O. A. Yuzhakova, I. D. Romanishkin, N. I. Philipova, Yu. S. Zhizhimova, S. A. Gonchukov, Yu. M. Romanova, and V. B. Loschenov, "Photodynamic inactivation of Pseudomonas aeruginosa bacterial biofilms using new polycationic photosensitizers," Laser Physics Letters 16(11), 115603 (2019).
12. B. W. Pogue, L. Lilge, M. S. Patterson, B. C. Wilson, and T. Hasan, "Absorbed photodynamic dose from pulsed versus continuous wave light examined with tissue-simulating dosimeters," Applied Optics 36(28), 7257–7269 (1997).
13. V. A. Svyatchenko, S. D. Nikonov, A. P. Mayorov, M. L. Gelfond, and V. B. Loktev, "Antiviral photodynamic therapy: Inactivation and inhibition of SARS-CoV-2 in vitro using methylene blue and Radachlorin," Photodiagnosis and Photodynamic Therapy 33, 102112 (2021).
14. R. I. Yakubovskaya, E. A. Plotnikova, A. D. Plyutinskaya, N. B. Morozova, V. I. Chissov, E. A. Makarova, S. V. Dudkin, E. A. Lukyanets, and G. N. Vorozhtsov, "Photophysical properties and in vitro and in vivo photoinduced antitumor activity of cationic salts of meso-tetrakis(N-alkyl-3-pyridyl)bacteriochlorins," Journal of Photochemistry and Photobiology B: Biology 130, 109–114 (2014).
15. N. B. Morozova, R. I. Yakubovskaya, V. I. Chissov, V. M. Negrimovskiy, and O. A. Yuzhakova, "In vivo photo-induced activity of positively charged zinc phthalocyanine used for photodynamic therapy for malignancies," Russian Journal of Oncology 17(1), 23–28 (2012) [in Russian].

Tissue Spectroscopy and Optical Clearing of Colorectal Mucosa in the Pursuit of New Cancer Diagnostic Approaches

Luís Fernandes[1], Hugo Silva[1,2], Inês Martins[1,2], Sónia Carvalho[3,4], Isa Carneiro[3], Rui Henrique[3,5], Valery V. Tuchin[6,7,8], and Luís M. Oliveira[1,2*]

[1] Physics Department, School of Engineering, Polytechnic Institute of Porto,
Rua Dr. António Bernardino de Almeida 431, 4249-015 Porto, Portugal
[2] Center of Innovation in Engineering and Industrial Technology, ISEP, Rua Dr. António Bernardino de Almeida 431, 4249-015 Porto, Portugal
[3] Department of Pathology and Cancer Biology and Epigenetics Group-Research Center,
Portuguese Oncology Institute of Porto, 4200-072 Porto, Portugal
[4] Department of Pathology, Santa Luzia Hospital, ULSAM, 4904-858 Viana do Castelo, Portugal
[5] Department of Pathology and Molecular Immunology, Institute of Biomedical Sciences Abel Salazar-University of Porto (ICBAS-UP), 4050-313 Porto, Portugal
[6] Science Medical Center, Saratov State University, 83 Astrakhanskaya str., Saratov 410012, Russian Federation
[7] Laboratory of Laser Molecular Imaging and Machine Learning, National Research Tomsk State University,
36 Lenin's av., Tomsk 634050, Russian Federation
[8] Laboratory of Laser Diagnostics of Technical and Living Systems, Precision Mechanics and Control Institute of the Russian Academy of Sciences, 24 Rabochaya str., Saratov 410028, Russian Federation

*** e-mail:** lmo@isep.ipp.pt

Abstract. In this paper we present three studies that demonstrate the applicability of spectroscopy methods and optical clearing treatments in pathology identification and monitoring. In the first study, by obtaining the absorption spectra of human healthy and pathological (adenocarcinoma) colorectal mucosa tissues, it was possible to identify a higher content of a pigment in the diseased tissues. This study also shows that machine learning methods can be used to reach the same differentiated results *in vivo* through diffuse reflectance spectroscopy. In the second study, the combination of collimated transmittance spectroscopy with optical clearing treatments allowed to obtain the diffusion coefficients of glucose in healthy and pathological colorectal mucosa as: $D_{\text{glucose}}=5.8\times10^{-7}$ cm^2/s and $D_{\text{glucose}}=4.4\times10^{-7}$ cm^2/s, respectively. This study also demonstrated that the diseased tissues contains about 5% more mobile water than the healthy tissues. The third study was performed to evaluate the protein dissociation mechanism of optical clearing. By treating both healthy and pathological colorectal mucosa tissues with 93%-glycerol, a protein dissociation rate of about 3 times higher was obtained for the pathological mucosa. All the discriminating parameters that result from these studies can be obtained in the *in vivo* situation through diffuse reflectance spectroscopy and further studies to evaluate their values in different stages of cancer progression are of great importance to develop disease monitoring protocols. © 2021 Journal of Biomedical Photonics & Engineering.

Keywords: colorectal cancer; tissue optical clearing; optical clearing mechanisms; cancer detection; enhanced tissue spectroscopy.

Paper #3447 received 31 Jul 2021; revised manuscript received 24 Aug 2021; accepted for publication 27 Aug 2021; published online 8 Sep 2021. doi: 10.18287/JBPE21.07.040302.

1 Introduction

Current diagnostic of oncologic malignancies relies on imaging methods that use ionizing radiation [1]. Such procedures present a great number of disadvantages, since ionizing radiation can induce, among others, DNA double-strand breaking [2, 3] and cell death in surrounding healthy tissues [4, 5]. To avoid such side effects of ionizing radiation, biophotonics suggests alternative optical methods that, by the harmless use of light, can perform reliable and noninvasive diagnostic procedures. To develop such methods, the cancer-related biophotonics research has been growing in the past 30 years, with an increasing number of publications, as we have found in *Pubmed*, *Google Scholar* and *ScienceDirect*, when searching with the term "Optical cancer detection".

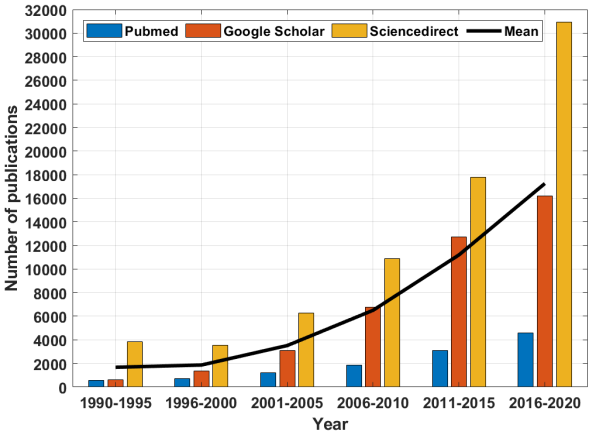


Fig. 1 Number of publications related to optical detection of cancer between 1990 to 2020.

The optical methods used in the studies of most of these publications are basically included in two groups: spectroscopy methods, which include optical, Raman, light scattering, near infrared and fluorescence, and imaging methods, which include optical coherence tomography (OCT), fluorescence microscopy, laser scanning microscopy and confocal microscopy.

Considering the development of any type of cancer, space- and time-dependent variations, such as abnormal cell growth, occur in tissues. When the later stages of cancer progression are reached, malignant tumors develop and cancer cell metastasis occur, creating the major cause of morbidity and mortality in a high number of patients [1, 6–13]. Nowadays, the classification of the cancer types is made according to the associated fatality degree or according to the anatomical area where they occur [14–17]. The detection, explanation and control of cancer progression are difficult for clinicians, since it can occur in different anatomical areas of the body without any apparent reason and cancer cells can spread to other areas. An additional fact is that any therapeutic procedure to eliminate cancer becomes ineffective when the diagnosis is established at a later stage of progression, which is the most common case [1, 18].

To overcome such difficulties, biophotonics methods can be used to detect cancer, even at early stages of development, and eventually aid in creating a delay in its progression.

In the case of early stage of cancer development, if the polyps or tumors arise at the outermost tissue layers, noninvasive or minimally invasive imaging or spectroscopy methods may be used directly or through endoscopy to perform a diagnosis. In such clinical exams, due to the early stage of cancer development, the clinician may have doubts to establish a reliable diagnosis, but through the precise optical identification of cancer biomarkers, a correct diagnosis can be established and treatment measures can be adopted to extend life expectancy for the patient. One such example was recently reported by our group with the identification of discriminated content of a lipofuscin-type pigment in healthy and pathological (colorectal cancer – adenocarcinoma) tissues of the human colorectal mucosa [19]. Although such study was made with *ex vivo* tissues, a similar evaluation of the discriminated pigment content can be made *in vivo*, as recently reported by Fernandes et al. [20]. In this study, diffuse reflectance measurements that mimic the noninvasive *in vivo* situation were used as input to develop machine learning (ML) algorithms to calculate the absorption coefficient spectra of healthy and pathological colorectal mucosa. The results obtained in this study were similar to the ones previously obtained in our study [19], with invasive measurements performed from *ex vivo* tissue samples collected from surgical specimens, and allowed to discriminate the lipofuscin-type pigment as before. Such results obtained by the ML approach open the way for *in vivo* evaluation of the pigment content in pathological tissues as a function of cancer progression to establish a diagnosis and identify the stage of cancer evolution.

For the case where such cancer biomarkers arise at the inner tissue layers, the direct application of imaging or spectroscopic procedures is not efficient, since tissues present high scattering properties, which limits the light probing depth [21]. Considering in particular the spectroscopy approach, biological tissues have various components, with individual absorption bands, which most of the times overlap one another, especially in the ultraviolet (UV) spectral range [22]. The discrimination of such useful spectral signatures for the establishment of a precise diagnosis may also be camouflaged by the strong and multiple light scattering that occur in biological tissues [23].

To overcome, such high and multiple scattering and reach deeper tissue layers to perform a reliable diagnosis, the application of optical clearing (OC) treatments to the tissues may be adopted [24]. Such method has been intuitively applied by Man since ancient times [25], but the first scientific evidence of the induced transparency increase in biological tissues was reported more than a century ago by a German anatomist, named Werner Spalteholz [26, 27]. No practical use of this method existed by that time, but with the development of new

optical instruments in the second half of the XX century, such as the laser, optical fibers or light-emitting-diodes (LEDs) of different colors, with efficient emission, a new era of light application in biology and medicine has arisen [21]. Consequently, new interest to study the light propagation in biological tissues, the light beam interaction with biological components in tissues and also the light scattering reduction that occurs as a consequence of the OC treatments has emerged [28].

The study of OC treatments has been intensively performed in the last 20 years, allowing to obtain good results in many biological applications, both on *ex vivo* and *in vivo* tissues [21, 24]. New approaches for cancer detection and the possibility of early stage detection and cancer progress monitoring can be provided by the combination of OC treatments with imaging or spectroscopic methods [18, 21].

The main purpose of the OC treatments is to increase the transparency of biological tissues through the reduction of light scattering inside. Such transient effect allows to reach deeper light probing depths through the partial replacement of tissue water by a harmless agent, designated as optical clearing agent (OCA) [21]. These OCAs have a higher refractive index (RI) than water, better matched to the RI of the other tissue components, which are commonly designated as tissue scatterers [21, 28, 29]. Due to heterogeneous composition of biological tissues, the various biological components such as protein fibers and globules, lipid droplets, phospholipid membranes, cells and their organelles, like mitochondria and nucleus, are surrounded by the tissue fluids, e.g., the interstitial fluid (ISF) or cell cytoplasm [30]. These tissue fluids contain a small amount of salts, minerals and organic compounds, which are dissolved in the main fluid component – water [24, 31, 32]. Water in tissue fluids can reach values above 95% [28], which decreases the RI of fluids strongly. Part of tissue water is also bound to tissue scatterers to keep them hydrated, but such amount of water is small, meaning that the RI of tissue scatterers is significantly higher than the RI of tissue fluids. As an example, the RI values of dry proteins in skeletal muscle and skin melanin at 589.6 nm are 1.584 and 1.47 [21 ,24, 32, 33], respectively, while the RI of the ISF in most tissues is of the order of 1.35–1.37 [24]. The strong and multiple light scattering that occurs in biological tissues is originated due to this RI mismatch between the ISF and the tissue scatterers [21].

As a result of the intense research in this field, various OCAs have given proof of efficiency in the creation of temporary and reversible transparency in different soft and hard tissues and in blood [21, 24]. Considering safety issues, the great majority of these OCAs have not induced side effects in tissues [21, 24], but some exceptions have been reported for some tissues under treatment with highly concentrated solutions of glycerol, dimethyl sulfoxide (DMSO) and propylene glycol (PG) [21, 34, 35]. The OCAs that are known today can have different nature, but they are in general classified in three main groups: sugars, alcohols and electrolyte solutions [21]. In the group of sugars, we find maltose, fructose and glucose, while in the group of alcohols we can find glycerol, sorbitol or PG. Considering the group of electrolyte solutions, these are commercial products to be used as contrast agents in medical imaging procedures, and some examples are Trazograph™, Hypaque™ and Gadolinium™ [21, 23, 24, 36]. Tests with these and other OCAs have been made in various animal and human tissues, both *in vivo* and *ex vivo* and the created transparency varies both in magnitude and duration from tissue to tissue [21]. Such transparency created by these OCAs in biological tissues is obtained by the cooperation of three main mechanisms, designated as: tissue dehydration, RI matching and protein dissociation [21].

To explain in detail how these mechanisms work and lead to a reduction in light scattering in tissues, we will consider a simple *ex vivo* tissue sample, which was prepared to have a slab-form with 0.5 mm thickness and a diameter of ~1 cm. This sample is submitted to collimated transmittance (T_c) measurements, both in its natural state and during OC treatment to evaluate its kinetics. The Beer-Bouguer-Lambert law states that T_c is a function of the attenuation coefficient, μ_t, and sample thickness, d [23]:

$$T_c(\lambda) \approx e^{-\mu_t(\lambda)\times d}, \quad (1)$$

where λ represents the wavelength and μ_t is the sum of the absorption coefficient, μ_a, with the scattering coefficient, μ_s.

Considering as a reference the T_c spectrum for a selected wavelength range that was measured from the natural sample, when the treatment begins by immersing the tissue sample in a solution that contains an OCA, an increase in T_c will be seen as a result of the OC mechanisms. In the first few minutes of treatment, the osmotic pressure of the OCA in the solution induces the water flux out from the tissue. This is the dehydration mechanism [21]. Depending on the bounding strength, there are four stages of water in biological tissues that have been reported [37, 38]: strongly bound, tightly bound, weakly bound and free water. The combination of weakly bound with free water is commonly designated as mobile water, since both can move to the outside of the tissue when stimulated by the osmotic pressure of the OCA used in the treatment [21]. The osmotic pressure created by the OCA is not strong enough to break the connections between the strongly and tightly bound water and the other biological components. Such water maintains the hydration of those biological components in the tissues and provide nutrients to the cells, but it can also be converted into mobile water and flow out if the osmotic pressure of the OCA is maintained for several hours or days [21]. As a result of the fast loss of mobile water in the first few minutes of treatment, sample thickness decreases, leading to the close approximation of the tissue scatterers [21, 29, 39]. A more compact and better organized packing of tissue scatterers is created

inside the sample [23, 24, 40, 41]. Mechanical compression or stretching may also induce such internal variations, since mechanical forces also remove water from the compressed or stretched area of the tissue [21, 24]. An increase in μ_s and in μ_a should be expected with the creation of a denser scatterer distribution inside the tissue, but due to a better scatterer ordering inside and to the decreased sample thickness, an increase in transparency occurs [23, 33, 39].

As the mobile water flows out, the diffusion of the OCA molecules into the interstitial locations is facilitated. Since these molecules have a higher RI than the water, the OCA positioning in the interstitial locations, and in particular close to the tissue scatterers, provides the RI matching mechanism [21, 39]. As the OCA molecules start their diffusion into the tissue, they begin their interaction with the outermost tissue layers, but with the continuous flux of the water molecules going out, the OCA molecules flow into deeper locations and eventually fill all the interstitial areas of the tissue. The OCA diffusion into the tissues takes several minutes to occur, as demonstrated by various studies [40, 42, 43]. Since both fluxes initiate at the beginning of the treatment, during the first few minutes of treatment both the water flux going out and the OCA flux going in occur simultaneously. This means that methods for flux discrimination and characterization are necessary.

The replacement of interstitial water by the OCA molecules results in an increase of the mean RI in the ISF, approaching it to the RI of tissue scatterers – this is the RI matching mechanism, which is provided by the OCA inclusion in the interstitial locations [40–42]. This mechanism decreases the light scattering inside the tissue, leading also to the increase of tissue transparency [43]. Since the OCA molecules can be washed out by the water that flows from adjacent tissues *in vivo* or by immersing the *ex vivo* tissue sample in saline, both the tissue dehydration and the RI matching mechanisms are reversible [39]. One OC study demonstrated that the increased transparency created in skin by these two mechanisms has provided better contrast images from deeper tissue layers [44]. Another study performed with human *ex vivo* healthy and diseased colorectal tissues to discriminate and characterize the OC mechanisms demonstrated a 5% higher content of mobile water in the pathological tissues [43, 45]. Similar results for a higher mobile water content in pathological tissues were observed in a study performed with tissues from healthy and diabetic mouse [46].

A third OC mechanism that also leads to the increase of tissue transparency is designated as protein dissociation. This third mechanism of OC was first observed in 2003, in a study where multiphoton microscopy was used to generate second harmonic generation (SHG) images from *ex vivo* skin samples under treatment with glycerol solutions [47–49]. In this study, and as a result of the applied treatments, it was observed that collagen I dissociation occurs in the extracellular skin matrix due to the action of glycerol. Since the reassembly of skin matrix collagen I was observed after tissue rehydration in saline in a later study by the same group, the reversibility of this third OC mechanism was demonstrated [47, 50]. The protein dissociation mechanism and its reversibility after washing out the OCA from the tissues have also been demonstrated with other OCAs, such as ethylene glycol (EG) and sorbitol [47, 49]. These studies showed that the clearing potential of an OCA is related to its protein dissociation capability, proving that the protein dissociation is also an OC mechanism [47–50]. More recently, other studies have showed that this mechanism also occurs in other tissues such as colorectal muscle [25], or colorectal mucosa [29]. In the first of these studies it was demonstrated that the protein dissociation increases in magnitude with the osmolarity of glycerol in the treating solution [25]. In the later study [29], Carneiro et al. demonstrated that the protein dissociation rate can be discriminated in healthy and pathological colorectal mucosa for the same high glycerol osmolarity in the treating solution. Such result of discriminated protein dissociation rates in healthy and cancer tissues is to be expected due to the higher protein contents that cancer tissues are known to have [51].

In the past 5 years, the cooperation between our groups, located in Porto (Portugal) and in Saratov (Russian Federation), has originated various results with studies using *ex vivo* healthy and diseased tissues, that can be used to develop future noninvasive optical methods for cancer and diabetes detection and monitoring. The purpose of this paper is to review those discriminating results obtained for the case of human colorectal cancer. Section 2 describes the methodologies used in these studies and the obtained results are presented in Section 3.

2 Materials and methods

The studies that originated the results presented in Section 3 were all conducted with *ex vivo* tissue samples. The following Subsections describe the tissue collection and preparation, the spectroscopy and thickness measurements and the calculation procedures used in the different studies to obtain the results that discriminate colorectal cancer.

2.1 Tissue samples

Human colorectal surgical resections were collected from adult patients under treatment at the Oncology Institute of Porto (Portugal). These patients have previously signed a written consent, allowing the use of surgical specimens for diagnostic and research purposes.

The healthy and pathological areas of the surgical resections were separated and the tissue samples were prepared using only the mucosa layer of the colorectal wall. Such samples were prepared using a cryostat (Leica, model CM 1850 UV) to have an approximately circular-slab form with a diameter of ~1 cm and a uniform thickness of 500 μm. The number of healthy and pathological samples used in the various studies are indicated in the following subsections.

2.2 Experimental studies

To perform the various studies, it was necessary to conduct both spectroscopy and thickness measurements. In the first study to estimate the differentiated accumulation of a pigment in healthy and pathological mucosa, only spectroscopy measurements were made. To conduct this study, 10 healthy and 10 pathological mucosa samples were submitted to total transmittance (T_t), total reflectance (R_t) and T_c measurements [19]. An additional set of 10 healthy and 10 pathological mucosa samples was later used to measure the diffuse reflectance (R_d) spectra, with the objective of estimating the μ_a spectra for both tissues using ML algorithms.

In the second study to obtain the differentiated mobile water content in healthy and pathological mucosa, T_c measurements were made from samples under treatment with aqueous solutions containing different glucose concentrations: 10%, 15%, 20%, 25%, 30%, 35%, 40%, 45%, 50% and 54%. Three studies with each type of tissue were made for each treatment with the previous solutions to obtain statistical data. To calculate the diffusion coefficients of water and glucose in healthy and pathological mucosa, additional thickness measurements were made during treatment with some of the above solutions [43, 45]. A total of 6 healthy and 6 pathological tissue samples were used in the thickness measurements.

In a previous study [25], we observed that OC treatments with strong OCA osmolarity induce the creation of a high magnitude UV window between 200 and 260 nm. Due to this knowledge, we planned a new study to evaluate the protein dissociation rate in healthy and pathological colorectal mucosa. In this third study, 5 healthy and 5 pathological tissue samples were submitted to T_c spectral measurements during treatment with 93%-glycerol [29].

The following sub-sections present the experimental setups and describe the measuring procedures adopted in the three studies.

2.2.1 Total transmittance

Fig. 2 presents the experimental setup used to measure the T_t spectra from the tissue samples.

In these measurements, the sample was irradiated with a high-power pulsed broad-band xenon lamp through an optical fiber cable and collimating lens. The incident beam had a diameter of 6 mm, which is limited by the lens aperture (indicated in Fig. 2 as the pinhole). The light that is transmitted by the tissue sample enters the integrating sphere to be reflected several times on its inside wall (integration) before being delivered to the spectrometer through a second optical fiber cable. All these equipments were acquired from Avantes™ (Netherlands). All spectra measured with this setup from 10 healthy and 10 pathological mucosa samples were acquired between 200 and 1000 nm to be used in the first study that is presented in Section 3.

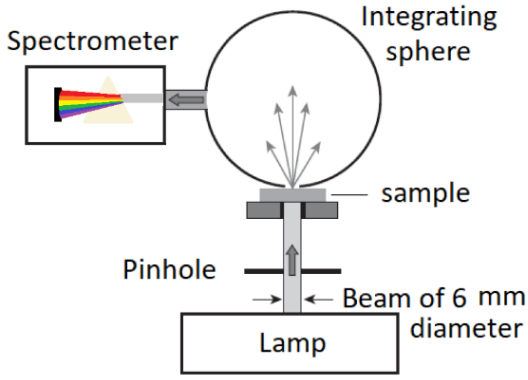


Fig. 2 Total transmittance T_t measuring setup with integrating sphere.

2.2.2 Total reflectance

The setup used to measure the R_t spectra from samples is presented in Fig. 3.

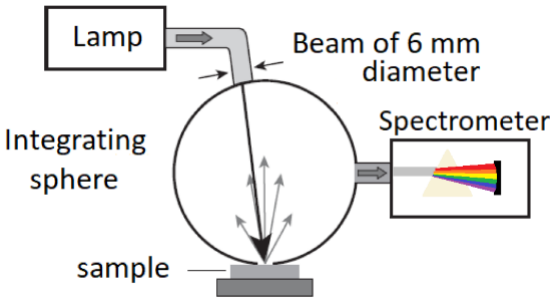


Fig. 3 Total reflectance R_t measuring setup with integrating sphere.

In a similar manner to what was described for the measurements with the T_t setup, a high-power pulsed broad-band xenon lamp is used to irradiate the tissue sample through an optical fiber cable and collimating lens. Such sample irradiation is made at 8º with the vertical axis of the integrating sphere. The beam is reflected by the sample and then is submitted to the integration process inside the sphere, meaning that it undergoes multiple reflections before being delivered to the spectrometer through an optical fiber cable. Considering these measurements for the first study that is presented in Section 3, 10 spectra were acquired from healthy tissue samples and other 10 from the pathological samples. All spectra were acquired between 200 and 1000 nm.

2.2.3 Diffuse reflectance

Fig. 4 presents the experimental setup that was used to measure the R_d spectra that were used to estimate $\mu_a(\lambda)$ for both mucosa tissues with the ML algorithms.

In these measurements, a broad-band beam from a deuterium-halogen lamp (Avantes™, Netherlands) irradiates the sample through an optical fiber that is placed inside the R_d optical fiber sensor (ArtPhotonics™, Germany). The tip of this sensor is maintained 2 mm

above the surface of the tissue sample. The diffusively reflected light is collected by other 6 optical fibers in the sensor, which deliver such reflected light to the spectrometer. R_d spectra were acquired from 10 healthy and from 10 pathological mucosa tissue samples, between 200 and 1000 nm.

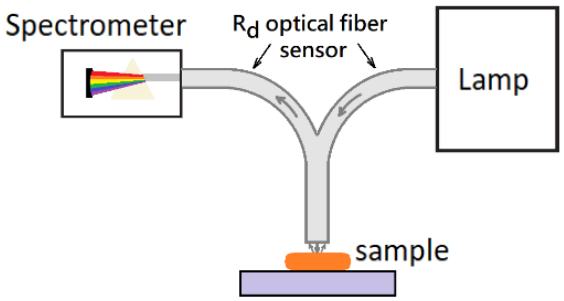


Fig. 4 Diffuse reflectance R_d measuring setup.

2.2.4 *Collimated transmittance*

The T_c setup that is presented in Fig. 5 was used to acquire spectra from tissues in all studies.

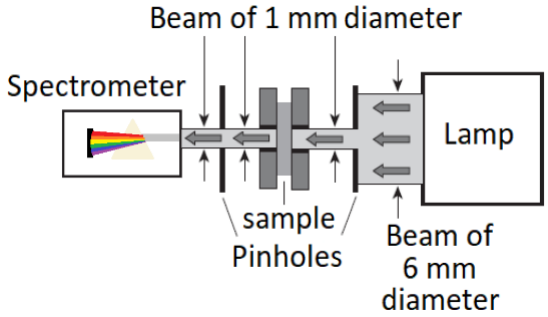


Fig. 5 Collimated transmittance T_c measuring setup.

In all measurements made with this setup, a beam from a broad-band deuterium-halogen lamp (the same that was used in the R_d measurements) was delivered to the right side of the sample through an optical fiber cable and collimating lens. Having a beam diameter of 6 mm as it exits the lens, the beam crosses a pinhole that reduces its diameter to 1 mm, before irradiating the tissue sample. A second pinhole and another collimating lens placed on the left side of the sample are the collecting optics used to deliver the transmitted beam to an optical fiber cable that is connected to the spectrometer. All spectra acquired with this setup are registered between 200 and 1000 nm. The space between the two pinholes is inside a dark cuvette that prevents the entrance of ambient light and contains the OC solution surrounding the tissue sample when measurements are to be made during the treatments. The sample is fixed at the center of this cuvette by a mechanical system, which is represented by the four dark-grey rectangles on both sides of the sample in Fig. 5. The beam entrance and exit in the cuvette is made through two special glasses that have flat transmittance (above 90%) through the entire spectral range of interest (200 to 1000 nm). For measurements regarding the first study, 10 spectra were acquired from the same number of samples. For the spectral measurements performed in the second study, three independent studies were performed with the same number of tissue samples for the treatments with each glucose concentration. In the case of the third study, 5 healthy and 5 pathological tissue samples were submitted to measurements with the setup in Fig. 5 during treatment with 93%-glycerol. In all studies, when measuring the native T_c spectra of the tissue samples, the setup is used as represented in Fig. 5. For the measurements during treatments in the second and third studies, the cuvette is filled with the OCA solution to immerse the sample before starting the measurements. In these measurements, a T_c spectrum is acquired at each 5s during 30 min.

2.2.5 *Thickness measurements*

In the second study, which was made to obtain the mobile water content in the healthy and pathological colorectal mucosa tissues and the diffusion properties of glucose in these tissues, thickness measurements were necessary during treatment of the tissues with some solutions. Those measurements were made by placing the tissue sample inside two microscope glasses as represented in Fig. 6.

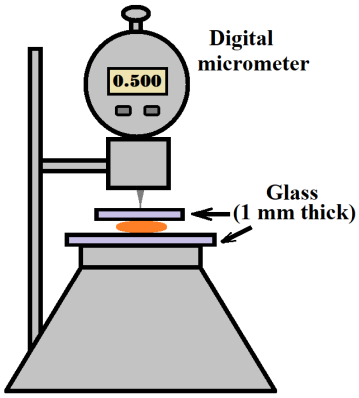


Fig. 6 Setup for measuring of tissue sample thickness.

Each of the two glasses had a fixed thickness of 1 mm, but to avoid excessive force over the sample and unwanted sample compression during measurements, the one on top had a smaller area (1.5 × 1.5 cm) than the one at the bottom (1.5 × 7.5 cm) [48].

The digital micrometer represented in Fig. 6 had a precision of 0.001 mm and was used to measure the global thickness of the tissue sample between the two glasses. To perform a thickness kinetics study the micrometer was adjusted to have a reading of 2.500 mm at the beginning. Then, a significant amount of the treating solution was injected in-between the two glasses to immerse the entire sample and initiate the treatment. The micrometer was adjusted smoothly to measure new thickness values at each 15 sec in the first 2 min and at each min after that. Considering the healthy mucosa tissues, thickness measurements were performed during

treatment with the 40%- and 54%-glucose solutions. For the case of pathological mucosa tissues, those measurements were performed during treatment with the 35%- and 54%-glucose solutions. Three sets of thickness measurements were made from independent mucosa samples under treatment with each of these solutions to obtain statistical thickness kinetics variations [43, 45].

2.3 Calculations

After terminating the experimental measurements for each study, some calculations needed to be performed. Considering the first study to evaluate the differentiated pigment content in the healthy and pathological mucosa tissues, the first calculation consisted on obtaining the spectrum of μ_a from the T_t and R_t spectra. Such calculation was made 10 times for the healthy and 10 times for the pathological mucosa, using Eq. (2) [19]:

$$\mu_a(\lambda) = \frac{1 - \frac{T_t(\lambda) + R_t(\lambda)}{100}}{0.05}. \quad (2)$$

In Eq. (2), the number 100 is a normalization factor for the spectral measurements and the number 0.05 represents the sample thickness in cm. Once the mean $\mu_a(\lambda)$ was calculated for each tissue, we observed that the ratios between the hemoglobin peaks at 415 and 550 nm and the minimal value of μ_a in the near infrared (NIR) were significantly low when compared to others previously published for similar mucosal tissues [52]. This difference between our data and the one that was previously published means that some pigment is creating an additional absorption in the entire spectral range in our tissues, and consequently camouflaging their real blood content. By obtaining information from the patient records at the Portuguese Oncology Institute of Porto, we found that due to a natural product that was administered to the patients in the two days before the colorectal surgery, some lipofuscin-type pigment was detected in the complementary histological analysis. Obtaining the absorption spectrum of lipofuscin ($\mu_{a\text{-}pigment}$) from literature, as measured from other tissues [53], we reconstructed it as in Eq. (3) [19], to be subtracted to the μ_a of the healthy colorectal mucosa and obtain appropriate ratios for the absorption bands of hemoglobin in this tissue.

$$\mu_{a-pigment}(\lambda) = A \times \left[5.2 + e^{(3.524 - 0.01087 \times \lambda)} \right]. \quad (3)$$

In Eq. (3) λ is to be used in nm to obtain the values of $\mu_{a\text{-}pigment}$ in cm^{-1}. A represents the percentage of the pigment in the tissue, which for the case of the healthy mucosa assumes the value 1 (100% content). For the case of the pathological mucosa a similar calculation could be made, but considering A in Eq. (3) as 1.1 (110% content). By subtracting the pigment content from the absorption spectra of both tissues, we obtained proper ratios for the hemoglobin bands in the healthy tissue and a higher blood content in the pathological mucosa as it was expected [19]. The results of this study are presented in Section 3.

Regarding the second study to calculate the mobile water content and the diffusion coefficients of glucose in healthy and pathological mucosa, we used both thickness and T_c kinetics data obtained from the various treatments with glucose solutions. Since both the healthy and the pathological mucosa presented an almost linear increasing behavior of T_c with wavelength between 600 and 800 nm [45], we selected individual wavelengths within this range to calculate the T_c kinetics for each treatment. To calculate these kinetics, we used mean spectra from three studies for each particular treatment [43, 45]. Since the T_c kinetic measurements are sensitive to the variations induced by glucose during the treatments, we adjusted such kinetics data set obtained for each individual wavelength with a curve as described by Eq. (4) [45]:

$$T_c(\lambda, t) = \frac{C_a(t)}{C_{a0}} \cong \left[1 - \exp\left(-\frac{t}{\tau} \right) \right], \quad (4)$$

with

$$\tau = \frac{d^2}{\pi^2 D_{OCA/water}}, \quad (5)$$

where $C_a(t)$ is the OCA concentration inside the tissue at a particular time of treatment t, C_{a0} is the initial OCA concentration in the treating solution, τ represents the characteristic diffusion time of the effective global flux between the treating solution and the tissue, which is related through Eq. (5) to the characteristic diffusion coefficient of that effective global flux ($D_{OCA/water}$) and d represents the sample thickness at a time of treatment that corresponds to τ [45]. Our objective in this study was to discriminate the characteristic diffusion properties (τ and D) for glucose and water in both mucosa tissues. Those properties can only be retrieved using data from treatments where a unique glucose or water flux occurs between the treating solution and the tissue. The unique water flux is obtained from a treatment with a high concentration of the OCA in the treating solution. In our case we were using glucose and the highest glucose concentration possible in aqueous solution is 54% [21]. The unique glucose flux is obtained when the water in the treating solution is in equilibrium with the mobile water in the tissue, but we did not know this value for the healthy and pathological mucosa tissues before the study was made. This way, we needed to perform various studies with treating solutions containing different glucose concentrations. From each treatment with a particular solution, we obtained various τ values in the fittings of the T_c kinetics data for each selected wavelength with Eq. (4). By representing the mean τ values obtained for each treatment as a function of the glucose concentration in the treating solution for each

tissue, we obtained a dependence that provided a maximum and a minimum τ value. For any tissue, the minimum τ value represents the characteristic diffusion time of water and the maximum τ value represents the characteristic diffusion time of glucose in that tissue. These τ values that were retrieved from those graphical representations were used in Eq. (5) to calculate the diffusion coefficients of glucose and water in the healthy and pathological mucosa tissues. When performing these calculations, we considered the corresponding thickness values obtained at a time of treatment equal to τ and for the treatment with the same glucose concentration as the one that originates a minimum (for water) and a maximum (for glucose) τ value for each tissue [45]. The results of these calculations are presented in Section 3 and they show that the maximum τ occurs for each tissue at different glucose concentrations in the treating solution. Such difference in the glucose concentration in the treating solution between the healthy and pathological mucosa indicates a different mobile water content in the two tissues, a parameter that can be used to discriminate cancer.

In the third study, T_c spectra were also measured from healthy and pathological mucosa tissues during treatment, but now using only 93%-glycerol as a treating solution [29]. Due to the fact that proteins have a strong absorption band between 200 and 230 nm [39, 54], it was necessary to evaluate the kinetic variations created by the treatments in that deep-UV range. When T_c spectra are represented as a function of the time of treatment, we see that the kinetics in the deep-UV range are insignificant and not perceptible when compared to the variations observed in the visible-NIR range. To get access to those kinetic variations in the deep-UV, we need to calculate the relative variations of T_c over the time of treatment. We used Eq. (6) to perform those calculations and designated the relative variations as optical clearing efficiency (OC_{eff}) [25, 29]:

$$OC_{eff}(\lambda,t)=\frac{T_c(\lambda,t)-T_c(\lambda,t=0)}{T_c(\lambda,t=0)}\times 100\%, \quad (6)$$

where $T_c(\lambda, t)$ represents the T_c spectrum of the tissue acquired at a time of treatment t and $T_c(\lambda, t = 0)$ represents the T_c spectrum of the tissue in its native state ($t = 0$). In a previous study [25], we observed that the OC_{eff} is much higher in the deep-UV range when compared to the visible-NIR range, a fact that demonstrates a more efficient RI matching and a higher scattering reduction in that range. Due to this stronger scattering reduction in the deep-UV, we were able to use the calculated OC_{eff} data to evaluate the protein dissociation mechanism in healthy and pathological mucosa tissues. During this evaluation, we observed that at 200 nm the OC_{eff} presented the highest values for both tissues. This way, we selected that wavelength to characterize the kinetics obtained for both tissues and retrieved a parameter, which we designated as the protein dissociation rate.

In a first analysis of the OC_{eff} kinetics of both tissues at 200 nm, we observed that for the treatment duration (30 min) it can be characterized by a combination of an initial square root dependence with a later linear dependence on time [29]. It was also observed that for the time interval between 3 and 10 min, both tissues present an almost perfect linear dependence between OC_{eff} and time. With the objective of developing future noninvasive and fast optical methods for cancer diagnosis, we analyzed the slope of such linear fitting for both tissues between 3 and 10 min. For the pathological mucosa the slope was approximately 3× bigger than the one obtained for the healthy mucosa. This difference indicates a higher protein dissociation rate as a result of the greater protein content in the pathological mucosa, which has been reported in literature [51]. Section 3 presents these results and the discussion for the three studies.

3 Results and discussion

Due to the fact that we have performed three studies that produced discriminating results, which can be used to diagnose colorectal cancer, the presentation of results and the corresponding discussion for each study will be presented in the following three sub-sections.

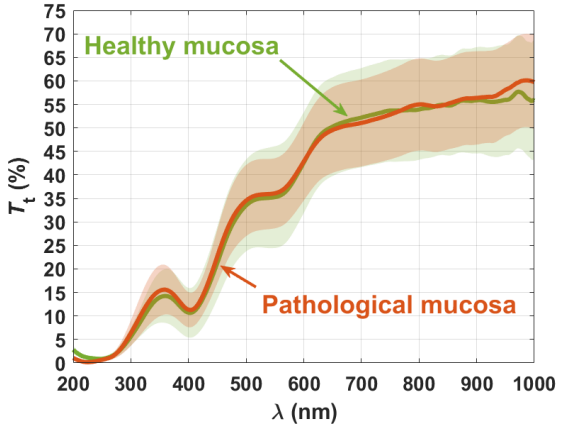
3.1 Pigment as a marker of colorectal cancer

In this first study, we measured 10 T_t and 10 R_t spectra from healthy and a similar number from pathological mucosa samples. Such measurements were made using the setups presented in Fig. 2 and in Fig. 3, respectively. Fig. 7 presents the mean and standard deviation (SD) bars of these measurements for both mucosa tissues [19].

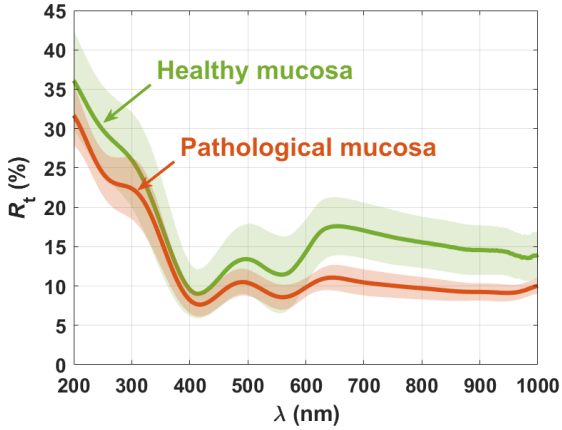
To calculate the wavelength dependency of μ_a for all tissue samples used in this study, we used the individual T_t and R_t spectra that originated the mean data presented in Fig. 7 in Eq. (2) with the sample thickness of 0.05 cm. The mean results of this calculation for the healthy and pathological mucosa are presented in Fig. 8 [19].

Analyzing the ratios between the hemoglobin peaks at 415 and 550 nm and the lowest μ_a value (at 875 – 980 nm), we obtained for both tissues a 2.7-fold at 415 nm and a 1.8-fold at 550 nm. These values are too low (~6 × less) when compared to the similar data that has been published for other mucosal tissues [52]. Such low ratios indicate the presence of some particular absorber that camouflages the true blood content in the colorectal mucosa tissues. Obtaining from patient's records that complementary histological analysis indicated the presence of a lipofuscin-type absorber in the mucosa tissues, we obtained the wavelength dependence of μ_a for lipofuscin ($\mu_{a\text{-}pigment}(\lambda)$, see Eq. (3)) from literature [53] to subtract it to the $\mu_a(\lambda)$ of the healthy mucosa. Considering $A = 1$ in Eq. (3) and after subtracting $\mu_{a\text{-}pigment}(\lambda)$ from $\mu_a(\lambda)$ of the healthy mucosa, we obtained acceptable ratios at 415 and 550 nm: 19.7-fold at 415 nm and 10.1-fold at 550 nm. Using the same procedure for the pathological mucosa, but now with $A = 1.1$ in Eq. (3) (an additional 10% lipofuscin

accumulation), we obtained the hemoglobin ratios: 33.1-fold at 415 nm and 17.3-fold at 550 nm [19]. Analyzing these data, we see that the pathological mucosa presents higher blood content than the healthy mucosa, as expected [55]. The results obtained after subtracting lipofuscin to the $\mu_a(\lambda)$ of the colorectal mucosa tissues and the new hemoglobin ratios are presented in Fig. 9.



(a)



(b)

Fig. 7 Mean $T_t(a)$ and $R_t(b)$ spectra for the healthy and pathological mucosa.

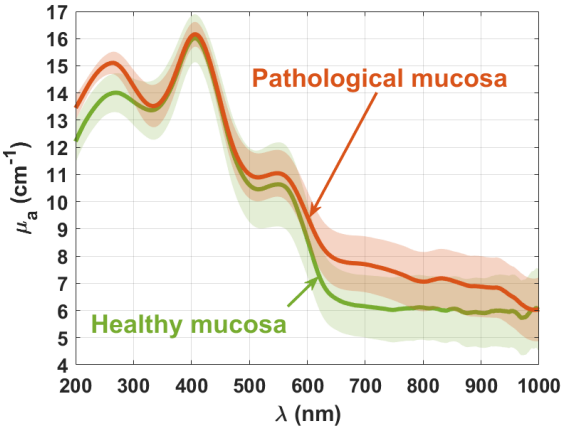
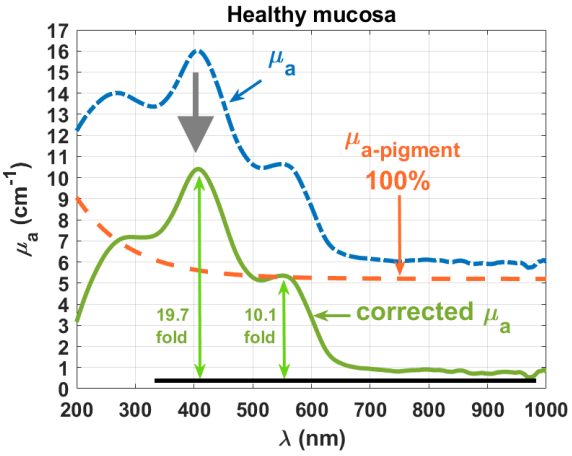
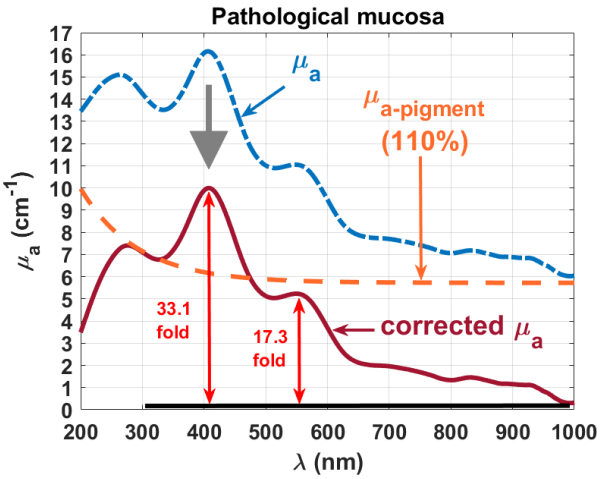


Fig. 8 Mean wavelength dependence for μ_a of both mucosa tissues.



(a)



(b)

Fig. 9 Absorption coefficient $\mu_a(\lambda)$ for the pigment, for healthy (a) and for pathological (b) mucosa, before and after subtracting the absorption of the pigment.

Since the results obtained for the $\mu_a(\lambda)$ of the mucosa tissues were calculated from spectra that were acquired in an invasive manner, we wanted to check if these results could be obtained from noninvasive measurements and allow for the development of a diagnostic procedure without the need of surgical resections. Due to the fact that this research is at an early stage of development, no conditions were assembled to perform measurements *in vivo* from patients. Still, using the configuration presented in Fig. 4, we acquired the R_d spectra from 10 healthy and 10 pathological mucosa samples to mimic the noninvasive *in vivo* measurements. This is a new set of tissue samples, that we have prepared only to test the hypothesis of reconstructing $\mu_a(\lambda)$ from measurements that mimic the *in vivo* approach. Using the 20 R_d spectra (10 from healthy and 10 from pathological mucosa) as input to various ML algorithms, we were able to select the *Random Forrest Regression* (RFR) algorithm as the best choice to reconstruct the $\mu_a(\lambda)$ of healthy and pathological mucosa tissues [20]. The resulting μ_a spectra, as obtained from RFR reconstruction and after

subtracting the pigment absorption are presented in Fig. 10.

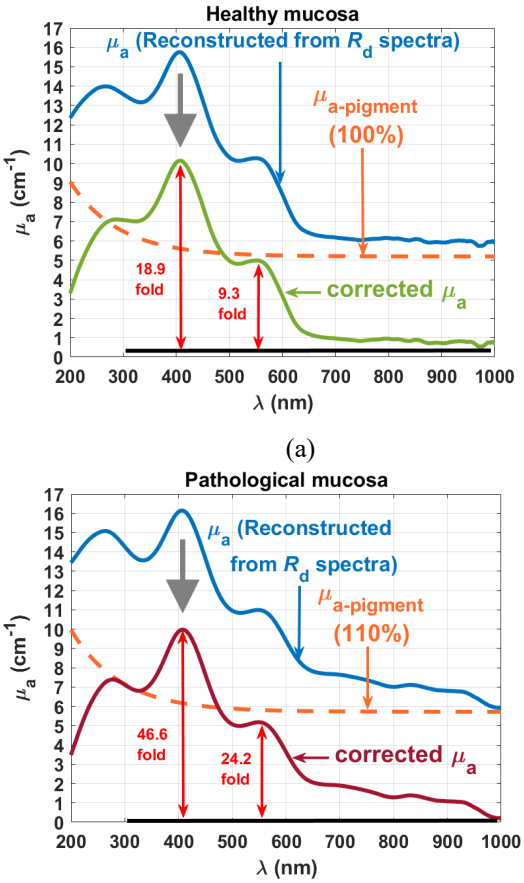


Fig. 10 Absorption coefficient $\mu_a(\lambda)$ for the pigment, for healthy (a) and for pathological (b) mucosa, as reconstructed by the RFR algorithm and after subtracting the absorption of the pigment.

Comparing the ratios obtained in Fig. 10 with the ones presented in Fig. 9, we see that for the healthy mucosa they have similar magnitude. For the case of the pathological mucosa, we obtained higher magnitude ratios with the ML approach, both at 415 and at 550 nm. This means that the pathological samples used to measure the R_d spectra that was used in the ML estimation might have a higher blood content than the ones used to obtain the original results that are presented in Fig. 8.

The results presented in Fig. 10 show that it is possible to measure broad-band R_d spectra from tissues *in vivo* and use them in ML algorithms to reconstruct $\mu_a(\lambda)$ for those tissues. Moreover, when the diagnostic information is directly available in those absorption spectra, or can be calculated in a simple manner, as in the case presented above, the ML algorithms are a good choice for a noninvasive diagnostic approach. Such method presents an additional advantage, since it can be used to perform a diagnosis in an early stage of cancer development, provided that the pigment content is known for the different stages of cancer progression.

3.2 Mobile water content as a marker of colorectal cancer

In this second study, to evaluate the diffusion properties of glucose and water in the colorectal mucosa tissues, the tissue samples were treated with aqueous solutions containing different osmolarities of glucose. Three studies were performed for each glucose osmolarity to obtain mean T_c kinetics at discrete wavelengths between 600 and 800 nm over the time of treatment [43, 45]. The mean T_c kinetics obtained for such wavelengths in some of the treatments applied to the healthy and pathological mucosa are presented in Fig. 11.

The various graphs in Fig. 11 show that when the treatment is made with low glucose osmolarity, T_c increases until a maximum is reached after a few minutes of treatment. The time when such maximum is reached depends on the glucose concentration in the treating solution. After reaching such maximum, a smooth decrease in the T_c kinetics is observed for the treatments with 25%-glucose in graphs (a) and (b) of Fig. 11. Such smooth decrease indicates a possible water back-flux into the tissue and some tissue swelling. Such T_c kinetics indicate that the effective glucose flux into the tissue is limited to the first few minutes of treatment, nearly 6 min for the healthy and 8 min for the pathological mucosa. As the glucose concentration in the treating solution increases to intermediate values, a smooth increase in T_c is obtained during the entire treatment. Such behavior is seen in graphs (c) and (d) of Fig. 11, for the treatments of pathological mucosa with 35%-glucose and healthy mucosa with 40%-glucose. In these treatments, the smooth increase is observed for the entire treatment duration – 30 min, without reaching a maximum before that time. Such behavior indicates a unique glucose flux into the tissue as a result of a water balance between the treating solution and the mobile water in the tissue. If we increase the glucose concentration in the treating solution to higher values, we see that the smooth increase in the T_c kinetics becomes limited to shorter times of treatment (see graphs (e) and (f) in Fig. 11), as observed for the treatments with low glucose concentrations (graphs (a) and (b) in Fig. 11). The difference between the treatments with low and high glucose concentrations is that in the later no smooth T_c decrease is observed at the end of the treatment. In these treatments, T_c stays almost unchanged at the end of treatment, indicating that no effective net flux occurs.

The data in graphs of Fig. 11 and similar data obtained from the other treatments with other glucose concentrations needed to be processed to obtain the mean τ for each treatment. This way, for a particular treatment, and considering the time span where the T_c kinetics show increasing behavior, each dataset that correspond to an individual wavelength was first displaced to have $T_c\,(t = 0) = 0$. The next step was to normalize the dataset to its highest value, so that it varies between 0 and 1. Finally the rearranged dataset was fitted with a curve described by Eq. (4) to estimate the corresponding τ value.

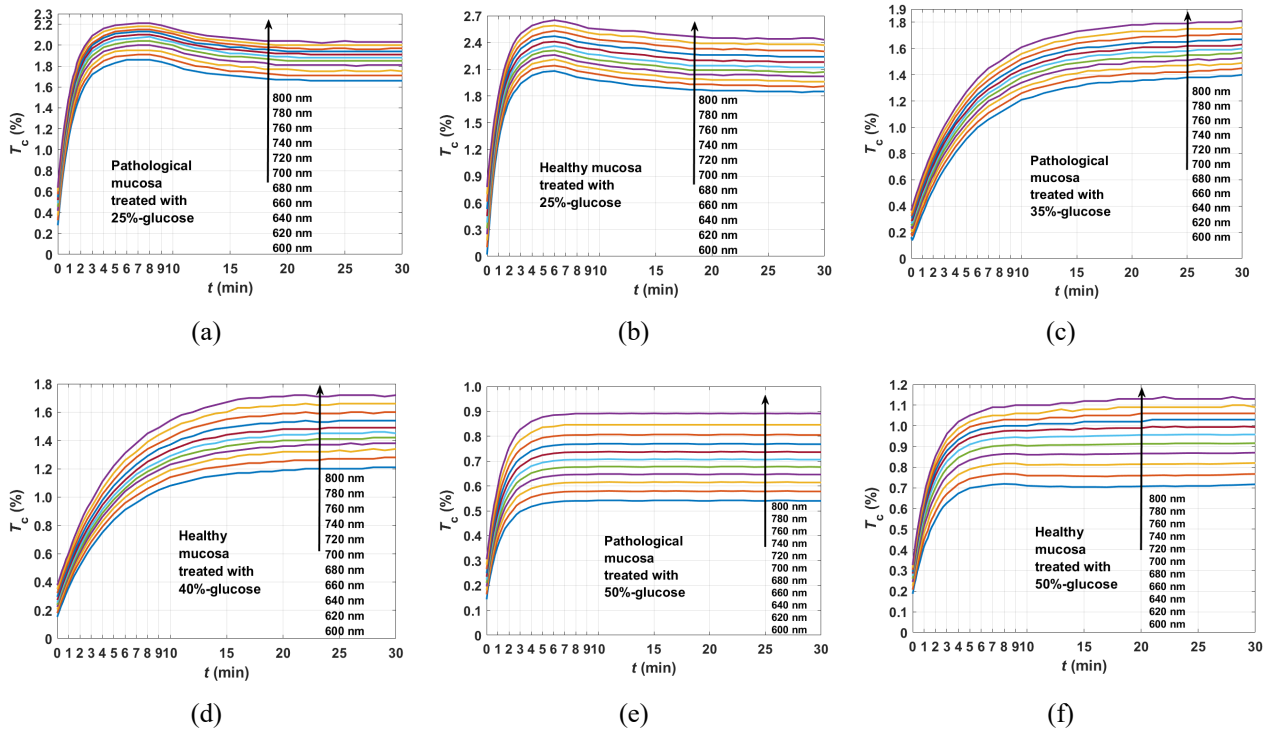


Fig. 11 Mean T_c kinetics for the healthy and pathological mucosa under treatment with: 25%-glucose (a and b), 35%-glucose (c), 40%-glucose (d) and 50%-glucose (e and f).

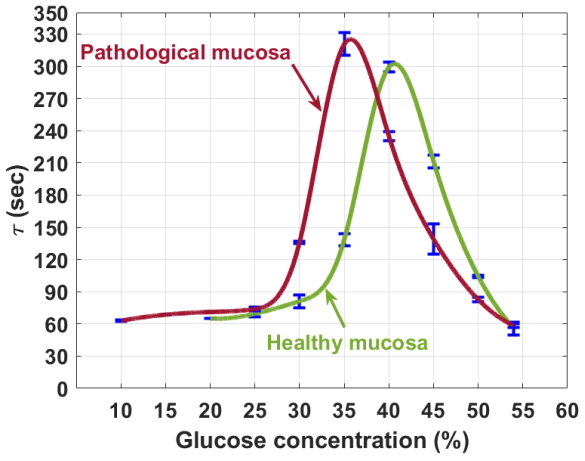


Fig. 12 Mean τ as a function of glucose concentration in the treating solution for human healthy and pathological colorectal mucosa tissues.

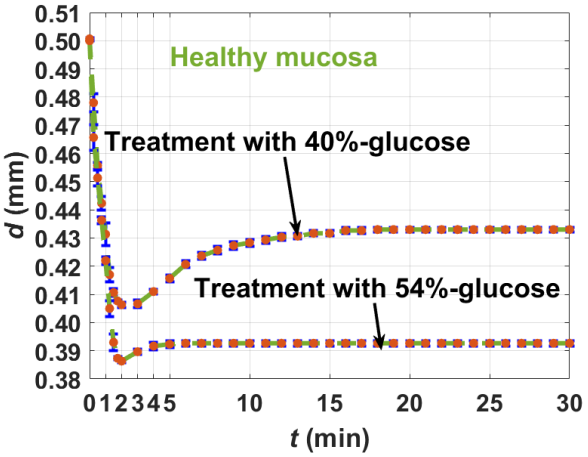
Since we have obtained various τ values for each treatment, the mean and SD for τ were calculated for each treatment. Fig. 12 presents such values for the treatments applied to the healthy and pathological mucosa tissues [43, 45].

Considering each tissue, the points in Fig. 12 were adjusted with a spline to obtain the dependence between the τ values that characterize the effective flux that occurs in each treatment and the glucose concentration in the treating solution. These curves show a peak at particular glucose concentrations in the treating solution. The τ values at these peaks represent the true glucose diffusion time in the healthy and pathological mucosa tissues, and the glucose concentration where they occur is indicative of the mobile water content in each case. For the healthy mucosa we see that the maximum τ is 302.4 sec and it occurs for a glucose concentration of 40.6%. This means that the mobile water content in the healthy mucosa is 59.4%. For the pathological mucosa, the maximum τ is 325.1s and it occurs for a glucose concentration of 35.7%, meaning that the mobile water content in this tissue is 64.3%. These results show that the mobile water content is almost 5% higher in the pathological mucosa [43, 45], which leads us to believe that during cancer progression, part of the bound water is converted into mobile. For the treatment with 54%-glucose, we retrieve from Fig. 12 a minimum value for τ in both tissues: 55.7 sec in the healthy and 58.4 sec in the pathological mucosa.

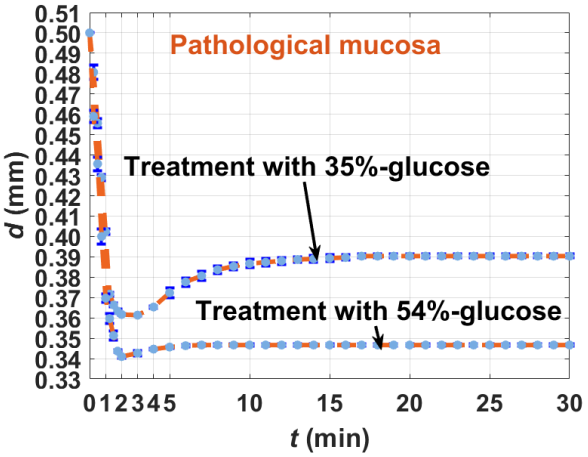
In face of the results obtained from Fig. 12 and with the objective of calculating the diffusion coefficients of glucose and water in both tissues, we performed thickness kinetic measurements from the healthy mucosa under treatment with 40%- and 54%-glucose and from the pathological mucosa under treatment with 35%- and 54%-glucose. These measurements were made three times with individual samples for each treatment and were done using the setup presented in Fig. 6. The mean results of thickness kinetics obtained from these measurements are presented in Fig. 13.

To calculate the diffusion coefficients of water and glucose in the mucosa tissues and considering each

treatment for which we performed the thickness measurements, we retrieved from the corresponding dataset in graphs of Fig. 13 the thickness value that correspond to the mean τ value obtained for that treatment. Using both the mean τ and mean thickness values, as retrieved for each treatment from graphs in Figs. 12 and 13, in Eq. (5), we calculated the diffusion coefficients of water and glucose in the healthy and pathological mucosa tissues. The results of these calculations were: $D_{glucose} = 5.8\times10^{-7}$ cm^2/sec and $D_{H2O} = 3.3\times10^{-6}$ cm^2/sec in the healthy mucosa and $D_{glucose} = 4.4\times10^{-7}$ cm^2/sec and $D_{H2O} = 2.4\times10^{-6}$ cm^2/sec in the pathological mucosa [21, 43, 45]. These values can also be used for colorectal cancer discrimination, since they differ from the healthy to the pathological mucosa.



(a)



(b)

Fig. 13 Mean thickness kinetic measurements from mucosa tissues: healthy mucosa under treatment with 40%- and 54%-glucose (a), and pathological mucosa under treatment with 35%- and 54%-glucose (b).

To finalize this study, it is important to say that, although we have obtained these results based on invasive measurements, they can also be obtained using *in vivo* noninvasive optical procedures. The estimation of the τ values from T_c kinetics, can be done if we replace the invasive measurements of T_c spectra by noninvasive measurements of R_d spectra, which are also sensitive to the changes created in the tissue by the OC treatments. Regarding the thickness kinetics that are necessary to calculate the diffusion coefficients, they can also be obtained by noninvasive OCT measurements [21]. This way, combining R_d kinetics with OCT thickness measurements obtained from *in vivo* tissues under treatment with OCA solutions, the diffusion properties can be evaluated, a procedure that ultimately allows the estimation of the mobile water content in the tissues, a parameter that can be used to perform a diagnosis.

3.3 Differentiated protein dissociation rate in healthy and pathological mucosa

In this final study, both healthy and pathological colorectal mucosa tissues were submitted to T_c measurements during treatment with 93%-glycerol [29]. To obtain statistical data, 5 healthy and 5 pathological samples were submitted to these treatments, and the spectra were acquired between 200 and 1000 nm for a treatment time of 30 min. After terminating the measurements, the mean time dependence for the T_c spectra was calculated for each tissue, showing neglectable variations in the deep-UV range when compared to the variations observed for the visible-NIR range [29]. Since proteins present a strong absorption band in the 200–230 nm range [39, 54], we wanted to get access the variations induced by the glycerol molecules in that range. To obtain significant kinetic variations in the deep-UV, we used the mean T_c spectra in Eq. (6) to calculate the OC_{eff} as a function of time and wavelength in each tissue [29]. Fig. 14 presents the results of these calculations for both tissues.

According to literature [39, 54], the major absorption band of proteins occurs in the 200–230 nm range, but from graphs in Fig. 14, we see that the highest OC_{eff} is located at 200 nm. This means that the protein dissociation mechanism in colorectal mucosa tissues is translated in a higher efficiency at this wavelength. For this reason, we selected this wavelength to perform a further analysis and try to discriminate the pathology.

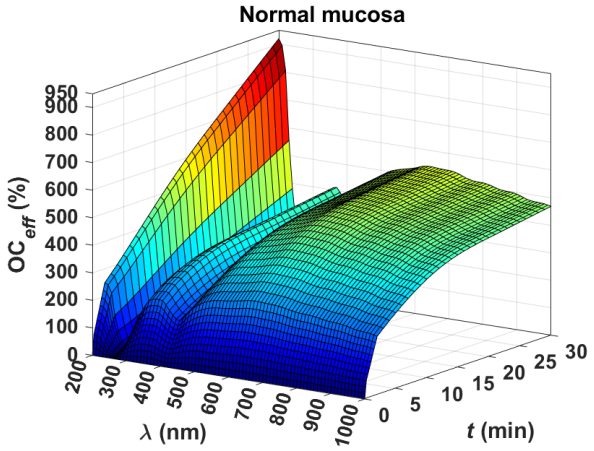
To perform such further analysis, we represented the OC_{eff} kinetics at 200 nm for both tissues in Fig. 15.

Considering the mean OC_{eff} points for each tissue in Fig. 15, we see that both kinetics are well fitted by a curve that is described by a square-root of time at the beginning of the treatment and a linear dependence on time at later treatment (purple lines in Fig. 15) [29]. With the objective of developing future noninvasive diagnostic procedures that should be fast, we observed that the OC_{eff} kinetics for both tissues also present a linear time dependence between 3 and 10 min of treatment (brown and green lines in Fig. 15). We calculated the linear fitting of the OC_{eff} points for each tissue in the 3–10 min range, obtaining the following equations [29]:

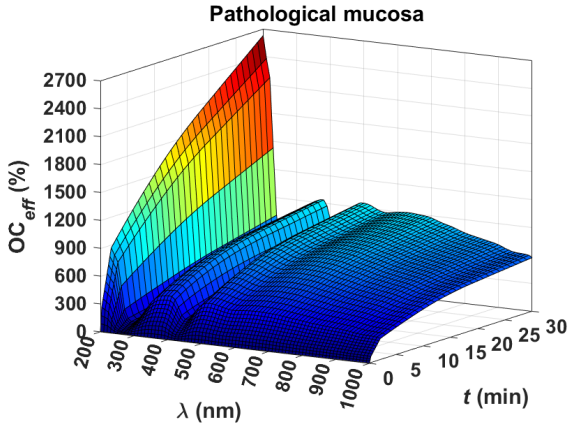
$$OC_{eff-nm} = 27.4\times t + 189.6, \qquad (7)$$

$$OC_{eff-pm} = 79.1 \times t + 721.5, \quad (8)$$

where $OC_{eff\text{-}nm}$ is the OC_{eff} for the healthy mucosa and $OC_{eff\text{-}pm}$ is the OC_{eff} for the pathological mucosa, both represented in % and t represents the time of treatment in min.



(a)



(b)

Fig. 14 Mean OC_{eff} kinetics for the treatments of healthy mucosa (a) and pathological mucosa (b) with 93%-glycerol.

From the resulting equations we see that the slope obtained for the pathological mucosa is almost 3× higher than the one obtained for the healthy mucosa, meaning that the diseased tissue contains more proteins that are dissociated during the OC treatments. The discriminated slope of the OC_{eff} kinetics can be used as a measure of the protein dissociation rate for future cancer diagnostic procedures, which based on noninvasive R_d measurements in the deep-UV can reproduce the results obtained in this study.

Due to the known fact that proteins accumulate in a higher amount in cancer tissues [51], and such accumulation should increase with cancer progression, further studies should be made to obtain a relation between the protein dissociation rate and the stage of cancer development. Due to the different nature of the various types of cancer, such studies should be performed not only for colorectal cancer, but for other cancers as well.

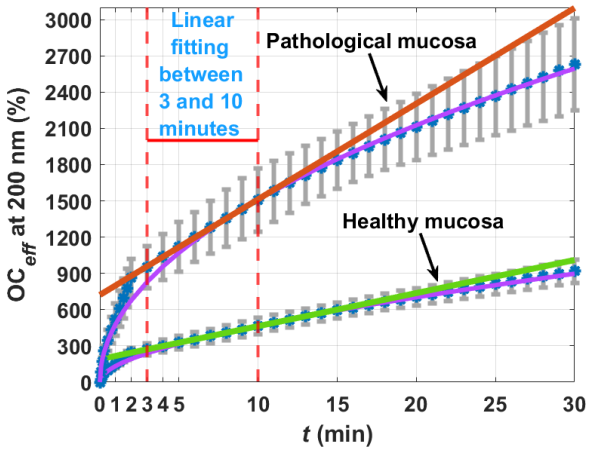


Fig. 15 Mean OC_{eff} kinetics at 200 nm for healthy and pathological mucosa during treatment with 93%-glycerol, dual time dependence fitting for the entire treatment (purple lines) and linear fitting between 3 and 10 min (brown and green lines).

4 Conclusions

The results obtained in the above studies show that it is possible to discriminate colorectal cancer through optical spectroscopy methods. Although these results were obtained from *ex vivo* transmittance spectroscopy, noninvasive R_d spectroscopy methods can be applied in the *in vivo* situation, since both the T_c and R_d configurations are sensitive to obtain the parameters and variations presented above, which can be used for cancer discrimination and monitoring.

In the first study, the simple measurements of T_t and R_t spectra allowed to identify a discriminated content of a pigment in healthy and pathological colorectal mucosa tissues. The detection of such pigment and the evaluation of different content in healthy and diseased tissues was made with simple calculations, using the absorption coefficient spectra of both tissues. Such spectral optical property is traditionally obtained from data that is measured with invasive procedures from *ex vivo* tissues, but with the application of ML techniques, we have demonstrated that it is possible to estimate it with significant precision from noninvasive R_d measurements, which can be applied to the *in vivo* situation.

When performing the second and third studies, we wanted to acquire information to characterize the three OC mechanisms, but the methods used and their application both to healthy and pathological colorectal tissues has proven that diagnostic information can also be acquired during OC treatments. One important result from the second study is the different water content that was found in both tissues. Such different water content values in healthy and cancer tissues show that bound water is converted into mobile water during the progress of cancer in tissues and the evaluation of its content

provides diagnostic information. Similar studies to investigate the water content in healthy and cancer tissues should be performed for other types of cancer and in different stages of cancer progression to establish a dependence relation and use the water content to monitor cancer progression. Although such study was based on invasive *ex vivo* T_c measurements, the method and calculations involved can easily be adapted to use noninvasive and *in vivo* R_d spectra to reach similar results.

In the third study, by knowing that the protein content is higher in cancer-diseased than in healthy tissues, we applied a solution with high-osmolarity glycerol to treat the tissues and study the OC mechanism of protein dissociation. Since proteins present their strong absorption in the deep UV, a spectral range where scattering is also strong, tissues present the lowest transmittance in that range. When OC treatments are applied, low-magnitude variations are observed in the T_c kinetics, a fact that does not allow for direct evaluation of the protein dissociation mechanism. To overcome such difficulty and evaluate the protein dissociation rates in healthy and pathological mucosa tissues, we calculated the OC efficiency as the relative variations of T_c during treatment. Analyzing such calculated data, we obtained a higher rate for protein dissociation in the pathological tissue (~3× higher), a result that is consistent with the fact of higher protein content in cancer tissues. Once again such discriminating data may be useful for cancer diagnosis, and it can also be obtained from *in vivo* R_d measurements. Nevertheless, further studies should be made with other types of cancer and in different stages of their progression to quantify the protein content in tissue from different stages of cancer progression. Only by obtaining such information, it will be possible to develop a clinical *in vivo* procedure to diagnose cancer and monitor its progression.

Disclosures

All authors declare that there is no conflict of interests in this paper.

Acknowledgements

The authors of the article knew well and communicated with Ekaterina Borisova for many years, especially Valery Tuchin and in recent years Luís Oliveira. We had many joint plans to organize conferences and joint research projects, but COVID-19 mercilessly interrupted our communication. We have lost a great scientist and a person with a huge soul, sociable, but at the same time modest and kind. We will always remember our warm meetings and fruitful work with Ekaterina.

This research was supported by the Portuguese grant FCT-UIDB/04730/2020.

VVT was supported by grant under the Decree of the Government of the Russian Federation No. 220 of 09 April 2010 (Agreement No. 075-15-2021-615 of 04 June 2021).

References

1. V. V. Tuchin, L. M. Oliveira, "Recent progress in tissue enhanced spectroscopy for cancer detection," Asian Journal of Physics 30(3), 427–444 (2021).
2. J. Vignard, G. Mirey, and B. Salles, "Ionizing-radiation induced DNA double-strand breaks. A direct and indirect lighting up," Radiotherapy and Oncology 108(3), 362–369 (2013).
3. G. Borrego-Soto, R. Ortiz-López, and A. Rojas-Martinez, "Ionizing radiation-induced DNA injury and damage detection in patients with breast cancer," Genetics and Molecular Biology 38(4), 420–432 (2015).
4. J.-M. Cosset, "Side effects of ionizing radiation on healthy tissues and organs at risk," Cancer Radiotherapie : Journal de la Societe Francaise de Radiotherapie Oncologique 14(4–5), 228–231 (2010).
5. O. Popanda, J. W. Marquardt, J. Chang-Claude, and P. Schmezer, "Genetic variation in normal tissue toxicity induced by ionizing radiation," Mutation Research/Fundamental and Molecular Mechanisms of Mutagenesis 667(1–2), 58–69 (2009).
6. T. N. Seyfried, R. E. Flores, A. M. Poff, and D. P. D'Agostino, "Cancer as a metabolic disease: implications for novel therapeutics," Carcinogenesis 35(3), 515–527 (2014).
7. M. B. Sporn, "The war on cancer," The Lancet 347(9012), 1377–1381 (1996).
8. A. V. Lichtenstein, "Strategies of the War on Cancer: To kill or to Neutralize?" Frontiers in Oncology 8, 667 (2018).
9. T. N. Seyfried, Cancer As a Metabolic Disease: On the Origin, Management, and Prevention of Cancer, John Wiley & Sons, Hoboken (NJ), USA (2012). ISBN: 978-0-470-58492-7.
10. I. J. Fidler, "The pathogenesis of cancer metastasis: the 'seed and soil' hypothesis revisited," Nature Reviews Cancer 3(6), 453–458 (2003).
11. G. P. Gupta, J. Massagué, "Cancer metastasis: building a framework," Cell 127(4), 679–695 (2006).
12. Y. Lazebnik, "What are the hallmarks of cancer?" Nature Reviews Cancer 10, 232–233 (2010).
13. D. Tarin, "Cell and tissue interactions in carcinogenesis and metastasis and their clinical significance," Seminars Cancer Biology 21(2), 72–82 (2011).

14. D. M. Parkin, J. Stjernswärd, and C. S. Muir, "Estimates of the worldwide frequency of twelve major cancers," Bulletin of the World Health Organization 62(2), 163–182 (1984).
15. V. V. Tuchin, J. Popp, and V. Zakharov (Eds.), Multimodal Optical Diagnostics of Cancer, Springer Nature, Switzerland (2020). ISBN: 978-3-030-44593-5.
16. J. Ferlay, I. Soerjomataram, R. Dikshit, S. Eser, C. Mathers, M. Rebelo, D. M. Parkin, D. Forman, and F. Bray, "Cancer incidence and mortality worldwide:sources, methods and major patterns in GLOBOCAN 2012," International Journal of Cancer 136(5), E359–E386 (2015).
17. F. Bray, J. Ferlay, I. Soerjomataram, R. L. Siegel, L. A. Torre, and A. Jemal, "Global cancer statistics 2018: GLOBOCAN estimates of incidence and mortality worldwide for 36 cancers in 185 countries," CA: A Cancer Journal for Clinicians 68(6), 394–424 (2018).
18. E. A. Genina, L. M. C. Oliveira, A. N. Bashkatov, and V. V. Tuchin, "Optical Clearing of Biological Tissues: Prospects of Application for Multimodal Malignancy Diagnostics," in Multimodal Optical Diagnostics of Cancer, V. V. Tuchin, J. Popp, V. Zakharov (eds.), Springer, Cham, Switzerland, 107–131 (2020).
19. S. Carvalho, I. Carneiro, R. Henrique, V. Tuchin, and L. Oliveira, "Lipofuscin-type pigment as a marker of colorectal cancer," Electronics 9(11), 1805 (2020).
20. L. Fernandes, S. Carvalho, I. Carneiro, R. Henrique, V. V. Tuchin, H. P. Oliveira, and L. M. Oliveira, "Diffuse reflectance and machine learning to differentiate colorectal cancer," Chaos: An Interdisciplinary Journal of Nonlinear Science 31, 053118 (2021).
21. L. M. C. Oliveira, V. V. Tuchin, The Optical Clearing Method: A New Tool for Clinical Practice and Biomedical Engineering, Springer, Cham, Switzerland (2019). ISBN: 978-3-030-33055-2.
22. Y. Zhou, J. Yao, and L. V. Wang, "Tutorial on photoacoustic tomography," Journal of Biomedical Optics 21, 061007 (2016).
23. V. V. Tuchin, Tissue Optics: Light Scattering Methods and Instruments for Medical Diagnosis, 3rd ed., SPIE Press, Bellingham (WA), USA (2015). ISBN: 978-1-628-41517-9.
24. V. V. Tuchin, Optical Clearing of Tissues and Blood, SPIE Press, Bellingham (WA), USA (2005). ISBN: 978-0-819-48110-8.
25. I. Carneiro, S. Carvalho, R. Henrique, L. Oliveira, and V. Tuchin, "Moving tissue spectral window to the deep-ultraviolet via optical clearing," Journal of Biophotonics 12(12), e201900181 (2019).
26. W. Spalteholz, Über das Durchsichtigmachen von menschlichen und tierischen Präparaten und seine theoretischen Bedingungen: Nebst Anhang: Über Knochenfärbung, Leipzig Hirzel, Germany (1911).
27. W. Spalteholz, Über das Durchsichtigmachen von menschlichen und tierischen Präparaten und seine theoretischen Bedingungen: Nebst Anhang: Über Knochenfärbung, Leipzig Hirzel, Germany (1914).
28. N. Gomes, V. V. Tuchin, and L. M. Oliveira, "Refractive index matching efficiency in colorectal mucosa treated with glycerol," IEEE Journal of Selected Topics in Quantum Electronics 27(4), 7200808 (2021).
29. I. Carneiro, S. Carvalho, R. Henrique, A. Selifonov, L. Oliveira, and V. V. Tuchin, "Enhanced ultravioleta spectroscopy by optical clearing for biomedical applications," IEEE Journal of Selected Topics in Quantum Electronics 27, 7200108 (2021).
30. L. Oliveira, M. I. Carvalho, E. Nogueira, and V. V. Tuchin, "Skeletal muscle dispersion (400-1000 nm) and its kinetics at optical clearing," Journal of Biophotonics 11(1), e20170094 (2018).
31. L. Oliveira, A. Lage, M. Pais Clemente, and V. V. Tuchin, "Rat muscle opacity decrease due to the osmosis of a simple mixture," Journal of Biomedical Optics 15(5), 0055004 (2010).
32. L. Oliveira, Study of the spectral transmission response of biological tissues under the influence of different osmotic agents, FEUP Edições, Porto, Portugal (2007).
33. L. Oliveira, A. Lage, M. Pais Clemente, and V. V. Tuchin, "Optical characterization and composition of abdominal Wall muscle from rat," Optics and Lasers in Engineering 47, 667–672 (2009).
34. X. Wen, Z. Mao, Z. Han, V. V. Tuchin, and D. Zhu, "In vivo skin optical clearing by glycerol solutions: mechanism," Journal of Biophotonics 3, 44–52 (2010).
35. D. Zhu, K. V. Larin, Q. Luo, and V. V. Tuchin "Recent progress in tissue optical clearing," Laser & Photonics Reviews 7(5), 732–757 (2013).
36. D. K. Tuchina, I. G. Meerovich, O. Sindeeva, V. V. Zherdeva, A. P. Savitsky, A. A. Bogdanov Jr, and V. V. Tuchin, "Magnetic resonance contrast agents in optical clearing: prospects for multimodal tissue imaging," Journal of Biophotonics 13, e20190249 (2020).
37. A. Y. Sdobnov, M. E. Darvin, J. Schleusener, J. Lademann, and V. V. Tuchin, "Hydrogen bound water profiles in the skin influenced by optical clearing molecular agents – quantitative analysis using confocal Raman microscopy," Journal of Biophotonics 12, e201800283 (2019).
38. C. S. Choe, J. Lademann, and M. E. Darvin, "Depth profiles of hydrogen bound water molecule types and their relation to lipid protein interaction in the human stratum corneum in vivo," Analyst 141, 6329–6337 (2016).
39. T. Yu, D. Zhu, L. Oliveira, E. Genina, A. Bashkatov, and V. V. Tuchin, "Tissue optical clearing mechanisms" in Tissue Optical Clearing: New Prospects in Optical Imaging, D. Zhu, E. Genina, V. Tuchin (Eds.), CRC Press, Boca Raton, USA (2021).

40. L. M. Oliveira, M. I. Carvalho, E. Nogueira, and V. V. Tuchin, "Diffusion characteristics of ethylene glycol in skeletal muscle," Journal of Biomedical Optics 20, 051019 (2015).
41. L. Oliveira, M. I. Carvalho, E. Nogueira, and V. V. Tuchin, "Optical clearing mechanisms characterization in muscle," Journal of Innovative Optical Health Sciences 9(5), 1650035 (2016).
42. L. M. Oliveira, M. I. Carvalho, E. Nogueira, and V. V. Tuchin, "The characteristic time of glucose diffusion measured for muscle tissue at optical clearing," Laser Physics 23, 075606 (2009).
43. I. Carneiro, S. Carvalho, R. Henrique, L. Oliveira, and V. V. Tuchin, "A robust ex vivo method to evaluate the Diffusion properties of agents in biological tissues," Journal of Biophotonics 12, e201800333 (2019).
44. R. Cicchi, D. Sampson, D. Massi, and F. S. Pavone, "Contrast and depth enhancement in two-photon microscopy of human skin ex vivo by use of optical clearing agents," Optics Express 13(7), 2337–2344 (2005).
45. S. Carvalho, N. Gueiral, E. Nogueira, R. Henrique, L. Oliveira, and V. V. Tuchin, "Glucose Diffusion in colorectal mucosa – a comparative study between normal and cancer tissues," Journal of Biomedical Optics 22(9), 091506 (2017).
46. D. K. Tuchina, A. N. Bashkatov, A. B. Bucharskaya, E. A. Genina, and V. V. Tuchin, "Study of glycerol diffusion in skin and myocardium ex vivo under the conditions of developing alloxan-induced diabetes," Journal of Biomedical Photonics & Engineering 3(2), 020302 (2017).
47. A. Yeh, B. Choi, J. S. Nelson, and B. J. Tromberg, "Reversible dissociation of collagen in tissues," Journal of Investigative Dermatology 121(6), 1332–1335 (2003).
48. J. Hirshburg, B. Choi, J. S. Nelson, and A. T. Yeh, "Collagen solubility correlates with skin optical clearing," Journal of Biomedical Optics 11(4), 040501 (2006).
49. J. Hirshburg, B. Choi, J. S. Nelson, and A. T. Yeh, "Correlation between collagen solubility and skin optical clearing using sugars," Lasers in Surgery and Medicine 39(2), 140–144 (2007).
50. J. Hirshburg, K. M. Ravikumar, W. Hwang, and A. T. Yeh, "Molecular basis for optical clearing of collagenous tissues," Journal of Biomedical Optics 15(5), 055002 (2010).
51. S. Peña-Llópis, J. Brugarolas, "Simultaneous isolation of high-quality DNA, RNA, miRNA and proteins from tissues for genomic applications," Nature Protocols 8, 2240-2255 (2013).
52. A. N. Bashkatov, E. A. Genina, V. I. Kochubey, V. V. Tuchin, E. E. Chikina, A. B. Knyazev, and O. V. Mareev, "Optical properties of mucous membrane in the spectral range 350-2000 nm," Optics ans Spectroscopy 97, 1043–1048 (2004).
53. J. D. Johansson, K. Wårdell, "Intracerebral quantitative chromophore estimation from reflectance spectra captured during deep brain stimulation implantation," Journal of Biophotonics 6(5), 435–445 (2013).
54. P. Brescia, "Micro-volume purity assessment of nuclei acids using A260/A280 ratio and structural scanning protein and nucleic acid quantification," (accessed July 2021). [https://www.biotek.com/resources/application-notes/micro-volume-purity-assessment-of-nucleic-acids-using-asub260/sub/asub280/sub-ratio-and-spectral-scanning/].
55. S. Carvalho, N. Gueiral, E. Nogueira, R. Henrique, L. Oliveira, and V. V. Tuchin, "Comparative study of the optical properties of colon mucosa and colon precancerous polyps between 400 and 1000 nm," SPIE Proceedings 10063, 100631L (2017).

Accuracy of Common Motion Estimators in Wave-Based Optical Coherence Elastography

Justin R. Rippy[1*], Manmohan Singh[1], Salavat Aglyamov[2], and Kirill V. Larin[1]
[1] Department of Biomedical Engineering, University of Houston, 3517 Cullen Blvd., Houston, TX 77204, USA
[2] Department of Mechanical Engineering, University of Houston, Houston, TX 77204, USA

*** e-mail:** jrrippy@uh.edu

Abstract. Motion estimators are commonly used in shear wave optical coherence elastography to compute small displacements. This work focuses on comparing three motion estimators: Kasai, Loupas, and the vector method. Our results show that the vector method is superior in low-SNR, low-amplitude situations for group velocity calculation and profile reconstruction. © 2021 Journal of Biomedical Photonics & Engineering.

Keywords: motion estimator; shear wave elastography; signal to noise ratio; Loupas; Kasai; vector method.

Paper #3450 received 4 Aug 2021; revised manuscript received 7 Sep 2021; accepted for publication 9 Sep 2021; published online 21 Sep 2021. doi: 10.18287/JBPE21.07.040303.

1 Introduction

In traditional shear wave elastography, mechanical waves are generated in a sample and measured by various imaging modalities [1]. One modality that is often used for this purpose is optical coherence tomography, which utilizes backscattered light to obtain images with micrometer resolution [2]. By determining the speed of the mechanical wave traveling through a material, mechanical properties can be estimated, which can be a powerful tool for early disease detection, disease progression monitoring, or therapy guidance [3]. Small displacements on the order of nanometers to micrometers are typically induced in optical coherence elastography (OCE), and the ability to evaluate these displacements determines the quality of speed estimation regardless of the speed calculation method. Motion estimators are often used for this task, which computes the motion between temporal and/or spatial samples utilizing the raw data acquired from the imaging system. Three of the most often used motion estimators are the Kasai [4] and Loupas [5] autocorrelation estimators and the recently introduced vector method [6]. The Kasai autocorrelator, which is also known as the 1D autocorrelator, was used extensively in initial elastography publications due to its computational simplicity [5]. Later, Loupas was able to derive a superior estimator known as the 2D autocorrelator, which deals with some of the limitations of the Kasai method (which are discussed in Ref. [5]). The most recent of the three, the vector method tracks subpixel displacements between scans to ensure that the same scatterers are compared when determining displacement [6, 9]. This method has been shown to be more accurate and more noise-tolerant than other methods but only for static/quasi-static elastography [6, 9]. However, its application to wave-based elastography has yet to be demonstrated. Though these three methods have been and continue to be used throughout elastography, there are no studies showing which motion estimator is best for a given set of circumstances.

In this work, we performed simulations and collected experimental data to determine what effect varying the amplitude and signal-to-noise ratio (SNR) had upon the measured group velocity. We used normalized fitted profiles to create ideal displacement profiles with infinite SNR to be used as a baseline for comparison. White Gaussian noise was added at various levels to match desired SNR values. Profiles were reconstructed using the three methods mentioned earlier and using only the raw data with and without averaging. Following this, the group velocity of the mechanical wave was calculated, and the results of each method were compared to the normalized fitted profiles. We show that there is an apparent lower bound on the SNR required to accurately obtain the wave speed with a given speed calculation method. We also show that the vector method is more resistant to the effects of noise than the Loupas or Kasai motion estimators but at the cost of a slight loss of accuracy.

2 Materials and Methods

2.1 Data acquisition

Elastography data was acquired from several gelatin phantom concentrations (8%, 12%, and 16%) with an optical coherence elastography imaging system. The system and acquisition procedure is described in a previous publication [7]. The OCE system contains a broadband swept-source laser (HSL 2000, Santec Corp., Hackensack, NJ, USA) with a central wavelength of 1310 nm, the axial resolution of 11 μm in air, transverse resolution of 16 μm, and a scan rate of 30 kHz. A focused micro air pulse [8] was synchronized with the frame trigger [9] to give an effective temporal resolution of 30 kHz. This air pulse generated a wave on the surface of the phantom, which was then recorded at 251 points in a line over ~6.3 mm. The excitation was performed in the center of this line, causing wave motion to the left and right. The OCE data was obtained as the raw spectral interference pattern, which was then converted to linear-in-wavenumber spectral data by linear interpolation based on calibration. The raw complex OCT data was then obtained by fast Fourier transform (FFT) of the linear-in-wavenumber data. In the following simulations, profiles were generated from this experimental OCT data at each concentration mentioned above.

2.2 Simulations

From the raw complex OCT data, the top surface of each phantom was determined using a surface tracking algorithm, and displacement profiles were taken for 50 pixels (~200 μm) below the surface. Stationary phase profiles were obtained from the experimental OCT phase data (i.e., angle of the raw complex OCT data). A Gaussian fit was performed on the stationary phase profiles to generate ideal noiseless profiles used in the following simulations. Following this, only the ideal noiseless profiles generated from the Gaussian fit were used. The width of the fit was fixed to eliminate any effect of dispersion on the results. For these simulations, the amplitudes and SNRs of the displacement profiles were modified before motion estimation. The displacement profiles were first normalized and multiplied by the desired amplitude to give profiles with infinite SNR but definite amplitude. An example profile corresponding to an amplitude of –0.1 is shown in Fig. 1.

To modify the SNR, white Gaussian noise was added to each profile using until the desired SNR was obtained, where the SNR was given by:

$$SNR = 20\,log_{10}\left(\frac{u_{peak}}{\sigma_{profile}}\right). \quad (1)$$

Here, u_{peak} is the average of the 3 central samples at the known maximum peak location obtained from the fitted profiles (e.g., the minimum in Fig. 1), and $\sigma_{profile}$ is the standard deviation of the profile after subtraction of the fitted profile.

Several example profiles with varying SNRs are shown in Fig. 2. Twelve individual amplitudes and SNR values were combined to study their effects on group velocity calculation. The amplitudes and SNRs investigated are listed in Table 1. From these noise-added profiles, the various motion estimators were applied: no motion estimator was applied (i.e., only the angle of the complex data was utilized), smoothing the noise-added profiles in-depth and time, Kasai estimator, Loupas estimator, and vector method. For all techniques, a kernel size of 5 pixels was utilized. Since some techniques, such as the Kasai and Loupas estimators, provide the particle velocity, i.e., the time derivative of the displacement, the cumulative sum was applied to obtain the displacement from the particle velocity.

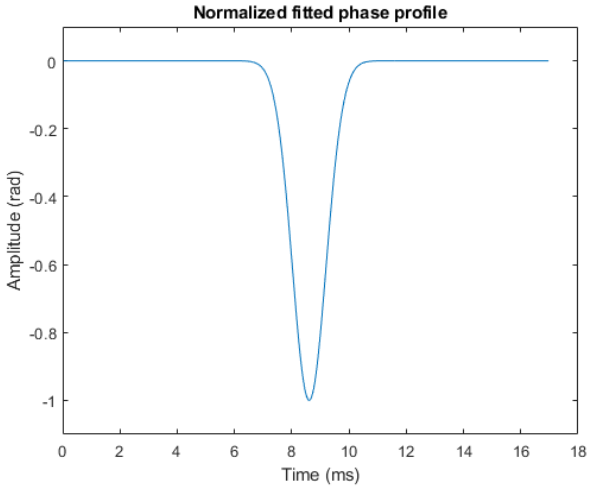


Fig. 1 A normalized fitted phase profile with amplitude 1 is shown here.

Table 1 Amplitude and SNR values used in the simulations.

Amplitude (radians)	0.1, 0.5, 1.0, 1.5, 2.0, 2.5, 5, 7.5, 10, 25, 50, 100
SNR (dB)	0.1, 0.5, 1.0, 1.5, 2.0, 2.5, 5, 7.5, 10, 25, 50, 100

3 Motion Estimation Algorithms

The Kasai autocorrelation algorithm can be used to calculate the average phase change over a given axial range, $\overline{\Delta\phi}$:

$$\overline{\Delta\phi} \approx \approx -\tan^{-1}\left(\frac{\sum_{i=1}^{N-1}[Q(i)I(i-1)-I(i)Q(i-1)]}{\sum_{i=1}^{N-1}[I(i)I(i-1)+Q(i)Q(i-1)]}\right), \quad (2)$$

where Q and I are the imaginary and real parts of the complex OCT signal, respectively; N is the number of averaged A-scans, and i is the signal of the i^{th} A-scan at a given depth [10, 11].

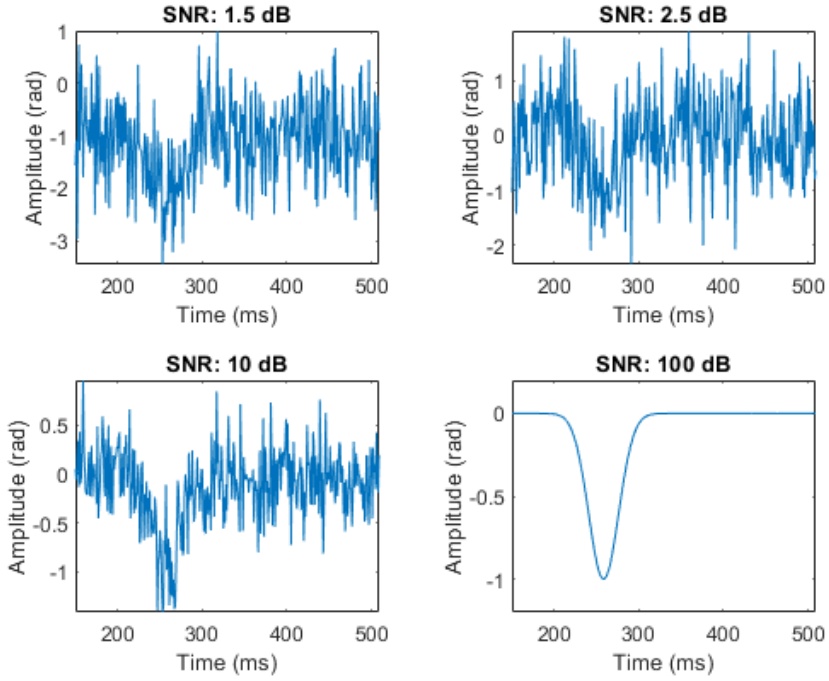


Fig. 2 Example profiles at various SNR values. Each profile started with an amplitude of 1.

The Loupas autocorrelator can similarly be used to find Δϕ [1, 10]:

$$\Delta\phi(z) = \frac{tan^{-1}\left(\frac{\sum_{m=0}^{M-1}[Q(z_m,t_0)I(z_m,t_1)-I(z_m,t_0)Q(z_m,t_1)]}{\sum_{m=0}^{M-1}[I(z_m,t_0)I(z_m,t_1)+Q(z_m,t_0)Q(z_m,t_1)]}\right)}{1+\frac{tan^{-1}\left(\frac{\sum_{m=0}^{M-2}\sum_{n=0}^{N-1}[Q(z_m,t_n)I(z_{m+1},t_n)-I(z_m,t_n)Q(z_{m+1},t_n)]}{\sum_{m=0}^{M-2}\sum_{n=0}^{N-1}[I(z_m,t_n)I(z_{m+1},t_n)+Q(z_m,t_n)Q(z_{m+1},t_n)]}\right)}{2\pi}}, \quad (3)$$

where z_m is the m^{th} element along the z-axis, M is the size of the window in the axial direction, N is the size of the window in time, and Q and I are the imaginary and real parts of the complex OCT signal, respectively.

In the vector method, there are four steps [6]. First, the complex data from two temporally consecutive OCT frames are multiplied together according to

$$b(m,j) = a_1(m,j) \cdot a_2^*(m,j), \quad (4)$$

where a_1 is the first frame, a_2 is the second frame, and $m = 1 \ldots N_x$ and $j = 1 \ldots N_z$ are the horizontal and vertical indices of the processing window, respectively. Then, b is averaged laterally across a window of the desired length, giving the vector $B(j)$:

$$\overline{b(j)} \equiv B(j)\exp[i \cdot \Phi(j)] = \sum_{m=1}^{N_x} b(m,j), \quad (5)$$

where Φ is the phase variation. After this, complex-valued quantities $c(j)$ are formed via:

$$c(j) = \overline{b(j+1)} \cdot \overline{b(j)}^*, \quad (6)$$

and averaged across the vertical index as:

$$\bar{c} = \sum_{j=1}^{N_z-1} c(j) = \bar{C}exp[i \cdot \overline{\Delta\Phi}], \quad (7)$$

where C is the complex vector. The angle $\overline{\Delta\Phi}$ is the desired quantity and is the averaged inter-pixel phase-variation across the processing window.

4 Group Velocity Calculations

A cross-correlation-based algorithm was utilized to quantify the elastic wave group velocity [12]. The temporal phase profiles along the propagation path for a given depth were cross-correlated with a reference signal near the excitation to obtain the wave propagation lags. The least-squares regression fitting of the wave propagation lags with the propagation distances resulted in the wave speed. The speed was calculated for the various motion estimators: noiseless fitted profiles, noise-added data, averaged noise-added profiles, Kasai estimated motion, Loupas reconstructed profiles and vector method data.

5 Comparison with Noiseless Profiles

Following the wave propagation simulations, the results of each method were compared with the results of the noiseless profiles. For the 8%, 12%, and 16% phantoms, the group velocities of the noiseless fitted profiles were 2.518 m/s, 3.139 m/s, and 8.085 m/s, respectively. The mean and standard deviation of the group velocities for each method were calculated and used to calculate percent error for each method, with the group velocity generated from the noiseless profiles serving as the true value. The mean and standard deviation were taken for

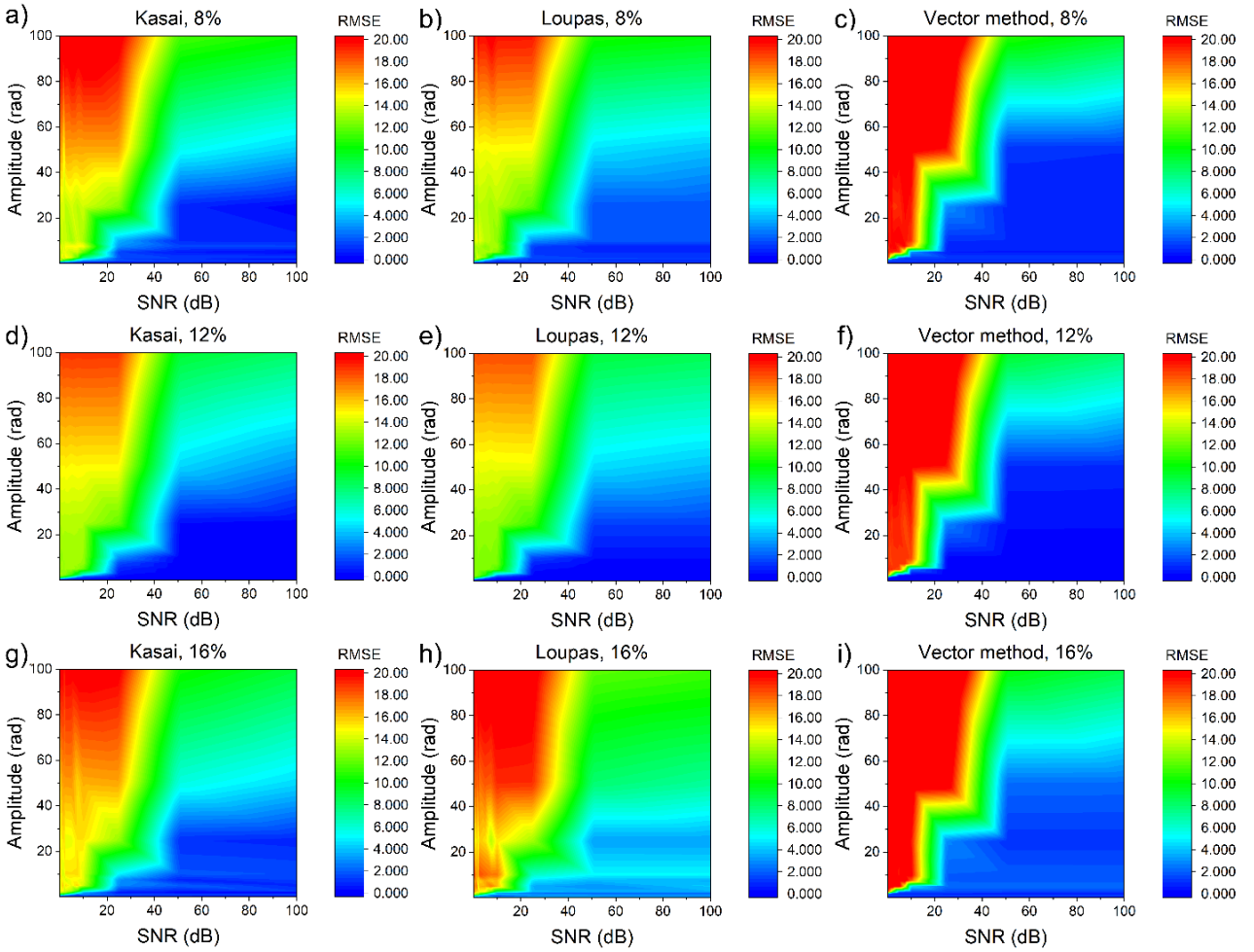


Fig. 3 Comparison of the RMS error of the three motion estimators from 8%, 12%, and 16% gelatin phantom data.

the 50 depth-wise pixels. The root-mean-square (RMS) error of the individual profiles as compared to their noise-added counterparts, which was the given motion in the samples, was also calculated to estimate the accuracy of each method to reconstruct the given motion. Finally, a summary of the SNR improvement was also quantified, where the SNR is given by Eq. 4.

6 Results

Fig. 3 shows the RMS error between the reconstructed phase profiles and the noiseless profiles for each method. In these figures, RMS error is capped at 20% to provide better contrast. The vector method has a larger area of RMS error less than 5% (indicated by the blue region) than either of the other two methods. Kasai outperforms Loupas here as well. In the low-SNR region, the vector method largely performs worse than either method except at very low SNR and amplitude.

Group velocity results for the three motion estimation methods are shown in Fig 4. The percent error is capped at 100% in these figures to provide better contrast for the lower values. The average percent error across all three phantom concentrations at SNRs greater than 50 was $1.94 \pm 1.56\%$, $2.07 \pm 1.44\%$, and $2.30 \pm 2.10\%$ for the Kasai, Loupas, and vector methods, respectively. For an SNR of 25, only the amplitudes less than 10 rad had percent error values less than 10%, at $3.09 \pm 2.29\%$ for Kasai, $2.3 \pm 1.62\%$ for Loupas, and $2.39 \pm 2.22\%$ for the vector method. However, for SNR values lower than 10 dB all methods had difficulty accurately determining wave speed except at extremely low amplitudes ($< 1 - 2$ rad), with percent errors sometimes exceeding 900%. The vector method accurately determined the group velocity in the areas where low SNR meets with low amplitudes in all cases, unlike either Kasai or Loupas. This can be seen in the lower-left corner of Fig. 4 in plots (c), (f), and (i).

7 Discussion

All three methods allowed for highly accurate ($< 5\%$ error) group velocity calculations regardless of amplitude above an OCE SNR of ~50 dB. However, at SNRs above 50 dB, motion estimation algorithms are not necessary, as the group velocities can be calculated directly from the raw phase data, as shown in Fig 5. This may not be the case for samples with more complicated excitation patterns (e.g., chirps) or in cases with irregular noise. More complicated excitation patterns, especially those with multiple excitation waveforms, may present difficulty in retrieving group velocity due to errors in

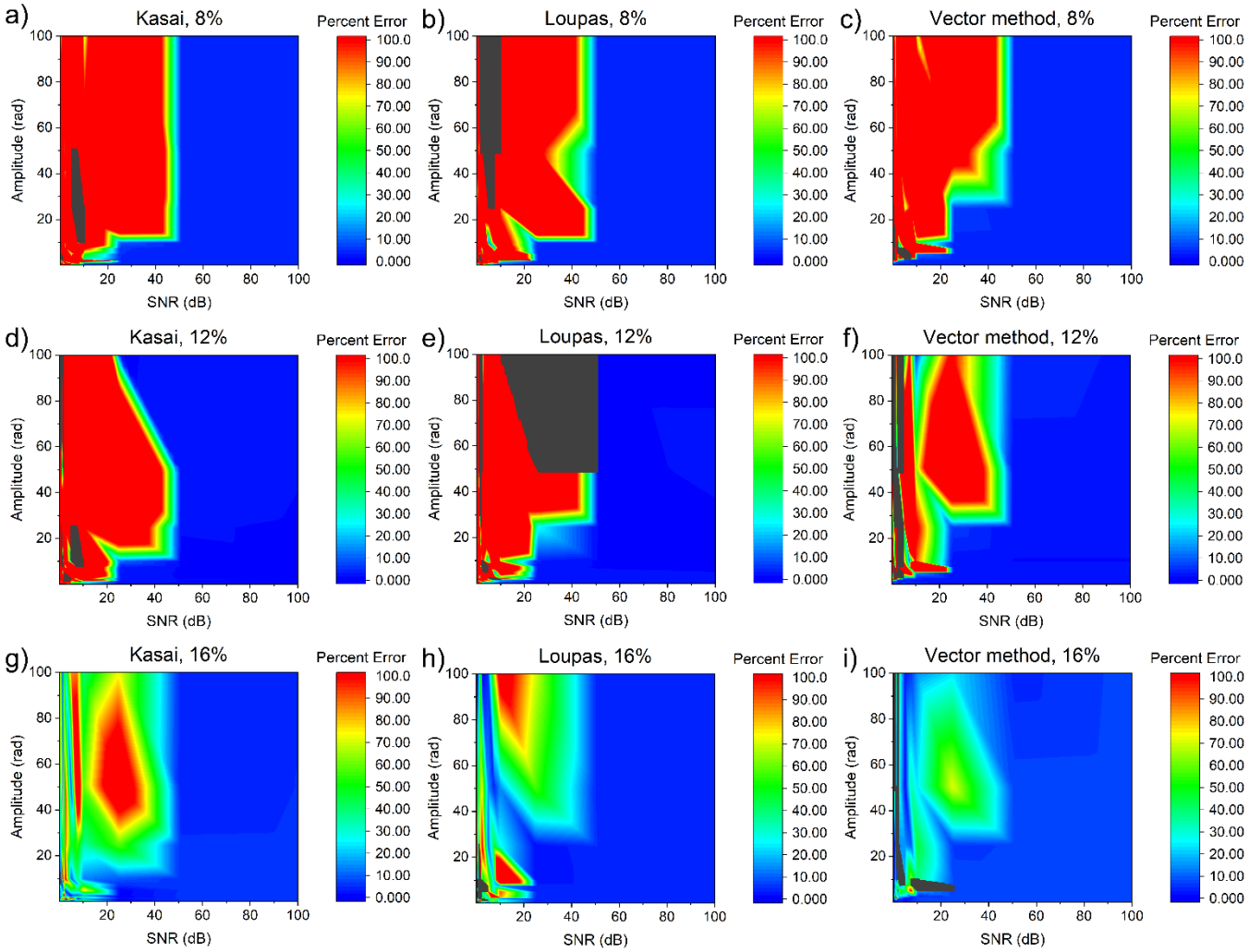


Fig. 4 Comparison of the percent error of the three motion estimators from 8%, 12%, and 16% gelatin phantom data. Gray areas indicate that values could not be calculated in that region.

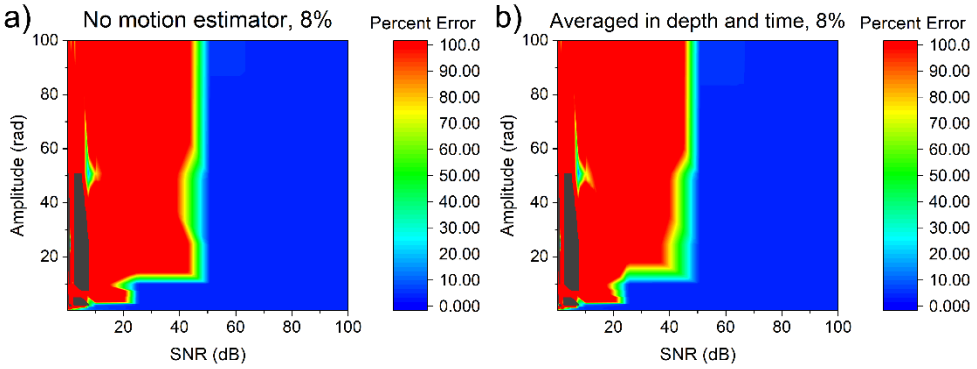


Fig. 5 Comparison of the percent error using (a) no motion estimator and (b) after averaging in-depth and time.

cross-correlation. Hence, other techniques for velocity calculation can be applied, such as frequency-domain methods. This result indicates that the SNR can be purposefully lowered by adjusting other parameters such as detector speed without any penalty in velocity error, provided that the SNR remains greater than 50 dB.

In this paper, we discuss the OCE SNR (i.e., the SNR of the displacement of the elastic wave), not the OCT SNR. However, Park showed in Ref. [13] that the minimum detectable phase difference, $\sigma_{\Delta\phi}$, is related to the OCT SNR by

$$\sigma_{\Delta\phi} = (SNR)^{-\frac{1}{2}}. \quad (8)$$

This means that having a high OCT SNR will contribute to having a high OCE SNR.

As shown in Fig. 4, averaging the phase information in-depth and time did not improve group velocity calculation. Though the vector method also involves similar averaging, it averages the complex data. The averaging of the real and imaginary parts of the vectors instead of directly averaging their angles makes the vector method robust and noise-tolerant [6].

There is also a lower bound on SNR required for accurate group velocity retrieval regardless of the method or amplitude at ~20 dB. Above this SNR, at least some amplitudes allow for group velocity retrieval, but below 20 dB, errors increase for all methods. Typical SNRs of modern imaging systems are well above this, but this could be a factor when measuring extremely weak waves, designing low-cost imaging systems with relatively weak lasers in optical coherence tomography and other optical techniques, in portable single-fiber-based probes, etc. The minimum phase difference that can be detected depends on the image SNR and is given by:

$$\sigma_{\Delta\phi} = \frac{1}{\sqrt{SNR_{OCT}}}. \quad (8)$$

This equation assumes that the SNR is $\gg 1$ [13]. At an SNR of ~20 dB and an amplitude of ~20 rad, both the vector method and Loupas allow for reliable group velocity calculations, but Kasai does not. This is likely due to the limitations mentioned previously [5, 10, 14] by virtue of the Kasai autocorrelator being a 1D technique. In the square region from 20 dB to 50 dB and 0 rad to 25 rad, the vector method is more reliable across all wave speeds (i.e., elasticities). This is due to phase unwrapping and the errors that may result from using phase unwrapping algorithms. When the SNR and amplitudes are low, the amplitudes of the profiles remain wrapped (i.e., $< \pm\pi$), and there are no unwrapping errors, leading to very low error in the final group velocity estimation. As the noise increases and/or the phase jumps increase above $\Delta 2\pi$, the unwrapping algorithm accumulates errors causing a significant final error in the final group velocity estimation due to large erroneously unwrapped jumps. The focus of this manuscript was to isolate the motion estimators, so various phase unwrapping algorithms were not examined. However, phase unwrapping is still not well solved [15]. It should be given consideration when attempting to reconstruct profiles that are either particularly noisy or that have signals significantly above the $\Delta 2\pi$ threshold. When considering the entirety of the contour map, the vector method typically produces more reasonable group velocities than either Loupas or Kasai techniques, as evident by comparing the regions in Fig. 3. However, this effect is limited to a very small range of SNRs and amplitudes, indicating that either the vector method or the Loupas autocorrelator can be used in the majority of circumstances.

As the wave speed increases, the ability of the estimators to accurately determine velocity also increases. This is likely due to differences in the amount of peak shifting, also known as jitter, occurring during cross-correlation. Several factors can contribute to these shifts, including signal decorrelation, noise, and finite window length. This causes a jitter in the cross-correlation values computed as the wave propagation lag, which is measured as the standard deviation of the displacement error [10]. As the group velocity slope increases, the error decreases.

The RMS error results show that the vector method reconstructed the motion most accurately, while Kasai and Loupas showed similar performance. This comparison eliminates the effects of cross-correlation and fitting and shows that the vector method is superior to the other methods for profile reconstruction over a higher range of SNRs and amplitudes. Averaging the raw phase profiles did improve the signal, but the vector method was superior because it averages the complex data instead of only the phase data. This accounts for the speckle properties inherent to coherence imaging systems, such as ultrasound imaging and OCT.

The Kasai autocorrelator works by measuring the average phase shift with respect to a central frequency but assumes a constant mean frequency. Because of this assumption, Kasai's algorithm can be inaccurate if there are fluctuations [10]. Additionally, Kasai's algorithm was useful at a time when computing power was limited. Computing power has increased exponentially since the introduction of the algorithm, meaning that more accurate but computationally expensive methods can be used without a significant time penalty.

The Loupas autocorrelator uses information from two dimensions instead of only using axial information for filtering [5]. Hence, the Loupas autocorrelator outperforms the Kasai algorithm. However, in some situations, the denominator of Loupas' algorithm can become small enough that the algorithm yields nonphysical results, and therefore a filter must be used to limit the displacement range to $-\frac{\lambda}{2}$ to $\frac{\lambda}{2}$ [10]. The Loupas algorithm is also relatively computationally inexpensive, meaning that results can be obtained quickly. In fact, it was implemented on the GPU for real-time displacement estimation ten years ago [16].

The vector method, which was first published in 2018, maintains low error by using complex data for calculations until the last step and avoiding phase unwrapping [6]. Though it was designed for static/quasi-static elastography, these results show that it can also be utilized for dynamic elastography [6]. Though it is the most computationally intense of the three, numerous computational approaches optimized for vector arithmetic can perform these calculations with minimal time penalties.

8 Conclusions

The primary goal of this work was to look at the relationship between amplitude and SNR when considering motion estimation algorithms for various mechanical wave propagation speeds in impulsive wave-based elastography. Our results show that there is a lower

bound on SNR at approximately 20 dB that is required for accurate group velocity measurement for any of the methods. After an OCE displacement SNR of 50 dB, the percent error remains below 5% regardless of amplitude and motion estimator, which may be useful when trying to balance other parameters that may lower SNR. Additionally, the vector method has greater coverage of lower error values than either Kasai or Loupas methods, though Loupas is nearly as good. The role of amplitude in profile reconstruction is very small, with SNR being the key parameter, except at very low amplitudes.

Disclosures

All authors declare that there is no conflict of interests in this paper.

References

1. F. Zvietcovich, J. P. Rolland, J. Yao, P. Meemon, and K. J. Parker, "Comparative study of shear wave-based elastography techniques in optical coherence tomography," Journal of Biomedical Optics 22(3), 035010 (2017).
2. C. E. Psomadakis, N. Marghoob, B. Bleicher, and O. Markowitz, "Optical coherence tomography," Clinics in Dermatology, (2021).
3. B. J. Fahey, R. C. Nelson, S. J. Hsu, D. P. Bradway, D. M. Dumont, and G. E. Trahey, "In vivo guidance and assessment of liver radio-frequency ablation with acoustic radiation force elastography," Ultrasound in Medicine & Biology 34(10), 1590–603 (2008).
4. C. Kasai, K. Namekawa, A. Koyano, and R. Omoto, "Real-time two-dimensional blood flow imaging using an autocorrelation technique," IEEE Transactions on Sonics and Ultrasonics 32(3), 458–464 (1985).
5. T. Loupas, R. Peterson, and R. W. Gill, "Experimental evaluation of velocity and power estimation for ultrasound blood flow imaging, by means of a two-dimensional autocorrelation approach," IEEE Transactions on Ultrasonics, Ferroelectrics, and Frequency Control 42(4), 689–699 (1995).
6. A. Matveyev, L. Matveev, A. Sovetsky, G. Gelikonov, A. Moiseev, and V. Y. Zaitsev, "Vector method for strain estimation in phase-sensitive optical coherence elastography," Laser Physics Letters 15(6), 065603 (2018).
7. J. R. Rippy, M. Singh, S. R. Aglyamov, and K. V. Larin, "Ultrasound Shear Wave Elastography and Transient Optical Coherence Elastography: Side-by-Side Comparison of Repeatability and Accuracy," IEEE Open Journal of Engineering in Medicine and Biology 2, 179–186 (2021).
8. S. Wang, K. V. Larin, J. Li, S. Vantipalli, R. K. Manapuram, S. Aglyamov, S. Emelianov, and M. D. Twa, "A focused air-pulse system for optical-coherence-tomography-based measurements of tissue elasticity," Laser Physics Letters 10(7), 075605 (2013).
9. S. Wang, K. V. Larin, "Shear wave imaging optical coherence tomography (SWI-OCT) for ocular tissue biomechanics," Optics Letters 39(1), 41–44 (2014).
10. G. F. Pinton, J. J. Dahl, and G. E. Trahey, "Rapid tracking of small displacements with ultrasound," IEEE Transactions on Ultrasonics, Ferroelectrics, and Frequency Control 53(6), 1103–1117 (2006).
11. V. X. Yang, M. L. Gordon, A. Mok, Y. Zhao, Z. Chen, R. S. C. Cobbold, B. C. Wilson, and I. A. Vitkin, "Improved phase-resolved optical Doppler tomography using the Kasai velocity estimator and histogram segmentation," Optics Communications 208(4–6), 209–214 (2002).
12. S. Wang, A. L. Lopez, Y. Morikawa, G. Tao, J. Li, I. V. Larina, J. F. Martin, and K. V. Larin, "Noncontact quantitative biomechanical characterization of cardiac muscle using shear wave imaging optical coherence tomography," Biomed. Opt. Express 5(7), 1980–1992 (2014).
13. B. H. Park, M. C. Pierce, B. Cense, S.-H. Yun, M. Mujat, G. J. Tearney, B. E. Bouma, and J. F. de Boer, "Real-time fiber-based multi-functional spectral-domain optical coherence tomography at 1.3 μm," Optics Express 13(11), 3931–3944 (2005).
14. D. Morofke, M. C. Kolios, I. A. Vitkin, and V. X. D. Yang, "Wide dynamic range detection of bidirectional flow in Doppler optical coherence tomography using a two-dimensional Kasai estimator," Optics Letters 32(3), 253–255 (2007).
15. K. Wang, Y. Li, Q. Kemao, J. Di, and J. Zhao, "One-step robust deep learning phase unwrapping," Optics Express 27(10), 15100–15115 (2019).
16. S. Rosenzweig, M. Palmeri, and K. Nightingale, "GPU-based real-time small displacement estimation with ultrasound," IEEE Transactions on Ultrasonics, Ferroelectrics, and Frequency Control 58(2), 399–405 (2011).

Assessing Porcine Iris Elasticity and Mechanical Anisotropy with Optical Coherence Elastography

Christian Zevallos-Delgado[1], Taye T. Mekonnen[1], Fernando Zvietcovich[1], Manmohan Singh[1], Salavat R. Aglyamov[2], and Kirill V. Larin[1*]

[1] Department of Biomedical Engineering, University of Houston, 3517 Cullen Blvd., Room 2027, Houston, TX 77204, USA

[2] Department of Mechanical Engineering, University of Houston, Houston, TX 77204, USA

*** e-mail:** klarin@Central.UH.EDU

Abstract. The relaxation and contraction of the sphincter and dilator muscles of the iris play a critical role in vision, yet little is known about the biomechanical properties of these muscles. This study aimed to determine the elastic properties of the iris as a function of its anatomy and intraocular pressure. A high-resolution phase-sensitive OCE system was employed to detect acoustic radiation force induced propagation of elastic waves in the porcine iris in situ. Experiments were conducted at four different intraocular pressures (5, 10, 20, and 30 mmHg) with mechanical excitation at 1 kHz. We found that there was no significant difference in the wave speed at the different intraocular pressures. The results show that the stiffness of the iris was significantly higher in the semi-azimuthal orientation (mean wave speed of 2.5 m/s) than in the radial orientation (mean wave speed of 1.5 m/s). These measurements provide essential insights into the elastic properties of the iris, and they can be used for the characterization of eye conditions. © 2021 Journal of Biomedical Photonics & Engineering.

Keywords: optical coherence elastography; iris; acoustic radiation force; biomechanics; elasticity; Young's modulus; intraocular pressure.

Paper #3443 received 21 Jun 2021; revised manuscript received 7 Sep 2021; accepted for publication 7 Sep 2021; published online 29 Oct 2021. doi: 10.18287/JBPE21.07.040304.

1 Introduction

The iris is located between the sclera and the pupil in the eye and is physically protected by the cornea. The movements of the iris (contraction and dilation) are supported by its structure, which is shaped by sphincter (for contraction) and dilator muscles (for dilation). The iris sphincter is in the pupillary circle, controlling accommodation and the amount of light reaching the retina. The exterior surface is divided into two different portions by the collarette. The collarette is the zone where the sphincter and the dilator muscles overlap [1–3]. The iris possesses two layers, the stroma, which contains most of the vascular tissue and is connected to the sphincter and dilator muscles, and the posterior, which is the pigmented layer mainly composed of melanocytes and fibroblasts [4, 5]. The iris can suffer several lesions and can be altered by diseases such as glaucoma, uveitis, cancer, and physical trauma [5–7]. These lesions can cause severe morphological changes to the iris structure and modify its biomechanical properties [8, 9]. The iris structure can also be altered by drugs which can modify the normal miosis and mydriasis of the iris [10]. In addition to abnormal morphological changes, the iris also undergoes natural variations due to its function in the eye (contraction and expansion) [11]. Several studies have shown interest in determining the biomechanical properties of the iris, under different conditions (*in vivo* or *ex vivo*) using animal models [12–14] or human volunteers [11], using different techniques such as Atomic Force Microscopy (AFM) [15], Optical Coherence Tomography (OCT) [9], and Optical Coherence Elastography (OCE) [11, 14, 16]. Although AFM showed a high capacity to determine the stiffness of the iris, it had several limitations. In AFM, the iris was dissected from the eye, limiting the capacity to study diverse areas of the iris and increasing the degradation of this tissue due to its exposure. Also, during the scanning process, the AFM tip adhered to the tissue, reducing the accuracy of indentation measurements [15]. On the other hand, OCE and OCT have the capacity to determine the biomechanical properties of the iris in its natural state inside the eye.

Dynamic OCE has been widely used in several studies to map the shear or Young's modulus of biological tissues. OCE can use several non-contact approaches to generate displacements in tissue, which is an important advantage when characterizing the biomechanical properties of ocular tissues [17–19]. In ophthalmology, OCE has been extensively used since it is based on a widely adopted imaging modality, OCT, which is also non-contact, high-resolution, and highly sensitive to motion [20, 21]. Thus, OCE is rapidly gaining popularity for assessing tissue biomechanical properties [22, 23]. OCE can describe the biomechanical differences among the different tissues of the same organs, such as the detailed description of the biomechanical properties of the inner structure of the eye [20, 24–26], including the iris [11, 16]. However, these studies have not investigated the effects of intraocular pressure (IOP) changes on the stiffness of the iris. These changes of IOP might cause variations in the iris structure and elasticity, which is related to diseases such as glaucoma [27–29]. Also, prior studies have reported the existence of rotational and translational movements of the iris during changes of IOP inside the eye. These movements could cause variations in the biomechanical properties of the iris [9]. To our knowledge, previous OCE methods used to analyze the iris biomechanics did not investigate possible stiffness variations caused by IOP changes [11, 16]. The aim of this work was to demonstrate the elastic properties of the iris using an animal model (porcine eyes) at different IOPs. Here, we demonstrate that the anatomical segments of the iris possess a significant difference in their biomechanical properties, suggesting their different roles during the iris contraction and expansion and their possible function in case of an abnormal deformation.

2 Materials and Methods

2.1 Biological sample preparation

Nine porcine eyes were used in this study (Sioux-Preme Packing Co., Sioux City, IA, USA). All eyes were used during the first 24 h after enucleation. All external tissues (fat and muscles) were manually removed, and whole eye-globes were placed in a custom holder. All samples were analyzed *in situ* using a closed-loop IOP control system simulating conditions of 5, 10, 20, and 30 mmHg of IOP for each sample [30]. To achieve the artificial IOP control, the micro-infusion pump and pressure transducer were connected via tubing, which was then connected to a needle that cannulated the porcine eye-globe. For each eye sample, one additional measurement was conducted before applying the artificial IOPs. Thus, this instance of OCE measurement was undertaken at the intraocular fluid pressure inside the eye-globe. The eyes were constantly hydrated using 1X PBS before and after each OCE imaging session at every IOP condition.

2.2 OCE system setup and measurement

The schematic of the experimental acquisition setup, which is mainly composed of a phase-sensitive spectral domain OCT (SD-OCT) system and an excitation source, is shown in Fig. 1(a). The SD-OCT system used a superluminescent diode light source (Broadlighter S840-I-B-20, Superlum, Cobh Cross, Ireland) with a ~49 nm bandwidth and ~840 nm of central wavelength. In air, the lateral resolution of the OCT beam was ~8 µm, the axial resolution was ~9 µm, and the axial sampling resolution of the system was ~3 µm/pixel. For this particular study, the A-line acquisition speed was set to 50 kHz (temporal resolution Δt = 20 µs) [31].

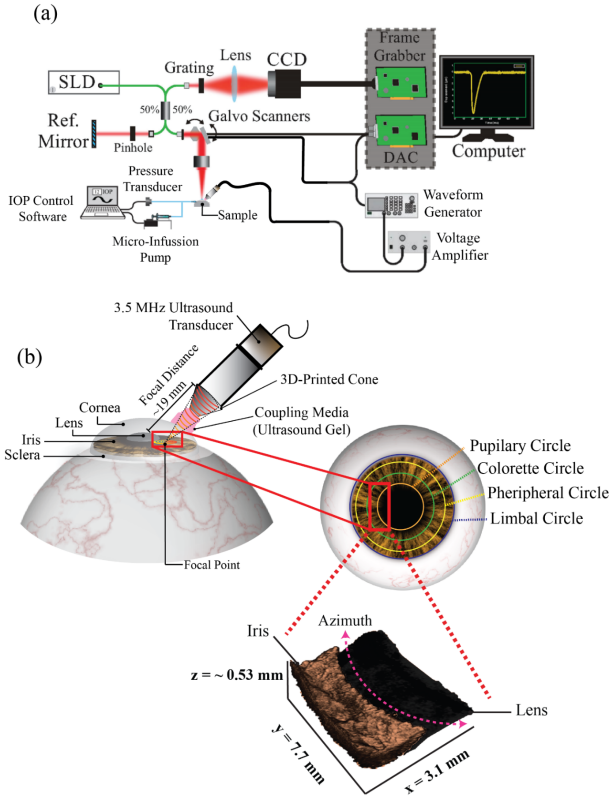


Fig. 1 (a) Schematic representation of the OCE scan setup, including the IOP control and an SD-OCT system. (b) Diagram of the scanned region using the immersion ultrasound transducer (inclined at ~45°) focused on the selected area of the iris.

The Acoustic Radiation Force (ARF) excitation used in this work was generated using an ultrasound immersion transducer with a central frequency of 3.5 MHz and a focal length of ~19 mm (V382-SU, Olympus Corp., Japan) connected to a waveform generator (DG4162, RIGOL Tech, China) and an RF signal amplifier (1040L, Electronics & Innovation Ltd., NY, USA). A custom 3D printed cone was attached to the transducer and filled with ultrasound gel (McKesson Ultrasound Gel Pink, Richmond, VA) to couple the ARF to the eye-globe. The acoustic beam was focused on the iris inside the eye, and the transducer was inclined at an angle of ~45° with respect to the OCT beam. The transducer sent an acoustic pulse that was synchronized with the OCT frame trigger for M-B mode imaging [32–34]. The acoustic excitation pulse was sent in a train

of pulses using a frequency of 1 kHz. The OCT beam was steered with a pair of galvanometer-mounted mirrors for 2D OCE acquisition. The 2D-OCE scanning on the iris was performed in two directions, radial (X-axis) and orthogonal oriented direction with respect to the radial direction (Y-axis). The Y-axis covers a section of the azimuthal orientation of the iris (i.e., near azimuthal), and hence, it will be referred to as semi-azimuthal in this paper (shown in Fig. 1(b)). The ARF-induced elastic waves were tracked during N = 251 A-line repetitions (~5 ms) in a line for Y-axis (7.7 mm) and X-axis (3.1 mm) (Fig. 1(b)). The ARF excitation was focused in the middle of the OCE field of view. Four measurements were performed for each sample at each IOP. The wave speed was quantified from the axial particle velocity, v_z, based on the depth dependent phase (φ) difference of two consecutive complex value A-lines for a given position (x_0, y_0) [35] using the following equation:

$$v_z(z,t) = \Delta\varphi(z,t)\frac{\lambda_0}{4\pi n \Delta t}, \quad (1)$$

where n was the refractive index of the sample (in this study, the refractive index of the cornea $n = 1.376$ was used) [24, 36], Δt was the temporal resolution, and $\Delta\varphi(z,t) = \varphi(z,t+\Delta t) - \varphi(z,t)$, and λ_0 was the central wavelength of the OCT system. The temporal phase change was used to extract temporal displacement changes ($\Delta d_z(z,t) = \Delta\varphi(z,t)\frac{\lambda_0}{4\pi n}$) along depth, resulting in a spatiotemporal image for each M-B mode OCT image. Subsequently, the elastic wave velocity was determined by computing the slope of the spatiotemporal images of the wave propagation [24]. At the scan area of interest, the presence of aqueous humor on the anterior surface of the iris forms a liquid-tissue interface while the posterior side of the iris rests on the lens (i.e., tissue-tissue interface) [37]. Here, a Scholte wave model is used to describe the elastic wave at the liquid-tissue interface. The velocity of shear wave (C_s) in an incompressible medium is related to the Scholte wave speed (C_{sch}) using the equation [11, 37]:

$$C_{sch} = 0.846\, C_s. \quad (2)$$

The Young's modulus (E) was estimated using the equation:

$$E = \frac{3\rho}{0.846^2} C_{sch}^2, \quad (3)$$

where ρ is the density of the iris (~1250 kg/m^3). All OCE data sets were analyzed using MATLAB R2020b (Mathworks, Inc., Natick, MA, USA).

The Student's t-test was employed to assess the statistical differences, if any, of the wave propagation speed and the iris stiffness between the semi-azimuthal and the radial directions. A one-way ANOVA was used to determine the significance of differences among the acquisition repetitions and the iris stiffness at the different IOPs. This statistical method was used in all measurements, and significant difference values are shown in the results section.

3 Results

The wave propagation in the porcine iris was quantified and compared at four artificially induced IOPs (5, 10, 20, and 30 mmHg) and in the eyeball with no intraocular pressure control. Also, we investigated the potential variation in the wave speed for two scan orientations: radial and semi-azimuthal. Figs. 2(a) and 2(f) show the OCT B-mode images, while the instantaneous wave propagation snapshots for the radial and semi-azimuthal scans are shown in Figs. 2(b) to 2(e) and 2(g) to 2(j), respectively, at the noted times after ARF excitation. For comparison purposes, a common excitation position was maintained for all samples and all IOPs for each direction. Fig. 2(a) shows the iris cross-section in the radial orientation where the transition between the dilator and sphincter regions is visible as a large bump near the middle of the OCT structural image. For all samples, two scans were performed in each orientation. In Figs. 2(a) and 2(f), the red arrows indicate the excitation positions. Hence, as shown by the colored patterns, in Figs. 2(b) – 2(e) and 2(g) – 2(j), the wave propagates in both the left and right direction with respect to the excitation position.

Fig. 3 is the box and whisker plots of the mean wave speed at IOPs of 5 mmHg, 10 mmHg, 20 mmHg, and 30 mmHg for all eye samples. In Fig. 3, the 'NAP' (i.e., no artificial intraocular pressure) indicates the additional measurement taken without any artificial IOP. The top and bottom boundaries of the box are the 25th and 75th percentiles, respectively, while the median and mean are shown by the horizontal line and dot inside the box, respectively. The whiskers extend from the 1st and 3rd quartiles to the lowest and largest wave speeds, which are indicated by an 'X'. Statistical testing by a one-way ANOVA showed no significant change in the wave speed as a function of the IOP in the radial ($F(4,48) = 1.00$, $p = 0.42$) or semi-azimuthal directions ($F(4,72) = 0.68$, $p = 0.61$).

As discussed in the methods section, two orthogonal M-B mode scans, one in the radial and the other in the semi-azimuthal orientation, were performed at each repetition. In this study, the semi-azimuthal scan was performed in the orthogonal direction to the radial orientation, and hence, the scan path does not perfectly follow the circumferential direction concentric to the curvature of the iris. But with sufficiently short lateral scan length, the measurements are sufficiently representative of the iris stiffness in the azimuthal direction. Fig. 4 shows the mean and standard deviations of wave speed as a function of IOP for all eye samples. The wave speed in the radial direction was consistently lower than that of the semi-azimuthal direction ($p < 0.001$). The Young's modulus was computed for both the radial and semi-azimuthal wave speed measurements. Table 1 shows the summary of the mean and standard deviations of the wave speed and Young's modulus at the five IOPs.

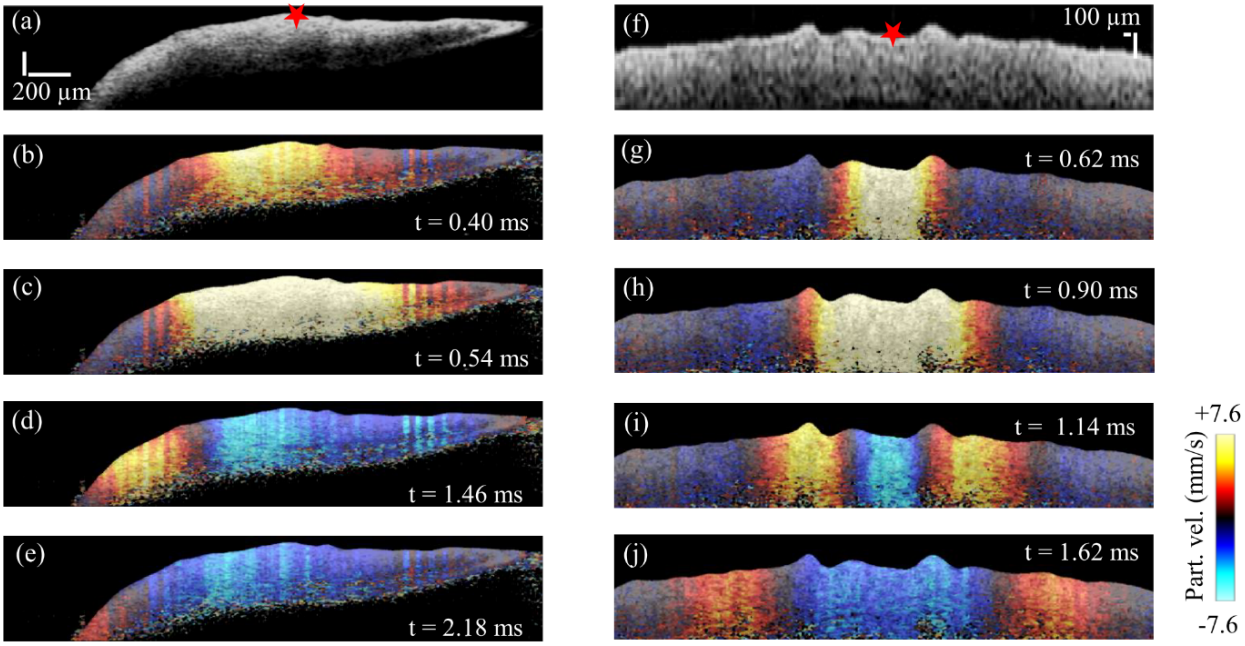


Fig. 2 Representative *ex vivo* OCT structural images of porcine iris scanned in (a) radial and (f) semi-azimuthal directions. The colored images in (b) to (e) and (g) to (j) show particle velocity snapshots extracted at the noted times after 1 kHz ARF excitation in the radial and semi-azimuthal directions, respectively. The excitation points are indicated by the red star in (a) and (f). In the color bar, Part. vel. refers to axial particle velocity in mm/s.

Table 1 Inter-sample mean and standard deviation of Scholte wave speed and Young's modulus at different IOPs (N = 9 samples). SD stands for standard deviation.

	Radial		Semi-azimuthal	
IOP (mmHg)	**Elastic wave speed Mean ± SD (m/s)**	**Young's Modulus Mean ± SD (kPa)**	**Elastic wave speed Mean ± SD (m/s)**	**Young's Modulus Mean ± SD (kPa)**
NAP	1.56 ± 0.52	14.25 ± 8.65	2.32 ± 0.40	28.95 ± 9.22
5	1.65 ± 0.63	16.42 ± 12.77	2.62 ± 0.63	37.95 ± 18.90
10	1.59 ± 0.56	14.92 ± 10.19	2.65 ± 0.65	39.01 ± 18.72
20	1.20 ± 0.42	8.45 ± 5.59	2.46 ± 0.46	32.81 ± 13.99
30	1.61 ± 0.51	14.87 ± 9.50	2.48 ± 0.61	34.09 ± 17.62
Mean	1.52 ± 0.53	13.78 ± 9.34	2.50 ± 0.55	34.56 ± 15.69

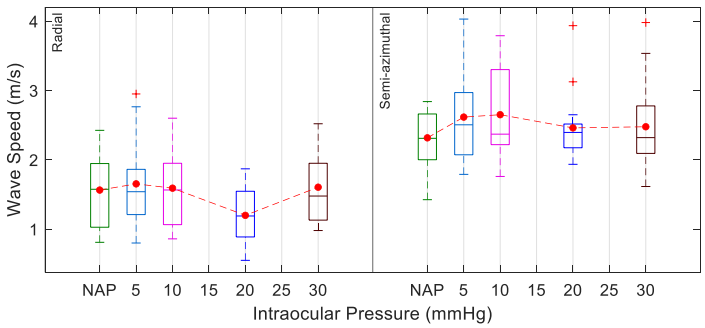


Fig. 3 Box-whisker plot of the mean wave speed for (a) radial and (b) semi-azimuthal OCE measurements in porcine iris at different IOPs. NAP = no artificial intraocular pressure and number of eye samples. N = 9. The red plus ('+') signs indicate outliers in each data set.

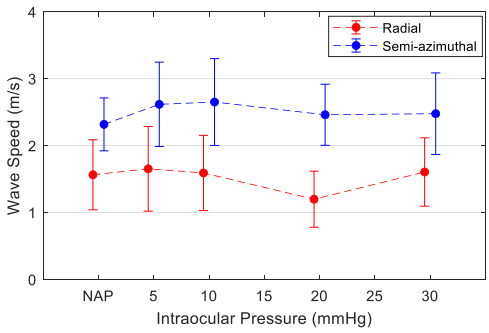


Fig. 4 Mean wave speed comparison between radial and semi-azimuthal orientation. NAP = no artificial intraocular pressure, and the number of eye samples, N = 9.

4 Discussion

One of the main findings of this study was the demonstration that the effect of intraocular pressure on the wave propagation speed in the iris was not significant for either radial or semi-azimuthal directions (Fig. 2).

Despite the similarity in the wave speed trends shown in Fig 3, it appears that the IOP effect on the speed in both the radial and semi-azimuthal orientations is minimal. From this point of view, the iris behavior is similar to the behavior of the crystalline lens under IOP elevation and can be explained by low deformation of these parts of the eye located inside the eye-globe [26, 38–40]. Therefore, hyperplastic properties of the iris and lens do not play a significant role in the wave propagation – in opposite to the cornea and sclera. Lee et al. [9] used OCT imaging to measure the changes in the iris deformation and then quantified iris biomechanical properties with numerical simulations based on the OCT measurements. Their results also showed that there was no consistent trend in the change with iris radial length over different IOPs for murine iris. However, the numerical simulation was produced assuming an isotropic iris and hence, does not reliably reflect the effect of IOP on iris anisotropy as our measurements show a significant degree of elastic anisotropy in the iris.

The current work has shown that the elastic wave speed and hence, the stiffness of the iris is different in the radial and semi-azimuthal orientations. Firstly, the estimated Young's modulus of elasticity in both orientations (Table 1) is comparable to the elasticity of most smooth muscles (i.e. 6 kPa to 2.08 MPa) [41]. Secondly, the higher semi-azimuthal Young's modulus, as compared to the radial Young's modulus, is in agreement with the findings in the previous works [41]. However, to the best of our knowledge, this is the first OCE-based measurement to demonstrate the existence of a significant difference in iris stiffness in the radial and semi-azimuthal orientations. As shown in Fig. 4, the wave speed in the semi-azimuthal orientation is consistently higher. Contrary to the assumptions in some prior studies [11], these results demonstrate the elastic anisotropy of the iris, which is intuitively attributed to the anatomical structure of the dilator and sphincter muscles. The change in the biomechanical properties of these muscles is a common factor for primary angle closure glaucoma [8, 15]. Thus, the accurate quantification of iris elasticity might be used as a potential biomarker of certain eye diseases (e.g., glaucoma) and may help to devise targeted treatment methods. With its high spatial and temporal resolutions and high displacement sensitivity, phase-sensitive OCE promises to be an excellent diagnostic tool for clinical translation to accurately assess the biomechanical properties of the fine muscle fibers of the iris.

In the recent development of OCE-based iris stiffness quantification, Ye et al. [11] employed air-puff for non-contact excitation of elastic waves in the iris. The excitation method avoids the use of an ultrasound gel between the tip of the ARF transducer and the eye-globe. However, unlike the ARF method in which a focused acoustic beam can be directed to the target tissue, the air-puff method does not enable a localized excitation and thus, results in wave motion in various sections of the eye-globe. Moreover, the limited bandwidth afforded by the air puff limits the mechanical resolution and is heavily influenced by the boundary conditions. In earlier OCE-based iris stiffness studies, human [11] and rabbit [16] subjects were used while excised porcine eyeballs were employed for our study, and thus, these might have contributed to the difference in the wave speed results among the three studies.

However, it is important to note the limitations of the current study. Though the semi-azimuthal and radial measurements provided insight into the anisotropic nature of the iris, more accurate elasticity characterization of the dilator and sphincter muscles could be achieved by performing full azimuthal scans in these two regions of the iris. *In situ* studies for various iris colors and different age groups would provide a broader understanding of the iris biomechanical properties. Although a coupling media was utilized in this work, previous work has shown that contact with ocular tissues is well tolerated for brief times even without topical anesthetics [42].

The model of wave propagation used to evaluate Young's modulus in the iris has significant limitations because of the small thickness of the iris (mean thickness of iris in this study was 0.527 mm), and the effect of the contact between the iris and the crystalline lens. While in the model the iris is considered as a homogeneous elastic half-space, such assumption is an obvious simplification and a comprehensive model should include the effects of the lens, anisotropic nature of the iris, viscosity and finite thickness of the iris. Future work will involve the development of an appropriate wave model that incorporates the complex iris biomechanics and geometry.

5 Conclusion

The iris is a fundamental organ in the eye with the crucial role of controlling the amount of light that passes through the lens to the retina. The anatomy of the iris controls the dynamics of contraction and expansion, dominating the biomechanical properties of this tissue structure. In this study, we have shown the changes of the biomechanical properties among the different anatomical parts of the iris, supporting the conclusion that the iris is an anisotropic tissue with different viscoelastic properties in the sphincter, collarette, and dilator muscles. In addition to these changes of the biomechanical properties, the iris is able to keep its shape and properties, even if the ocular globe is under mechanical stress (in this study, the mechanical stress is caused by the internal changes of IOP in the eye). In conclusion, our results suggest that the most significant changes of the biomechanical properties of the iris are related to its anatomical changes caused by natural conditions (contraction and dilation because of variation in the light of the environment) or abnormal modifications (presence of tumors, diseases, or other non-natural modifications). These results suggest the potential use of

OCE to evaluate iris biomechanical properties for disease detection or screening.

Disclosures

All authors declare that there is no conflict of interests in this paper.

Acknowledgments

The authors would like to thank the support provided by NIH grants R01EY022362, R01EY030063, P30EY007551.

References

1. F. Jan, N. Min-Allah, S. Agha, I. Usman, and I. Khan, "A robust iris localization scheme for the iris recognition," Multimedia Tools and Applications, Multimedia Tools and Applications 80(3), 4579–4605 (2021).
2. J. Bloom, M. Motlagh, and C. N. Czyz, "Anatomy, Head and Neck, Eye Iris Sphincter Muscle," In StatPearls, StatPearls Publishing, Treasure Island (2018).
3. K. T. Moazed, The Iris: Understanding the Essentials, Springer Nature, Switzerland (2020). ISBN: 978-3-030-45755-6.
4. L. Di Cecilia, F. Marazzi, and L. Rovati, "A hyperspectral imaging system for the evaluation of the human iris spectral reflectance," Proceedings of SPIE 10045, 100451S (2017).
5. I. Georgalas, P. Petrou, D. Papaconstantinou, D. Brouzas, C. Koutsandrea, and M. Kanakis, "Iris cysts: a comprehensive review on diagnosis and treatment," Survey of Ophthalmology 63(3), 347–364 (2018).
6. W. Xue, S. Lin., X. Chen, Y. Jia, X. Fang, Y. Suo, Y. Ma, Y. Wang, and H. Zou, "In vivo noninvasive imaging and quantitative analysis of iris vessels," Ophthalmic Research 64(5), 754–761 (2021).
7. Z. Da Soh, S. Thakur, S. Majithia, M. E. Nongpiur, and C. Y. Cheng, "Iris and its relevance to angle closure disease: a review," British Journal of Ophthalmology 105(1), 3–8 (2021).
8. J. Hao, H. Fu, Y. Xu, Y. Hu, F. Li, X. Zhang, J. Liu, and Y. Zhao, "Reconstruction and Quantification of 3D Iris Surface for Angle-Closure Glaucoma Detection in Anterior Segment OCT," In International Conference on Medical Image Computing and Computer-Assisted Intervention, Springer, Cham, 704–714 (2020).
9. C. Lee, G. Li, W. D. Stamer, and C. R. Ethier, "In vivo estimation of murine iris stiffness using finite element modeling," Experimental Eye Research 202, 108374 (2021).
10. N. Rashidi, A. D. Pant, S. D. Salinas, M. Shah, V. S.Thomas, Ge Zhang, S.Dorairaj, and R. Amini, "Iris stromal cell nuclei deform to more elongated shapes during pharmacologically-induced miosis and mydriasis," Experimental Eye Research 202, 108373 (2021).
11. S. Ye, Y. Zhou,C. Bao,Y. Chen, F. Lu, and F. Lu, "In vivo non-contact measurement of human iris elasticity by optical coherence elastography," Journal of Biophotonics 14(9), e202100116 (2021).
12. J. E. Whitcomb, R. Amini, N. K. Simha, and V. H. Barocas, "Anterior–posterior asymmetry in iris mechanics measured by indentation," Experimental Eye Research 93(4), 475–481 (2011).
13. Y. Lei, K. Zhang, C. Chen, H. Song, T. Lin, and Z. Liu, "Experimental research on the mechanical properties of porcine iris," Clinical Biomechanics 23, S83–S87 (2008).
14. R. K. Tan, X. Wang, A. S. Y. Chan, M. E. Nongpiur, C. Boote, S. A. Perera, and M. J. A. Girard, "Permeability of the porcine iris stroma," Experimental Eye Research 181, 190–196 (2019).
15. A. Narayanaswamy, M. H. Nai, M. E. Nongpiur, H. M. Htoon, A. Thomas, T. Sangtam, C. T. Lim, T. T. Wong, and T. Aung, "Young's modulus determination of normal and glaucomatous human iris," Investigative Ophthalmology & Visual Science 60(7), 2690–2695 (2019).
16. Y. Zhu, Y. Zhang, G. Shi, Q. Xue, X. Han, S. Ai, J. Shi, C. Xie, and X. He, "Quantification of iris elasticity using acoustic radiation force optical coherence elastography," Applied Optics 59(34), 10739–10745 (2020).
17. M. Singh, A. Nair, S. Aglyamov, and K. V. Larin, "Compressional Optical Coherence Elastography of the Cornea," Photonics 8(4), 111 (2021).
18. V. Y. Zaitsev, A. L. Matveyev, L. A. Matveev, A. A. Sovetsky, M. S. Hepburn, A. Mowla, and B. F. Kennedy, "Strain and elasticity imaging in compression optical coherence elastography: The two-decade perspective and recent advances," Journal of Biophotonics 14(2), e202000257 (2021).
19. V. Y. Zaitsev, A. L. Matveyev, L. A. Matveev, E. V. Gubarkova, A. A. Sovetsky, M. A. Sirotkina, G. V. Gelikonov, E. V. Zagaynova, N. D. Gladkova, and A. Vitkin, "Practical obstacles and their mitigation strategies in compressional optical coherence elastography of biological tissues," Journal of Innovative Optical Health Sciences 10(06), 1742006 (2017).
20. M. A. Kirby, I. Pelivanov, S. Song, L. Ambrozinski, S. J. Yoon, L. Gao, D. Li, T. T. Shen, R. K. Wang, and M. O'Donnell, "Optical coherence elastography in ophthalmology," Journal of Biomedical Optics 22(12), 121720 (2017).
21. V. S. De Stefano, M. R. Ford, I. Seven, and W. J. Dupps Jr., "Live human assessment of depth-dependent corneal displacements with swept-source optical coherence elastography," PLoS One 13(12), e0209480 (2018).

22. B. F. Kennedy, P. Wijesinghe, and D. D. Sampson, "The emergence of optical elastography in biomedicine," Nature Photonics 11(4), 215–221 (2017).
23. K. V. Larin, D. D. Sampson, "Optical coherence elastography–OCT at work in tissue biomechanics," Biomedical Optics Express 8(2), 1172–1202 (2017).
24. F. Zvietcovich, A. Nair, M. Singh, S. R. Aglyamov, M. D. Twa, and K. V. Larin, "Dynamic Optical Coherence Elastography of the Anterior Eye: Understanding the Biomechanics of the Limbus," Investigative Ophthalmology & Visual Science 61(13), 7 (2020).
25. R. Wallace, M. Kirby, L. Gao, S. Song, I. Pelivanov, K. Zhou, R. K. Wang, M. O'Donnell, and T. Shen, "Time-resolved detection of corneal UV Collagen Cross-linking (CXL) using Non-contact Optical Coherence Elastography (OCE)," Investigative Ophthalmology & Visual Science 60(9), 6831–6831 (2019).
26. Y. Li, J. Zhu, J. J. Chen, J. Yu, Z. Jin, Y. Miao, A. W. Browne, Q. Zhou, and Z. Chen, "Simultaneously imaging and quantifying in vivo mechanical properties of crystalline lens and cornea using optical coherence elastography with acoustic radiation force excitation," APL Photonics 4(10), 106104 (2019).
27. S. Jouzdani, R. Amini, and V. H. Barocas, "Contribution of different anatomical and physiologic factors to iris contour and anterior chamber angle changes during pupil dilation: theoretical analysis," Investigative Ophthalmology & Visual Science 54(4), 2977–2984 (2013).
28. H. A. Quigley, "Iris cross-sectional area decreases with pupil dilation and its dynamic behavior is a risk factor in angle closure," Journal of Glaucoma 18(3), 173–179 (2009).
29. F. Aptel, P. Denis, "Optical coherence tomography quantitative analysis of iris volume changes after pharmacologic mydriasis," Ophthalmology 117(1), 3–10 (2010).
30. M. D. Twa, J. Li, S. Vantipalli, M. Singh, S. Aglyamov, S. Emelianov, and K. V. Larin, "Spatial characterization of corneal biomechanical properties with optical coherence elastography after UV cross-linking," Biomedical Optics Express 5(5), 1419–1427 (2014).
31. S. Wang, K. V. Larin, "Noncontact depth-resolved micro-scale optical coherence elastography of the cornea," Biomedical Optics Express 5(11), 3807–3821 (2014).
32. S. Wang, K. V. Larin, "Shear wave imaging optical coherence tomography (SWI-OCT) for ocular tissue biomechanics," Optics Letters 39(1), 41–44 (2014).
33. F. Zvietcovich, M. Singh, Y. S. Ambekar, S. R. Aglyamov, M. D. Twa, and K. V. Larin, "Micro Air-Pulse Spatial Deformation Spreading Characterizes Degree of Anisotropy in Tissues," IEEE Journal of Selected Topics in Quantum Electronics 27(4), 1–10 (2020).
34. J. R. Rippy, M. Singh, S. R. Aglyamov, and K. V. Larin, "Ultrasound Shear Wave Elastography and Transient Optical Coherence Elastography: Side-by-Side Comparison of Repeatability and Accuracy," IEEE Open Journal of Engineering in Medicine and Biology 2, 179–186 (2021).
35. F. Zvietcovich, J. P. Rolland, J. Yao, P. Meemon, and K. J. Parker, "Comparative study of shear wave-based elastography techniques in optical coherence tomography," Journal of Biomedical Optics 22(3), 035010 (2017).
36. K. M. Meek, C. Knupp, "Corneal structure and transparency," Progress in Retinal and Eye Research 49, 1–16 (2015).
37. W. M. Ewing, W. S. Jardetzky, and F. Press, "Elastic waves in layered media," Graw-Hill Book Company, USA (1957).
38. C. Wu, S. R. Aglyamov, H. Zhang, and K. V. Larin, "Measuring the elastic wave velocity in the lens of the eye as a function of intraocular pressure using optical coherent elastography," Quantum Electronics 49(1), 20 (2019).
39. S. Park, H. Yoon, K. V. Larin, S. Y. Emelianov, and S. R. Aglyamov, "The impact of intraocular pressure on elastic wave velocity estimates in the crystalline lens," Physics in Medicine & Biology 62(3), N45 (2017).
40. C. Wu, S. R. Aglyamov, Z. Han, M. Singh, C.-H. Liu, and K. V. Larin, "Assessing the biomechanical properties of the porcine crystalline lens as a function of intraocular pressure with optical coherence elastography," Biomedical Optics Express 9(12), 6455–6466 (2018).
41. J. Heys, V. Barocas, "Mechanical characterization of the bovine iris," Journal of Biomechanics 32(9), 999–1003 (1999).
42. A. M. G. Baptista, R. A. R. C. De Sousa, P. M. Serra, C. M. D. S. Abreu, and C. M. L. R. Da Silva, "Evaluation of discomfort of Goldmann tonometry without anaesthetic," Ophthalmic and Physiological Optics 30(6), 854–859 (2010).

Laser Applications for Estimation of Microbial Activity and Investigation of NIR Skin Autofluorescence

Alexey Lihachev[1], Dmitrijs Bļizņuks[2], Jānis Liepiņš[3], and Ilze Lihacova[1]

[1] University of Latvia, Institute of Atomic Physics and Spectroscopy, Biophotonics Laboratory, 3 Jelgavas str., Riga LV-1004, Latvia

[2] Riga Technical University, Faculty of Computer Science and Information Technology, 10 Zunda krastmala, Riga LV-1050, Latvia

[3] University of Latvia, Institute of Microbiology and Biotechnology, 1 Jelgavas str., Riga LV-1004, Latvia

*** e-mail:** aleksejs.lihacovs@lu.lv

Abstract. The presented paper demonstrates the ongoing results of the joint research of University of Latvia and Riga Technical University aimed at the development of new laser based optical methods and technologies for fast evaluation of microbial activity in solid media. The second part of the paper represents the results of joint research conducted together with Katya Borisova during our visit to the Institute of Electronics, Bulgarian Academy of Sciences (Bulgaria, Sofia). © 2021 Journal of Biomedical Photonics & Engineering.

Keywords: laser speckles; microorganisms; near infrared skin autofluorescence; melanoma cells.

Paper #3454 received 23 Aug 2021; revised manuscript received 20 Sep 2021; accepted for publication 23 Sep 2021; published online 4 Nov 2021. doi: 10.18287/JBPE21.07.040305.

1 Introduction

1.1 Laser speckle imaging for microorganisms' growth analysis in solid media

Enumeration of live microbial cells in the sample is one of the basic quantitative measurements in microbiology. Currently counting microorganisms in the early stages of colony formation is possible only by microscope, which is limited to small sample areas. Also, determination of colony size increase dynamics (microorganism growth speed estimation) is an extremely labor-intensive task. Automated counting is possible only by using regular cameras that are limited in optical resolution and therefore are capable of detecting signs of microbial colonies only after a certain size threshold is reached (minimal diameter 0.2 mm and / or 8–22 h). Therefore, the development of new cost-effective methods for *in situ* estimation of microorganisms' activity to reduce detection time and labor expenses raise a great practical interest for the scientists and technology developers. One of the options for the fast and early evaluation of microorganisms' activity is a non-contact optical technique called laser speckle contrast imaging. Laser speckle is an interference pattern produced by coherent light reflected or scattered from different parts of the illuminated surface. In the case of non-moving, static scatters, the scattered light generates constant laser speckle patterns. However, if scatterers are spontaneously moving (e.g., Brownian motion, bacteria doubling and chemotaxis) such as particles in a fluid, the individual speckle appears to be "twinkle" or "boiling". This phenomenon is called a "time-varying speckle". Regarding this phenomenon, the laser speckle imaging technique has been proved to monitor moving particles in optically inhomogeneous media by analyzing time-varying laser speckle patterns. Thereby, the analysis of laser speckles patterns provides a powerful opportunity for quantifying the movement activity at the micro and macroscale. Literature data points to the significant progress and potential applications of laser speckle imaging technique to evaluate the dynamic processes in microbiological media. Technology using speckle decorrelation time maps has been demonstrated for the detection of *E. coli* and *B. cereus* on a meat (chicken breast) [1]. Speckle analysis has also been applied to biomass growth kinetic measurements in liquid culture, characterization of Colony Forming Units (CFU) morphology, determination of antibiotic susceptibility [2–5]. As well as laser speckle imaging techniques in combination with Deep Learning (DL) and Artificial Neural Networks (ANN) have demonstrated a fast system response of antibacterial susceptibility evaluation in MIC (Minimum Inhibitory Concentration) tests [6]. In the presented paper, we will prove that dynamic laser speckle

image analysis methods can be used to detect and predict the CFU of different microbes in solid media.

1.2 Investigation of Near Infrared Autofluorescence under continuous laser excitation

The phenomenon of autofluorescence in the near infrared region (NIR AF) under continuous laser excitation was described by many authors. The first mention of NIR AF was described by Z. Huang et al. [8] where the NIR AF was analyzed during Raman spectroscopy investigations under 785 nm excitation. Authors demonstrate promising sensitivity of NIR AF intensity analysis for evaluation of pigmented lesions, as well as, demonstrated applications for melanoma diagnostics. The physical explanation of the NIR AF and its origin are still under discussion, mainly it can be described by absence of absorption spectra of main tissue fluorophores in the NIR region. Several hypotheses describing this phenomenon are discussed in literature, mainly attributing NIR AF to the melanin, endogenous porphyrins and lipofuscin [9–11]. Analysis and detection of NIR AF is a challenging task, since the NIR AF intensity usually is very weak and requires a high sensitivity detecting system equipped with high >8 OD filters. The artefacts caused by reflected laser light significantly complicate the adequate detection of the NIR AF from living tissues. In presented research we have tried to investigate the phenomenon of NIR AF. The experiments were conducted in close collaboration with Ekaterina Borisova during our secondment to the Institute of Electronics, Bulgarian Academy of Sciences. The obtained results and discussion are described below.

2 Material and methods

2.1 Laser speckle imaging system

The system was assembled for burst capturing of macro scale images under white light and laser illumination. The optical measurement system consists of a laser source, white light source LED, 35mm CS lens @F18, optical attenuator, a testing agar plate (with inoculated bacteria) and a CMOS camera (Fig. 1). The laser speckles were generated by a linearly polarized 635 nm diode pumped solid state laser (output power 50 mW). To achieve optimal exposure for image capturing as well as to avoid heating effects of illuminated plate the optical attenuator was used enabling 3–5 mW/cm^2 power density of the scattered laser light on the whole agar plate surface. Main components of the system are presented in Fig. 1. The speckle images with 10 MPix resolution were captured by a CMOS camera with different frame rates, for different experiments: 1 frame per 2, 5, 6, 10, 20, or 30 sec, and different durations of experiments about 10–25 h. The white light LED illumination was used for acquisition of RGB images of growing bacteria colonies. Further RGB images was used for referential visual determination of bacteria colonies.

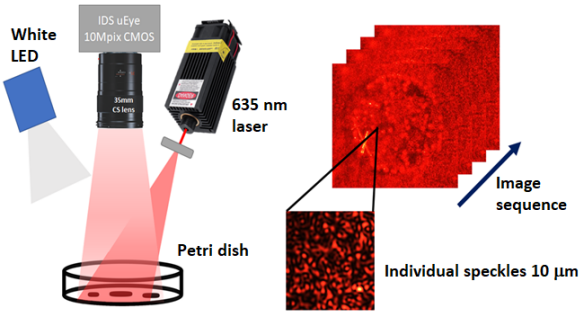


Fig. 1 Setup scheme for burst image capturing of bacteria growing process under 635 nm laser and white LED illumination.

2.1.1 Evaluation of colony growth under white light illumination

Microbial growth on the agar surface and formation of colony is a self-limiting process which starts with the maximum rate, which is gradually inhibited by exhaustion of necessary nutrients, accumulation of end products of microbial metabolism. The most common mathematical model describing microbial colony growth is the Gompertz model, which mathematical expression is presented in Eq. (1).

$$\mu(t) = \mu \cdot e^{-\mu_i(t-t_0)}, \quad (1)$$

where μ is specific growth rate (h^{-1}), μ_0 – specific growth rate at beginning of colony formation (h^{-1}), μ_i – specific growth rate at infliction (or specific inhibitory rate), t_0 represents time at beginning of the colony growth and t is the actual time (h).

$$r(t) = r_{max} \cdot e^{-\left(ln\left(\frac{r_{max}}{r_0}\right)\cdot e^{-\left(\mu_i\cdot(t-t_0)\right)}\right)}. \quad (2)$$

Eq. (2) shows the growth of the colony radius, where r_{max} is the maximal radius that the colony can reach in the given environmental conditions, r_0 is the initial radius at t_0, μ_i is the specific growth rate at the inflexion point of the area curve. Over time gradual inhibition of colony growth occurs, which can be described by μ_i. To use these equations to simulate growth of real CFU, μ_0 and μ_i should be found. A specific set of parameters should be found to describe microbial colony growth using the Gompertz model. It was done experimentally for each microbial species and cultivation conditions (temperature and media). Fast growing sea bacteria *Vibrio natriegens* were chosen for the experiments. Bacteria were grown on salt rich, agar plates in room temperature (see the materials and methods section). First, the series of micro images were used to find the growth rate at the beginning of CFU formation (when colony growth rate is practically equal to μ_0). Thus, μ_0 for *V. natriegens* in the room temperature was determined approximately 3.875 ± 0.25 h^{-1}. Also, a series of CFU images under white light were taken to experimentally find the specific *V. natriegens* CFU inhibitory rate (μ_i). For this purpose,

the growth of the *V. natriegens* CFU was recorded (one image in 15 min, from 0 to 20 h or more) to estimate the growth of the colony radius under white light illumination. The diameter of each CFU was determined from images using the ImageJ program. The CFU was identified from images by visual inspection (without photo enhancing). Due to the low cell concentrations, the contrast of RGB images under white light illumination was low and CFU diameters were determined not earlier than after 8–12 h. Colony diameters were determined from the image series over time. Using Eq. (2) the μ_i for *V. natriegens* were calculated at given temperature and media conditions. Example of obtained results under white light illumination presented in Fig. 4 (white light experiments curves 1–4).

$$RMSE = \sqrt{\frac{1}{n}\sum_{i=1}^{n}\left(R_{Gompertz}[i] - R_{measured}[i]\right)^2}. \quad (3)$$

According to the experimentally obtained colony results, we set maximum colony radius to be 170 pix and initial colony radius (r_0) 0.1 pix (1 pix equals 5 μm). When simulating μ_i for *V. natriegens* in the room temperature for the given colony growth, the μ_i was 0.11 h^{-1}. However, μ_i is not a fixed number. This coefficient characterizes decreasing of the colony growth rate over the time. The colony growth rate is dependent on many factors such as: temperature, number of surrounding colonies, and local concentration gradient of nutrients. Usually, the μ_i can vary by 20–50% among the same organism. To extract parameters from the given experimental data set, parameter scan was used. As a criterion we used Root Mean Square Error (RMSE) to minimum Eq. (3) to find μ_i and t_0. Where $R_{Gompertz}$ is the radius estimated from the Gompertz model, $R_{measured}$ is the radius determined experimentally, n is the number of measurement points. RMSE values can vary in each experiment as they represent a match between theoretical and experimental curves.

2.1.2 Evaluation of colony growth by the processing of laser speckle time series images

For the analysis of speckle images, the growth of the *V. natriegens* colony under laser light illumination was recorded. The time interval between subsequent frames was 30 sec, which corresponds to a sampling frequency of 33.3 mHz. The frequency domain of the observed signal is up to 16.7 mHz. According to our previous research described in paper [12, 13] "signal" (or time signal) represents the result of the correlation and interpolation algorithm between each pair of consecutive speckle image frames. Further, the scatter of the specific growth rate μ_i, with the average experimental value of 0.17 h^{-1} (Fig. 3) was calculated. To obtain a curve representing growth of colony radius the following steps on processing of speckle images were performed: 1) the location of the colonies was manually marked and automatically divided into 20 × 20 pix sections; 2) converting each 20 × 20 pix section into a time series; 3) determination of signal threshold and rising time at low frequencies according to Eq. (4):

$$spectrogram[k,f] = |STFT[k,f]|^2, \quad (4)$$

where $STFT[k,f]$ is the Fourier transform of $sig[n]\cdot w[n-k]$, a complex function representing the phase and magnitude of the signal over time and frequency; 4) marking and determination of the times and spatial locations of detected signals; 5) marking the growth start times of each 20 × 20 pix square, knowing the location of each square in space and its distance from the colony center (marked manually in step 1), finally the colony radius was calculated as a function of time (Fig. 3, red line). In general, the above-mentioned processing approach determines time events that characterize dynamic changes in speckle signals for all spatial sections (20 × 20 pix each) throughout the whole experimental data set.

2.2 Detection and processing of NIR autofluorescence under 785 nm laser excitation

The spectral measurements were conducted by an experimental spectroscopic system for analysis of AF emission under 785 nm laser excitation. The experimental setup comprises a diode laser (785 nm, 100 mW, CW), a USB 4000 portable spectrometer (3.5 nm resolution, Ocean Optics, Inc., Dunedin, USA), 400 μm fiber-optic probe, and a computer (Fig. 2). To block the reflected laser light in-line filter holder with 810 nm long pass filter was used. The diameter of laser spot on the measurement surface (skin, cuvette, samples) was approximately 4 mm^2. Experimental setup was used for detection of AF emission from cells cultures, *ex vivo* formalized skin lesion samples and *in vivo* skin.

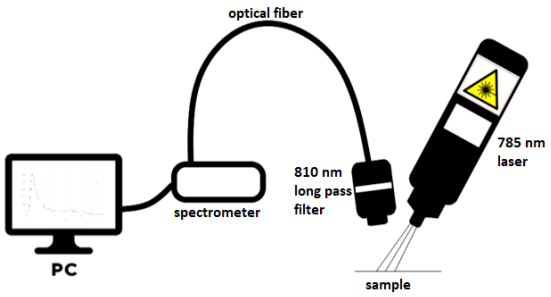


Fig. 2 Experimental setup for detection and analysis of NIR AF under 785 nm continuous laser excitation. Setup comprises CW laser with output power 100 mW, optical probe with 810 nm long pass filter (OD > 4), optical fiber, spectrometer, and computer.

For cells experiments each cell culture (b16f10 and DC-3F) line was cultivated in growth DMEM (Sigma-Aldrich, St. Louis, USA) medium containing 10% fetal bovine serum (Sigma-Aldrich, St. Louis, MO, USA), 1% L-glutamine solution (Invitrogen Inc., Carlsbad, CA,

USA). The cells were grown in 96 mm culture dish (TPP, Trasadingen, Switzerland) at 37 °C in humidified 5% CO_2 atmosphere in the incubator. After trypsinization, cells were suspended in medium (0.25 M glucose, 1 mM $MgCl_2$, 10 mM Na_2HPO_4 (pH 7.4)) at a concentration of ~3 Mio cells/ml. After the preparation, the cells suspension was filled to the quartz cuvette (filling volume 3.5 ml, pathlength 1 cm) for further detection of NIR AF emission. The detection of NIR AF emission was performed separately for each cell culture suspension. Spectrometer integration time for collection of AF and dark signal was set to 10 sec. Dark signal was acquired from the media (0.25 M glucose, 1 mM $MgCl_2$, 10 mM Na_2HPO_4 (pH 7.4)) containing no cells. The distance between fiber probe and measurement cuvette was set to 4 mm, the diameter of the laser spot on cuvette surface was 4 mm^2.

For the detection of AF spectra from formalinized *ex vivo* skin lesion samples the 5 sec integration time was used. For each *ex vivo* sample, three spectra from the lesion area and three spectra from the surrounding healthy skin were collected. Further, all collected spectra were averaged and divided to the two groups: pigmented lesions and healthy skin. As result, the averaged spectra of pigmented lesions and healthy skin were depicted in the graph. In total, 10 *ex vivo* samples were included in the study: 3 melanomas, 3 dysplastic nevi and 4 dermal nevi.

For the *in vivo* experiments the same experimental setup was used. The spectra were collected from the outside part of fingertips where melanin concentration is higher. In total, 3 healthy 30–40 years old persons with different skin phototypes were participated in the study. To minimize intensity fluctuations three AF spectra were collected on the outside of fingertips and further averaged. Averaged spectra were normalized to the AF maximum value at 825 nm. According to the geometry of experimental setup the laser spot diameter on the skin surface was approximately 4 mm^2, providing optical density ~250 mW/cm^2. To avoid painful effects caused by heating the laser exposition time was minimized to 1 sec.

3 Results and discussion

3.1 Microbial growth analysis

Fig. 3 shows the colony radius growth as a function of time for speckle image obtained according to the Gompertz model (Eg. 2). Using the scanning method for several parameters (growth rate, growth start time, maximum radius of colony) it is possible to get the most optimal suitable Gompertz curve in which the Root Mean Square Error value will be minimal. The numerous experiments were performed using speckle imaging technique and image analysis under white light illumination (see results in Fig. 4) to understand the typical signal dynamics of *V. natriegens* colony growth.

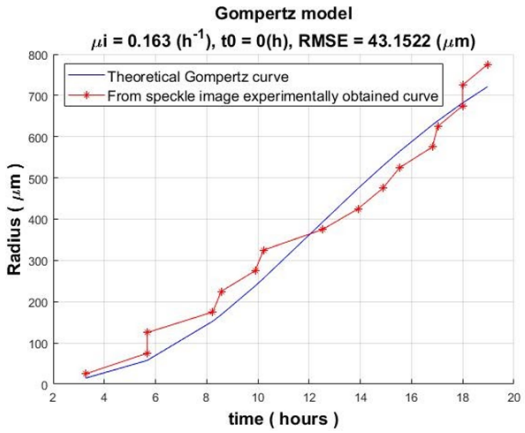


Fig. 3 *V. natriegens* colony radius obtained by speckle image experiment (red) and theoretical Gompertz curve (blue).

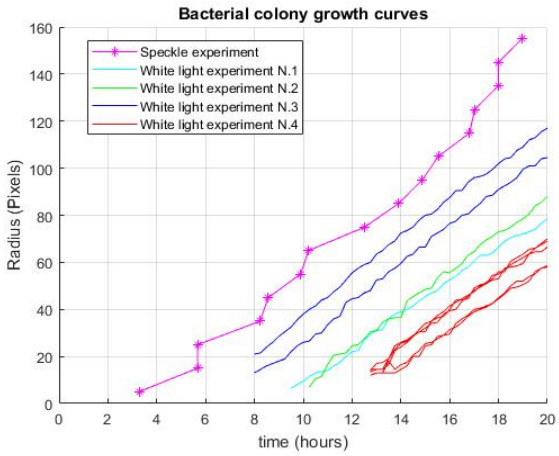


Fig. 4 Comparison of growth curves of a colony of bacteria *V. natriegens* measured by analysis of laser speckle images and visual examination under white light illumination.

Comparing these two (laser speckle and white light imaging) analyses techniques, it was obtained that with the speckle imaging technique it is possible to detect microbial activity earlier than using white light imaging. The colony formation on the agar media was observed 3 h after bacterial inoculation, while the CFU growth of the colony in white light could be detected after 8–13 h. All signals depicting CFU growth (obtained from speckle and white light images) demonstrate similar dynamics (the graphs of radius increase over time are parallel to each other). However, the growth signal graphs are scattered across *OX*-axes, which can be attributed to fluctuated room temperature across the experiments thus affecting growth speed and colony detection. To conclude, the proposed method based on analysis of laser speckle time series images provides earlier responses of growing bacteria in comparison with classical CFU growth detection under white light illumination. The results (growing curves) demonstrate wide distribution which can be attributed to unstable ambient temperature, which fluctuated across the experiments and therefore altered growth speed. Undoubtedly, further additional

studies performed in a controlled microbiological environment are necessary.

3.2 Analysis of NIR autofluorescence under 785 nm laser excitation

The practical use of NIR AF for tissue characterization and diagnostics has a great scientific interest. Moreover, the exact determination of endogenous fluorophores responsible for NIR AF emission is still under discussion. In this paper, in collaboration with Ekaterina Borisova, we have conducted series of experiments in different conditions to find spectral features suitable for skin diagnostics. NIR AF experiments were performed at in-vitro cells cultures, at *in vivo* skin and formalinized skin lesion *ex vivo* samples.

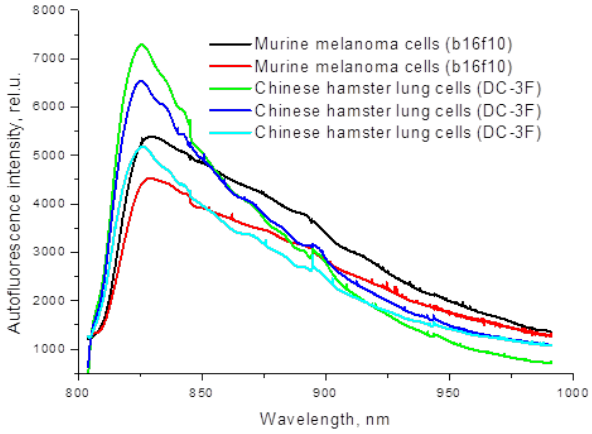


Fig. 5 NIR AF spectra obtained from melanocytic (murine melanoma cells) and melanocytic (Chinese hamster lung cells) cells under 785 nm laser excitation.

NIR AF spectra obtained from two different types of cells is presented in Fig. 5. As shown, all obtained AF spectra has a wide intensity distribution, and can be characterized by main maxima at ~825 nm.

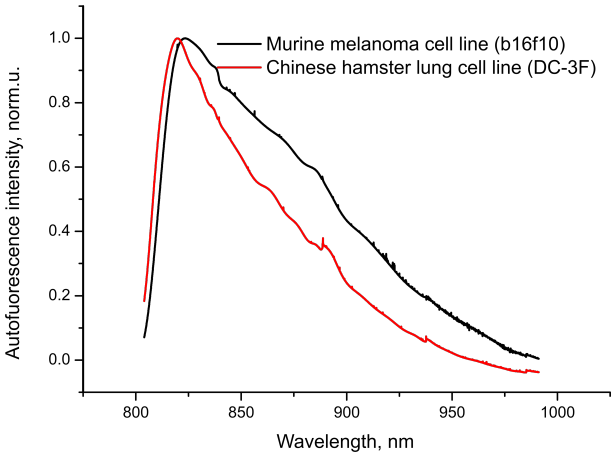


Fig. 6 Normalized NIR AF spectra of murine melanoma and Chinese hamster lung cells under 785 nm laser excitation.

In general, the AF spectra of highly pigmented melanoma cells can be described by the lower AF relative intensity in comparison with lung cells. After the spectra normalization (Fig. 6) the significant differences in shape of the spectra become more visible. In particular, the normalized averaged AF spectrum of melanoma cells demonstrates higher integral square in comparison with lung cells spectrum. Further we have examined AF *in vivo* spectra acquired from healthy volunteers with different skin photo-types. The Fig. 7 represents NIR AF spectra collected on the top of the finger where the melanin concentration is higher. The obtained spectra demonstrate higher AF intensity in volunteers with phototype III in comparison with skin phototype II. Remarkably, that spectra acquired from cell cultures (Fig. 5) demonstrates an opposite trend melanocytic cells had a lower AF intensity in comparison with melanocytic cells.

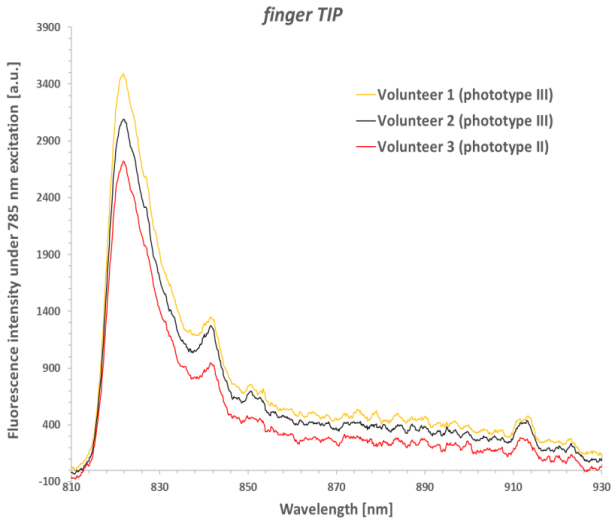


Fig. 7 Averaged autofluorescence spectra for 3 different volunteer's fingertips *in vivo*.

Moreover, all collected *in vivo* NIR AF (Fig. 7) spectra can be characterized by three emission maxima: main peak at ~825 nm, and two smaller peaks located at ~840 nm and ~850 nm. The local peak at ~910 nm most probably is attributed to the CCD etaloning effects and could be neglected for the analysis. Obtained AF spectral features (peaks at 840 nm and 850 nm) are in a good agreement with available literature data, fully described by I. Bratchenko et al. [7] Normalization (Fig. 8) of AF spectra acquired from healthy *in vivo* skin demonstrates that all processed spectra are nearly equal. No spectral shift of emission maxima appeared. However, the intensity variations of AF peaks at 840 nm and 850 nm can be observed. In particular, the intensity of skin phototype II has a lowest AF intensity at 840 nm. Undoubtedly, the number of collected signals is statistically very low, as well as relative concentration of melanin content in skin phototypes III and II does not provide strong scientific evidence to draw any conclusions. However, the obtained data is in quantitative agreement with earlier published papers available in literature [7–11].

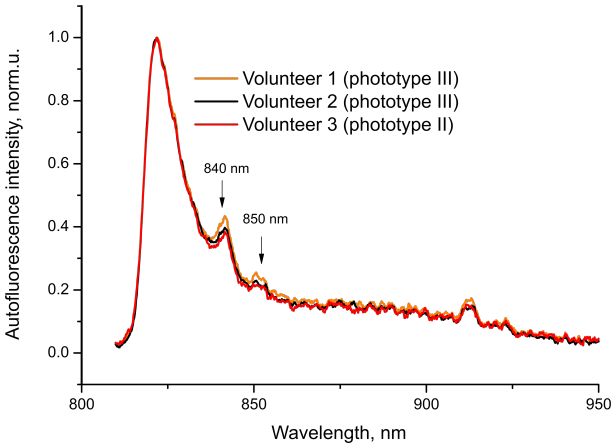


Fig. 8 Normalized AF spectra for 3 different volunteer's fingertips *in vivo*.

Further in collaboration with Ekaterina Borisova at the Institute of Electronics, Bulgarian Academy of Sciences we have collected NIR AF signals from formalinized *ex vivo* skin lesion samples (Fig. 6). The obtained spectra were divided into two groups: 1) NIR AF spectra from melanocytic lesions and 2) spectra obtained from surrounding healthy skin.

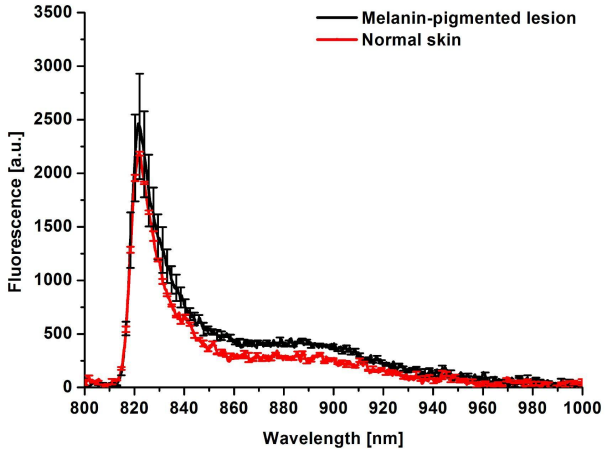


Fig. 9 NIR AF spectra collected from *ex vivo* skin lesion samples under 785 nm laser excitation.

Obtained averaged spectra also demonstrates (Fig. 9) the same trend acquired in *in vivo* skin the highly pigmented melanocytic lesions have a higher AF intensity in comparison with healthy skin. The shape of the formalinized spectra differs in comparison with spectra collected *in vivo*. In particular, the emission peaks of AF at ~840 nm and ~850 nm were not observed in *ex vivo* samples. Probably, it can be attributed to the dehydration of the skin samples due to its formalization. Also, the destruction of the responsible fluorophores under influence of formalin is not excluded. Notably, the integral spectral square of the melanocytic lesions has is higher in comparison with healthy skin. The same tendency has been acquired in cell cultures AF spectra (Fig. 6).

To summarize, in presented paper we have analyzed NIR AF spectra obtained at different conditions. The acquired spectral shapes of melanocytic cells and *ex vivo* lesions have a similar spectral feature. In particular, the integral square of the melanoma cells and melanocytic lesions is higher in comparison with healthy skin and amelanocytic lung cells. The relative intensities at AF emission maxima (820 nm) does not provide strong correlation with tissue and cells experiments, and most probably could not be used for diagnostics purpose. However, the analysis of AF spectra at the spectral regions between 840–900 nm seems to be potential for assessment of melanocytic lesions and melanoma diagnostics. Moreover, the development of imaging techniques intended for visualization of suspicious areas of the skin should be implemented at spectral bands including AF maxima (825 nm) and regions between 840 nm and 900 nm. Undoubtedly, the future studies complemented with hypotheses and theoretical models are necessary to understand the exact phenomenon of the NIR AF.

4 Conclusions

To conclude the presented paper demonstrates a potential of laser applications for evaluation of microbial activity and skin lesion diagnostics. Analysis of laser speckle time series images provides an earlier response of growing bacteria in comparison with classical CFU growth detection under white light illumination.

Obtained AF spectra under 785 nm laser excitation deliver a quantitative correlation between *in vitro* melanoma cells and *ex vivo* melanocytic lesions. The analysis of AF intensity at spectral maxima does not provide strong correlation with tissue and cells melanin content. Further studies should be focused on investigation of *in vivo* tissue and native histology samples in order to identify key morphological features responsible for NIR AF spectral variations.

Disclosures

All authors declare that there is no conflict of interests in this paper.

Funding

This research is funded by the European Regional Development Fund project "Fast and cost effective machine learning based system for microbial growth analysis" (agreement No: 1.1.1.1/19/A/147).

Acknowledgments

This article is dedicated to Ekaterina Borisova, whose contribution in science we greatly appreciate and respect. In the short time we spent doing experiments together, we found that Ekaterina was also a passionate lover of Latvian ballet. Unfortunately, we did not manage to organize a joint ballet visit to Latvia, which we had planned. May she rest in peace.

References

1. J. Yoon, K. Lee, and Y. Park, "A simple and rapid method for detecting living microorganisms in food using laser speckle decorrelation," arXiv:1603.07343 (2016).
2. H. Loutfi, F. Pellen, B. Le Jeune, R. Lteif, M. Kallassy, G. Le Brun, and M. Abboud, "Real-time monitoring of bacterial growth kinetics in suspensions using laser speckle imaging," Scientific Reports 10(1), 408 (2020).
3. H. Kim, A. K. Singh, A. K. Bhunia, and E. Bae, "Laser-induced speckle scatter patterns in Bacillus colonies," Frontiers in Microbiology 5, 537 (2014).
4. H. C. Grassi, L. C. García, M. L. Lobo-Sulbarán, A. Velásquez, F. A. Andrades-Grassi, H. Cabrera, J. E. Andrades-Grassi, and E. D. J. Andrades, "Quantitative laser biospeckle method for the evaluation of the activity of trypanosoma cruzi using VDRL plates and digital analysis," PLoS Neglected Tropical Diseases 10(12), e0005169 (2016).
5. H. C. Grassi, A. Velásquez, O. M. Belandria, M. L. Lobo-Sulbarán, J. E. Andrades-Grassi, H. Cabrera, and E. D. Andrades, "Biospeckle laser digital image processing for quantitative and statistical evaluation of the activity of Ciprofloxacin on Escherichia coli K-12," Laser Physics 29(7), 075603 (2019).
6. K. Zhou, C. Zhou, A. Sapre, J. H. Pavlock, A. Weaver, R. Muralidharan, J. Noble, J. Kovac, Z. Liu, and A. Ebrahimi, "Dynamic laser speckle imaging meets machine learning to enable rapid antibacterial susceptibility testing (DyRAST)," ACS Sensors 5(10), 3140–3149 (2020).
7. I. A. Bratchenko, Y. A. Khristoforova, L. A. Bratchenko, A. A. Moryatov, S. V. Kozlov, E. G. Borisova, and V. P. Zakharov, "Optical Biopsy of Amelanotic Melanoma with Raman and Autofluorescence Spectra Stimulated by 785 nm Laser Excitation," Journal of Biomedical Photonics & Engineering 7(2), 020308 (2021).
8. Z. Huang, H. Lui, D. I. McLean, M. Korbelik, and H. Zeng, "Raman spectroscopy in combination with background near-infrared autofluorescence enhances the in vivo assessment of malignant tissues," Photochemistry and Photobiology 81(5), 1219–1226 (2005).
9. E. G. Borisova, I. A. Bratchenko, Y. A. Khristoforova, L. A. Bratchenko, T. I. Genova, A. I. Gisbrecht, A. A. Moryatov, S. V. Kozlov, P. P. Troyanova, and V. P. Zakharov, "Near-infrared autofluorescence spectroscopy of pigmented benign and malignant skin lesions," Optical Engineering 59(6), 061616 (2020).
10. S. Wang, J. Zhao, H. Lui, Q. He, and H. Zeng, "In vivo near-infrared autofluorescence imaging of pigmented skin lesions: methods, technical improvements and preliminary clinical results," Skin Research and Technology 19(1), 20–26 (2013).
11. M. Saif, W. J. Kwanten, J. A. Carr, I. X. Chen, J. M. Posada, A. Srivastava, J. Zhang, Y. Zheng, M. Pinter, S. Chatterjee, S. Softic, C. R. Kahn, K. van Leyen, O. T. Bruns, R. K. Jain, and M. G. Bawendi, "Non-invasive monitoring of chronic liver disease via near-infrared and shortwave-infrared imaging of endogenous lipofuscin," Nature Biomedical Engineering 4(8), 801–813 (2020).
12. I. Balmages, J. Liepins, S. Zolins, D. Bliznuks, I. Lihacova, and A. Lihachev, "Laser speckle imaging for early detection of microbial colony forming units," Biomedical Optics Express 12(3), 1609–1620 (2021).
13. I. Balmages, D. Bliznuks, J. Liepins, S. Zolins, and A. Lihachev, "Laser speckle time-series correlation analysis for bacteria activity detection," Proceedings of SPIE 11359, 113591D (2020).

Influence of Melanin Content on Laser Doppler Flowmetry and Tissue Reflectance Oximetry Signal Formation

Viktor Dremin[1,2*], Nadezhda Golubova[1], Elena Potapova[1], and Andrey Dunaev[1]

[1] Research and Development Center of Biomedical Photonics, Orel State University, 95 Komsomolskaya str., Orel 302026, Russia

[2] College of Engineering and Physical Sciences, Aston University, Aston Triangle, Birmingham B4 7ET, UK

*** e-mail:** v.dremin1@aston.ac.uk

Abstract. The article presents the results of studies of the melanin effect on recorded signals in laser Doppler flowmetry (LDF) and tissue reflectance oximetry (TO). By investigating the properties of recorded microvascular blood flow and skin oxygenation signals, we have gained new knowledge about race-related differences in the formation of these signals. The effect of the skin melanin content on the intensity of the recorded signals in the LDF and TO methods was evaluated, and the limitations in the use of these methods in representatives of different ethnic groups were shown. © 2021 Journal of Biomedical Photonics & Engineering.

Keywords: laser Doppler flowmetry; blood perfusion; tissue reflectance oximetry; tissue oxygen saturation; melanin.

Paper #3452 received 15 Aug 2021; revised manuscript received 5 Oct 2021; accepted for publication 11 Oct 2021; published online 5 Nov 2021. doi: 10.18287/JBPE21.07.040306.

1 Introduction

Disorders of the blood microcirculation system are diverse both in their pathogenesis and clinical manifestations, in this regard, the microhaemodynamic state assessment is quite relevant. This is especially important in cardiology, diabetology, oncology, as well as in violation of microcirculation in dermatology, dentistry, surgery, and resuscitation.

Currently, laser Doppler flowmetry (LDF) and laser Doppler imaging are widely used methods for *in vivo* evaluation of the state of microcirculatory blood flow [1–5]. Laser Doppler measures the total local microcirculatory blood perfusion. This technique is based on tissue sensing by laser light and analysis of the light scattered by the tissue. Light impinging on moving red blood cells undergoes a Doppler shift in frequency, while light hitting static objects remains unchanged. A photodetector ultimately registers the scattered radiation. This allows for a continuous measurement of tissue perfusion based on Doppler-shifted and non-shifted photons registered by the photodetector.

Tissue reflectance oximetry (TO) is a technique employed for the non-invasive *in vivo* monitoring of system microhaemodynamics [6]. The tissue reflectance oximetry method provides information about the tissue oxygen saturation (S_tO_2) of the examined biological tissue microcirculation and allows for calculation of the relative blood volume (V_b) in the surface layers of soft tissues (skin, mucous membranes). This technology is based on the difference in the optical properties of oxygenated (HbO_2) and deoxygenated (Hb) haemoglobin when irradiated with green and red light [7–9]. Furthermore, in conjunction with LDF and other optical methodologies, tissue oximetry is a powerful tool capable of providing non-invasive measurements of parameters such as oxygen consumption within a living tissue. Tissue oxygen saturation is defined as the percentage composition of oxyhaemoglobin in the sum of two haemoglobin fractions, oxyhaemoglobin and deoxyhaemoglobin [10]:

$$S_tO_2 = \frac{C_{HbO_2}}{C_{HbO_2} + C_{Hb}} \times 100\%, \quad (1)$$

where, if the molar concentration of HbO_2 in the blood is designated as C_{HbO2} and the overall molar concentration of all the fractions of haemoglobin in the blood, including HbO_2, is designated as the sum of C_{HbO2} and C_{Hb}, then the parameter V_b can be calculated as follows:

$$V_b = \frac{C_{HbO_2} + C_{Hb}}{C_{HbO_2} + C_{Hb} + C_{other}} \times 100\%, \quad (2)$$

where C_{other} is the molar concentration of all secondary cellular structures in the examined volume of tissue.

The value of the molar concentration is determined by the absorption by biological tissue of radiation at different wavelengths. On the basis of the well-known Beer-Lambert law and taking into account multicomponent biotissue, the absorption coefficient can be calculated using the following formula:

$$\mu_a(\lambda) = \sum_i \varepsilon_i(\lambda) \cdot C_i, \quad (3)$$

where ε_i (λ) is the molar extinction coefficient for the biochemical medium component *i*, while C_i is the molar concentration of component *i* in the tested region.

Taking into account certain restrictions, the molar concentrations of the haemoglobin fractions vital for the calculation of S_tO_2 and V_b can be calculated using the following system of linear equations [10–12]:

$$\begin{cases} \mu_a(\lambda_1) = \varepsilon_{Hb}(\lambda_1) \cdot C_{Hb} + \varepsilon_{HbO_2}(\lambda_1) \cdot C_{HbO_2} + \varepsilon_{other}(\lambda_1) \cdot C_{other} \\ \mu_a(\lambda_2) = \varepsilon_{Hb}(\lambda_2) \cdot C_{Hb} + \varepsilon_{HbO_2}(\lambda_2) \cdot C_{HbO_2} + \varepsilon_{other}(\lambda_2) \cdot C_{other} \end{cases}, \quad (4)$$

where $\varepsilon_{other}(\lambda_j)$ is the sum molar extinction coefficient of light at different wavelengths by all other skin structures.

Human skin is a multicomponent turbid absorbing and scattering medium. Absorption of radiation is one of the characteristics of the interaction of light and skin, due to the presence of a large number of different chromophores in tissues [13]. However, such a chromophore as melanin has an individual pattern of absorption (see Fig. 1a), since its concentration can vary greatly from one person to another and depending on the place of measurement, which can lead to incorrect diagnostic results. The melanocytes located in the cell basal layer produce melanin and transfer it to neighbouring cells of the epidermis keratinocytes in order to protect their nucleus from UV radiation. Regardless of the ethnicity in the skin of each person is the same amount of melanocytes, but the amount of melanin, which these cells produce, is different. The amount of produced melanin determines the colour of the skin and its sensitivity to light. In people with different ethnic skin types, the concentration of melanin varies approximately in the range of 1.3–43%. In low-pigmented skin, the melanin content is 1.3–1.6%, 11–16% in middle-pigmented, 18–43% in blacks [13].

In this regard, in the methods of optical diagnostics, including LDF and TO, there is a problem of correct assessing of the microhaemodynamics state and determining the concentration of oxyhaemoglobin in people belonging to different ethnic groups, since the differences in the optical properties of the skin of these people are not taken into account. The work [14] presents studies of race-specific differences in the dynamics of blood flow and tissue oxygenation and shows the specificity of the difference in the phase coherence of LDF signals and tissue oximetry. This paper discusses the natural physiological difference in the recorded parameters of the cardiovascular dynamics between people of Sub-Saharan African descent and European descent. In the current work, we consider the effect of melanin as an optical filter, both in experimental studies on various ethnic skin types, and using computational modelling.

2 Experimental System and Methodology

Experimental studies were carried out using a multi-functional laser non-invasive certified diagnostic system "LAKK-M" (SPE "LAZMA" Ltd., Moscow, Russia), the appearance of which is presented in Fig. 1b [15–17]. The system is designed for research and diagnostics in various fields of biomedicine by simultaneously using the methods of pulse oximetry, laser Doppler flowmetry (LDF), tissue reflectance oximetry, and fluorescence spectroscopy. It allows one to study of a number of microcirculatory parameters, including perfusion (by LDF) and oxygen saturation (S_tO_2) of skin tissue (by TO). The device apparatus includes a fibre-optic system to allow for analysing at selected points on the body. The wavelength of the probe laser radiation in the LDF channel is 1064 nm, in the TO channels – 530 nm and 630 nm, accordingly. A multioptical fibre probe was used to delivery of radiation

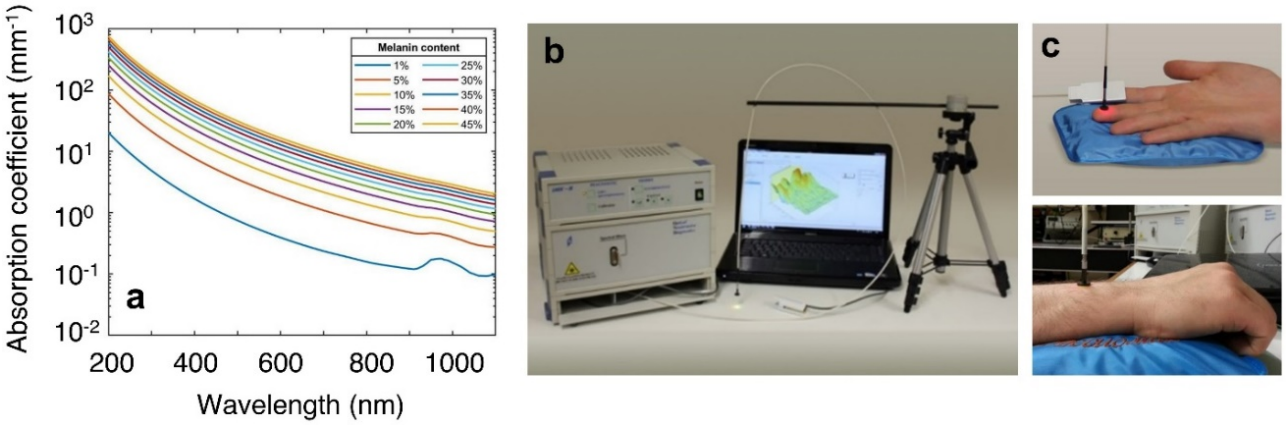


Fig. 1 (a) Absorption spectra of the epidermis with different melanin content [18]. (b) The multi-functional laser non-invasive diagnostic system "LAKK-M". (c) Measurements areas are the finger pad and the forearm.

and registration of backreflected radiation from the tissue. The probing single-mode fibre of the LDF channel has a diameter of 6 μm and the probing fibre of the TO channel – 400 μm. All receiving fibres have a diameter of 400 μm. The numerical aperture of the fibres is 0.22. The output power of LDF and TO lasers does not exceed 1.5 mW and 1 mW, respectively.

We studied the effect of the skin melanin on the LDF and TO parameters as recorded on different ethnicities including Caucasian (type II of Fitzpatrick scale, 4 volunteers, totalling 92 records), Indian (type IV of Fitzpatrick scale [19], 1 volunteer, 30 records), Middle Eastern (type V of Fitzpatrick scale, 1 volunteer, 16 records) and African (type VI of Fitzpatrick scale, 3 volunteers, 4 records). The inclusion of a large number of measurements with Caucasian skin type allowed to demonstrate that even with high individual variability of the measured parameters, statistically significant differences remain in different ethnic skin types. Recordings on volunteers with Caucasian skin type were carried out during the calendar year, which allowed us to additionally take into account the seasonal effects of skin melanin.

The study was performed approximately at the same time of day (around 12:00) to avoid circadian rhythms influence on the blood circulation, at ambient room temperature (21–22 °C) in a sitting position after a 30 min rest period (allowed for acclimatization). The temperature of the volunteers was measured in the tested regions of the skin using an infrared clinical thermometer. All temperatures recorded were within the range of 34–36 °C. Measurements were performed on the inner surface (palmar) of the right middle finger (slightly pigmented area for all volunteers), and on the skin of the forearm in the area with the differences in the melanin content (Fig. 1c). An equal number of records were recorded from each skin area. Recording of the signals lasted 3 min.

3 Results

3.1 Laser Doppler Flowmetry Measurements

LDF signals were obtained for people with different ethnic skin types, typical graphs of which are shown in Figs. 2 (a, b).

The analysis of LDF signals within the groups was carried out using statistical mean values of blood perfusion, standard deviation, confidence interval, and coefficient of variation (see Fig. 2 (c, d) and Table 1). A statistically significant differences between the groups were confirmed by the Kruskal-Wallis test with the post-hoc analysis ($p < 0.05$). Evaluating the results obtained in the area of the finger pad (Fig. 2c), it can be noted that the perfusion values are the same, which is probably due to approximately the same level of melanin content. Analysing the results in the forearm area, one can notice that in the group of volunteers with African skin type, there was a decrease in signal compared to other groups of volunteers (Fig. 2d).

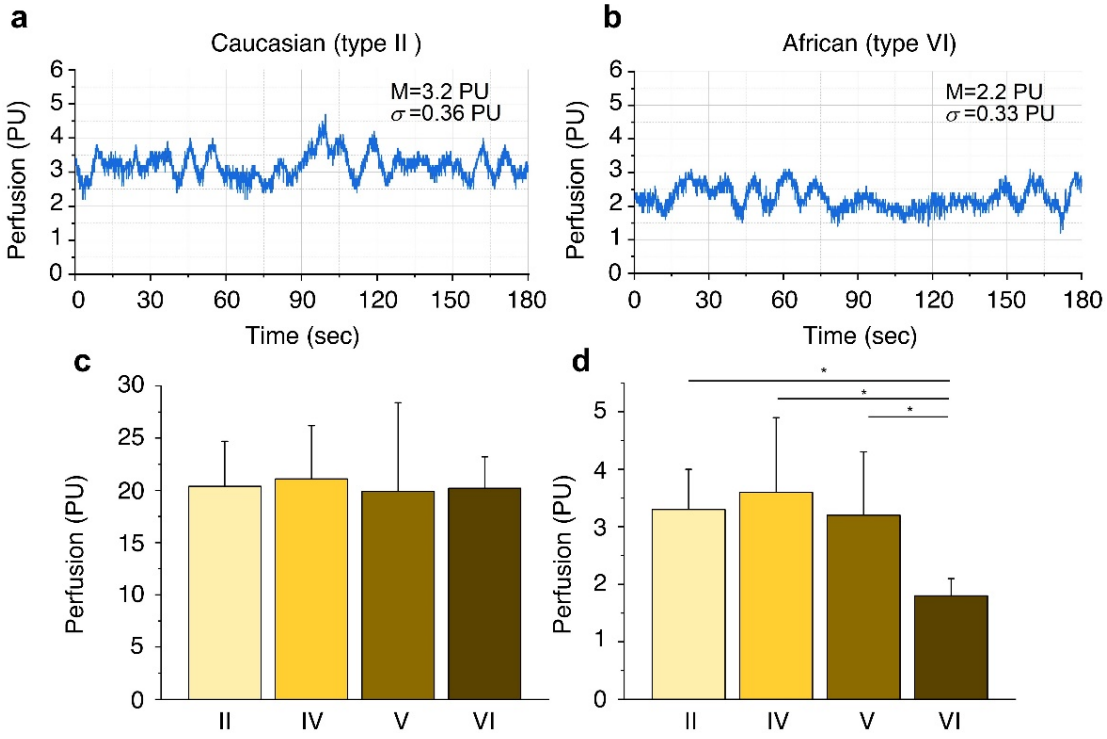


Fig. 2 Typical LDF signals for (a) Caucasian and (b) African skin types in area of the forearm. Average values and standard deviation of perfusion for different ethnic groups in the area of (c) the finger and (d) the forearm. II, IV, V, and VI are Fitzpatrick skin tone types. * Confirmed statistically significant differences ($p < 0.05$).

Table 1 Confidence interval and coefficient of variation of the measured and calculated parameters within the groups.

Statistic	Fitzpatrick scale	Finger			Forearm		
		Perfusion	StO_2	V_b	Perfusion	StO_2	V_b
Confidence interval	II	19.5–21.3	74.2–78.2	10.4–11.4	3.1–3.5	67.08–71.12	5.57–6.23
	IV	18.9–23.3	72.3–75.3	11.4–13.0	3.0–4.2	60.89;65.11	10.02–11.58
	V	14.6–25.2	65.2–71.0	10.8–12.3	2.5–3.9	53.72–58.08	14.59–16.21
	VI	13.9–26.5	52.6–85.2	7.7–16.9	1.2–2.4	31.41;40.59	19.32–37.28
Coefficient of variation, %	II	21	11	18	21	12	24
	IV	24	5	15	36	8	17
	V	43	7	10	34	6	8
	VI	15	11	18	17	6	15

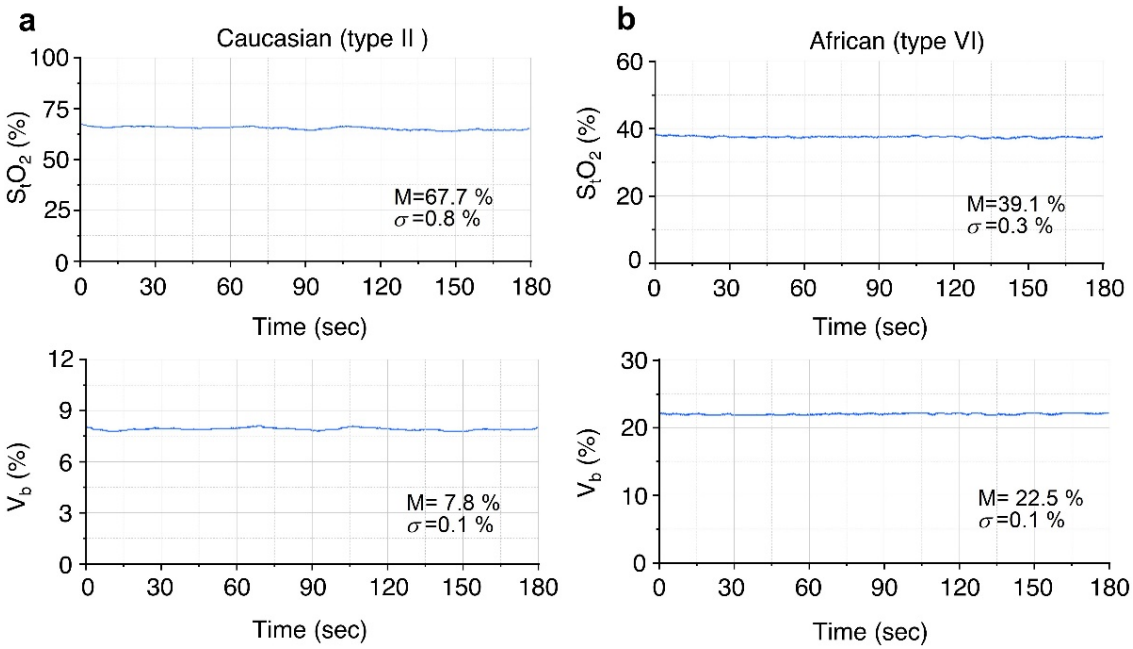


Fig. 3 Typical StO_2 and V_b signals recorded on the forearm for (a) European and (b) African skin types.

3.2 Tissue Reflectance Oximetry Measurements

Examples of typical StO_2 and V_b records for European and African skin types (area on the forearm) are shown in Figs. 3 (a, b), respectively. The tissue saturation parameter for the European skin type in this area of research is equal to the average, since normally this parameter is approximately within the range of 60–80%. The obtained parameter represents tissue oxygenation and corresponds to the average between the oxygen saturation of the arterial (95–99%) and venous (70–75%) blood [20]. However, in the presented TO signals for African skin type, tissue saturation equals 39%, which clearly demonstrates the inadequacy results for people with an increased content of skin melanin. The same applies to the V_b parameter. Confirmation of the thesis that the differences are not due to ethnic physiological characteristics, but to the absorption capacity of melanin, is the different values of oxygenation in different areas of the skin for the same volunteer.

The obtained results registered in TO during the experiments were statistically processed according to the Kruskal-Wallis test (Fig. 4). As a result of the processing, a statistical difference was found in the calculated values obtained during the forearm measurements in ethnic groups with an increased melanin content compared to the type of white European skin type ($p < 0.05$). Thus, the measurements results are strongly dependent on the level of melanin present in the skin.

In the next Section, to describe and predict the effect of melanin on the intensity of the diffusely reflected radiation component, a Monte Carlo (MC) simulation was performed.

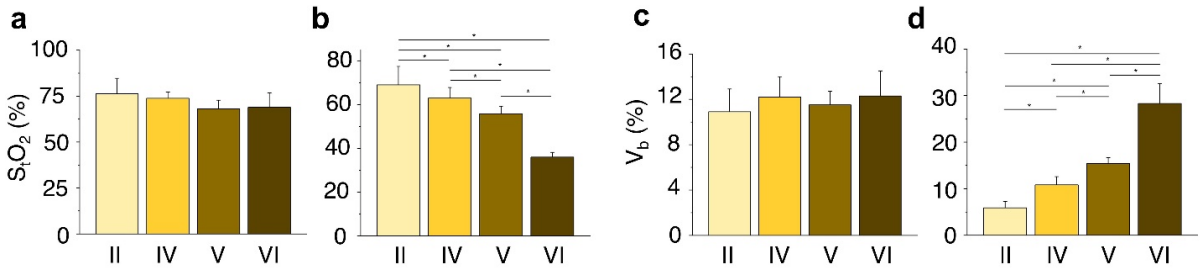


Fig. 4 The average values and standard deviation of S_tO_2 and V_b parameters for different ethnic groups in the (a, c) finger and (b, d) forearm area. II, IV, V, and VI are Fitzpatrick skin tone types. * Confirmed statistically significant differences ($p < 0.05$).

3.3 Monte Carlo Simulation of Diffuse Reflectance Intensity

MC simulation consists of a sequential generation of trajectories of so-called photon packets from the site of photons' entrance into the medium to the area where the photon leaves the. In this study, a GPU-accelerated MC distributed online computational platform that implements an object-oriented concept [21] was used for a routine simulation of diffuse reflectance intensity. A seven-layer skin model was used to calculate the diffuse reflectance intensity. The basics of the considered model have been previously described in Refs. [22, 23]. The absorption coefficient of each layer takes into account the blood volume fraction in various vascular beds, oxygen saturation, water and melanin content [24, 25]. The melanin content varied in the range of 1-45%.

Optical properties of tissues used in MC simulations is provided in Ref. [25]. MC simulations were performed for the actual probe geometry used in the experiment using the detected photon packets. The total diffuse reflectance intensity has been calculated as the normalized sum of statistical weights of the photon packets satisfying the detection condition according to the microscopic Beer-Lambert law as follows:

$$I(\lambda) = \frac{1}{N_{ph} W_0} \sum_{j}^{N_{ph}} W_j \exp\left(-\sum_{i=1}^{K_i} \mu_{ai}(\lambda) l_i \right). \qquad (5)$$

Here, N_{ph} is the number of detected photon packets, W_0 is the initial statistical weight of a photon packet entering a scattering medium, W_j is the final weight of the j^{th} detected photon packet, K_i represents the total number of scattering events experienced by the photon packet within the medium, μ_{ai} is the medium local absorption and l_i is the path length of the photon packet at i^{th} step.

The results of the MC simulations are shown in Fig. 5.

The results presented in Fig. 5 demonstrate the changes in the intensity of diffuse reflectance of human skin resulting from variations in melanin content. Reflectance intensity for wavelength 1064 nm decreases by 33% for highly pigmented skin, for wavelengths of 530 nm and 630 nm, these values are 86% and 85%, respectively.

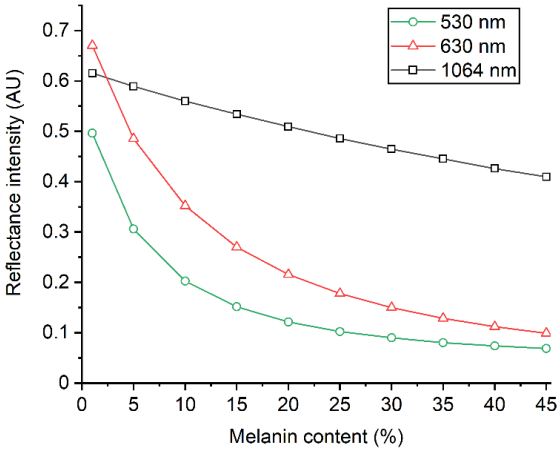


Fig. 5 The results of MC simulation of diffuse reflectance intensity while varying the melanin content in epidermis. The wavelengths of light used in the modelling are 530 nm, 630 nm, and 1064 nm.

4 Discussion

For many years of experience in using devices for assessing microcirculation by LDF and TO methods, most of the studied healthy volunteers and patients with various pathologies were with a slightly pigmented skin type. Most of the devices that implement these methods were probably calibrated without taking into account the data on the melanin content in the skin. Furthermore, diagnostic methods indicating the norm and pathology were developed in most cases for people with light skin.

Studies of the effect of the melanin pigment on the recorded optical signals by methods of optical non-invasive diagnostics show that this aspect is important to take into account when developing various types of devices. Most studies on the influence of skin type on recorded signals are devoted to photoplethysmography and pulse oximetry due to their widespread use in medical practice. It has been shown that a dark skin colour can affect the performance and accuracy of pulse oximeters from various manufacturers [26, 27]. For the correct interpretation of the diagnostic results, it is necessary to take into account the influence of skin type and wavelength on light reflection [28]. A device with an automatic adaptation module with an optimal choice of suitable lighting was proposed for different skin types [29]. In our early studies, we studied the effect of

melanin on the attenuation of fluorescence intensity and proposed methods for assessing this effect [30, 31]. A group led by Prof. Aneta Stefanovska showed differences in cardiovascular and microvascular dynamic processes between black Africans and Europeans, using records obtained using NIRS, white light spectroscopy and LDF methods [14].

In the present paper, we study the effect of melanin on LDF and TO signals in both experimental studies and using modelling. It was found that the influence of melanin on the recorded signals strongly depends on the location of the recorded signal: statistically significant differences were found in the forearm area, which is due to the fact that in this area of research, differences in the influence of melanin are most pronounced. The results obtained demonstrate that the skin type on the Fitzpatrick scale significantly affects the measured parameters. In the area of strong pigmentation (forearm) for groups II, IV, and V, there were no statistically significant differences in the perfusion parameter. However, an increase in pigmentation to group VI (melanin content of more than 20%) can lead to a decrease in perfusion by 45% compared to type II skin. StO_2 and V_b parameters are even more sensitive to the melanin content. A sequential increase in melanin from group II to IV, from IV to V, and from V to VI causes a decrease in the StO_2 parameter by 9, 11, and 36%, respectively. At the same time, there is an increase in the V_b parameter by 83, 43, and 84%, respectively.

Since the development of wearable devices, including those implementing the LDF and TO methods [32, 33], which most often use this area for research, is gaining momentum in medical instrumentation, the presented results are important and should be taken into account.

Currently, various wavelengths are used in laser Doppler flowmetry devices. Moor Instruments Ltd. (Axminster, UK) and Oxford Optronix Ltd. (Oxford, UK) devices use a wavelength of 785 nm, Perimed AB (Järfälla, Sweden) – 780 nm, , SPE "LAZMA" Ltd. (Moscow, Russia) – 1064 nm. As can be seen in Fig. 1a, as the wavelength increases, the absorption of the optical signal by melanin decreases. In this regard, a longer wavelength is considered to be more suitable for measurements on highly pigmented skin. The wavelengths used in the TO channel (530 nm and 630 nm) are strongly influenced by the absorption of melanin (Fig. 1a). In this sense, the intensity of back-reflected radiation decreases in the forearm area with an increase in skin pigmentation, which ultimately affects the signal-to-noise ratio and the values of the calculated parameters. This is important to take into account when developing new wearable devices, and in the instructions for existing devices, it is necessary to specify restrictions related to skin colour.

The simulation results confirm the need to develop methods and algorithms for taking into account the effect of melanin on the results of optical measurements, in particular, approaches for personalized calibration of diagnostic systems. In this direction, the use of neural networks to restore the concentrations of various skin chromophores seems promising. In works [24, 34], the possibilities of such an approach were demonstrated, in which the melanin content was taken into account when determining the oxygenation of the skin by hyperspectral imaging.

It is important to note that our study has some limitations. We tested a small group of volunteers and only one type of diagnostic system. A further perspective of the study is the frequency analysis of the rhythmic components of skin blood flow at different concentrations of melanin and probing wavelengths (from 600 to 1100 nm), as well as the expansion of the experimental data base.

5 Conclusion

By investigating the properties of recorded microvascular blood flow and skin oxygenation signals, we have gained new knowledge about race-related differences in the formation of these signals.

The experimental data and simulation results are a clear illustration of the fact that the levels of signals recorded in LDF and TO when probing the skin with the radiation of green, red and infrared sources for groups of people with different ethnic skin types is significantly different. And as a result, the calculated values (perfusion, StO_2, V_b) are incorrect for ethnic skin types with an increased level of melanin, in contrast to the European type, for which the current instrumental implementation of the LDF and TO channels is calibrated.

Therefore, it can be concluded that it is necessary to take into account the individual optical parameters of the human skin. For example, in subjects with different levels of skin melanin, one should choose areas of investigation that will help avoid the effect of shielding optical signals from hyperpigmented skin (e.g., the ventral surface of the hand). The contribution to the total absorption of cutaneous melanin should be taken into account both when creating mathematical models for these diagnostic technologies, and for their instrumental implementations.

Disclosures

All authors declare that there is no conflict of interests in this paper.

Acknowledgments

The team of the R&D Center of Biomedical Photonics (Orel, Russia) has been inspired by the works of Dr. Ekaterina Borisova for many years. We knew Dr. Borisova personally and collaborated with her on some projects. Our team expresses its deep condolences to her relatives and colleagues. We mourn the loss of an important scientist in the world of biophotonics.

VD acknowledges for personal support from the European Union's Horizon 2020 research and innovation programme under the Marie Sklodowska-Curie grant agreement No. 839888.

The authors acknowledge the support of the grant of the President of the Russian Federation for state support of young Russian scientists No. MK-398.2021.4.

References

1. R. Bonner, R. Nossal, "Principles of laser-Doppler flowmetry," in Laser-Doppler blood flowmetry. Developments in Cardiovascular Medicine, A. P. Shepherd, P. A. Öberg (Eds.), Springer, Boston, 17–45 (1990). ISBN: 978-1-4757-2083-9.
2. V. Dremin, E. A. Zherebtsov, I. N. Makovik, I. O. Kozlov, V. V. Sidorov, A. I. Krupatkin, A. V. Dunaev, I. E. Rafailov, K. S. Litvinova, S. G. Sokolovski, and E. U. Rafailov, "Laser Doppler flowmetry in blood and lymph monitoring, technical aspects and analysis," Proceedings of SPIE 10063, 1006303 (2017).
3. A. I. Zherebtsova, V. V. Dremin, I. N. Makovik, E. A. Zherebtsov, A. V. Dunaev, A. Goltsov, S. G. Sokolovski, and E. U. Rafailov, "Multimodal optical diagnostics of the microhaemodynamics in upper and lower limbs," Frontiers in Physiology 10, 416 (2018).
4. I. Makovik, A. V. Dunaev, V. V. Dremin, A. I. Krupatkin, V. V. Sidorov, L. S. Khakhicheva, V. F. Muradyan, O. V. Pilipenko, I. E. Rafailov, and K. S. Litvinova, "Detection of angiospastic disorders in the microcirculatory bed using laser diagnostics technologies," Journal of Innovative Optical Health Sciences 11(01), 1750016 (2018).
5. K. Kandurova, V. Dremin, E. Zherebtsov, E. Potapova, A. Alyanov, A. Mamoshin, Y. Ivanov, A. Borsukov, and A. Dunaev, "Fiber-optic system for intraoperative study of abdominal organs during minimally invasive surgical interventions," Applied Sciences 9(2), 217 (2019).
6. H. Liu, M. Kohl-Bareis, and X. Huang, "Design of a tissue oxygenation monitor and verification on human skin," Proceedings of SPIE-OSA Biomedical Optics 8087, 80871Y (2011).
7. C. Casavola, L. A. Paunescu, S. Fantini, M. A. Franceschini, P. M. Lugara, and E. Gratton, "Application of near-infrared tissue oxymetry to the diagnosis of peripheral vascular disease," Clinical Hemorheology and Microcirculation 21(3–4), 389–393 (1999).
8. M. Wallace, A. Wax, D. N. Roberts, and R. N. Graf, "Reflectance spectroscopy," Gastrointestinal endoscopy clinics of North America 19(2), 233–242 (2009).
9. E. Potapova, V. V. Dremin, E. A. Zherebtsov, I. N. Makovik, A. I. Zherebtsova, A. V. Dunaev, K. V. Podmasteryev, V. V. Sidorov, A. I. Krupatkin, L. S. Khakhicheva, and V. F. Muradyan, "Evaluation of microcirculatory disturbances in patients with rheumatic diseases by the method of diffuse reflectance spectroscopy," Human Physiology 43(2), 222–228 (2017).
10. A. V. Dunaev, V. V. Sidorov, A. I. Krupatkin, I. E. Rafailov, S. G. Palmer, N. A. Stewart, S. G. Sokolovski, and E. U. Rafailov, "Investigating tissue respiration and skin microhaemocirculation under adaptive changes and the synchronization of blood flow and oxygen saturation rhythms," Physiological Measurement 35(4), 607–621 (2014).
11. O. Khalil, "Metabolites, noninvasive optical measurements," in Wiley Encyclopedia of Biomedical Engineering, Wiley, New York (2006).
12. H. Heusmann, J. Koelzer, and G. Mitic, "Characterization of female breasts in vivo by time-resolved and spectroscopic measurements in the near infrared spectroscopy," Journal of Biomedical Optics 1(4), 425–434 (1996).
13. S. Jacques, "Optical properties of biological tissues: A review," Physics in Medicine & Biology 58(11), 37–61 (2013).
14. Y. Abdulhameed, P. McClintock, and A. Stefanovska, "Race-specific differences in the phase coherence between blood flow and oxygenation: A simultaneous NIRS, white light spectroscopy and LDF study," Journal of Biophotonics 13(4), e201960131 (2020).
15. K. Litvinova, I. E.Rafailov, A. V. Dunaev, S. G. Sokolovski, and E. U. Rafailov, "Non-invasive biomedical research and diagnostics enabled by innovative compact lasers," Progress in Quantum Electronics 56, 1–14 (2017).
16. D. Rogatkin, L. G. Lapaeva, E. N. Petritskaya, V. V. Sidorov, and V. I. Shumskiy, "Multifunctional laser noninvasive spectroscopic system for medical diagnostics and some metrological provisions for that," Proceedings of SPIE-OSA Biomedical Optics 7368, 73681Y (2009).
17. D. Rogatkin, S. G. Sokolovski, K. A. Fedorova, N. A. Stewart, V. V. Sidorov, and E. U. Rafailov, "Basic principles of design and functioning of multifunctional laser diagnostic system for non-invasive medical spectrophotometry," Proceedings of SPIE 7890, 78901H (2011).
18. S. Jacques, D. McAuliffe, "The melanosome: threshold temperature for explosive vaporization and internal absorption coefficient during pulsed laser irradiation," Photochemistry and Photobiology 53(6), 769–775 (1991).
19. T. Fitzpatrick, "The validity and practicality of sun-reactive skin types I through VI," Archives of Dermatology 124(6), 869–871 (1988).
20. K. Akons, E. Dann, and D. Yelin, "Measuring blood oxygen saturation along a capillary vessel in human," Biomedical Optics Express 8(11), 5342–5348 (2017).
21. A. Doronin, I. Meglinski, "Online object oriented Monte Carlo computational tool for the needs of biomedical optics," Biomedical Optics Express 2(9), 2461–2469 (2011).

22. G. Petrov, A. Doronin, H. T. Whelan, I. Meglinski, and V. V. Yakovlev, "Human tissue color as viewed in high dynamic range optical spectral transmission measurements," Biomedical Optics Express 3(9), 2154–2161 (2012).
23. I. Meglinski, A. Doronin, A. N. Bashkatov, E. Genina, and V. V. Tuchin, "Dermal component-based optical modeling ofskin translucency: Impact on skin color," in Computational Biophysics of the Skin, B. Querleux (Ed.), Pan Stanford Publishing Ltd., 25–62 (2014).
24. E. Zherebtsov, V. Dremin, A. Popov, A. Doronin, D. Kurakina, M. Kirillin, I. Meglinski, and A. Bykov, "Hyperspectral imaging of human skin aided by artificial neural networks," Biomedical Optics Express 10(7), 3545–3559 (2019).
25. V. Dremin, E. Zherebtsov, A. Bykov, A. Popov, A. Doronin, and I. Meglinski, "Influence of blood pulsation on diagnostic volume in pulse oximetry and photoplethysmography measurements," Applied Optics 58(34), 9398–9405 (2019).
26. A. Ries, L. Prewitt, and J. Johnson, "Skin color and ear oximetry," Chest 96(2), 287–290 (1989).
27. P. Bickler, J. Feiner, and J. Severinghaus, "Effects of skin pigmentation on pulse oximeter accuracy at low saturation," Anesthesiology 102(4), 715–719 (2005).
28. B. Fallow, T. Tarumi, and H. Tanaka, "Influence of skin type and wavelength on light wave reflectance," Journal of Clinical Monitoring and Computing 27(3), 313–317 (2013).
29. L. Yan, S. Hu, A. Alzahrani, S. Alharbi, and P. Blanos, "A multi-wavelength opto-electronic patch sensor to effectively detect physiological changes against human skin types," Biosensors 7(2), 22 (2017).
30. A. Dunaev, V. V. Dremin, E. A. Zherebtsov, I. E. Rafailov, K. S. Litvinova, S. G. Palmer, N. A. Stewart, S. G. Sokolovski, and E. U. Rafailov, "Individual variability analysis of fluorescence parameters measured in skin with different levels of nutritive blood flow," Medical Engineering & Physics 37(6), 574–583 (2015).
31. V. Dremin, A. Dunaev, "How the melanin concentration in the skin affects the fluorescence-spectroscopy signal formation," Journal of Optical Technology 83(1), 43–48 (2016).
32. M. Saha, V. Dremin, I. Rafailov, A. Dunaev, S. Sokolovski, and E. Rafailov, "Wearable laser Doppler flowmetry sensor: a feasibility study with smoker and non-smoker volunteers," Biosensors 10(12), 201 (2020).
33. A. Fedorovich, Y. L. Loktionova, E. V. Zharkikh, M. A. Mikhailova, J. A. Popova, A. V. Suvorov, and E. A. Zherebtsov, "Body position affects capillary blood flow regulation measured with wearable blood flow sensors," Diagnostics 11(3), 436 (2021).
34. V. Dremin, Z. Marcinkevics, E. Zherebtsov, A. Popov, A. Grabovskis, H. Kronberga, K. Geldnere, A. Doronin, I. Meglinski, and A. Bykov, "Skin complications of diabetes mellitus revealed by polarized hyperspectral imaging and machine learning," IEEE Transactions on Medical Imaging 40(4), 1207–1216 (2021).

Activation of Apoptosis and Autophagy by Gratiola Officinalis Extract in Human Tumor Cell Lines

Natal'ya V. Polukonova[1], Maria A. Baryshnikova[2], Dmitry A. Khochankov[2], Evgeniya V. Stepanova[2], Eliso S. Solomko[2], Anna V. Polukonova[1], Dmitrij A. Mudrak[1], Artem M. Mylnikov[1], Alla B. Bucharskaya[1], Galina N. Maslyakova[1], and Nikita A. Navolokin[1*]

[1] Saratov State Medical University named after V. I. Razumovsky, 112 Bolshaya Kazachya str., Saratov 410012, Russian Federation

[2] National Medical Research Center of Oncology named after N. N. Blokhin, 24 Kashirskoe highway, Moscow 115478, Russian Federation

*** e-mail:** nik-navolokin@yandex.ru

Abstract. The problem of creating antitumor drugs with new mechanisms of action that predominantly induce apoptosis is still topical. The extract of *Gratiola officinalis* is a potential antitumor agent containing mainly flavonoids. The aim of this research is to study the effects of *Gratiola officinalis* extract on activation of apoptosis and autophagy in breast adenocarcinoma SK-BR-3 and kidney carcinoma A-498 lines. Apoptotic activity of the extract was studied by flow cytofluorometry using Hoechst stain and double staining with annexin V plus propidium iodide. There was 96.3% of cells in SK-BR-3 culture in late apoptosis phase detected by flow cytofluorometry method at the extract concentration of 0.88 mg/ml, 86.3% of cells were in apoptosis by Hoechst stain. The concentration of 0.82 mg/ml caused apoptosis in half of the cells. The extract has cytoprotective activity at low concentration (0.0352 mg/ml). The cytoprotection mechanism is realized through the activation of autophagy. The maximum number of autophagosomes in kidney carcinoma cells is observed at the extract concentration of 0.056 mg/ml. Thus, *Gratiola officinalis* extract is able to block cytoprotective autophagy with increasing the extract concentration and to activate apoptosis in 85% of tumor cells. Detailed research should be continued to understand the mechanisms of antitumor activity of *Gratiola officinalis* extract.
© 2021 Journal of Biomedical Photonics & Engineering.

Keywords: autophagy; apoptosis; antitumor agents; Gratiola officinalis; antitumor agents; tumor; flavonoids.

Paper #3449 received 1 Aug 2021; revised manuscript received 7 Oct 2021; accepted for publication 11 Oct 2021; published online 10 Nov 2021. doi: 10.18287/JBPE21.07.040307.

1 Introduction

High biological and toxic activity of antitumor agents determines their damaging effect not only on tumor cells, but also on healthy cells. Antitumor agents cause hematopoietic disorders, including sterilization, growth retardation in children, deterioration of wound healing, hair loss and teratogenic effect [1, 2].

Plant derived drugs, namely alkylating agents (antimetabolites, antitumor antibiotics, herbal preparations, hormones and their antagonists) are the main groups of antitumor agents. The alkaloids of various plants are most commonly used as antitumor agents. These compounds act as mitotic poisons or as topoisomerase inhibitors. They can stop the cell cycle in M-phase stages or in S- and G2-periods. In the tumor, they also may cause damage, necrotic changes, cell polymorphism, fibrosis, and hyalinosis [3].

A number of flavones and flavonols have been found to possess antitumor activities [4]. The property of bioflavonoids to enhance the effectiveness of cytostatic therapy due to the weakening of its toxic effect on healthy cells has been studied, and the direct ability of Wogonin flavonoid and structurally related natural flavones, for example, apigenin, chrysin and luteolin to activate apoptosis in tumor cells has been revealed [5–6].

Wogonin, one of the active flavones of the most popular Chinese herbal remedy Huang-Qin (*Scutellaria baicalensis Georgi*), induces apoptosis in a wide spectrum of human tumor cells *in vitro* and inhibits tumor growth *in vivo* in different mouse tumor models [7]. In addition, *Scutellaria* extracts were successfully tested in patients with advanced breast cancer in early clinical trials [6, 8, 9]. Importantly, at doses lethal to tumor cells, wogonin showed no or little toxicity for normal cells and had also no obvious toxicity in animals [10].

However, no one had previously conducted a comprehensive study of morphological changes in a tumor under the influence of flavonoids. Data on the morphological changes in tumor cells under the influence of flavonoids would open up the prospect of their further active screening as potential antitumor agents.

For this study, we selected the plant *Gratiola officinalis* L. The plant is harvested whilst in flower in the summer and dried for later use [11, 12]. It is used in the herbal medicines for the treatment of a variety of ailments like scrofula, cystitis, colic, certain stomach and menstrual disorder, skin and liver diseases as well as enlargement of the spleen, dropsy, jaundice, intestinal worms, etc. The dried top of the *G. officinalis* has diuretic and emetic effect. *G. officinalis* is also used as biostimulating medicine in hematopoietic, liver and respiratory disorders in human [13–15]. Side effects of its overuse include nausea, acrid poisoning, nymphomania, leanliness, abortion, kidney damage and bowel hemorrhage [12, 16, 17]. The presence of alkaloids, flavonoids, saponins, glycoside-like substances, coumarin derivatives, mannitol and betulinic acid in *G. officinalis* has been found in studies [13, 18, 19]. *G. officinalis* also contains the following substances: gratiogenin, 16-hydroxygratiogenin, cucurbitacins-E and I, glycosides gratiogenin-3beta-D-glucoside, gratioside, elaterinide, lignans, which have many medicinal uses. Caffeic acid glycoside esters, verbascoside and arenarioside, have been isolated from *G. officinalis* [20]. Caffeic acid has been shown to inhibit carcinogenesis. Caffeic acid also shows immunomodulatory and anti-inflammatory activity [13].

One of the chemotypes is characterized by the production of 8-hydroxylated flavone O-glycosides including the new plant substances 8-hydroxychrysoeriol 8-Oglucuronide, hypolaetin 7-O-sophoroside, 8-hydroxychrysoeriol 7-O-sophoroside, and isoscutellarein 8-O-sophoroside [21, 22]. According to data of other researches, new flavonoid named ligniside and C-glycosyl derivatives were also extracted from *G. officinalis* [23, 24]. Apigenin, 4, 5, 7- trihydroxyflavone ($C_{15}H_{10}O_5$), Cosmosiin ($C_{21}H_{20}O_{10}$), one form of saponaretin ($C_{21}H_{20}O_{10}$), and a form of vitexin ($C_{21}H_{20}O_{10}$) were among the nine found [25].

The extract of *G. officinalis* obtained us by the author's method contains flavonoids and has no toxic effects [26]. Earlier, we revealed antioxidant, antitumor, antiexical and immunomodulatory properties of *G. officinalis* L. extract in laboratory animals with transplanted tumors [27–36]. This extract also has antituberculous, anti-inflammatory, antipyretic, and antimicrobial activity, which indicates its polyvalent action [29, 31].

The aim of this research was to study the activation of autophagy and apoptosis in human tumor cell lines – breast adenocarcinoma SK-BR-3 and kidney carcinoma A-498 under the influence of *Gratiola officinalis* extract.

2 Material and methods

Gratiola officinalis extract was obtained by the author's method from herbal raw materials, which was collected on the Volga River island near the village of Chardym (Saratov region) [26, 27, 35].

According to gas chromato-mass spectrometry, chemical analysis of this extract showed the presence of the following substances: quercetin; 4-vinyl-2-methoxyphenol; 2,3-dihydroxy-3,5-dihydroxy-6-methyl-4H-pyran-4-on; 2,3-dihydrobenzofuran; 3-furancarboxylic acid; 5-hydroxymethyl-2-furaldehyde; ethyl-4-riboside-propylphenol; pyrocatechin; L-luxose(pentose); 6-deoxyhexoses of L-galactose; ethyl ester of benzoylacetic acid; palmitic acid; homovanilic acid; glucose; 1,4-anhydro-d-mannitol; benzoic acid; Gallic acid [26, 35].

Dried extract mixed with water and ethyl alcohol in any ratio has a yellow-brown color. The average value of quercetin in this extract is specified in the calibration schedule using the standard sample of quercetin (Sigma, 98%) amounts to 0.66%. The amount of quercetin in the dry residue of the extractive substances from 10 g of dry *Gratiola officinalis* grass, established by liquid chromatography (HPLC), was 350 μg.

The authenticity of the extract of *Gratiola officinalis* is confirmed by the qualitative reactions with the crystalline magnesium reagent and Wagner-Bouchard. Qualitative reactions indicate the presence of bioflavonoids and the absence of alkaloids in the extract.

We used the concentration of the extract at which its apoptotic effect and the ability to cause (or not to cause) autophagy were obvious, preliminary work on the analysis and selection of extract concentrations was carried out earlier [36].

2.1 Cell line

The following cultures of human tumor cells from the Bank of cell lines of the National Medical Research Center of Oncology named after N. N. Blokhin were used in the studies: human breast carcinoma SK-BR-3, human kidney carcinoma A-498. Studies on cell cultures were conducted at the Core Facilities of Saratov State Medical University named after V. I. Razumovsky.

Cell lines were cultured at 37 °C in an atmosphere of 5% CO_2 in a complete nutrient medium RPMI-1640 (Paneco, Russia): 10% embryonic calf serum (TPP, HyClone, USA); 2 mg/ml glutamine (Paneco, Russia), 50 mg/ml penicillin streptomycin (Paneco, Russia).

The cells were grown on the slides up to 70% of the monolayer. After incubation with the test extracts for 24 h, cells were fixed in alcohol and acetone, then they were stained with Hoechst 33258 dye (1 μg/ml, PanEco, Russia). Cells were covered with coverslips using fluorescent mounting medium (Dako, Denmark), the samples were analyzed by a Nikon 80i fluorescence microscope (Japan) at 435–485nm.

The following parameters were used in the analysis of cells stained with Hoechst 33258: *average number of living cells (ANLC) in the field of view*; *culture growth activity* is ratio of average number of exposed cells in the field of view to the average number of all cells in the field of view in control samples; *absolute number of mitoses* in the field of view; percentage of cells in mitosis (total number of cells); *mitotic activity index* is ratio of number of cells in mitotic stages to the total number of cells in the field of view, multiplied by 100; absolute number of apoptosis in the field of view; *apoptotic activity index* is the ratio of cells in apoptosis to the total number of cells in the field of view, multiplied by 100; the ratio of cells with pycnosis to the total number of cells with signs of apoptosis (%); the ratio of apoptotic bodies to the total number of cells with apoptotic signs (%).

The cells in each group were counted in at least 10 fields of view at 200× magnification.

2.2 Determination of apoptosis by double staining with Annexin and Propidium iodide

Apoptosis induction was studied after incubation of cell lines with *Gratiola officinalis* extract at a concentration of 0.88 mg/ml for 24 h. The study was carried out using the Annexin-V FITC Apoptosis Kit (Invitrogen). Annexin-V binds to phosphatidylserine, which exits the cell membrane in the early stage of apoptosis. Propidium iodide (PI) binds to the DNA of destroyed cells and it is a marker of late-stage apoptosis or necrosis.

To set the reaction, the cells were removed, washed in PBS and resuspended in an Annex-binding buffer in the amount of 1 million cells/ml, then 100 μl cells were transferred to tubes containing 5 μl Annexin-V-FITC and 5 μl PI and incubated at room temperature in the dark for 15 min.

Then 400 μl of the annexin-binding buffer was added and cells were counted on a flow cytometry (FACS Canto II, Becton Dickenson).

2.3 Determination of the induction of autophagy

Determination of the induction of autophagy was performed on the Muse cell analyzer (Millipore, Sigma) with the Muse reagents Autophagy LC3-Antibody Based Kit (Abcam, USA).

Kidney carcinoma cell lines were treated with *G. officinalis* extract in different concentrations at two-fold dilutions, starting at 3.6 mg/ml for a day: 3.6; 1.8; 0.9; 0.45; 0.225; 0.113; 0.056; 0.028; 0.014; 0.007; 0.004 mg/ml. Cells were stained for LC3B protein (Muse Autophagy LC3-Antibody Based Kit (Millipore Sigma)), cell nuclei were stained with Hoechst 33258 dye. As a result of staining with LC3-Antibody reagents, cells acquired a dull red glow when autophagosomes formed, and a bright scarlet glow when autophagosomes bound to lysosomes and the digestion started. The indicators were compared: Mean Autophagy Intensity and Autophagy Induction Ratio at different Concentration of extract. Indicators were calculated automatically on Millipore Sigma.

2.4 Statistical analysis

The normality of the group distribution was tested using the Shapiro-Wilk criterion. The Cramer-Welch criterion (T) was used to compare the obtained mean values, in which the difference of the arithmetic mean of the two samples (control and experimental) is divided by the natural estimate of the standard deviation of this difference. With this method, the difference in the mean is determined with a 95% probability at $T \geq 1.96$ at a significance level of $p < 0.05$. All statistical analyses are performed by using STATISTICA 10.0 Enterprise software.

3 Results and discussion

3.1 Analysis of apoptotic activity in tumor cells of lines A-498 and SK-BR-3 using double staining with annexin V and propidium iodium

Cell lines were incubated with *Gratiola officinalis* extract at a concentration of 0.88 mg/ml. Annexin V labelled with FITC, stained cells in early apoptosis phase. Double staining with annexin and propidium iodide indicated the presence of late apoptosis phase in cells.

As a result, the *Gratiola officinalis* extract showed antitumor activity against all tested human tumor cells (Fig. 1).

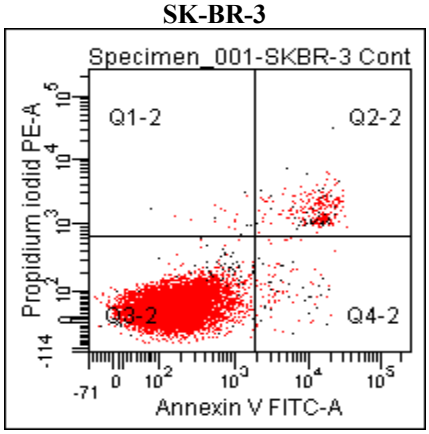
An increase in the number of apoptotic cells was observed in all studied human tumor cell lines under the action of *G. officinalis* extract at a concentration of 0.88 mg/ml, in contrast to the control (Fig. 1).

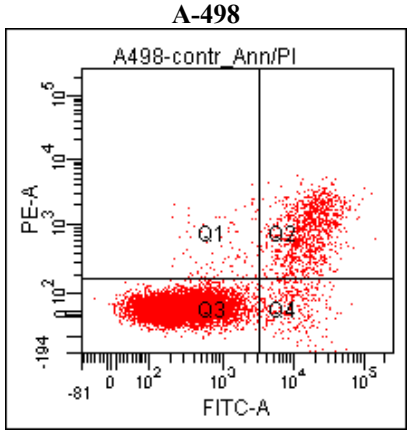
After one day, mainly cells in late apoptosis phase were detected: $96.3 \pm 2.7\%$ of SK-BR-3 breast carcinoma cells and $89.5 \pm 3.3\%$ of A-498 kidney carcinoma cells at tested concentration of *G. officinalis* extract (Fig. 1).

However, the A-498 kidney carcinoma culture was also characterized by an increase in the number of cells in early apoptosis phase to $6.4 \pm 1.8\%$. These results confirm the fact of varying degrees of sensitivity of tumor cells to the extract, but all studied cultures were susceptible to the effects of *G. officinalis* extract, which caused the activation of apoptosis.

SK-BR-3 **A-498**

Control group

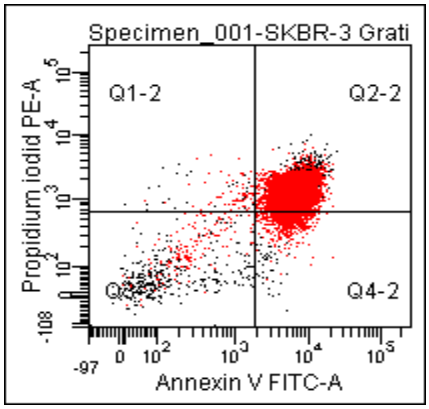


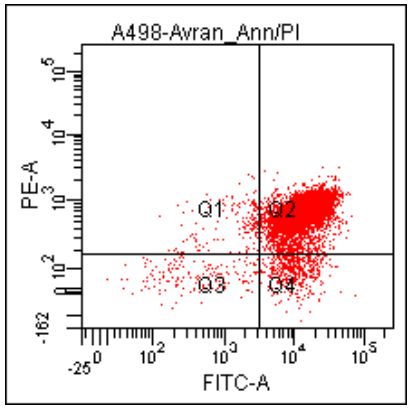


Square Q3 – Living cell (AnV^-/PI^-), 96.7%;
Square Q4 – Early apoptotic cells (AnV^+/PI^-), 0.9%;
Square Q2 – Late apoptotic cells (AnV^+/PI^+), 2.3%;
Square Q1 – Necrotic cells (AnV^-/PI^+), 0.2%

Square Q3 – Living cell (AnV^-/PI^-), 82.9%;
Square Q4 – Early apoptotic cells (AnV^+/PI^-), 3.8%;
Square Q2 – Late apoptotic cells (AnV^+/PI^+), 12.2%;
Square Q1 – Necrotic cells (AnV^-/PI^+), 1.1%

After incubation with Gratiola extract





Square Q3 – Living cell (AnV^-/PI^-), 1.3%;
Square Q4 – Early apoptotic cells (AnV^+/PI^-), 1.5%;
Square Q2 – Late apoptotic cells (AnV^+/PI^+), 96.3%;
Square Q1 – Necrotic cells (AnV^-/PI^+), 0.9%

Square Q3 – Living cell (AnV^-/PI^-), 2.1%;
Square Q4 – Early apoptotic cells (AnV^+/PI^-), 6.4%;
Square Q2 – Late apoptotic cells (AnV^+/PI^+), 89.5%;
Square Q1 – Necrotic cells (AnV^-/PI^+), 2.0%

Fig. 1 Percentage distribution of tumor cells after incubation with *Gratiola officinalis* extract and control group according to flow cytometry. Square Q3 – Living cell, Square Q4 – Early apoptotic cells, Square Q2 – Late apoptotic cells, Square Q1 – Necrotic cells. Control: a) SK-BR-3, b) A-498. *Gratiola officinalis* extract: c) SK-BR-3; d) A-498.

However, the A-498 kidney carcinoma culture was also characterized by an increase in the number of cells in early apoptosis phase to 6.4 ± 1.8%. These results confirm the fact of varying degrees of sensitivity of tumor cells to the extract, but all studied cultures were susceptible to the effects of *G. officinalis* extract, which caused the activation of apoptosis.

3.2 Analysis of apoptotic activity at different extract concentrations in the cell line of breast carcinoma (SK-BR-3) by immunocytochemical method

In the control of cell culture SK-BR-3 in a day the average number of living cells (ANLC) was 365 cells, 0.68% of which were at the stages of metaphase, anaphase and telophase of mitosis and 0.56% in the form of apoptotic cells. In this case, the chromatin of the cell nuclei was not intensely colored (Fig. 2).

After incubation with *Gratiola officinalis* extract in a concentration of 0.0352 mg/ml, an increase of 1.2 times the ANLC was observed compared to the control. The data showed an increase in proliferative activity, apparently due to the cytoprotective effect of the extract. At the same time, the number of cells in mitosis at the stage of metaphase, anaphase and telophase did not differ from the control (Fig. 2, Table 1).

The number of cells in apoptosis increased by 3.5 times compared to the control. At the same time, all cells with signs of apoptosis were represented by apoptotic corpuscles (Table 1, Fig. 2).

Table 1 Comparison of viability and death of SK-BR-3 tumor cells after extract exposure.

Groups	ANLC	Index of proliferation	Fraction of metaphase, anaphase and telophase, %	Fraction of cells in apoptosis (in field of view), %	Fraction of cells in apoptosis (in the field of view), %	
					with pyknosis	with apoptotic cells
Control	365 ± 24.59	–	0.68 ± 0.13	0.56 ± 3	0	0
after *Gratiola* extract exposure						
0.0352 mg/ml	454 ± 14.9*	1.24	0.56 ± 0.14	1.96 ± 0.37**	0	100
0.176 mg ml	354.6 ± 4.2	0.97	0.46 ± 0.15	2.3 ± 0.04*	25	75
0.88 mg/ml	236.6 ± 7.8***	0.65	0***	86.3 ± 1.4***	100	0

Note: proliferation index is the ratio of ANLC after extract exposure to ANLC in the control. Differences are significant between values of experimental and control groups at (*) $p < 0.05$; (**) $p < 0.005$; (***) $p < 0.001$.

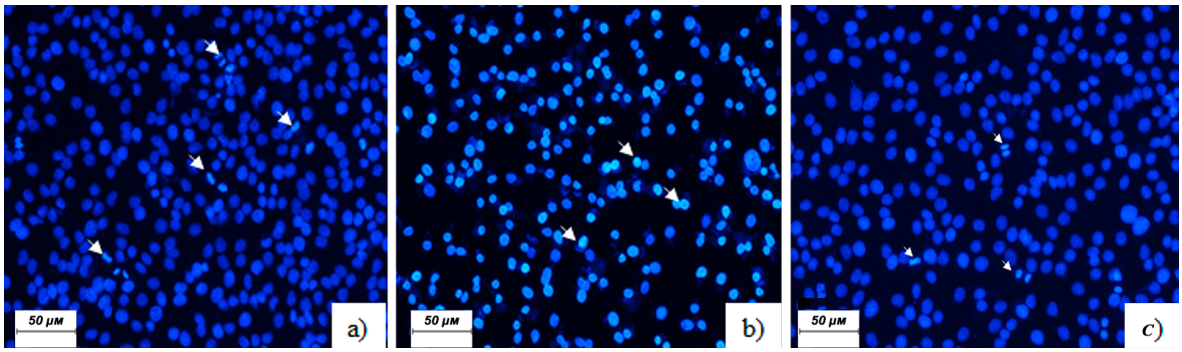


Fig. 2 The breast carcinoma cell line SK-BR-3 after incubation with *Gratiola* extract at a concentration of: a) 0.0352 mg/ml. The cells in process of mitosis are marked with the arrows: b) 0.88 mg/ml. The nuclei in condition of a pyknosis are marked with the arrows; c) control – the cells in process of mitosis are marked with the arrows. The fluorescence mode at 435–485 nm, the color of the dye Hoechst 33258. Magnification 200×.

At exposure of *Gratiola officinalis* extract in a concentration of 0.176 mg/ml, ANLC and the number of cells in mitosis (at the stages of metaphase, anaphase and telophase) did not differ from the control (Table 1). The number of cells with signs of apoptosis increased by 1.6 times, most of which were detected in the form of apoptotic cells (75%), the remaining cells are with nuclear pyknosis (25%), which was expressed in bright staining of the nuclei.

At incubation with *Gratiola officinalis* extract in a concentration of 0.88 mg/ml (Fig. 2) there was a 35% decrease in ANLC compared to control and no cells at the stages of metaphase, anaphase and telophase of mitosis (Table 1). Such data indicate the presence of cytostatic activity in the extract, due to the lack of cytoprotective action in high concentrations. The vast majority of cells (86%) were in apoptosis; namely, with condensed brightly colored chromatin of the nucleus (Fig. 2, Table 1). Such results indicated the presence of expressed apoptotic activity in the extract.

The half of the cells with signs of apoptosis (AC50) were determined per day in comparison with the control at 0.815 mg/ml concentration of *Gratiola officinalis* extract.

Thus, *Gratiola officinalis* extract in all concentrations had apoptotic activity against breast carcinoma cells SK-BR-3, which was consistent with the data of flow cytometry. At low concentrations (0.0352 mg/ml) extract had cytoprotective activity, which was concentration-dependent.

At double staining with Annex V and propidium iodide, the apoptotic activity of *Gratiola officinalis* extract at a concentration of 0.88 mg/ml in respect of SK-BR-3 cells were in good agreement with the data obtained at Hoechst staining. Thus, if flow cytometry revealed 96.3% of late apoptotic cells, Hoechst staining revealed 86.3% of cells in apoptosis.

3.3 Analysis of autophagic activity of Gratiola officinalis extract in cell line of human kidney carcinoma A-498

Cells of kidney carcinoma line A-498 were treated with *Gratiola officinalis* extract in different concentrations in two-fold dilution, ranging from 3.6 mg/ml: 3.6; 1.8; 0.9; 0.45; 0.225; 0.113; 0.056; 0.028; 0.014; 0.007; 0.004. Cells were stained with LC3 marker, cell nuclei were stained with Hoechst. As a result, the cells acquired a dull red glow when autophagosomes were formed. A bright scarlet glow

appeared when autophagosomes were associated with lysosomes and the process of digestion took place (Fig. 3). Fig. 4 shows the induction of autophagy in human kidney carcinoma A-498 cells in the control and under the action of *Gratiola officinalis* extract in concentrations ranging from 0.028 to 0.45 mg/ml.

In the control, the autophagy induction coefficient was 1, starting with the extract concentration of 0.004 mg/ml, the autophagy induction coefficient increases, reaching a maximum at a concentration of 0.056 mg/ml. When the concentration of the extract increased, the coefficient of induction of autophagy decreased and returned to the initial state (Fig. 3, Table 2).

The dependence of cells with autophagosomes and autophagolysosomes was generally linear; the distribution was normal: the maximum number of autophagolysosomes in kidney carcinoma cells was observed at 0.056 mg/ml extract concentration.

Muse Autophagy LC3-Antibody Based Kit revealed a dull red glow of cells when autophagosomes formed, and a bright scarlet glow when autophagosomes bound to lysosomes and the digestion started.

There is no unequivocal opinion in the literature on the significance of autophagy in tumor cells nowadays. Some authors have reported a better prognosis in patients with autophagosomes in tumor cells [37], but most researchers believe that LC3b expression is associated with an unfavorable prognosis [38–40]. All authors agree that autophagy can develop in tumor cells as a protective mechanism of the tumor cell in response to the treatment [38–41], as we prove in our study.

Thus, we demonstrate that there is an activation of autophagy in kidney carcinoma cells under the action of low concentrations of *Gratiola officinalis* extract, which explains the mechanism of its cytoprotective activity that we also found in an experiment on SK-BR-3 breast carcinoma cells.

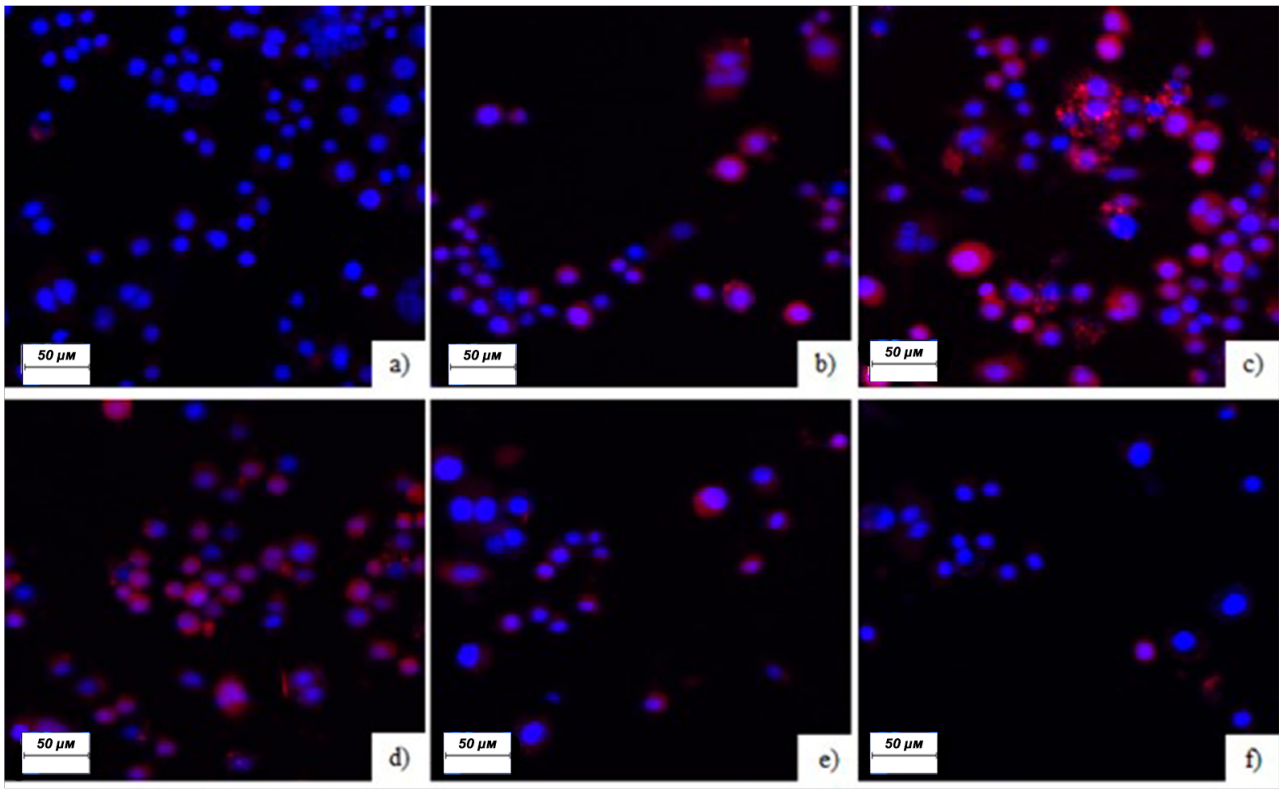
The increase in the number of living SK-BR-3 cells was observed under the influence of extract in 0.0352 mg/ml concentration. The significant increase in autophagy in A-498 cells was observed after incubation with extract within the range concentrations from 0.028 to 0.45 mg/ml. The maximum number of autophagolysosomes was observed in kidney carcinoma cells after incubation with extract in 0.056 mg/ml concentration. Whereas after extract exposure in 0.88 mg/ml concentration, no increase in autophagosome formation was detected (Table 2), but apoptosis was pronounced (Fig. 1).

Induction of autophagy at low concentrations of the extract, on the one hand, indicates sensitivity of tumor cells of the A-498 line in response to exposure to *G. officinalis* extract.

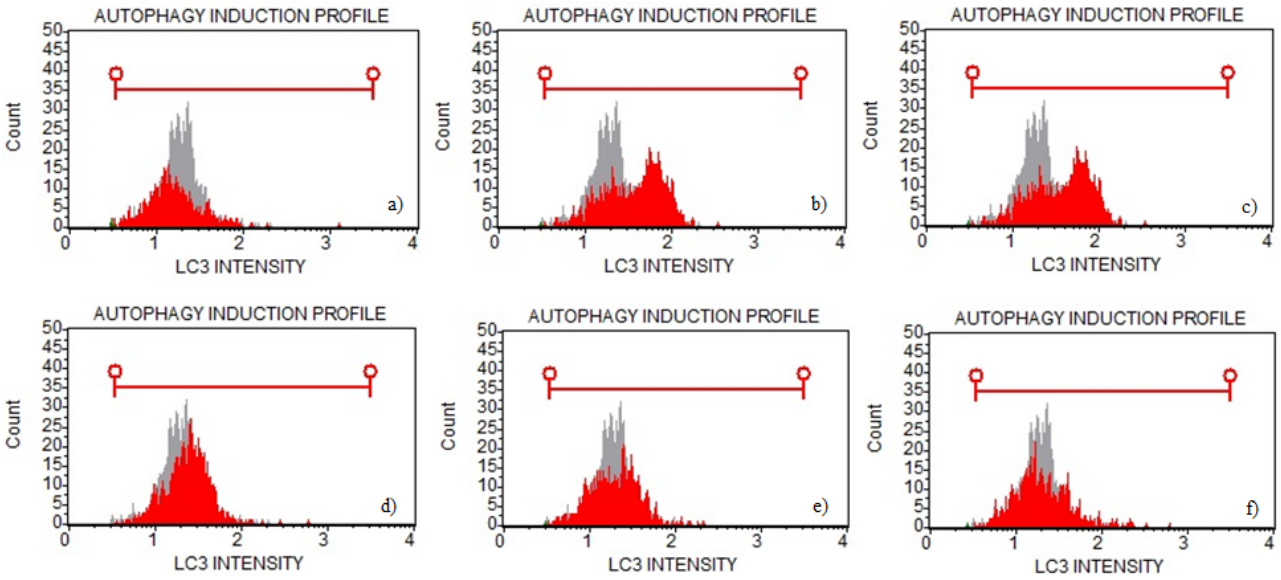
Table 2 Percentage distribution of kidney carcinoma tumor cells (A-498) with autophagosomes after *Gratiola officinalis* extract exposure at different concentrations for 24 h according to flow cytometry

Concentration of extract (mg/ml)	**Mean Autophagy Intensity**	**Autophagy Induction Ratio**	**Total of cells**
0 (control)	22.2 ± 1.5	1	739 ± 41
3.6	24.3 ± 2.3	1.1	**447 ± 20***
1.8	**27.4 ± 3.2***	1.2	**479 ± 24***
0.9	25.8 ± 2.1	1.2	**431 ± 19***
0.45	**28.5 ± 3.4***	1.3	585 ± 28*
0.225	25 ± 1.7	1.1	605 ± 31*
0.113	29.5 ± 2.4	1.3	707 ± 38
0.056	**50.3 ± 4.8***	2.3	694 ± 28
0.028	31.1 ± 2.5*	1.4	699 ± 25
0.014	25.5 ± 1.9	1.2	683 ± 27
0.007	**27.8 ± 2.1***	1.3	**657 ± 23***
0.004	25.8 ± 1.8	1.2	649 ± 25*

Note: Differences are significant between values of experimental and control groups at (*) $p < 0.05$.



(A)



(B)

Fig. 3 Induction of autophagy in human kidney carcinoma cells A-498 in control and after *Gratiola officinalis* extract exposure in various concentrations a) control; b) the extract concentration was 0.028 mg/ml), c) the extract concentration was 0.056 mg/ml; d) the extract concentration was 0.113 mg/ml; e) the extract concentration was 0.225 mg/ml; f) the extract concentration was 0.45 mg/ml. On the above (A) shows cells with double staining for LC3B protein (red and red) and Hoechst dye (blue color); below (B) – autophagosome induction after *Gratiola officinalis* extract exposure (flow cytometry results).

On the other hand, a cascade of events occurred: under the influence of low concentrations of the extract (0.056 mg/ml), cytoprotective autophagy was induced in the tumor cell, resulting in cell survival and resistance to exposure. However, at a higher concentration of 0.88 mg/ml, activation of apoptosis occurred in kidney carcinoma cell culture. In our opinion, the cytoprotective

autophagy is blocked at higher concentrations of the extract and cells die in a non-programmed way.

Activation of the mechanisms of autophagy, apoptosis, necrosis may occur under the influence of different components of the extract.

Thus, apigenin, described as component of the *G. officinalis* extract, is structurally related to the flavonoid Wogonin [4–6]. Wogonin is known to have an apoptotic effect on a wide range of human tumor cells in *in vitro* experiments and an inhibitory effect on tumor growth *in vivo* in various mouse tumor models [6–9, 41, 42]. Wogonin and structurally related natural flavones such as apigenin, chrysin and luteolin are inhibitors of cyclin-dependent kinase 9 (CDK9) and block-phosphorylation of the carboxy-terminal domain of RNA polymerase II in Ser(2). This effect leads to a decrease in ribonucleic acid synthesis, followed by rapid suppression of Mcl-1 and activation of apoptosis in tumor cell [4–6]. The *G. officinalis* extract causes tumor cell death and has no toxic effect on normal cells, that is similar with effects of the flavonoids in *Scutellaria baicalensis Georgi* extract, it has been demonstrated in both *in vitro* and *in vivo* experiments [6–9].

4 Conclusion

The antitumor effect of the *G. officinalis* extract has been shown on cell cultures of two human tumor lines: SK-BR-3 breast carcinoma and A-498 kidney carcinoma. The extract at concentration of 0.815 mg/ml causes apoptosis in half of the cells (AC50). However, in low concentration (0.0352 mg/ml), the extract has cytoprotective activity. This effect has a concentration dependence. The mechanism of cytoprotective activity of the extract in low concentrations is realized by activation of autophagy, which provides resistance of tumor cells to the therapeutic action. The maximum number of autophagosomes in carcinoma cells was observed at an extract concentration of 0.056 mg/ml.

Thus, *G. officinalis* extract is a multicomponent flavonoid-containing composition, with a polyvalent effect, which form its "shrapnel" effect. The polyvalence of the therapeutic effect and the mutual potentiation of extract's effects with a proven broad spectrum of action is an undeniable advantage of this extract in complex chemotherapy. Detailed research should be continued to decipher and understand the mechanisms of antitumor activity of the individual components of the *G. officinalis* extract.

Disclosures

All authors declare that there is no conflict of interests in this paper.

Acknowledgments

The reported study was funded by project №SSMU-2021-003 of Saratov State Medical University named after V. I. Razumovsky.

References

1. E. D. Goldberg, A. B. Syrkina, "Guidelines for the preclinical study of agents with the ability to inhibit the process of metastasis and increase the effectiveness of cytostatic therapy of malignant tumors," in The Guidelines for experimental (preclinical) study of new pharmacological substances, R.U. Khabriev (Ed.), Meditsina, Moscow (2005). ISBN: 5-225-04219-8.
2. D. B. Korman, "Targets and mechanisms of anticancer drugs," Practical Medicine, 333 (2014).
3. V. M. Perelmuter, M. V. Zavjalova, S. V. Vtorushin, E. M. Slonimskaya, and O. V. Savenkova, "Association between the morphologic heterogeneity of infiltrating ductal breast carcinoma and various forms of tumor progression," Siberian Journal of Oncology 3, 58–64 (2007).
4. G. Polier, J. Ding, B. V. Konkimalla, D. Eick, N. Ribeiro, R. Köhler, M. Giaisi, T. Efferth, L. Desaubry, P. H. Krammer, and M. Li-Weber, "Wogonin and related natural flavones are inhibitors of CDK9 that induce apoptosis in cancer cells by transcriptional suppression of Mcl-1," Cell death & disease 2(7), e182 (2011).
5. D. Patel, S. Shukla, and S. Gupta, "Apigenin and cancer chemoprevention: progress, potential and promise (review)," International Journal of Oncology 30(1), 233–245 (2007).
6. G. Seelinger, I. Merfort, U. Wolfle, and C. M. Schempp, "Anti-carcinogenic effects of the flavonoid luteolin," Molecules 13(10), 2628–2651 (2008).
7. C. F. Tsai, W. L. Yeh, S. M. Huang, T. W. Tan, and D. Y. Lu, "Wogonin induces reactive oxygen species production and cell apoptosis in human glioma cancer cells," International Journal of Molecular Sciences 13(8), 9877–9892 (2012).
8. H. Chung, Y. M. Jung, D. H. Shin, J. Y. Lee, M. Y. Oh, H. J. Kim, K. S. Jang, S. J. Jeon, K. H. Son, and G. Kong, "Anticancer effects of wogonin in both estrogen receptor-positive and -negative human breast cancer cell lines in vitro and in nude mice xenografts," International Journal of Cancer 122(4), 816–822 (2008).
9. M. Li-Weber, "New therapeutic aspects of flavones: the anticancer properties of Scutellaria and its main active constituents wogonin, baicalein and baicalin," Cancer Treatment Reviews 35(1), 57–68 (2009).
10. J. Peng, Q. Qi, Q. You, R. Hu, W. Liu, F. Feng, G. Wang, and Q. Guo, "Subchronic toxicity and plasma pharmacokinetic studies on wogonin, a natural flavonoid, in Beagle dogs," Journal of Ethnopharmacology 124(2), 257–262 (2009).

11. D. Bown, Encyclopaedia of Herbs and their Uses. The Royal Horticultural Society, Dorling Kindersley Limited, London, UK (1995).
12. E. Launert, Edible and Medicinal Plants, Hamlyn, London (1981).
13. M. Zia-Ul-Haq, A. Kausar, S. A. Shahid, M. Qayum, S. Ahmad, and I. Khan, "Phytopharmacological profile of Gratiola officinalis Linn.: A review," Journal of Medicinal Plants Research 6(16), 3087–3092 (2012).
14. M. Ahmad, N. Muhammad, J. Mehjabeen, N. Jahan, M. Ahmad, and S. Habib, "Pharmacological and biological evaluation of extracts from Gratiola officinalis L. (Scrophulariaceae)," Pakistan Journal of Pharmaceutical Sciences 25(3), 657–663 (2012).
15. N. Muhammad, M. Ahmad, Mehjabeen, N. Jahan, M. Ahmad, and Z. Khan, "Spasmogenic and spasmolytic activity of Gratiola officinalis Linn," International Journal of Biology, Pharmacy and Allied Sciences 1(5), 636–644 (2012).
16. J. Lust, The Herb Book, Bantam Books, USA (1974).
17. G. Graves, Medicinal Plants, Bracken Books, Randam House, London (1996).
18. L. Ali, T. S. Rizvi, M. Ahmad, and F. Shaheen, "New iridoid glycoside from Gratiola officinalis (Scrophulariaceae)," Journal of Asian Natural Product Research 14(12), 1191–1195 (2012).
19. S. Boryczka, E. Bebenek, M. Jastrzebska, J. Kusz, and M. Zubko, "Crystal structure of betulinic acid-DMSO solvate," Zeitschrift für Kristallographie 227(6), 379–384 (2012).
20. J. Rothenburger, E. Haslinger, "Caffeic acid glycoside esters from Gratiola officinalis L," Liebigs Annalen der Chemie 11, 1113–1115 (1994).
21. R. J. Grayer-Barkmeijer, F. A. Tomas-Barberan, "8-Hydroxylated flavone-O-glycosides and other flavonoids in chemotypes of Gratiola officinalis," Phytochemistry 34(1), 205–210 (1993).
22. S. Kumar, A.K. Pandey, "Chemistry and Biological Activities of Flavonoids: An Overview," The Scientific World Journal 2013, 162750 (2013).
23. T. Rudolf, H. Annemarie, and U. Triterpene, "Gratiosid, ein Triterpenglykosid aus Gratiola officinalis L," Berichte der deutschen chemischen Gesellschaft Weinheim 85 (11), 1067–1077 (1952).
24. L. I. Borodin, V. I. Litvinenko, and N. V. Kurinnaya, "New flavonoid C-glycosides from Gratiola officinalis," Chemistry of Natural Compounds 6(1), 19–24 (1970).
25. V. I. Litvinenko, L. I. Borodin, and N. V. Kurinnaya, "Apigenin and its glycosides from Gratiola officinalis," Chemistry of Natural Compounds 5(4), 328–329 (1969).
26. N. V. Polukonova, N. A. Durnova, M. N. Kurchatova, N. A. Navolokin, and A. G. Golikov, "Chemical analysis of the new biological active composition from medicative herb hedge-hissop (Gratiola Officinalis L.)," Khimija Rastitel'nogo Syr'ja 4, 165–173 (2013) [in Russian].
27. N. A. Navolokin, A. V. Ivlichev, D. A. Mydrak, and G. A. Afanasjeva, "Influence of flavonoid-containing extract (Gratiola Officinalis L.) on the content of vitamin E and intensity of peroxidation processes in the blood of rats with transplanted liver cancer PC-1," Eksperimental'naya i Klinicheskaya Farmakologiy 80(10), 40–43 (2017) [in Russian].
28. N. A. Navolokin, D. A. Mydrak, N. V. Polukonova, and A. B. Bucharskaya, "Effects of Gratiola Officinalis L. extract containing flavonoids on pathomorphism of inoculated renal cancer in rats," Eksperimental'naya i Klinicheskaya Farmakologiy 80(6), 19–23 (2017) [in Russian].
29. N. A. Navolokin, D. A. Mydrak, N. V. Polukonova, and S. A. Tychina, "Evaluation of the antitumor and anticachexia activity of Gratiola Officinalis L. extract in rats with transplanted sarcoma," Siberian Journal of Oncology 5(1), 37–43 (2016) [in Russian].
30. N. V. Polukonova, N. A. Durnova, and N. N. Khakhulina, "Phytocenoses Gratíola Officinális L., productivity and its inventories of raw materials in the islands chardymskogo r. Volga Saratov region," Bulletin of the Botanical Garden of the Saratov State University 14(2), 56–61 (2016) [in Russian].
31. N. V. Polukonova, N. A. Navolokin, and S. V. Raykova, "Anti-inflammatory, antipyretic and antimicrobial activity flavonoid-containing extract of Gratiola officinalis L," Eksperimental'naya i Klinicheskaya Farmakologiy 78(1), 34–38 (2015).
32. N. V. Polukonova, M. N. Kurchatova, N. A. Navolokin, A. B. Bucharskaya, N. A. Durnova, and G. N. Maslyakova, "A new extraction method of bioflavanoids from poisonous plant," Russian Open Medical Journal 3(3), 304 (2014).
33. N. A. Navolokin, D. A. Mydrak, A. B. Bucharskaya, O. V. Matveeva, S. A. Tychina, N. V. Polukonova, and G. N. Maslyakova, "Effect of flavonoid-containing extracts on the growth of transplanted sarcoma 45, peripheral blood and bone marrow condition after oral and intramuscular administration in rats," Russian Open Medical Journal 6(3), 304 (2017).
34. N. V. Tkachenko, E. V. Bykova, A. B. Pravdin, N. A. Navolokin, N. V. Polukonova, A. B. Bucharskaya, D. A. Mudrak, and A. Y. Prilepskii, "Comparison of membrane-protective activity of antioxidants quercetine and Gratiola officinalis L. extract under conditions of photodynamic haemolysis," Proceedings of SPIE 9917, 99170L (2016).
35. N. A. Navolokin, N. V. Polukonova, G. N. Maslyakova, A. B. Bucharskaya, and N. A. Durnova, "Effect of extracts of Gratiola officinalis and Zea mays on the tumor and the morphology of the internal organs of rats with trasplanted liver cancer," Russian Open Medical Journal 1(2), 0203 (2012).

36. A. Mylnikov, N. Navolokin, D. Mudrak, N. Polukonova, A. Bucharskaya, and G. Maslyakova, "Tumor cell death visualization of renal cell carcinoma under the combined effect of the Gratiola officinalis extract and cyclophosphamide using fluorescent staining methods," Journal of Innovative Optical Health Sciences 14(05), 2142004 (2021).
37. Z. Yang, R. A. Ghoorun, X. Fan, P. Wu, Y. Bai, and J. Li, "High expression of Beclin-1 predicts favorable prognosis for patients with colorectal cancer," Clinics and Research in Hepatology and Gastroenterology 39(1), 98–106 (2015).
38. J. Y. Tang, E. Hsi, Y. C. Huang, N. C. Hsu, P. Y. Chu, and C. Y. Chai, "High LC3 expression correlates with poor survival in patients with oral squamous cell carcinoma," Human Pathology 44(11), 2558–2562 (2013).
39. J. L. Liu, F. F. Chen, J. Lung, C. H. Lo, F. H. Lee, and Y. C. Lu, "Prognostic significance of p62/SQSTM1 subcellular localization and LC3B in oral squamous cell carcinoma," British Journal of Cancer 111(5), 944–954 (2014).
40. K. Lai, S. Matthews, J. S. Wilmott, M. C. Killingsworth, J. L. Yong, N. J. Caixeiro, J. Wykes, A. Samakeh, D. Forstner, M. Lee, J. McGuinness, N. Niles, A. Hong, A. Ebrahimi, and C. S. Lee, "Differences in LC3B expression and prognostic implications in oropharyngeal and oral cavity squamous cell carcinoma patients," BMC Cancer 18, 624 (2018).
41. D. H. Wu, C. C. Jia, J. Chen, Z. X. Lin, D. Y. Ruan, and X. Li, "Autophagic LC3B overexpression correlates with malignant progression and predicts a poor prognosis in hepatocellular carcinoma," Tumor Biology 35(12), 12225–12233 (2014).
42. W. Wang, Q. L. Guo, Q. D. You, K. Zhang, Y. Yang, and J. Yu, "The anticancer activities of wogonin in murine sarcoma S180 both in vitro and in vivo," Biological and Pharmaceutical Bulletin 29(6), 1132–1137 (2006).
43. S. Baumann, S. C. Fas, M. Giaisi, W. W. Muller, A. Merling, and K. Gulow, "Wogonin preferentially kills malignant lymphocytes and suppresses T-cell tumor growth by inducing PLCgamma1- and Ca2+-dependent apoptosis," Blood, The Journal of the American Society of Hematology 111(4), 2354–2363 (2008).

Devices for Photodynamic Studies Based on Light-Emitting Diodes

Gennady A. Meerovich[1,2*], Kirill G. Linkov[1], Alexei V. Nekhoroshev[2], Alexander V. Borodkin[1], Ekaterina V. Akhlyustina[2], Ivan P. Angelov[3,4], Denis A. Glechik[2], and Victor B. Loschenov[1,2]

[1] Prokhorov General Physics Institute of the Russian Academy of Sciences, 38 Vavilov str., Moscow 119991, Russia
[2] National Research Nuclear University "MEPHI", 31 Kashirskoe shosse, Moscow 115409, Russia
[3] Institute of Organic Chemistry with Centre of Phytochemistry, Bulgarian Academy of Sciences, 9 acad. Georgi Bonchev str., Sofia 1113, Bulgaria
[4] Institute of Electronics, Bulgarian Academy of Sciences, 72 Boulevard Tzarigradsko shose, Sofia 1784, Bulgaria

*** e-mail:** gennadymeerovich@gmail.com

Abstract. Light sources based on light-emitting diodes (LED) can be created for almost any wavelength suitable for exciting photosensitizers (PS). This paper presents the main approaches to develop LED-based light sources for well-controlled photodynamic exposure and the results of their implementation. High power density LED light sources were designed and tested for both in vitro and in vivo and photodynamic studies, as well as for irradiation of various pathological foci during photodynamic therapy. © 2021 Journal of Biomedical Photonics & Engineering.

Keywords: light emitting diode; power density; wavelength; light divergence; distribution of light energy.

Paper #3457 received 8 Sep 2021; revised manuscript received 25 Oct 2021; accepted for publication 26 Oct 2021; published online 11 Nov 2021. doi: 10.18287/JBPE21.07.040308.

1 Introduction

The photodynamic action (PDA) causes photo-oxidative destruction of molecular structures important for functioning of tumor cells and pathogens such as bacteria and viruses. Photosensitizer (PS) molecules catalyze the generation of reactive oxygen species (ROS) upon excitation with light. Light transfers the energy necessary for this process to the medium containing the PS. However, only part of the light energy is absorbed by PS. The relative absorbed photodynamic dose (RAPD) [1] depends on properties of PS (extinction, concentration in a sensitized medium, wavelength and shape of the spectral contour at this concentration) and properties of the medium (scattering and absorption by endogenous pigments and other components, in particular, hemoglobin and water). PDA is enhanced with increasing the volume density of the energy absorbed by PS, which depends on the light intensity and the RAPD.

Light-emitting diodes (LED) are widely used as light sources for PDA [2–7]. These sources provide light with high intensity, and their light spectrum is narrow ($\Delta\lambda_{LED}$ = 20–30 nm) in comparison with the spectral width of the PS absorption band. LED can generally be created with most wavelengths suitable for PS excitation (at least in the red and near infrared spectral ranges).

Modern LEDs form a diverging beam of light with a power of up to hundreds of milliwatts coming out of the surface of chip with dimensions of less than 2 mm^2. The light power density is uniformly distributed over the chip surface, but non-uniformly distributed over the angle. Installing a short-focus semi-spherical lens close to the chip can significantly reduce the angle in which the main part of the light power is concentrated, but an angle distribution of power density after this lens remains non-uniform. Typically, the such LED with a lens has a bell-shaped angular distribution of power, close to a Gaussian distribution, and consequently the light power density distribution of such a single high power LED on irradiated surface of any significant size will be non-uniform. Angular divergence of LED light can be characterized by the value of the characteristic angle at which the light intensity decreases to the level of 1/e of the value perpendicular to the LED surface.

For many applications, it is important to ensure a uniform light power density over the irradiated area (in particular, for multi-sample PDA studies in microplates, it is advantageous to be able to uniformly irradiate a large area with dimensions of at least 8×12 cm or 14.5 cm in diameter). This requires designing special LED sources with the proper spatial uniformity of the light power density at some distance. As a solution of this problem a

matrix device was created that contained a large number of identical LEDs [8], however, it was an insufficient approach since power density in the peripheral part of irradiated zone at about half of the power density at the center of it. To compensate for this inhomogeneity, it was necessary to use separate regulation and power supply of LEDs [9], which significantly increased the cost and complicated the devices. But such a device, being a set of local LEDs, can align values only in those specific wells, the centers of which are located strictly along the axis of the LED light beam. Due to the finite geometric dimensions of the LED, it is almost impossible to equalize the power density in all wells of multi-well (96 or more wells) plates.

The main approaches to the use of LED for PDA are related to the spatial distribution of the exciting light energy, which should ensure its efficient use for PS excitation. The sources of light based on LED can be used to irradiate tumor foci of both small (about 1 cm) sizes and superficial foci of a large area. An important task in photodynamic therapy of tumors is to achieve a high intensity of PDA in the deep layers of tumor nodes, which makes it necessary to provide high values of the light energy absorbed by the PS in these layers. The main loss of light energy in biological tissue is caused by the absorption of endogenous substances (hemoglobin and water), the total absorption of which is minimal in the range of 660–950 nm (so-called "spectral window of bio-tissue transparency"). The absorption of melanin (in the skin of dark-skinned patients, as well as in PDT of melanoma) can also decrease the density of light power in the deep layers of the tumor and reduce the effectiveness of PDT. Another approach of using LEDs for PDA is photodynamic inactivation (PDI) of pathogens [10, 11]. PDI is usually carried out on surfaces of a sufficiently large area in thin layers of a sensitized biological medium. PDA in thin sensitized layers is also executed during in vitro screening studies of PS, that are carried out to assess the sensitivity of different cells to PDT, to study its mechanisms and properties of PS [6, 12]. For small layer thickness and low PS concentrations (less than 10 μM) used for such a PDA, a significant part of the light can pass through the layer without participating in the PDA process. This loss results in decreased PDA efficiency. It can also lead to errors in screening studies of PS with various extinction and concentration since both the losses and the amount of the absorbed energy in the sensitized layer for various PS will be different. To increase the efficiency of the PDA in thin layers, the LED wavelength should be close to the spectral absorption maximum of the PS [13].

2 Results and Discussion: New LED Devices for PDA

Our study used a number of PS with excitation maxima within ranges of 662–665 nm (methylene blue, as well as chlorin derivatives Radachlorin, Photoran and Photolon), 670–675 nm (Photosens), 682–686 nm (Cholosens), 760–765 nm (derivatives of synthetic bacteriochlorin). The wavelength of excitation light was usually chosen near the spectral maximum of the PS absorption band. Light sources of suitable wavelengths required for PS excitation were designed using LED models (LC-1DR-G30 for the spectral range of 660–665 nm, LC-1IR1-G42 for 680–690 nm, LC-1IR3-G42 for 760–770 nm) manufactured by Shenzhen Cai Mingzhu Co., LTD (China).

Power and power density of the incident light as well as homogeneity of its distribution within the illuminated area were evaluated with the PM180T Power Meter (Thorlabs GmbH, Germany). Spectra of emission of illumination devices were recorded using fiber optic spectra-analyzer LESA-01-BIOSPEC (Biospec Ltd, Russia).

A range of compact devices intended for different spectral ranges based on single powerful LED with an optical projecting system the chip image onto the irradiated foci have and a miniature cooling system has been created for the irradiation of small tumor foci. Developed devices (Fig. 1) provided irradiation of areas with dimensions that can be adjusted by the optical system from 0.8×0.8 cm to 3×3 cm. The light power of devices reached 160 mW; the inhomogeneity of the power density over the irradiated area in all cases did not exceed ±7%. Optimum light power density and uniformity was achieved at a distance of 8–12 cm from the device. Such a compact powerful device is very useful and convenient both in clinical application for photodynamic therapy of small skin, head and neck tumors, as well as and in experimental oncology for PDT of model tumors of laboratory animals.



Fig. 1 Device based on single powerful LED.

A powerful device based on a group of LED, equipped with a heat sink in the shape of a segment of a spherical surface, has been developed to irradiate large surface tumor nodes. The optical axes of the LED light beams with a light divergence of about 48° are directed to the center of the spherical surface. This design made it possible to evenly distribute the light of 36 powerful LED in the irradiated area while keeping compact arrangement of LEDs and providing good conditions for heat

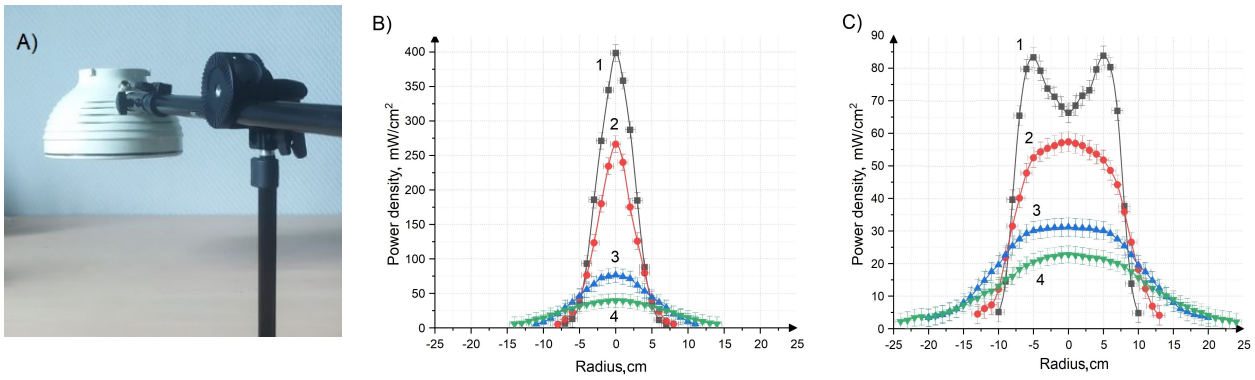


Fig. 2 Powerful device based on a group of LED: A) device with a manipulator for adjusting the aiming at the irradiated area; B) bell-shaped distribution of power density; C) uniform distribution of power density. Distances between the device and irradiated surface asfollows: (1) 8 cm, (2) 12.5 cm, (3) 18.5 cm, (4) 22 cm.

dissipation (Fig. 2A). The device forms a light spot in the irradiation zone with an area of about 20 cm^2 and a bell-shaped distribution of the power density reaching about 400 mW/cm^2 at the center of the spot (Fig. 2B). Such a powerful device is used for photodynamic therapy of large superficial tumors, in particular, basal cell skin cancer.

The above device was modified for highly uniform irradiation of large areas, in particular, for in vitro multi-sample PDA studies in standard 96-well or similarly sized microplates. To increase the uniformity of the power density on the irradiated plate, the LEDs located near the center of the in the mount had lower divergence of light beam of about 23°), while LEDs at the periphery – larger of about 48°. Such arrangement provided a high uniformity of a power density of light with an average value of about 25 mW/cm^2 and deviation below to ±10% over an area exceeding 100 cm^2 (Fig. 2C).

Increasing this distance will make it possible to implement uniform irradiation of a sufficiently large area (about 1000 cm^2) with light power density of about 2.5 mW/cm^2, which can be used for photodynamic antiviral disinfection [11].

Another group of light sources has been developed based on single high-power LEDs of different spectral ranges to use in studies of PDA *in vitro* in individual optical cells of 1×1 cm size. The optical system of the device projected the image of the chip onto the surface of the sensitized layer in the optical cell containing sensitized biological objects and provided uniform PDA in them. The devices are equipped with a system of optical fibers (Fig. 3), which also made it possible to investigate the fluorescence, absorption and scattering in sensitized layer during PDA, as well as to evaluate the concentration and state of irradiated PS and biological micro-objects. This has been used to study the photodynamic inactivation of viruses and bacteria [11, 14].

Developed devices were powered from adapters through programmable timers to ensure a given dose of light irradiation, which can also operate in a periodic mode to study the dependence of the effect on the irradiation dose and for group studies.

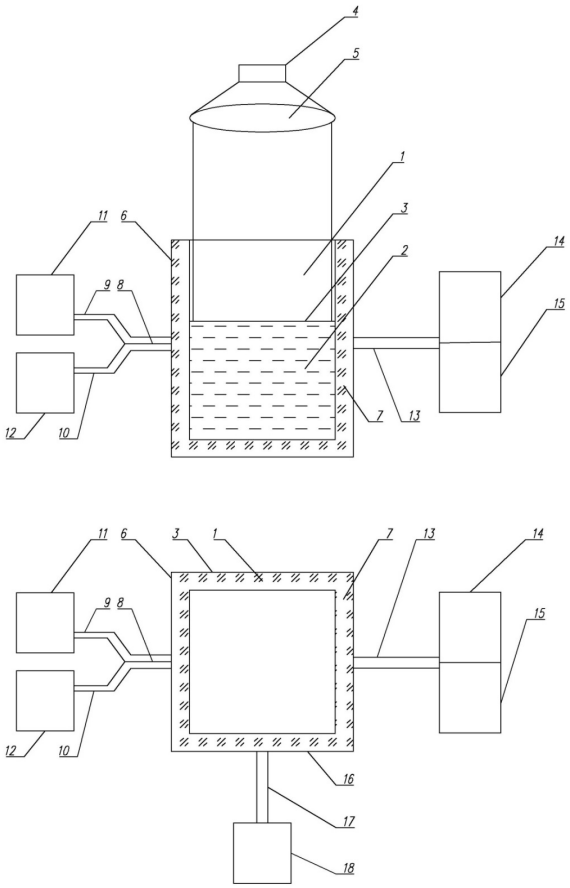


Fig. 3 Functional diagram of a device for *in vitro* PDA research: 1 – optical cell; 2 – sensitized layer containing biological micro-objects; 3 – surface of layer; 4 – LED; 5 – optical projecting system; 6, 7, 16 – transparent walls of optical cell; 8 – optical fiber bundle; 9 – optical fiber connected to the laser 11 output; 10 – fiber connected to the input of the spectra-analyzer; 11 – laser for fluorescence excitation; 12 – spectra-analyzer LESA-01-BIOSPEC; 13 – optical fiber connected to the output of a broadband light source (for absorption studying) or to the output of an additional laser (for scattering studying); 14 – broadband light source; 15 – laser for scattering studying; 17 – optical fiber connected to the input of the dynamic light scattering spectrometer 18.

3 Conclusion

A range of LED sources have been developed with high light power and power density for excitation of photosensitizers of different spectral ranges. They can be widely used as light sources for *in vivo* and *in vitro* photodynamic research and various PDT applications.

Disclosures

All authors declare that there is no conflict of interests in this paper.

Acknowledgments

The research of E. Akhlyustina was funded by RFBR according to the project #20-04-60084.

The research of G. Meerovich and I. Angelov was funded by RFBR and BNSF according to the bilateral project (RFBR #20-52-18008, BNSF #KP- 06- Russia/9- 2020).

References

1. B. W. Pogue, L. Lilge, M. S. Patterson, B. C. Wilson, and T. Hasan, "Absorbed photodynamic dose from pulsed versus continuous wave light examined with tissue-simulating dosimeters," Applied Optics 36(28), 7257–7269 (1997).
2. V. B. Loschenov, K. G. Linkov, T. A. Savelieva, M. V. Loschenov, S. S. Model, and A. V. Borodkin, "Hardware and tool equipment for fluorescence diagnostics and photodynamic therapy," Photodynamic Therapy and Photodyagnosis 2(3), 17–25 (2013) [in Russian].
3. J. Neupane, S. Ghimire, S. Shakya, L. Chaudhary, and V. P. Shrivastava, "Effect of light emitting diodes in the photodynamic therapy of rheumatoid arthritis," Photodiagnosis and Photodynamic Therapy 7(1), 44–49 (2010).
4. A. Erkiert-Polguj, A. Halbina, I. Polak-Pacholczyk, and H. Rotsztejn, "Light-emitting diodes in photodynamic therapy in non-melanoma skin cancers – own observations and literature review," Journal of Cosmetic and Laser Therapy 18(2), 105–110 (2016).
5. E. Sorbellini, M Rucco, and F. Rinaldi, "Photodynamic and photobiological effects of light-emitting diode (LED) therapy in dermatological disease: an update," Lasers in Medical Science 33(7), 1431–1439 (2018).
6. R. I. Yakubovskaya, E. A. Plotnikova , A. D. Plyutinskaya, N. B. Morozova, V. I. Chissov,E. A. Makarova , S. V. Dudkin, E. A. Lukyanets, and G. N. Vorozhtsov, "Photophysical properties and in vitro and in vivo photoinduced antitumor activity of cationic salts of meso-tetrakis (N-alkyl-3-pyridyl)bacteriochlorins," Journal of Photochemistry and Photobiology B: Biology 130, 109–114 (2014).
7. I. Meerovich, M. G. Nichols, and A. K. Dash, "Low-intensity light-induced paclitaxel release from lipid-based nano-delivery systems," Journal of Drug Targeting 27(9), 971–983 (2019).
8. A. V. Belikov, Yu. V. Semyashkina, M. A. Modin, and D. R. Zhubrev, "LED illuminator for photodynamic therapy of onychomycosis," Scientific and Technical Bulletin of Information Technologies, Mechanics and Optics 17(5), 782–789 (2017).
9. N. Yu. Shilyagina, I. V. Balalaeva, I. V. Turchin, N. M. Shakhova, V. I. Plekhanov, and A. A. Brilkina, A device for studying the light activity of photosensitizers in vitro, Utility model No. RU 150108, 27.01.2015.
10. M. G. Strakhovskaya, G. A.Meerovich, A. N. Kuskov, S. A. Gonchukov, and V. B. Loschenov, "Photoinactivation of coronaviruses: going along the optical spectrum," Laser Physics Letters 17(9), 093001 (2020).
11. K. Sharshov, M. Solomatina, O. Kurskaya, I. Kovalenko, E. Kholina, V. Fedorov, G. Meerovich, A. Rubin, and M. Strakhovskaya, "The Photosensitizer Octakis(cholinyl)zinc Phthalocyanine with Ability to Bind to a Model Spike Protein Leads to a Loss of SARS-CoV-2 Infectivity In Vitro When Exposed to Far-Red LED," Viruses 13(4), 643 (2021).
12. G. A. Meerovich, E. V. Akhlyustina, I. G. Tiganova, E. A. Lukyanets, E. A. Makarova, E. R. Tolordava, O. A. Yuzhakova, I. D. Romanishkin, N. I. Philipova, Yu. S. Zhizhimova, Yu. M. Romanova, V. B. Loschenov, and A. L. Gintsburg, "Novel Polycationic Photosensitizers for Antibacterial Photodynamic Therapy," in Advances in Experimental Medicine and Biology, Springer, New York, 1–19 (2019).
13. G. Meerovich, I. Romanishkin, E. Akhlyustina, M. Strakhovskaya, E. Kogan, I. Angelov, V. Loschenov, and E. Borisova, "Photodynamic Action in Thin Sensitized Layers: Estimating the Utilization of Light Energy," Journal of Biomedical Photonics & Engineering 7(4), 040301 (2021).
14. G. A. Meerovich, E. V. Akhlyustina, D. S. Denisov, E. G. Kholina, E. A. Makarova, E. A. Lukyanets, V. B. Loschenov, and M. G. Strakhovskaya, "Photodynamic inactivation of Escherichia coli bacteria by cationic photosensitizers," Laser Physics Letters 18(11), 115601 (2021).

A Review of EEG Signal Analysis for Diagnosis of Neurological Disorders using Machine Learning

Vandana Joshi* **and Nirali Nanavati**
Computer Engineering Department, Sarvajanik College of Engineering and Technology, Dr. R.K. Desai Marg, Opp. Mission Hospital, Athwalines, Surat 395001, Gujarat, India

*** e-mail:** vandana.joshi@scet.ac.in

Abstract. Neurological disorders are diseases that affect the brain and the central autonomic nervous systems. These disorders take a huge toll on an individual's health and general well-being. After cardiovascular diseases, neurological disorders are the main cause of death. These disorders include epilepsy, Alzheimer's disease, dementia, cerebrovascular diseases including stroke, migraine, Parkinson's disease and numerous other disorders. This manuscript presents a state-of-the-art consolidated review of research on the diagnosis of the three most common neurological disorders using electroencephalogram (EEG) signals with machine learning techniques. The disorders discussed in this manuscript are the more prevalent disorders like epilepsy, Attention-deficit/hyperactivity disorder (ADHD), and Alzheimer's disease. This manuscript helps in understanding the details about EEG signal processing for diagnosis and analysis of neurological disorders along with a discussion of the datasets, limitations, results and research scope of the various techniques. © 2021 Journal of Biomedical Photonics & Engineering.

Keywords: neurological disorders; electroencephalogram (EEG); epilepsy; attention-deficit/hyperactivity disorder (ADHD); Alzheimer.

Paper #3435 received 2 Jun 2021; revised manuscript received 15 Jul 2020; accepted for publication 11 Aug 2021; published online 7 Sep 2021. doi: 10.18287/JBPE21.07.040201.

1 Introduction

It has been analyzed in various studies that neurological disorders are growing at a high rate. According to the WHO, at some point in their lives, one out of four people in the world would have neurological disorders [1]. Neurological disorders are the world's second most prevalent diseases, following ischemic heart disease [1, 2]. Neurological disorders affect the brain as well as the nervous system of the human body [3].

The specific causes of the disorder can vary significantly depending upon the type of disorder as well as the specific area of the body that is affected. The causes may be due to genetic disorders, congenital abnormalities, infection, brain injury, etc. There are many known, relatively common neurological disorders but many are rare. Neurological disabilities include a wide range of disorders such as epilepsy, learning disabilities, neuromuscular disorders, autism, Alzheimer's disorder, ADHD, multiple sclerosis, Parkinson's disease, sleep disorder, and cerebral palsy. On the other hand, mental disorders are "psychiatric diseases" or diseases that mainly appear as abnormalities in thought, feeling, or conduct, which lead to distress or function impairment [4].

Several brain-imaging tools are available for the diagnosis of these neurological disorders, including Positron Emission Tomography (PET), Near Infrared Spectroscopy (NIRS), Magnetoencephalogram (MEG), Electroencephalography (EEG), and Functional Magnetic Resonance Imaging (fMRI) [2]. This manuscript focuses on EEG analysis because it is a low-cost, non-invasive, portable technique, which is widely used. A standard electroencephalogram (EEG) measures and records the electrical activity of a case's brain to evaluate cerebral functions. There are numerous contributions in literature that analyze EEG signals for the detection of neurological disorders, early diagnosis of neuro-developmental disorders, detection of acute neurological events and monitoring the behavior of patients [1, 5].

Numerous works in literature on EEG analysis have focused on epilepsy as one of the most common neurological disorders. Neurological disorders such as ADHD and Alzheimer's, however account for approximately one-third of the total diseases in developing nations. These disorders are often associated with an abnormal pattern of EEG and to analyze these EEG signals we need a well-trained neurologist. EEG signals are non-linear in nature. Some neuronal activity occurs because of minor changes in the voltage fluctuation of the EEG measures. The visual inspection of these signals, therefore, varies with the expertise. In addition, the long EEG recordings take a lot of time to review manually and the results sometimes cannot be exact and consistent [6]. This situation necessitates an automated system, which can be used, for neurological disorder detection and brain function monitoring with minimal human intervention [7]. This review will give an insight into the basics of EEG and how it is used to diagnose and analyze different neurological disorders.

The rest of the paper is organized as follows: in Section II and III, we discuss EEG principles and their processing phases respectively. Further, we discuss the investigation of three neurological disorders: Epilepsy in Section 4, ADHD in Section 5, and Alzheimer in Section 6 along with the results obtained by various works in literature. In Section 7, we discuss the problems and limitations for the detection of each disorder. The list of acronyms and abbreviations is summarized in Appendix A.

2 EEG Overview

In electroencephalogram (EEG), electrical currents are measured, generated by a group of specialized pyramidal cells within the brain which measure neuronal activity [6]. The electrical activity of a brain (EEG) exhibits significantly complex behavior with strong non-linear and dynamic properties. Brain activity is measured by placing the electrodes on the scalp of the subjects. Positions of electrodes are defined by the 10–20 International Electrode Positioning System.

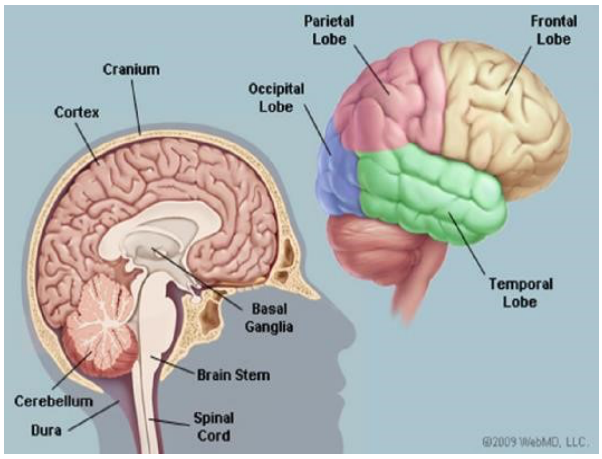


Fig. 1 Anatomical areas of the brain [8].

The brain is divided into three important parts anatomically: the cerebrum, cerebellum and brainstem, as illustrated in Fig. 1. The cerebrum contains two hemispheres: the right and left hemispheres. Each hemisphere is divided into four lobes: frontal, parietal, occipital and temporal. Each part is associated with brain functions related to thoughts, movements, emotions and motor functions. Table 1 illustrates the responsibility of each part.

Table 1 Anatomical region of brain associated with activity based on work [8].

Regions	**Involve with / Responsible for**
Cerebral cortex	Higher order cognitive tasks, such as problem solving, language comprehension, movement and processing of complex visual information
Frontal lobe	Personality, emotions, problem solving, motor development, reasoning, planning, parts of speech and movement
Parietal lobe	Sensation (e.g., pain, touch), sensory comprehension, recognition, perception of stimuli, orientation and movement
Occipital lobe	Visual processing
Temporal lobe	Involved in dealing with the recognition of auditory stimuli, speech, perception and memory
Cerebellum	Motor control, sensory perception and coordination, voluntary muscle movements, fine motor skills, posture and balance regulation

The brain signals are a combination of different base frequencies. These broad frequency ranges have been divided into several subgroups, called EEG rhythms or frequency bands. Each frequency band reflects a different state of mind or cognition in the brain (Table 2). Types of rhythms such as theta, delta, alpha, beta, and gamma can be observed in the brain waves depending upon the different functional states of the brain. Any small changes to these waves' frequency patterns help identify neurological conditions [6, 9].

3 EEG Signal Processing

The dynamically changing functional states of the brain are easily captured in the small variations of the EEG readings. Moreover, the EEG of the normal person also varies from the abnormal person. Therefore, it is very important that these changes be detected by using computer-aided technology to use a variety of signal processing and test mechanisms. This takes place in three steps – preprocessing, feature extraction, and result analysis [6] as shown in Fig. 2.

Table 2 Brain Rhythms [9].

Rhythm	Frequency range (in Hz)	Regions	Activity
Delta (δ)	0.1–3.5 (<4)	Mostly in thalamus	Deep sleep, continuous-attention tasks, unconscious
Theta (θ)	4–7.5	Hippocampus region	Creativity, intuition, recall, imaginary dream
Alpha (α)	8–13	Occipital and parietal regions	Relaxation, but not drowsy
Beta (β)	14–30	Parietal, somatosensory, frontal, and motor areas	Memory, problem solving
Gamma (γ)	30–100	Cortex	Cognition, Information processing, Motor Functions, Higher mental activity

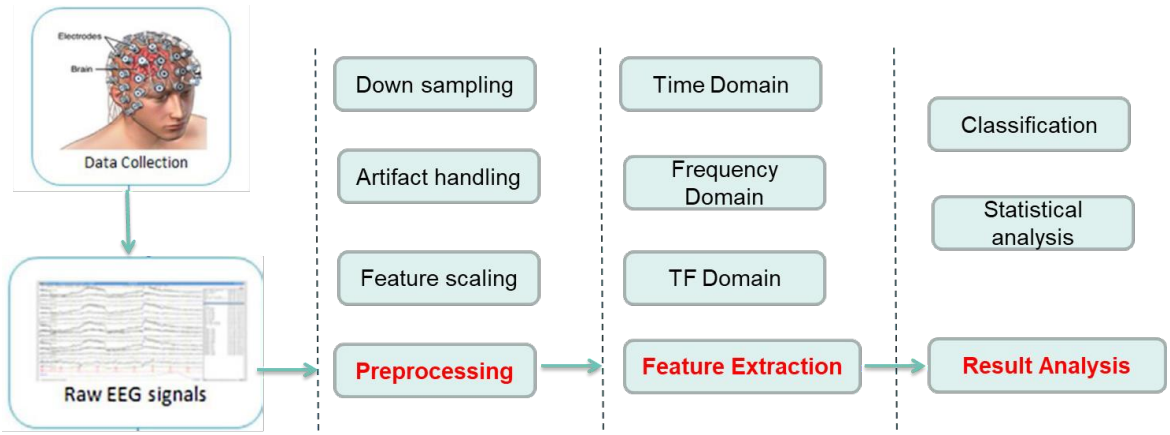


Fig. 2 EEG Signal Processing.

3.1 Pre-processing

Due to noise and different artifacts, it is essential to apply pre-processing and denoising methods to decrease their impact on the feature extraction stage. The pre-processing methods applied in the research studies are broadly divided into three categories – down sampling, artifact handling, and feature scaling, as explained below [10].

3.1.1 Down sampling

Different EEG devices have different sampling rates. To conserve memory and signal processing time, some of the researchers are down-sampled to certain ranges depending upon the requirement of an application. Down-sampling to 64 Hz from 512 Hz, 256 Hz to 16 Hz, and 2400 Hz to 600 Hz, are done in the research studies depending upon the requirement of an application.

3.1.2 Artifact Handling

While raw signals of EEG recordings tend to contain noise and artifacts, EEG signals measured from the scalp do not necessarily accurately represent signals originating from the brain. As summarized in Table 3,

Table 3 EEG Artifacts [9, 11].

Type	Name	Origin
Physiological Artifacts/Intrinsic	EOG	Eye blink, eye movement, eye flatter
	EMG	Chewing, Swallowing, Clenching, Talking, sniffing
	ECG	Heart potentials
Non-Physiological Artifacts/ Extrinsic	Instrumental	Electrode misplacement and cable movement, Malfunction of any part
	Interference	High voltage machine in surrounding (Power line)
	Movements	Head and body movement

artifacts embedded in the EEG recordings are generally subdivided into two categories: physiological and non-physiological artifacts. Physiological artifacts include electrical potentials elicited by biological activities, which are largely generated from the physical part proximal to the head (e.g., eyes, muscles, and heart) or due to the subjects' movements. Non-physiological Artifacts include the electrode-scalp interface, devices, and environment, which are generated anywhere near the EEG recording system. Variety of artifact removal techniques are used to handle all these kinds of artifacts. A large number of artifacts can be avoided through careful planning of experiments and recording sessions in an appropriate recording environment. Moreover, a variety of methods may also be used to reject noisy data, delete artifacts, and enhance data signal-to-noise ratio (SNR) [10, 12]. The major problem in the use of these processes is the loss of essential neuronal knowledge from artifactual epochs may lead to incorrect assumptions. Signal based automatic artifact removal algorithms are founded upon some presumption, that each channel is the total sum of pure EEG data and a proportion of an artifact. Several theories have been proposed based on signal transformation, some focusing on various filters for artifact deletion and some are using the blind source separation (BSS) method including a variety of unsupervised learning algorithms without prior information and extra reference channels [11].

The artifact removal techniques have been tabulated in Table 4. The type of artifact removal technique mentioned in the first column, while the rest of the columns denote the type of artifact removed, application in which the corresponding method has been applied with its advantage and limitation.

3.1.3 Feature Scaling

Normalization is one of the most widely used methods of function scaling in the literature to demonstrate symmetrical behavior. The scaling is performed either on the raw/filtered values or on the extracted features. For instance, in Ref. [19], the authors use Z-score (mean = 0, Std Dev = 1) before feature extraction similarly in Ref. [8], the authors apply Min-Max and unity method for Multi-class task recognition.

3.2 Feature Extraction

Various feature extraction methods are used to perform frequency domain, time domain, and time-frequency domain analysis of the signals [6, 19]. The feature extraction methods have been categorized into three categories: spectral estimation methods, family of transforms, and time decomposition methods.

Spectral estimation transforms a signal from the time domain to the frequency domain and can provide a description of the signal's power or energy distribution along frequency. Widely used spectral estimation methods of EEG, include Non-parametric (classical): Periodogram, Welch and Parametric and (non-classical): Autoregressive. In spectral analysis, the basic assumption is that the spectrum of an EEG signal is fixed and does not change over time. To reveal the time-varying spectrum of non-stationary EEG signals, time-frequency analysis (TFA) techniques are needed. Some popular methods include the short-time Fourier Transform (STFT), the Continuous Wavelet Transform (CWT) and Discrete Wavelet Transformation (DWT). Similarly, the decomposition method also helps to effectively analyze the signals. The signal is decomposed into a set of intrinsic mode functions (IMFs) that are used as sub-signals [8].

3.3 Result Analysis

The result analysis phase is explained through classification models and statistical analysis.

Classification Models. A variety of machine learning algorithms are used for the diagnosis of neurological disorders. The machine learning classifiers such as supervised, unsupervised, deep learning neural architectures and ensemble learning models are used for classification purposes in various EEG research studies [8, 20–23]. Some popular classifiers include LDA, SVM with linear and RBF kernel function, KNN, CNN, etc.

Statistical Analysis. Some application studies have used different statistical tests for EEG signal analysis. These tests are applied on features or parameters for different purposes or the application. For instance, T-test, One-Way ANOVA, and Wilcoxon rank-sum test, Kolmogorov-Smirnov test for normal distribution, and non-parametric Kruskal-Wallis test [6].

4 Diagnosis of Epilepsy

Epilepsy is a neurological condition that affects the nervous system. It is also known as a seizure disorder. It is usually diagnosed after a person had at least two seizures or after one seizure with a high risk that was not caused by some known medical condition. Epilepsy are divided into two categories [24]: generalized seizure and focal seizure. Subtypes of generalized seizures are absence seizures, tonic seizures; atonic seizures, etc. as is given in Fig. 3.

Epilepsy is caused by a sudden abnormal electrical discharge that occurs in the cerebral networks and usually lasts for less than a few minutes; so, the attacks are hard to predict. Epilepsy occurs in different phases as pre-ictal (immediately preceding seizure), ictal (during a seizure), inter-ictal (in-between seizures) and post-ictal (immediately following a seizure) [22]. EEG records of the epileptic patients are usually long (hours to days) and contain an immense amount of patient info. A visual assessment of such recordings is time-consuming, slow, and sensitive to errors and subjects to inter-observer variability [25]. Hence, several methods have been developed to help diagnose epileptic seizures by automatic computer-assisted therapy (CAD). EEG is commonly used for the diagnosis and analysis of epilepsy [8]. EEG helps to assess the types of seizure and epileptic condition of patients with epilepsy. The EEG finding makes a significant contribution to determine a

Table 4 Artifact removal techniques.

Sr. No	Method	Description	Type of artifact	Advantage	Limitation
1	Regression Methods [10–12]	It is applied under the assumption: each channel is the cumulative sum of pure EEG data and a proportion of artifact	EOG ECG	• computationally simple	• requires exogenous reference channels, outcomes are highly affected by bidirectional contamination; • it does not work successfully on other artifacts; • cannot perform on single channel
2	Wavelet Transform [10–13]	Threshold applied to discard the signal that contain artifacts	EOG EMG	• very good time frequency localization features relative to Fourier transform	• cannot remove artifacts completely if the spectral properties overlap with the spectral properties of the artifacts
			BSS		
3	Principal Component Analysis (PCA) [10–14]	Based on Eigenvalues of covariance matrix	EOG	• is more computationally efficient than linear regression methods	• fails to separate the interferences when the potential of drifts and EEG data are similar; fails on similar amplitude for neuronal and artifactual activity require the assumptions of orthogonality and Gaussian distributions
4	Independent Component Analysis (ICA) [10–14]	Assuming that signal sources are instantaneously linear mixtures of cerebral and artifactual sources can decompose observed signal into independent components (ICs). Once ICs are extracted from original signals, the clean signal reconstructed by discarding ICs contains artifacts	EMG ECG EOG	• does not require any prior information or additional reference channel for removal of artifacts; • shown promising results in cases where the neuronal and artifactual sources are not completely independent	• cannot perform on single channel; • the complex iterative procedure limits use in online/real time applications; • disregard of temporal or spatial relations within sources will result in the loss of relevant information; • require the assumptions of orthogonality and Gaussian distributions
5	Canonical Correlation Analysis [11, 12]	Use second order statistics, which bring shorter computational time. It finds the linear relation between two multi-dimensional random variables by maximizing the pairwise correlations across the two data sets	EMG	• uses second-order statistics with less computational cost than ICA; • does not require the assumptions of orthogonality and Gaussian distributions	• cannot perform on single channel

6	Morphological component analysis (MCA) [15, 16]	Used to decompose a signal into components that have different morphological aspects, signals can be represented as a linear combination of three morphological components using MCA full form theory	EOG	• fast computation of the estimation of the signal coefficients using the basis pursuit algorithm, less memory requirement	• always requires a database containing morphologies of different types of artifacts, and therefore, its performance is highly dependent on the available templates of artifacts
7	Empirical Mode Decomposition [11, 17]	Heuristic technique. for non-stationary and non-linear signal processing It decomposes/extracting the signal, x[n], into a set of components with amplitude and frequency modulated, b[n], patterns from time series data called intrinsic mode functions (IMFs)	EMG	• this technique is empirical and data driven technique, whereas other methods depend on the selections of basic functions, such as wavelet analysis	• it is very sensitive for noise which incurs mode mixing
		Filtering Methods			
8	Adaptive Filtering [11, 12]	To quantize the amount of artifactual contamination in the primary input, by iteratively adjusting the weights according the optimization algorithm, and subtract it from EEG with artifacts signals	EOG ECG	–	• reference channel is given, as one of the inputs to the filter; additional sensors are needed to provide reference inputs
9	Wiener [11, 18]	It is a linear statistical filtering technique used to estimating the true EEG data with the purpose to develop a linear time invariant filter to minimize the mean square error between the pure EEG data and the estimated signal	EOG EMG	• minimization is done using an estimation of the power; • spectral densities of the signal and artifact; hence it does not need a reference waveform	• calibration needed prior to usage and that it cannot run in real time

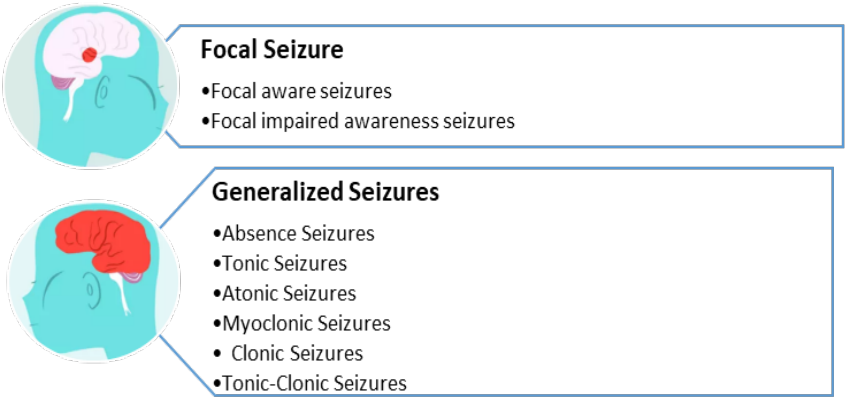


Fig. 3 Types of epilepsy.

multi-axial diagnosis of epilepsy, in terms of whether the seizure disorder is idiopathic or symptomatic, focal or generalized, part of a specific epilepsy syndrome [8].

4.1 Classification and prediction of seizure

EEG based epileptic seizure detection methods stem from the observation that EEG signal descriptors allow discrimination between normal and abnormal brain activity. A variety of EEG signal processing methods are available for the accurate detection of brain seizures. In EEG, signal analysis for epilepsy, classification / detection is done between epileptic and healthy subjects. Various approaches like supervised, unsupervised approaches are used to discriminate categories as normal vs. ictal, normal vs. pre-ictal, pre-ictal vs. ictal, focal vs. non-focal, seizure vs. non-epileptic etc.

Most methods employ classification techniques from the supervised machine. Among these methods, Support Vector Machine (SVM) is used more extensively as a supervised machine learning based classifier. In study [23], the authors employed a LS-SVM methodology, which proposes the use of decomposed EEG signals into six sub-bands namely D1-D5 and A5 using DWT. Then, the author uses approximate entropy (ApEn) feature, which performs the study of variation in subbands as an input function for SVM. Many researchers have used different types of SVM such as SVM (RBF), LS-SVM [26] with different feature extraction methods like PCA, wavelet transform (WT), ICA. Likewise, prediction of epileptic seizure is done by analyzing time series EEG signals using k-nearest neighbors (KNN) classifier [27].

In the same way random forest, back proposition, generalized relevance learning vector quantization (GRlVQ), WT with random forest, WT with SVM, fuzzy logic and, wavelet-bank filtering and dimensionality reduction using a generalized Gaussian distribution (GGD) with LDA [23, 28] are also used to classify epileptic signals. Focal epilepsy is a variant of epilepsy that mostly occurs in the limited area of the brain. Focal EEG signals are recorded from the brain area where first ictal EEG signal changes are detected and non-focal signals are recorded wherein, they do not take part in the seizure onset. In study [29], the authors apply empirical wavelet transform (EWT) with LS-SVM to separate the focal and non-focal rhythms from groups of EEG signals.

Neurologists are able to diagnose whether a person has epilepsy by monitoring EEG manually. However, it is also important to discriminate between the inter-ictal and ictal stages so that proper actions can be taken timely to avoid the risks of epilepsy. In Ref. [30], the authors discriminate between the inter-ictal and ictal EEGs using multi-basis maximal overlap discrete wavelet package transform MODWPT, six dimensionality reduction algorithms, and LS-SVM.

In the conventional methods where data is represented by features, there is a great loss of data. Feature extraction becomes very complex due to the presence of noise and artifacts in data. Thus, it is a challenging problem to produce a generalized automatic system with loyal performance, especially with low data availability. Currently, deep learning approaches substitute methods that integrate few sections of the data in the classification. The EEG signal can be processed as raw [31]. In Ref. [32], the authors apply a Deep Convolutional Neural Network (DCNN) on the raw EEG signals for the automatic identification of differentiated spatial features between inter-ictal and pre-ictal states and then used Bi-LSTM features that are created by the DCNN to classify inter-ictal or preictal segments of the incoming EEG section.

Early prediction is done by analyzing pre-ictal and intertidal stages. Various ML and DL are used for early prediction [22, 33]. These analyses are evaluated based on prediction time or other metrics like seizure occurrence period (SOP), the time duration in which there is a possibility of seizure and seizure prediction horizon (SPH), the duration of time between the alarm and the start of SOP.

4.2 Real time monitoring system

In real-time monitoring EEG recording and video surveillance videos are collected from epilepsy patients with some prior knowledge (label the different states of epilepsy patients from doctors). An expert observes the EEG recording and labels the seizure with the assistance of monitoring videos. It is based on change detection or event detection approaches, which find the change between brain states wherein the EEG changes from normal state to abnormal state [34].

Similarly, various warning systems are also available. Such systems utilize both ECG and EEG data to generate an alarm before seizure onset according to an ideal situation. Some systems combine accelerometer and electrodermal activity methods with several electronic mobile applications developed to electronically track seizure information Seizure record applications allow families to easily record seizures in an electronic format that is user friendly, mobile, and easily accessed by their treating epileptologist [35].

4.3 Comparative result Analysis for Epilepsy classification and Prediction

The various seizure classification methodologies are discussed in the earlier section. It is imperative to analyze the statistical evaluation of these methods' performance. The summary of methods, features used, the dataset used, and their performance in terms of accuracy is given in Table 5 According to the state-of-the-art, it has been observed that various methods perform differently for the different datasets. For instance, LS-SVM gives 100% accuracy for Bonn dataset [36] but it gives 90% for the Bern-Barcelona database [37]. Deep learning approaches are more robust irrespective of the dataset.

Table 5 Comparison of studies on classification for epilepsy.

Sr. no	Year of Publication	Dataset	Features	Method	Overall Accuracy (%)
			Bonn dataset [36]		
1	[23] (2017)	Five sets marked as (AE) Subject: 5-HC (A, B), 5-preictal (C, D), 5-Ictal (E) Channel: 1 Sampling rate: 173.61 Hz	DWT based ApEn	LS-SVM, SVM (RBF) for (A-E, AB-E, CE, CD-E, ABCD-E)	100
2	[25] (2019)		Discrete Wavelet + Arithmetic coding	k-NN, Naïve Bayes, MLP, and SVM for (A-E, AB-E, C-E, CD-E, ABCD-E)	100
3	[26] (2018)		Principal Component Analysis (PCA) and Wavelet Transform	Backpropagation	95.29
				GRLVQ	98.66
				WT+Randome Forest	98.05
				PCA+Randome Forest	98.22
				PCA+GRLVQ	98.45
4	[30] (2019)		Maximal overlap discrete wavelet package transform (MODWPT)	LS-SVM	
				Multi-basis MODWPT+PCA+ LK-LSSVM/ RK-LS-SVM	99.60/99.20
				Multi-basis MODWPT+ICA+ LK-LSSVM/ RK-LS-SVM	99.76/98.80
				Multi-basis MODWPT+LLE+ LK-LSSVM/ RK-LS-SVM	98.73/98.13
5	[31] (2019)		NA	CNN + Scalogram for A-E, A-D, D-E, AD-E, A-B-C-D	 99.5 100 98.5 99 93.6
			Boston database [38]		
6	[28] (2018)	Subject: considered 39 signals related to 13 seizures and 26 non-seizure signals Channel: 23 Sampling rate: 2561 Hz	Separation of brain rhythms: wavelet bank filtering, statistical model based on dimensionality reduction with GGD	Linear discriminant analysis for Delta band, Theta band, Alpha band, Beta band, Gamma band	 95.13 92.69 96.59 94.48 97
7	[32] (2018)	Subject: 13 seizures and 26 non-seizures Channel: 23 Sampling rate: 2561 Hz	NA	DCNN+BiLSTM	99.66

Bern-Barcelona database [37]					
8	[29] (2016)	Subject: 5 intracranial Channel: 64 Sampling rate: 512 Hz	Area computed from 2D Reconstructed phase space plot (RPS) of rhythms using CTM	Least-squares support vector machine (LSSVM) for 50 pairs of signals area, 750 pairs of signals	90 82.53

4.4 Datasets for Epilepsy Analysis and Prediction

EEG is a significant means for the identification, analysis, and prediction of epilepsy seizures. For these reasons, multiple open-access databases have been published by different hospitals and research centers. For instance, the Center of Epilepsy at Children's Hospital, Boston, and Temple University Hospital have made their EEG databases publicly available to the researchers. The database of Bonn University is not large enough but is extensively used for the detection of ES in the literature. It consists of 5 datasets A, B, C, D, and E. CHB-MIT database has data of 22 patients with 9–24 recordings of each patient and every recording is 1 h long with some discontinuities due to hardware limitation (some cases have 2–4 h long recordings) [23, 25]. Freiburg Hospital's database was one of the most notable databases, which contained iEEG data of 21 subjects with around 88 seizures, but recently it has been merged into EPILEPSIAE database to provide larger datasets due to which this database is not open-source now [22].

Bern-Barcelona Database containing intracranial EEG signals. The EEG signals were recorded from 5 epilepsy patients who were the candidates for surgery due to long-standing drug-resistant temporal lobe epilepsy. The database contains 3750 pairs of EEG signals for each focal and non-focal category. Each pair contains EEG signals, namely x and y, which were recorded from adjacent channels. The EEG signals were sampled at a rate of 512 Hz, and the duration of each signal is 20 sec [29]. Likewise, CHB-MIT Scalp EEG Database collected at the Children's Hospital Boston. Recordings, grouped into 23 cases, were collected from 22 subjects. Subjects were monitored for up to several days following withdrawal of anti-seizure medication in order to characterize their seizures and assess their candidacy for surgical intervention. All signals were sampled at 256 samples per second with 16-bit resolution [30].

5 Diagnosis of ADHD

ADHD is a common neuro-developmental disorder that begins in childhood and can continue through adolescence and adulthood. ADHD in children leads to a lack of interest in all things. The dilemma of the syndrome concerns children in their families, in the study area, and in the community. Kids have problems paying attention, listening attentively, following commands, keeping still. ADHD is divided into three types: Inattentive, Hyperactive / Impulsive, and combined (Fig. 4). Symptoms differ according to type [39, 40].

Diagnosis of ADHD is typically carried out using clinical interviews structured around the diagnosis classification systems of DSM-5 and ICD-11 [40–42]. Different diagnosis and analysis methods for ADHD are found in the literature. A more comprehensive description can be found in study [43]. Some specific symptoms of the disorder are simpler to identify than other disorder's symptoms. It is needed to conduct a diagnosis procedure followed by evaluation techniques for the disorder. Among all diagnosis methodology, EEG plays a key role to assess and evaluate the ADHD disorder. Human activities are related to neural functions. Many researchers adopted this main tool to diagnose ADHD in their research.

Numerous EEG studies utilized spectral analyses to reveal the EEG characteristics features to describe the difference between attentive and non-attentive states of ADHD children. Likewise, assessment of cognitive capability is also focused in ADHD-affected children.

5.1 Classification of EEG signals for ADHD

Machine learning methods can be used for finding some relevant discriminators between ADHD and control groups with different EEG characteristics viz. spectral features, nonlinear features, statistical features.

The majority of EEG analysis for ADHD is based on spectral power features which are measured with the Theta/beta ratio (TBR), Theta/alpha ratio, TBAR (Theta/(alpha + beta)), relative delta, theta, alpha, and beta power [4, 41].

In literature, many researchers have utilized different methods to analyze resting-state EEG (rsEEG) and time series recorded from an ADHD group and a control group. Authors [44, 45] contributed to discovering the best indicator of attention for ADHD. They applied the wavelet decomposition method to obtain different frequency bands of EEG. They extracted seven features (relative Delta, Theta, Alpha and Beta power, TBR, TAR, and TBAR) for each sample. Then, linear discriminant analysis (LDA) was used for classification. They proved that the TBR is a significant feature in discriminating between attentive and non-attentive states. Likewise [41], used relative spectral power, spectral power ratio, complexity analyses, and bicoherence to extract rsEEG features. To examine the

effect of these features on ADHD identification, they achieved an AUC of 0.9158 and an accuracy of 84.59% using a support vector machine (SVM).

TBR has been used as a measure for discriminating between children with and without ADHD in several studies. However, in some cases, researchers could not attain good accuracy using TBR. In study [39], the authors attempted 0.878 AUC using eight key feature descriptors for the ADHD/control classification and ranked based on the t-test. The results for beta (indicative of heightened cortical arousal) activity has been less consistent, with some studies reporting reduced beta activity in frontal and central regions and others not. There also tends to be a small number of ADHD children who display an abundance of beta activity [46]. In Refs. [20, 21], the authors apply machine-learning techniques for diagnosis of adult ADHD.

With the spectral features of EEG, non-linear features also play a vital role in ADHD analysis. Non-linear analysis of EEG waves has revealed new information on the complex dynamics of underlying neural networks [47]. Well-known entropy methods like Sample Entropy (SampEn), Dispersion entropy (DispEn), Multivariate Sample Entropy (mvSE), Approximate entropy, sample entropy are used to classify EEG signals [48]. Likewise, in study [49], fractal dimension as Higuchi's, Katz's, and Petrosian's has been applied to discriminate ADHD and healthy controls. Brief comparison of studies on classification for ADHD is given in Table 6.

5.2 Assessment of Cognitive Capability

EEG can be used for the assessment of the attention capability [51] and cognitive capability of ADHD-affected children. Based on this, new methodology or techniques of teaching can be adapted to enhance their learning capability. In order to investigate human cognitive patterns, Event-related potentials (ERPs) visual stimulation with the Oddball paradigm is used as the basis.

Table 6 Comparison of studies on classification for ADHD.

Sr. no	Year of Publication	Dataset	Features	Methods	Overall best Accuracy (%)
1	[39] 2019	Subject: 30 ADHD, 30 HC Channel: 21 Sampling rate: 256 Hz Recording: Resting state	Eight crucial feature descriptors were selected and ranked based on the t-test (refer reference for more detail)	SVM	84.44
2	[45] (2017)	Subject: 120 Channel: 1 Sampling rate: 256 Hz Recording: Working state	Feature Selection using Mutual Information	LDA	65.5
3	[47] (2016)	Subject: 30 ADHD, 30 HC Channel: 19 Sampling rate: 256 Hz Recording: Working state	Fractal dimension (FD) based features: Higuchi, Katz and Petrosian fractal dimensions, largest Lyapunov exponent and approximate entropy	Multi-Layer Perceptron (MLP)	93.65
4	[49] (2020)	Subject: 23 ADHD, 23 HC Channel: 4 Sampling rate: 2500 HZ Recording: Working state	Morphologic Features	SVM k-NN RF	89.13 86.95 82.6
			Non-linear Features, Wavelet	AdaBoost MLP NB LR	89.13 91.3 86.95 89.13
5	[50] (2019)	Subject: 50 ADHD, 51 HC Channel: 128, 32 selected Sampling rate: 1000 HZ Recording: Resting state	DF, Brain Network Measures	CNN MLP SVM	94.67 84.53 84.17

For instance, the probable region of the brain that shows abnormality due to ADHD syndrome can be used for assessment of learning capability of ADHD-affected children [43]. Similarity patients are asked to do some motor activity like to arrange the spoons and hand them over to their caretaker. Moreover, visual cues activity as colors, numbers, and animals, are identified to find out the attentive and cognitive capability [44].

Cognitive training is a commonly used therapy for ADHD. However, the main challenges with such training are illuminating the repetitive scenes, stimulating the user's interests, encouraging more engagement, and adjusting the difficulty level. Applying EEG signal is a familiar method towards the improvements in the sustained attention levels of children by designing video games [52] with the introduction of "serious games" attempted to measure attention to detect ADHD.

5.3 Datasets for ADHD Analysis

An extensive amount of literature has been researched by collaborating with the various medical associations. Data used for such research are not publicly available due to privacy issues. However, some research has been done on ADHD analysis on publicly available data.

EEG data for ADHD/Control children done EEG recording for 61 children with ADHD and 60 healthy controls (boys and girls, ages 7–12) is given in Ref. [47]. The ADHD children were diagnosed by an experienced psychiatrist with DSM-IV criteria, and have taken Ritalin for up to 6 months. EEG recording was performed based on 10–20 standard by 19 channels (Fz, Cz, Pz, C3, T3, C4, T4, Fp1, Fp2, F3, F4, F7, F8, P3, P4, T5, T6, O1, O2) at 128 Hz sampling frequency. The A1 and A2 electrodes were the references located on earlobes. Two electrodes that were placed below and above the right eye recorded the eye movement. EEG recording protocol was based on visual attention tasks. In the task, a set of pictures of cartoon characters was shown to the children and they were asked to count the characters.

Similarly, in FOCUS [52], EEG brain recording of ADHD and non-ADHD individuals during gameplay of a brain-controlled game, recorded with an EMOTIV EEG headset are collected. It can be used to design and test methods to detect individuals with ADHD.

6 Diagnosis of Alzheimer's disease (AD)

Dementia is a syndrome usually of a chronic or progressive nature in which there is deterioration in cognitive function. Worldwide, around 50 million people have dementia [53]. Alzheimer's disease is the most common form of dementia.

Alzheimer's disease is an irreversible, progressive brain disorder that slowly destroys memory and thinking skills, and, eventually, the ability to carry out the simplest tasks. In most people with Alzheimer's, symptoms (Fig. 5) first appear in their mid-60s. Estimates vary, but experts suggest that more than 5.5 million Americans, most of them age 65 or older, may have dementia caused by Alzheimer's.

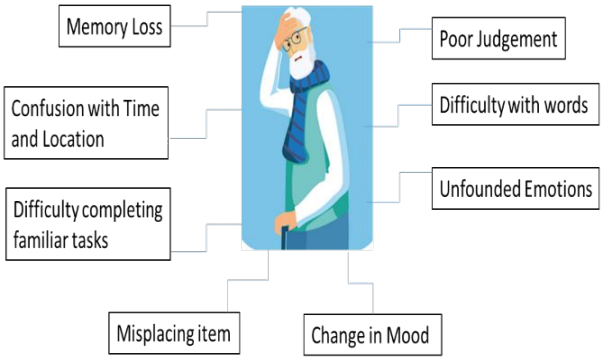


Fig. 5 Alzheimer's Symptoms.

Numerous neuroimaging techniques have been used with the aim of distinguishing AD and Mild Cognitive Impairment (MCI) patients from cognitively healthy control (HC) subjects: positron emission tomography (PET), magnetic resonance spectroscopy, functional magnetic resonance imaging (fMRI), magnetoencephalography (MEG), and electroencephalography (EEG) [54]. PET and fMRI show a good structural accuracy, but both offer a limited temporal resolution. By contrast, EEG and MEG are non-invasive techniques with high temporal resolution, allowing for studying the dynamic processes involved in the regulation of complex functional brain systems [55]. Particularly, EEG is widely used due to its portability, low cost, and availability. Moreover, EEG has already shown its usefulness to characterize brain dynamics in AD and MCI.

6.1 Early Diagnosis and classification

To diagnose Alzheimer using EEG, methods are divided into two approaches. The first accomplished in the resting state (awake at rest) in the absence of any stimulus. Since the patient is not required to perform a behavioral task, it is more comfortable and less stressful for patients. The second approach to EEG studies is conducted when the subject is performing a pre-defined task (task-oriented). Approach of task-oriented EEG studies is not ideal for most people with AD since patients have an increase of anxiety and anger.

The discrimination of early Alzheimer's disease (AD) and its prodromal form (i.e., mild Cognitive impairment, MCI) from cognitively healthy control (HC) subjects is crucial since the treatment is more effective in the first stages of the dementia. MCI is an early stage of Alzheimer's or another dementia. For early diagnosis in Refs. [54, 56], compared behavioral results (reaction time and accuracy), ERP and ERD/ERS responses when healthy elderly (HE) controls, MCI and mild AD patients were performing a three-level N-Back visual working memory task.

The anomalies that AD and MCI induce in EEG operation have been usually studied using simple signal processing approaches, such as spectral techniques via a power increase in low frequency bands, as well as a decrease in higher frequencies. Nonlinear analysis [57]

as permutation entropy methods have also been widely used in order to provide complementary details to spectral measures.

In Ref. [38], a combination of spectral measures and nonlinear methods applied to evaluate the diagnostic usefulness of an EEG-based methodology by means of different multiclass classifiers: quadratic discriminant analysis QDA, multi-layer perceptron neural network (MLP), and logistic discriminant analysis (LDA) is undertaken. The Relative Power (RP) in Deep Neural Network metric enumerates the abnormal EEG pattern and distinguishes HC and MCI. In Ref. [58], the authors analyze the Electroencephalogram (EEG) signal, extract the features using Fast Fourier Transform (FFT) and classify the disease by CNN with good accuracy. A brief comparative study for result analysis for Alzheimer's classification is shown in Table 7.

6.2 Dataset for Alzheimer's disease

The most widely used databases like ADNI (http://adni.loni.usc.edu), AIBL (http://aibl.csiro.au), and OA-SIS (www.oasis-brains.org) [54] provides clinical, genetic, MRI images open source databases for Alzheimer's. Most researchers have used EEG data recording with the permission of a clinical institution; in this case, data can be available upon request. As in Ref. [62], the database was recorded in real clinical conditions at Charles-Foix Hospital (Ivry-sur-Seine, France), data is available by mail request. Likewise, some researchers publish their data for research use, as in the study was conducted on mild AD and normal participants. This data includes EEG from 4 channels (Fp1-FzCz-Pz) with A1 earlobe as reference. The sampling frequency is 200 Hz.

7 Discussion

We conducted a comprehensive study for diagnosis of Epilepsy, ADHD and Alzheimer. This study demonstrated that EEG characteristics could be used for diagnosis of neurological disorders, but we found several limitations and issues also. The selection of methodologies used to compare the research between them is a significant challenge when examining the literature. Differences in the selection of participants, EEG acquisition method and interpretation, could influence performance. This lack of standards presents a general confound for the field that extends beyond the implications for particular study.

The core problem is the limited number of participants with respect to the large number of features and tests that have been applied, therefore overfitting may be unavoidable [25, 62]. Likewise, heterogeneity in etiology, symptoms and treatment outcomes have affected the accuracy of EEG analysis. Symptoms also change over time as the subject ages; features of EEG change accordingly.

Table 7 Comparison of Studies on classification for Alzheimer's.

Sr.no	Year of Publication	Dataset	Features	Methods	Overall best Accuracy (%)
1	[55] (2018)	Subject: 37 AD, 37 MCI, and 37 elderly HC Channel: 19 Sampling rate: 200Hz Recording: Resting state	Spectral and nonlinear	LDA QDA MLP for HC vs. All	76.47 78.43 78.43
				LDA QDA MLP for AD vs. Al	74.51 74.51 76.47
2	[59] (2016)	Subject: 50 AD ,50 HC Channel: 19 Sampling rate: 1024Hz Recording: Resting state	ICA/Wavelet/ Spectral	SVM	96
3	[60] (2019)	Subject: 63 AD, 63 MCI, 63 HC Channel: 19 Sampling rate: 1024Hz Recording: Resting state	Epoch	CNN for AD vs. HC AD vs. MCI MCI vs. HC AD vs. MCI vs. HC	92.95 84.62 91.99 83.3
			PSD	CNN for AD vs. HC AD vs. MCI MCI vs. HC AD vs. MCI vs. HC	91.88 78.63 90.17 78.49
4	[61] (2018)	Subject: AD 16, 10 HC Channel: 128 Sampling rate: 2000 Hz Recording: Resting state	FFT, CWT	Random Forest	83.49, 85.09

There is unavailability of long-term Open Access EEG Data for epilepsy. As epilepsy seizures do not occur continuously; the diagnosis of epilepsy needs long term EEG recording (more than 2–3 h at least). The lack of observations is one of the key explanations for the poor efficiency of prediction algorithms. The values in the observed data are almost zero, since the wearables or embedded devices with limited storage and storage space are not interconnected with each other for many potential reasons. Learning from corrupt or absent data did not take the machine learning community much into consideration. However, missing indicators must be added in models, which can provide important data to make predictions [22].

In Ref. [28], the authors use statistical models for classification, which allows seizure detection simultaneously in the different brain rhythms, complying with current medical practices. However, it has some limitations wherein firstly it is difficult to define the sliding time window and the overlap between epochs because of the very high dynamics of epileptic signals. Second, it must define regularization conditions for the training phase so that random peaks, noise and devices can be taken into account that can contribute to false positive effects. Third, seizures have variable and dynamic offsets that represent the complicated existence of the various forms of epilepsy. For instance, if brain waves slow down, it is difficult to monitor changes from seizure to seizure and classification errors are created. Although the majority of research in seizure warning systems has focused on EEG-based methods for seizure detection, currently available systems suffer from poor sensitivity and specificity [35].

Due to unnecessary extraction of features, time consumption and computing costs would increase. There is a need for quick predictions of relatively low power hardware and cheaper computer costs so that the ES prediction method can be implemented in real time. Even as DL have greatly rectified the problem of feature extraction from pre-processed data, the constraint is that these methods need a large amount of information to predict effectively [32].

Many EEG studies probably indicate that they are homogeneous in their clinical classes. If this is not so, the group variations that have been identified do not adequately represent the magnitude of the EEG deviation in individual kids with ADHD [40]. Other major issues not effectively addressed are that of comorbidity; the simultaneous presence of two or more diseases or medical conditions in a patient such as autism, which is a learning disorder falling in the ADHD spectrum. We should expect to see differing and contradictory results in such cases [40]. Different researchers are studying EEG for different age groups. Major evidence suggests that EEG abnormalities in ADHD are influenced by gender in childhood but requires further investigation [39].

Conclusion

EEG signals are used as an authentic indicator which allows observing mental states and diseases related to the brain. It is used as the analyzing tool of neurological diseases, classification and rehabilitation. The methodologies of analyzing the diseases also differ according to the diseases. Some of the techniques to analyze EEG waveform uses time-frequency pre-processing while others use focal waves to detect the active side in the EEG signal.

In this manuscript, different signal analysis methods including linear, frequency domain, time-frequency, and nonlinear techniques are discussed for the detection of neurological disorders. This paper has also explored several diagnosis techniques for three prominent neurological disorders like Alzheimer's disease, Epilepsy and ADHD along with a discussion on the limitations in the analysis of these disorders. With these details, various open sources data sets and tools are provided for further research for improving the automated prediction of neurological disorders.

Disclosures

All authors declare that there is no conflict of interests in this paper.

References

1. V. Janga, P. E. S. Reddy, "A review on Machine Learning Techniques for Neurological disorders estimation by Analyzing EEG Waves," International Journal of Trend in Scientific Research and Development 2(1), 824–831 (2017).
2. S. Siuly, Y. Zhang, "Medical Big Data: Neurological Diseases Diagnosis Through Medical Data Analysis," Data Science and Engineering 1(2), 54–64 (2016).
3. U. Raghavendra, U. R. Acharya, and H. Adeli, "Artificial Intelligence Techniques for Automated Diagnosis of Neurological Disorders," European Neurology 82(1–3), 41–64 (2020).
4. M. McVoy, S. Lytle, E. Fulchiero, M. E. Aebi, O. Adeleye, and M. Sajatovic, "A systematic review of quantitative EEG as a possible biomarker in child psychiatric disorders," Psychiatry Research 279, 331–344 (2019).
5. D. P. Subha, P. K. Joseph, R. Acharya U, and C. M. Lim, "EEG signal analysis: a survey," Journal of Medical Systems 34(2), 195–212 (2010).
6. A. Khosla, P. Khandnor, and T. Chand, "A comparative analysis of signal processing and classification methods for different applications based on EEG signals," Biocybernetics and Biomedical Engineering 40(2), 649–690 (2020).

7. G. Birajadar, C. Bhyri, "Comprehensive survey on EEG analysis for detecting brain disorders," Mukt Shabd Journal IX(VI), 2258–2262 (2020).
8. S. Siuly, Y. Li, and Y. Zhang, EEG Signal Analysis and Classification, Springer Intenational Publishing, Switzerland (2016). ISBN 978-3-319-47653-7.
9. U. Halici, E. Agi, C. Özgen, and I. Ulusoy, "Analysis and classification of EEG signals for brain computer interfaces," in International Conference on Cognitive Neuroscience X, 1–5 September, Turkey (2008).
10. M. Sheoran, S. Kumar, and S. Chawla, "Methods of denoising of electroencephalogram signal: A review," International Journal of Biomedical Engineering and Technology 18(4), 385–395 (2015).
11. X. Jiang, G. Bin Bian, and Z. Tian, "Removal of artifacts from EEG signals: A review," Sensors 19(5), 1–18 (2019).
12. M. M. N. Mannan, M. A. Kamran, and M. Y. Jeong, "Identification and removal of physiological artifacts from electroencephalogram signals: A review," IEEE Access 6, 30630–30652 (2018).
13. M. Lakshmi, D. Prasad, and D. Prakash, "Survey on EEG signal processing methods," International Journal of Advanced Research in Computer Science and Software Engineering 4(1), 84–91 (2014).
14. A. R. Mane, P. S. D. Biradar, and P. R. K. Shastri, "Review paper on Feature Extraction Methods for EEG Signal Analysis," International Journal of Emerging Trend in Engineering and Basic Sciences 2(1), 545–552 (2015).
15. M. Kazakeviciute, A. Juozapavicius, and R. Samaitiene, "Morphological filtering of EEG," Materials Physics and Mechanics 9, 185–193 (2010).
16. B. Singh, H. Wagatsuma, "A Removal of Eye Movement and Blink Artifacts from EEG Data Using Morphological Component Analysis," Computational and Mathematical Methods in Medicine 2017, 1861645 (2017).
17. O. K. Fasil, R. Rajesh, "Empirical Mode Decomposition of EEG Signals for the Effectual Classification of Seizures," Advances in Neural Signal Processing, 1–13 (2020).
18. A. Borowicz, "Using a multichannel Wiener filter to remove eye-blink artifacts from EEG data," Biomedical Signal Processing and Control 45, 246–255 (2018).
19. L. Hu, Z. Zhang, EEG signal processing and feature extraction, Springer, Singapore (2019).
20. M. Adamou, T. Fullen, and S. L. Jones, "EEG for Diagnosis of Adult ADHD: A Systematic Review With Narrative Analysis," Frontiers in Psychiatry 11, 871 (2020).
21. A. Tenev, S. Markovska-Simoska, L. Kocarev, J. Pop-Jordanov, A. Müller, and G. Candrian, "Machine learning approach for classification of ADHD adults," International Journal of Psychophysiology 93(1), 162–166 (2014).
22. K. Rasheed, A. Qayyum, J. Qadir, S. Sivathamboo, P. Kwan, L. Kuhlmann, T. O'Brien, and A. Razi, "Machine Learning for Predicting Epileptic Seizures Using EEG Signals: A Review," IEEE Reviews in Biomedical Engineering 14, 139–155 (2021).
23. M. Zuhair, S. Thomas, "Classificat ion f patient by analyzing EEG signal using DWT and least square support vector machine," Advances in Science, Technology and Engineering Systems 2(3), 1280–1289 (2017).
24. C.E. Stafstrom, L. Carmant, "Seizures and epilepsy: an overview for neuroscientists," Cold Spring Harbor Perspectives in Medicine 5(6), a022426 (2015).
25. H. U. Amin, M. Z. Yusoff, and R. F. Ahmad, "A novel approach based on wavelet analysis and arithmetic coding for automated detection and diagnosis of epileptic seizure in EEG signals using machine learning techniques," Biomedical Signal Processing and Control 56, 101707 (2020).
26. E. M. Imah, A. Widodo, "A comparative study of machine learning algorithms for epileptic seizure classification on EEG signals," in 2017 International Conference on Advanced Computer Science and Information Systems (ICACSIS), 401–407 (2017).
27. M. K. Hasan, M. A. Ahamed, M. Ahmad, and M. A. Rashid, "Prediction of Epileptic Seizure by Analysing Time Series EEG Signal Using k -NN Classifier," Applied Bionics and Biomechanics 2017, 6848014 (2017).
28. A. Quintero-Rincón, M. Pereyra, C. D'Giano, M. Risk, and H. Batatia, "Fast statistical model-based classification of epileptic EEG signals," Biocybernetics and Biomedical Engineering 38(4), 877–889 (2018).
29. A. Bhattacharyya, M. Sharma, and R. Bilas, "A novel approach for automated detection of focal EEG signals using empirical wavelet transform," Neural Computing and Applications 29, 47-57 (2016).
30. T. Zhang, W. Chen, and M. Li, "Classification of inter-ictal and ictal EEGs using multi-basis MODWPT, dimensionality reduction algorithms and LS-SVM: A comparative study," Biomedical Signal Processing and Control 47, 240–251 (2019).
31. Ö. Türk, M. S. Özerdem, "Epilepsy Detection by Using Scalogram Based Convolutional Neural Network from EEG Signals," Brain Science 9(5), 115 (2019).
32. H. Daoud, M. Bayoumi, "Deep Learning based Reliable Early Epileptic Seizure Predictor," in IEEE Biomedical Circuits and Systems Conference (BioCAS), 1–4 (2018).
33. K. Adalarasu, P. Shrisowmya, and M. Jagannath, "Identifying Pre-ictal Period of Seizure and Better Brain Lobes for Seizure Detection using EEG Biomarkers Identifying Pre-ictal Period of Seizure and Better Brain Lobes for Seizure Detection using EEG Biomarkers," Journal of Physics: Conference Series 1451, 012010 (2020).
34. Z. Gao, G. Lu, P. Yan, C. Lyu, X. Li, and W. Shang, "Automatic Change Detection for Real-Time Monitoring of EEG Signals," Frontiers in Physiology 9, 325 (2018).

35. S. Ramgopal, S. Thome-Souza, M. Jackson, N. E. Kadish, I. S. Fernández, J. Klehm, W. Bosl, C. Reinsberger, S. Schachter, and T. Loddenkemper, "Seizure detection, seizure prediction, and closed-loop warning systems in epilepsy," Epilepsy & Behavior 37, 291–307 (2014).
36. EEG Data Download (accessed 14 July 2021). [https://www.ukbonn.org/epileptologie/ag-lehnertz-downloads/].
37. Datasets – DTIC-MdM Strategic Program: Data-Driven Knowledge Extraction (UPF) (accessed 14 July 2021). [https://www.upf.edu/web/mdmdtic/datasets].
38. "CHB-MIT Scalp EEG Database v1.0.0," (accessed 14 July 2021). [https://physionet.org/content/chbmit/1.0.0/].
39. M.-Y. Chang, C.-S. Ouyang, C.-T. Chiang, R.-C. Yang, R.-C. Wu, H.-C. Wu, and L.-C. Lin, "A New Method of Diagnosing Attention-Deficit Hyperactivity Disorder in Male Patients by Quantitative EEG Analysis," Clinical EEG and Neuroscience 50(5), 339–347 (2019).
40. R. J. Barry, A. R. Clarke, and S. J. Johnstone, "A review of electrophysiology in attention-deficit/hyperactivity disorder: I. Qualitative and quantitative electroencephalography," Clinical Neurophysiology 114(2), 171–183 (2003).
41. H. Chen, W. Chen, Y. Song, L. Sun, and X. Li, "EEG characteristics of children with attention-deficit/hyperactivity disorder," Neuroscience 406, 444–456 (2019).
42. J. J. Newson, T. C. Thiagarajan, "EEG Frequency Bands in Psychiatric Disorders: A Review of Resting State Studies," Frontiers in Human Neuroscience 12, 521 (2019).
43. S. M, N. G. Cholli, and S. Nayak, "Classification of Attention Deficit Hyperactivity Disorder (ADHD) Considering Diagnosis and Treatment," International Journal of Modern Education and Computer Science 11(6), 26–42 (2019).
44. R. Gabriel, M. M. Spendola, A. Mesquita, and A. Z. Neto, "Identification of ADHD cognitive pattern disturbances using EEG and wavelets analysis," in IEEE 17th International Conference on Bioinformatics and Bioengineering (BIBE), 157–162 (2017).
45. F. Fahimi, C. Guan, W. B. Goh, K. K. Ang, C. G. Lim, and T. S. Lee, "Personalized features for attention detection in children with Attention Deficit Hyperactivity Disorder," in 39th Annual International Conference of the IEEE Engineering in Medicine and Biology Society (EMBC), 414–417 (2017).
46. A. Kamida, K. Shimabayashi, M. Oguri, T. Takamori, N. Ueda, Y. Koyanagi, N. Sannomiya, H. Nagira, S. Ikunishi, Y. Hattori, K. Sato, C. Fukuda, Y. Hirooka, and Y. Maegaki, "EEG power spectrum analysis in children with ADHD," Yonago Acta Medica 59(2), 169–173 (2016).
47. M. R. Mohammadi, A. Khaleghi, A. M. Nasrabadi, S. Rafieivand, M. Begol, and H. Zarafshan, "EEG classification of ADHD and normal children using non-linear features and neural network," Biomedical Engineering Letters 6(2), 66–73 (2016).
48. M. Rezaeezadeh, S. Shamekhi, and M. Shamsi, "Attention Deficit Hyperactivity Disorder Diagnosis using non-linear univariate and multivariate EEG measurements: a preliminary study," Physical and Engineering Sciences in Medicine 43(2), 577–592 (2020).
49. M. Altınkaynak, N. Dolu, A. Güven, F. Pektaş, S. Özmen, E. Demirci, and M. İzzetoğlu, "Diagnosis of Attention Deficit Hyperactivity Disorder with combined time and frequency features," Biocybernetics and Biomedical Engineering 40(3), 927–937 (2020).
50. H. Chen, Y. Song, and X. Li, "A deep learning framework for identifying children with ADHD using an EEG-based brain network," Neurocomputing 356, 83–96 (2019).
51. A. Alex, S. Coelli, A. M. Bianchi, L. Ponzini, E. Buzzi, and M. P. Canevini, "EEG analysis of brain activity in attention deficit hyperactivity disorder during an attention task," in IEEE 3rd International Forum on Research and Technologies for Society and Industry (RTSI), 1-4 (2017).
52. A. E. Alchalabi, S. Shirmohammadi, A. N. Eddin, and M. Elsharnouby, "FOCUS: Detecting ADHD patients by an EEGbased serious game," IEEE Transactions on Instrumentation and Measurement 67(7), 1512–1520 (2018).
53. C. Lynch, "World Alzheimer Report 2019: Attitudes to dementia, a global survey," Alzheimer's Dementia 16(S10), e038255 (2020).
54. M. Tanveer, B. Richhariya, R. U. Khan, A. H. Rashid, P. Khanna, M. Prasad, and C. T. Lin, "Machine learning techniques for the diagnosis of alzheimer's disease: A review," ACM Transactions on Multimedia Computing, Communications, and Applications 16(1s), 30 (2020).
55. S. J. Ruiz-Gómez, C. Gómez, J. Poza, G. C. Gutiérrez-Tobal, M. A. Tola-Arribas, M. Cano, and R. Hornero, "Automated multiclass classification of spontaneous EEG activity in Alzheimer's disease and mild cognitive impairment," Entropy 20(1), 1–15 (2018).
56. F. J. Fraga, G. Q. Mamani, E. Johns, G. Tavares, T. H. Falk, and N. A. Phillips, "Early diagnosis of mild cognitive impairment and Alzheimer's with event-related potentials and event-related desynchronization in N-back working memory tasks," Computer Methods and Programs in Biomedicine 164, 1–13 (2018).
57. L. Tylová, J. Kukal, V. Hubata-Vacek, and O. Vyšata, "Unbiased estimation of permutation entropy in EEG analysis for Alzheimer's disease classification," Biomedical Signal Processing and Control 39, 424–430 (2018).
58. L. D. Deepthi, D. Shanthi, and M. Buvana, "An intelligent Alzheimer's disease prediction using convolutional neural network (CNN)," International Journal of Advanced Research in Engineering and Technology 11(4), 12–22 (2020).
59. N. N. Kulkarni, V. K. Bairagi, "Extracting Salient Features for EEG-based Diagnosis of Alzheimer's Disease Using Support Vector Machine Classifier," IETE Journal of Research 63(1), 11–22 (2017).

60. C. Ieracitano, N. Mammone, A. Bramanti, A. Hussain, and F. C. Morabito, "A Convolutional Neural Network approach for classification of dementia stages based on 2D-spectral representation of EEG recordings," Neurocomputing 323, 96–107 (2019).
61. P. Durongbhan, Y. Zhao, L. Chen, P. Zis, M. D. Marco, Z. C. Unwin, A. Venneri, X. He, S. Li, Y. Zhao, D. J. Blackburn, and P. G. Sarrigiannis, "A dementia classification framework using frequency and time-frequency features based on EEG signals," IEEE Transactions on Neural Systems and Rehabilitation Engineering 27(5), 826–835 (2019).
62. N. Houmani, F. Vialatte, E. Gallego-Jutglà, G. Dreyfus, V.-H. Nguyen-Michel, J. Mariani, and K. Kinugawa, "Diagnosis of Alzheimer's disease with electroencephalography in a differential framework," PLoS One 13(3), 1–19 (2018).

Appendix A

AD: Alzheimer's disease
ADHD: Attention-deficit/hyperactivity disorder
ANOVA: Analysis of variance
ApEn: Approximate entropy
Bi-LSTM: Bidirectional Long short-term memory
BSS: Blind Source Separation
CNN: Convolutional Neural Network
CTM: Central tendency measure
CWT: Continuous Wavelet Transform
DCNN: Deep Convolutional Neural Network
DispEn: Dispersion entropy
DSM: Diagnostic and Statistical Manuel of Mental Disorders
DWT: Discrete Wavelet Transformation
ECG: Electrocardiogram
EEG: Electroencephalogram
EMD: Empirical Mode Decomposition
EMG: Electromyography
EOG: Electrooculogram
ERP: Event-related potentials
EWT: Empirical wavelet transform
fMRI: Functional Magnetic Resonance Imaging
GGD: Generalized Gaussian distribution
GRlVQ: Generalized relevance learning vector quantization
HC: Healthy control
ICA: Independent Component Analysis
ICD: International Classification for Diseases
iEEG: Invasive electroencephalography
IMFs: Intrinsic Mode Functions
KNN: K-Nearest Neighbor
LDA: Linear Discriminant Analysis
LS-SVM: Least-Squares Support Vector Machine
LSTM: Long short-term memory
MCA: Morphological component analysis
MCI: Mild Cognitive Impairment
MEG: Magnetoencephalogram
MLP: Multi-layer Perceptron Neural Network
MODWPT: Maximal over- lap discrete wavelet package transform
mvSE: Multivariate Sample Entropy
NIRS: Near Infrared Spectroscopy
PCA: Principal Component Analysis
PET: Positron Emission Tomography
PSD: Power spectral density
QDA: Quadratic Discriminant Analysis
RBF: Radial basis function
RK-LS-SVM: LS-SVM with RBF kernel
rsEEG: Resting-state EEG
SampEn: Sample Entropy
SNR: Signal Noise Ratio
SOP: Seizure Occurrence Period
SPH: Seizure Prediction Horizon
STFT: Short-time Fourier Transform
SVM: Support Vector Machine
TBAR: Theta/ (alpha + beta) ratio
TBR: Theta/beta ratio
TFA: Time-frequency Analysis
WHO: World Health Organizations
WT: Wavelet transform

The Sedimentation Rate of Free Erythrocytes and Their Associates, the Influence of a Standing Ultrasonic Wave

Valeri A. Doubrovski[1], Sergey V. Markov[1,2*], Stanislav O. Torbin[1], and Elena P. Karpocheva[3]

[1] Department of Medical and Biological Physics, Saratov Medical State University, 112 Bolshaya Kazachya str., Saratov, 410012, Russia

[2] Saratov State University, 83 Astrakhanskaya str., Saratov 410012, Russia

[3] Saratov Regional Blood Transfusion Center, 27 Gvardeyskaya str., Saratov 410033, Russia

*** e-mail:** markovsergeyv@inbox.ru

Abstract. A comparative analysis of the sedimentation rates of free erythrocytes and their associates – aggregates and agglutinates was carried out. The influence of a standing ultrasonic (US) wave on the blood sedimentation process was investigated. The problem was dictated not only by a purely scientific interest in the sedimentation of micro–objects in a liquid medium, but from a practical point of view also – the development of an instrumental acousto–optical method for human blood group typing. Registration of the blood sedimentation process was carried out by means of digital video recording with subsequent computer processing of the photographic images obtained. The magnitude of blood sedimentation rate was experimentally determined for various samples and conditions: 1) blood solutions with / without ultrasound exposure for different time dosages; 2) a mixture of blood samples with hemagglutinating substances (Tsoliklon) without / with ultrasonic action both for a positive agglutination reaction (formation of agglutinates) and negative ones (absence of agglutinates). Two approaches were used to process the photographic images: 1) in the case of agglutinates sedimentation the discrete counting and analysis of agglutinate parameters were used; 2) in other cases, the blood sedimentation rate was determined by the movement of the "supernatant – sediment" (plasma solution – erythrocytes mass) boundary. For the experimental conditions accepted the blood sedimentation rates were compared and, correspondently, the influence of the ultrasonic standing wave upon the process under study was estimated. It was shown that in the presence of ultrasound the sedimentation rate of RBC agglutinates (positive agglutination reaction) is more than an order higher than the sedimentation rate of free erythrocytes and their aggregates (negative agglutination reaction). Such a great difference in the sedimentation rates of agglutinates in comparison with free erythrocytes and their aggregates makes it possible to obtain a high degree of resolution of acousto–optical method for instrumental blood typing, and, hence, high reliability in blood group determination. © 2021 Journal of Biomedical Photonics & Engineering.

Keywords: blood typing; sedimentation; blood; ultrasound; sonication; agglutination; optical registration.

Paper #3410 received 15 Mar 2021; revised manuscript received 9 Jul 2021; accepted for publication 11 Jul 2021; published online 28 Jul 2021. doi: 10.18287/JBPE21.07.040501.

1 Introduction

Ultrasonic waves are widely used in clinical medicine [1], for example, ultrasound therapy and surgery, Doppler spectroscopy, ultrasound investigations. In parallel, the investigations are underway to use ultrasound in the field of biomedical technologies and laboratory diagnostics, for example, to control particles [2–4] and cells [4–7] in suspensions, to filter bacterial cells [8–11] and their separation [12]. A promising direction is to use ultrasound for the aims of biomedical immunological researches [13–20]. Note that immunological methods based on specific antigens – antibodies interactions *in vitro* with subsequent observation of the immune complexes formed are the basis of many medical laboratory diagnostic tests, in particular, for the instrumental human blood group determination.

It was for the first time when the authors were involved into the problem of automatic device creation for blood typing based on the use of a probing optical beam and stimulating ultrasonic radiation simultaneously in 1986 [13]. In the further studies and developments this method was carried out in analog [18–20] or digital forms [21–29] and in the whole it was named as "acousto–optical method for blood group determination".

An ultrasonic standing wave, oriented in the vertical direction, is grouping erythrocytes (RBC) in its nodal zones, what leads to the cells stratification in solution with a period equal to a half of the ultrasonic wavelength. The convergence of erythrocytes in the standing wave nodes increases the probability of their induced aggregation. In the presence of immunologically adequate hemagglutinating serum (or monoclonal antibodies), erythrocytes form large immune complexes – agglutinates ("positive reaction" of agglutination). These complexes, like "free" erythrocytes or their aggregates are levitating – they are held in suspension by an ultrasonic wave. The ultrasound turning off leads to a rapid sedimentation of large and rather strong RBC agglutinates. As a result, the biological object under investigation becomes transparent quickly and significantly.

In the case of immunological inconformity of the blood sample under study with the type of hemagglutinating serum or monoclonal antibodies ("negative reaction"), the formation of agglutinates in the nodes of ultrasonic standing wave is not observed, weak RBC aggregates are formed only, which basically disintegrate into individual cells when the ultrasound is turned off. Since the sedimentation rate of free erythrocytes is much lower than the rate of agglutinates, then free erythrocytes remain suspended for a long time in respect to agglutinates, and that is why the biological medium remains turbid, strongly absorbing and scattering the probing light beam. Naturally, the difference in optical properties of the samples under study (for example, optical density or transmittance) indicates the nature of the interaction of cells and the type of reaction, which ultimately makes it possible to determine the blood group of the sample. Note that the greater the difference in optical parameters for positive and negative agglutination reactions – the higher the "resolution" of the method, and, consequently, the higher the reliability of blood group sample determination.

Thus, the acousto–optical method of blood typing is based on two physical phenomena: the grouping of erythrocytes by a standing ultrasonic wave and the sedimentation of erythrocytes or their associates (RBC aggregates or agglutinates) after ultrasound turning off. The visualization of RBC grouping process and its modeling were carried out in Ref. [29] and Refs. [18 – 20, 29], respectively. The aim of this work is to visualize and study the features of the second component of the acousto–optical method of blood typing:

– measurement of the sedimentation rate of erythrocytes and their associates after ultrasound irradiation in comparison with the similar studies, but without acoustic action;

– quantitative comparison of sedimentation rates of different blood samples under different experimental conditions;

– the quantitative estimation of the magnitude of the acousto–optical method resolution of blood typing and its relationship with the sedimentation rate of biological object under study.

2 Objects and experimental technique

The research objects are:

– blood solutions in saline of various dilution levels (with / without ultrasound);

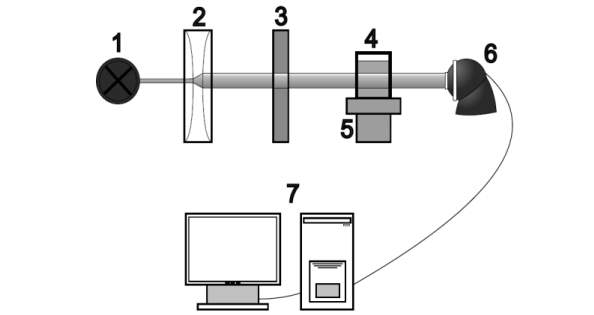
– blood solutions containing erythrocytes and naturally formed RBC aggregates, as well erythrocyte aggregates formed by ultrasound standing wave at a negative agglutination reaction;

– RBC agglutinates formed by / without ultrasonic wave action.

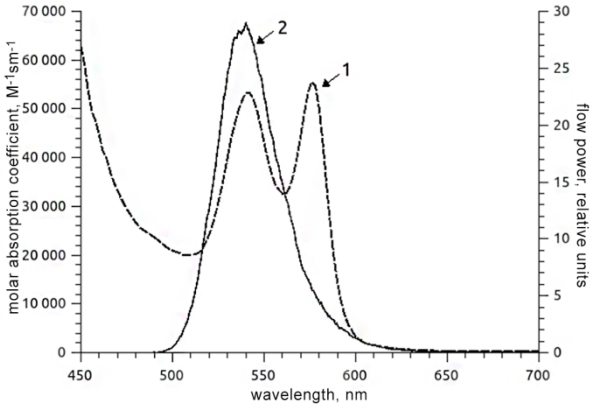
Experiments to record the process of blood solution sedimentation were carried out on the setup shown in Fig. 1a.

The dimensions of the internal cavities of the rectangular cuvettes used are 10×10×45 mm (experiments without monoclonal antibodies) or 5×18×32 mm (experiments with the participation of monoclonal antibodies). In the second case, a narrower (5 mm thick) cuvette was used to visualize individual large erythrocyte agglutinates and their subsequent computer processing. The biological object was probed by collimated radiation of an LXHL–G1S type LED, the spectrum of which corresponded to the absorption spectrum of hemoglobin in the green region (Fig. 1b). The selection of the probing light radiation spectrum was dictated by the need to increase the contrast of the photographic image boundary "plasma solution – suspension of erythrocytes", which contributes to an increase of the blood sedimentation rate accuracy measured. The probing light beam felt down

upon the Logitech QuickCam polychrome webcam after passing through the sample studied. The resultant videos were cropped into separate frames (files), which were decomposed then into RGB components and Green (G) component only was analyzed. The choice of the G component of the photographic image was associated with the absorption spectrum of light by hemoglobin in the green region and. naturally, with the spectrum of the probing radiation of the LED (Fig. 1b).



(a)



(b)

Fig. 1 The experimental setup (a) and the probing radiation and the biological object's spectra (b): a) 1 – light source (LED); 2 – telescopic lens system; 3 – light filter; 4 – cuvette with the test solution; 5 – table for fixing cuvettes; 6 – digital video camera; 7 – computer; b) 1 – absorption spectrum of hemoglobin (left ordinate), 2 – LED emission spectrum (right ordinate).

The experimental technique, the registration of blood sedimentation process and the computer processing highly depended on the nature of the object and the properties of its photographic image.

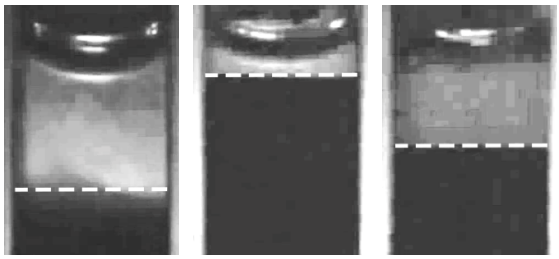
3 Sedimentation of erythrocytes and their aggregates under ultrasound action

The study of the objects sedimentation features and determination of the sedimentation rate for erythrocytes and /or their associates, it was revealed:

– there is a fairly clear boundary between the supernatant (supernatant fluid – plasma solution) and sediment (sediment – erythrocytes and erythrocyte aggregates) (Fig. 2);

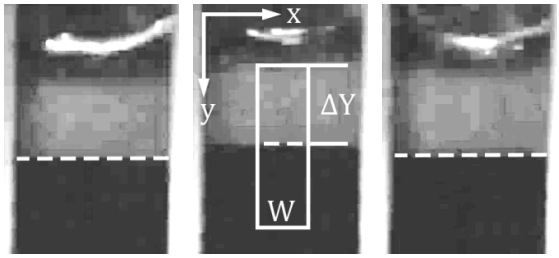
– let us get ahead – such a boundary is fundamentally absent at a positive agglutination reaction stimulated by ultrasound; naturally, it makes difficult to estimate the rate of blood sedimentation for such a case (to be discussed in Section 4.4).

I. US time duration t = 60 s



(a) (b) (c)

II. Blood concentration
C = 100% (whole blood)



(d) (e) (f)

Fig. 2 The images of samples after the standing ultrasound wave action for different content of the whole blood in solution: a) 1%, b) 30%, c) 100%, or different time duration of ultrasound action d) 30, e) 60, f) 90 sec. The experimental results illustrated for the case when monoclonal antibodies were not applied. The series of images (a–c) correspond to the time duration of ultrasonic action upon the blood samples t = 60 sec, and the series (d–f) was obtained for the whole blood. The images (a – c) correspond to the moment 60 sec after the ultrasound is turned off. Dotted lines are additionally drawn to improve the visualization of the supernatant – sediment boundary. The ΔY value is the displacement of the "supernatant – sediment" boundary during blood sedimentation, W is the area of computer processing of photographic images.

Photos (Fig. 2) indicate a rather strong dependence of the sedimentation rate on the concentration of erythrocytes in the blood solution in the presence of ultrasound. The processing of photographic images presented in Fig. 2 gives the dependence of blood sedimentation rate $v = \Delta Y/\Delta t$ on the degree of the whole blood dilution in saline (the proportion of blood in saline in %) (Fig. 3).

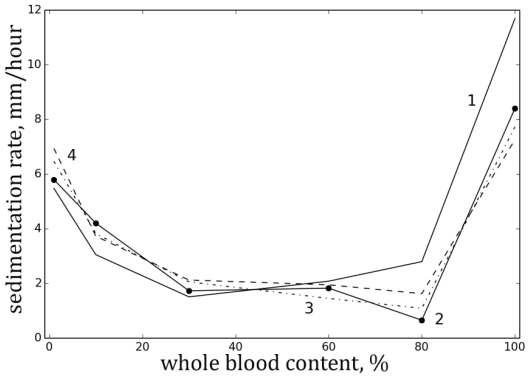


Fig. 3 The dependence of the sedimentation rate of blood solutions on whole blood content at various ultrasonic action duration: 1) t = 0 sec (no ultrasonic action), 2) t = 30 sec, 3) t = 60 sec, 4) t = 90 sec. Hemagglutinating antibodies (Tsoliklon) are absent; Graph 1 is borrowed from Ref. [30].

It is interesting to note that blood solution sedimentation rate without ultrasound action is minimal, when the whole blood content in the sample is in the range of 30–50%. At strong blood dilutions up to 0.25% of whole blood, the rate of its sedimentation increases significantly and is approximately equal to the sedimentation rate of an individual RBC cell. This is due to the fact that for such significant blood dilutions, the erythrocytes are so far apart from each other that the distance between them significantly exceeds the size of erythrocytes themselves. In this case, the velocity of the upcoming plasma solution flow displaced by erythrocytes sedimenting is not high; therefore, the inhibitory effect of this flow upon erythrocytes is small and, as a result, the RBC sedimentation rate increases [30]. For the same reason (the remoteness of erythrocytes from each other), the influence of ultrasound standing wave on the blood solution sedimentation rate is not too noticeable.

For weak blood dilutions by saline (quasi the whole blood) in the absence of ultrasound the blood solution sedimentation rate increases for the same reason (Fig. 3, Graph 1), but this time it takes place due to the increase of the distance between the erythrocytes aggregates formed spontaneously. Indeed, an increase in the proportion of the whole blood in saline over 80% increases the probability of large aggregates forming. In this case, the distance between the aggregates increases, the rate of the upcoming plasma solution flow decreases, and the rate of blood sedimentation, respectively, increases [30].

In this range of erythrocyte concentrations, the effect of ultrasound is more noticeable, since the standing wave is stimulating to enlarge the RBC aggregates and, accordingly, the distance between them increases. As a result, the sedimentation rate of RBC aggregates increases in comparison to the samples at a whole blood content about 30–80%. At the same time, in comparison with the case of blood sedimentation without ultrasound action in the blood content range 80–100% ultrasound does not increase the sedimentation rate, but, in contrary, decreases it. Multiple visual observations of blood solution sedimentation process after ultrasound action show that, when ultrasound is turned off, the aggregates formed are induced to sediment rather sharply at the initial moment, creating a certain upcoming fluid flow but at the same time they become rapidly destroyed – erythrocytes become free; that is why they sediment in about the same way as without ultrasound action. Moreover, the formed upcoming flow entrains a certain amount of erythrocytes, creating a certain obstacle to the process of blood sedimentation, which reduces the rate of its sedimentation.

4 Erythrocyte agglutinates sedimentation

4.1 Experimental technique, visualization of erythrocyte grouping by a standing ultrasonic wave

In experiments on the registration of blood sedimentation after positive or negative reactions of RBC agglutination with or without ultrasonic standing wave action, donor blood solutions of types Aβ and Bα, as well as the solutions of anti–A and anti–B monoclonal antibodies (ERYTHROTEST^{TM}–Tsoliklones) were used. Recall that the agglutination reaction is considered as positive if the result is an immune RBC complex – agglutinate ("+" in Table 1), otherwise the reaction is considered as negative ("–" in Table 1).

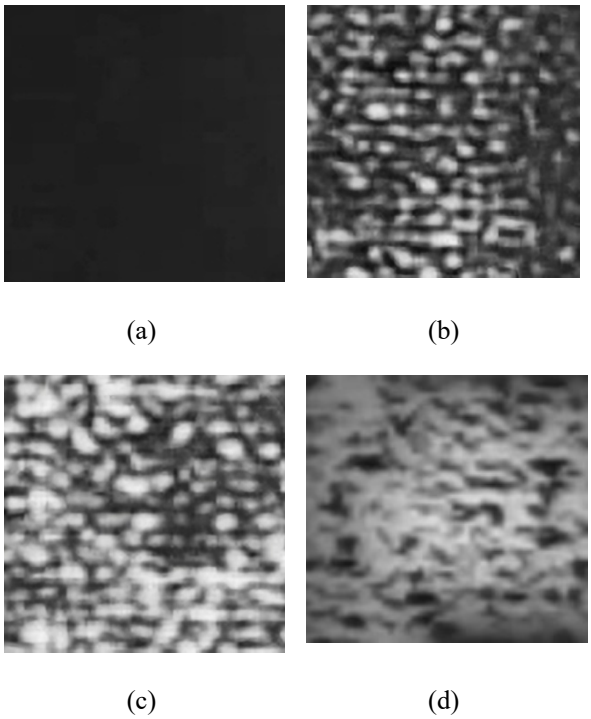
Table 1 – Human blood typing using tsoliclones.

Tsoliclones		**The tested blood belongs to the group**
anti–A	anti–B	
The RBC reaction type under investigation		
–	–	0(I)
+	–	A(II)
–	+	B(III)
+	+	AB(IV)

The components of the mixture "blood solution – hemagglutinating substance" were mixed in a cuvette mounted on a piezoceramic transducer. The dimensions of the rectangular cuvette were 5×18×32 mm, and the probing optical beam (Fig. 1a) fell on the cell wall with a maximum area of 18×32 mm. In the absence of ultrasound, a digital video camera was turned on in 10 s after mixing the components and the observed process was recorded.

In the presence of ultrasound, the erythrocytes grouping in the nodes of the standing wave occurred (it was noted in Section 1 Introduction) and, as a result, stratification of blood sample both for a positive or a negative agglutination reaction had taken place. The process of stratification of a suspension of erythrocytes,

and then the destruction of these layers due to erythrocyte aggregates sedimentation (negative agglutination reaction) is shown in Fig. 4. The initial moment of time, when the ultrasound is already on, but the process of stratification of the suspension "blood solution – monoclonal antibodies" has not practically started yet, corresponds to Fig. 4a. That moment of time the erythrocytes are distributed in the cuvette relatively uniformly, the cell suspension absorbs the light flux emitted by the LED with $\lambda \pm \Delta\lambda = 540 \pm 20$ nm (Fig. 1b) efficiently, so the brightness of the photo image is close to zero.



(a) (b)

(c) (d)

Fig. 4 The dynamics of erythrocytes grouping by a standing ultrasonic wave for the case of a negative agglutination reaction. The photo images in G channel of "blood solution – monoclonal antibodies" suspension during its irradiation by a standing ultrasound wave at different moments of time in respect to the start of ultrasound action are presented: a) t = 0 sec, b) t = 15 sec, c) t = 50 sec, d) t = 226 sec.

Fig. 4b demonstrates the stratification of the cell suspension at the 50th sec after the ultrasound is switched on: the dark stripes correspond to the areas of grouped erythrocytes that intensively absorb light; light stripes – areas with a small number of cells, light passes relatively freely through these areas. The layers of erythrocytes levitate, being held by a standing ultrasound wave, and some disturbance in the periodicity of the bands is caused by not an ideal distribution of the ultrasound field in the cuvette. By the 50th sec (Fig. 4c), the erythrocytes, being grouped in the nodes of the standing ultrasound wave, have formed such large aggregates that the ultrasound field is unable to hold such heavy aggregates, their layers are mixing, some of the aggregates are sedimenting, the image becomes less regular. The final destruction of the erythrocytes stratification picture can be seen in Fig. 4g (226th sec) – a few seconds before the ultrasound was turned off.

4.2 Experimental results

A more complete gallery of photographs – not only for a negative agglutination reaction (Fig. 2), but for a positive one also, as well as with and without the participation of an ultrasound standing wave is presented in Fig. 5.

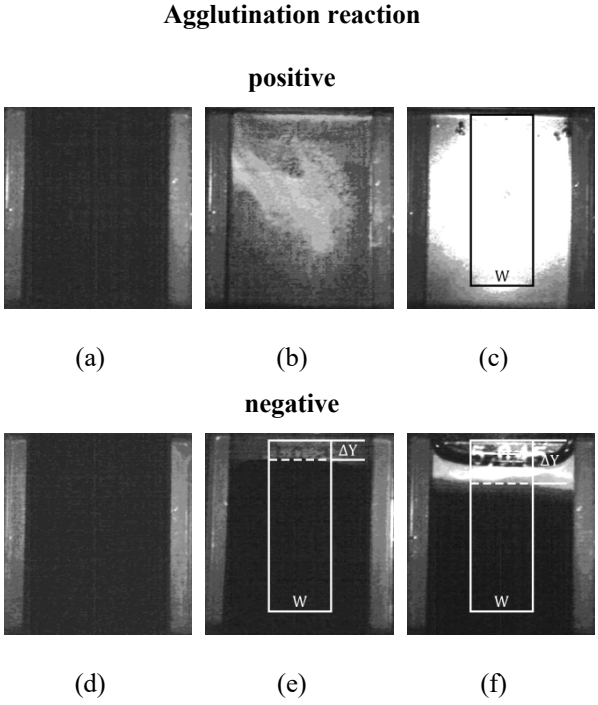


Fig. 5 Photographs of blood samples for a positive and negative agglutination reactions without ultrasonic action on a biological object and with the participation of ultrasound. Photo (a) and (d) – initial photographic images (for comparison with subsequent ones). Photographs for positive (b) and negative (e) agglutination reactions without ultrasound action on the mixture by the 14th and 54th min respectively. Photographs for positive (c) and negative (e) agglutination reactions at ultrasonic irradiation of the mixture by the 4th and 31st min. respectively. The whole blood content in the experiments was ~ 2%. The time duration of ultrasonic wave action upon the mixture was 50 sec. W – area for computer processing; ΔY – displacement of the "supernatant – sediment" border.

Fig. 5 shows the following.

A) For a negative agglutination reaction:

– Regardless of the suspensions irradiation by ultrasound or for its absence, the "supernatant – sediment" boundary is observed; the temporary movement of it gives information on the sedimentation rate of the blood sample solution.

– The grouping of erythrocytes by a standing ultrasound wave (Fig. 5f) leads to the formation of large aggregates, which increases the rate of blood sedimentation (comparison of Figs. 5e and 5f). Moreover, as the observations during ultrasonic irradiation of "blood solution – monoclonal antibodies" suspension show the blood sedimentation begins to occur even before the ultrasound is turned off, that is, in the process erythrocytes and their aggregates grouping. This is due to the fact that ultrasound forms such large erythrocyte aggregates that a standing ultrasound wave is not able to keep them in a state of levitation.

– In the absence of ultrasound, blood sedimentation does not occur immediately, but after several hundred seconds (delay time $t \approx 700$ sec, Fig. 5e). This phenomenon was observed consistently with various samples of blood solution. The explanation is based on the experimental observations: the formation of the supernatant – sediment boundary and its subsidence begins only after a portion of plasma solution in the form of a coming up flow in respect to the direction of erythrocytes (their aggregates) movement enters upward along the glass walls of the cuvette and is located above the layer of erythrocyte mass.

B) For a positive agglutination reaction

The processing of the photographic image corresponding to Fig. 5c is difficult: erythrocyte agglutinates are formed so quickly, their sizes and sedimentation rate are so high that there is no "supernatant – sediment" boundary and, therefore, the principle of processing of photographic images should be different in relation to the case, when such a boundary exists. The principle of the processing of photographic images like Fig. 5c to find the blood sedimentation rate is described in Section 4.4.

4.3 The principle of photographic images processing in the presence of a supernatant – sediment interface

For digital processing of photographic images in Fig. 5b, e, f, the zones W with dimensions 5×20 mm were chosen. For the photographs indicated, in contrast to Fig. 5c, it is fundamental that for these cases there is a "supernatant – sediment" boundary ("plasma solution – erythrocyte mass"). Within the selected zone, the photographic image (video frame) was transformed into a two–dimensional array, the elements of which were the brightness B (brightness) of pixels for the G component of RGB decomposition of the photographic image obtained. To get a more clear determination of the boundary the binarization of the photographic image was carried out: in the array studied the pixel brightness were averaged line by line (from left to the right and from top to bottom). As a result, the two–dimensional array was transformed into a one–dimensional $B_{av}(Y)$, which was then filtered according to a given threshold value B_{thr}, determined from the analysis of the photo image. The elements of a one–dimensional array with the brightness lower or equal to the threshold $B_{av}(Y) \le B_{thr}$ were assigned as the brightness equal to zero $B_{av}(Y) = 0$, the rest of the elements were assigned as a certain brightness $B_{av} = B_0$, different from zero.

In the limits of the zone W analyzed, each line of the photographic image scanned has its own Y coordinate. Therefore, when reading the results of the one–dimensional array, the transition from the "light" to "dark" part of the zone W indicates the location of the supernatant – sediment boundary. Naturally, such a boundary corresponds to a line of a photographic image with a maximum brightness gradient $\Delta B_{av} / \Delta Y$. The movement of boundary from frame to frame determines the rate of blood sedimentation in (pixels/s). It is possible to find the sedimentation rate of the object $v = \Delta Y/\Delta t$ in (mm/min), if to use the resolution r ($r = 38$ ps/mm) magnitude of the experimental setup (Fig. 1a). Indeed, the computer processing of the temporary photographic images series Fig. 5 (b, e, f) made it possible to determine the level of the "supernatant – sediment" boundary displacement along Y axis in time t (Fig. 6).

Comparison of Fig. 6 shows that the blood sedimentation rate is minimal for a negative agglutination reaction and, at the same time, in the absence of ultrasonic action upon the blood solution (Fig. 6e): there are no factors that would lead to the formation of large erythrocyte associates and in a large number.

Fig. 6f shows that for negative agglutination reaction the blood sedimentation rate is maximum when during ultrasonic irradiation of an object the ultrasound use to form large erythrocyte aggregates (not agglutinates), which are quickly sedimenting quickly. After that when ultrasound is switched off the fragile aggregates use to disintegrate into individual erythrocytes or smaller aggregates. They are sedimenting just as slowly as free erythrocytes or cells after a negative agglutination reaction (Fig. 6e). This is also evidenced by the fact that the slope of the curves (sedimentation rate) in Figs. 6e and 6f are practically the same.

As it was noted in Section 4.2 for a positive agglutination reaction with the participation of ultrasound (Fig. 6b), the process of RBC agglutinates sedimentation occurs so quickly and rather chaotically that the "supernatant – sediment" boundary is absent. That is why in Fig. 6c the ordinate shows the value of the "equivalent displacement" of a certain effective boundary "supernatant – sediment" (the introducing and the description of this parameter is presented in Section 4.4). For a positive agglutination reaction but without ultrasound action, the blood sedimentation (Fig. 6b), as in the case of a negative reaction (Fig. 6e), occurs with a time delay (the lag time $t \approx 350$ sec; Fig. 6b). Possible explanation: at whole blood content in the sample ~ 2% the mean statistical distance between erythrocytes is so great (2–3 times more than the erythrocyte diameter itself) that the probability of an antigen–antibody type of immune interaction (erythrocyte – monoclonal antibodies) with the formation of an erythrocyte complex is small.

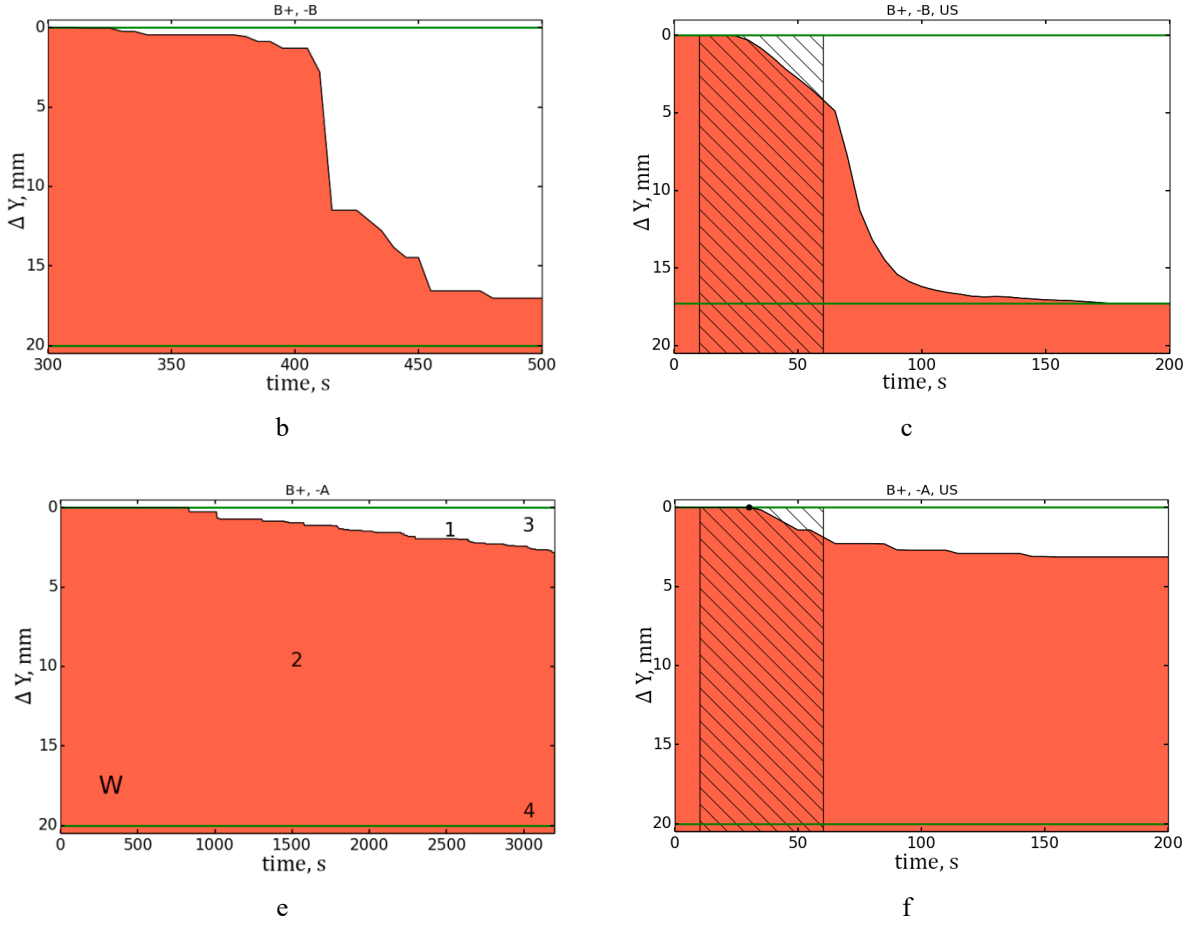


Fig. 6 Time dependence of the "supernatant – sediment" boundary displacement. (b), (c), (e), (f) correspond to the photographic images shown in Figs. 5 (b), (c), (e), (f) respectively. 1 – supernatant (plasma solution); 2 – sediment (erythrocyte mass), 3 – line corresponding to the meniscus of fluid in the cuvette – the level of the blood sedimentation start, 4 – line corresponding to the lower limit of the processing zone of experimental results W. The shaded area in (c) and (f) shows the time interval of ultrasonic irradiation of the sample. Note that the ultrasound was switched on 10 sec after the start of the video.

That is why small agglutinates are formed, which are suspended for a long time (several minutes). And only when small agglutinates combine into larger ones, a rather intensive process of agglutination and, consequently, their sedimentation starts. This interpretation is supported by Fig. 6f – here blood sedimentation takes place immediately, even during the process of ultrasound irradiation, so before it is turned off, since the aggregates (not agglutinates) created by ultrasound are larger than spontaneous (without ultrasound) agglutinates.

4.4 The principle of photographic images processing in the absence of the "supernatant – sediment" interface

The particular interest is the sedimentation of erythrocyte associates at a positive agglutination reaction in the presence of a standing ultrasonic wave (Fig. 5c). It is characteristic that in this case the agglutinates of large size are formed so extremely quickly that the photographic image of the suspension under study already at 10–20 sec after the ultrasound is turned off has a discrete structure Fig. 7a and the boundary "supernatant – sediment" is completely absent – Fig. 5c, as well as Fig. 7a. Naturally, without such a boundary it is not possible to estimate the blood sedimentation rate in the traditional way. On the other hand, agglutinates of different sizes and shapes sediment in different ways and at different rates. Under these conditions, it was proposed to determine the sedimentation rate of agglutinates by the rate of change in the integral area S occupied by all agglutinates of the investigated zone W for the photographic image under analysis (200×650 pixels). It can be seen from Fig. 7 (1a–4a) that in the process of agglutinates sedimentation, the integral area S decreases in time, so that S is a function of time t, and the derivative of this function $\Delta S/\Delta t$ can be taken as the rate of blood sedimentation.

The calculation of S(t) for each photo image of the video was carried out in accordance with the algorithm:

– in the general photo of the cuvette with the blood solution under study, the zone W was highlighted (Fig. 7 (1a)) so that the probing light beam was located in its center; its position and size did not change when the subsequent photographs were under processing;

– computer scanning of the zone W along the X and Y axes made it possible to determine the number of pixels, their coordinates in W zone, as well as the values of their brightness B ($0 < B < 255$ units of brightness); thus, the result of scanning the photo image W was a three–dimensional array of X, Y, B;

– the average brightness of the pixels which corresponded to erythrocytes and their associates B_{er}, as well as the same parameter for the "background" B_{bg} (space free from cells) were experimentally determined;

– then for each real photographic image W for a certain moment in time (for example, Fig. 7 (1a)), a corresponding artificial, equivalent image W_{eq} was constructed (for example, Fig. 7 (1b));

– for this purpose, an auxiliary image W_{aux} was preliminarily created with the dimensions identical to the processing area $W_{aux} = W$; moreover, the brightness of each pixel of this auxiliary image W_{aux} was set equal to B_{bg} for the green RGB component; this image W_{aux} will serve as a background for the equivalent photographs constructing for various frames;

– according to the results of B_{er} and B_{bg} measurements, a certain value of the threshold brightness B_{tb} was set so that $B_{er} < B_{tb} < B_{bg}$;

– the number of pixels on the photographic image area W (in any photo frame), for which $B_{er} < B_{tb}$ was asumed as the number of pixels, which corresponded to erythrocyte aggregates or agglutinates N_{er} (individual erythrocytes could not be visualized due to their relatively small size and insufficient resolution of the experimental setup); naturally, over time, from frame to frame, the N_{er} value gradually decreased (Fig. 7 (1a–4a));

– then, for each real photo frame, the number of pixels N_{er} counted was transferred on to the corresponding auxiliary background image W_{bg}; the transfer was carried out from bottom to top, and each such pixel was assigned a minimum brightness B_{min}; as a result, a dark area was formed in the lower part of the equivalent image, which illustrated the sediment; then the upper area symbolized the supernatant (Fig. 7b);

– thus, each real photographic image with a discrete structure of chaotically located erythrocyte associates (for example, Fig. 7 (1a)) was assigned an equivalent image (for example, Fig. 7 (1b)), and the area of the "sediment" was equal to the area of all elements of the discrete structure, that is, the areas of all associates.

– As a result, the photographic image, on which there is no real boundary "sediment – supernatant" (for example, Fig. 7 (1a)), was transformed to an equivalent form for which such a boundary exists (for example, Fig. 7 (1b)). Further, the "equivalent" images for each photo frame (for example, Figs. 7 (1b–4b)) were processed by analogy with the photo images of objects sedimentation with a real "supernatant – sediment" boundary (Section 4.3). The results of such processing are shown on Fig. 6c. By analogy with other Fig. 6, it is possible to determine the equivalent blood sedimentation rate v_{eq} for the case of a positive agglutination reaction when the object is exposed to an ultrasonic field.

5 Discussion of the Results

The order of magnitude of blood sedimentation rates for various experimental conditions is determined. In general, the results are summarized in Table 2.

Table 2 – Sedimentation rate comparison under different experimental conditions.

Object	**The properties of the object**	**Whole blood content (%)**	**Sonication time (sec)**	**Average rate of object sedimentation v/v_{eq} (mm/min)**	**v_1 (mm/min)**	**v_2 (mm/min)**
Blood solution	Dilution by saline (Fig. 3)	0.25	–	0.09	–	
			30–90	0.12		
		30–50	–	0.03		
			30–90			
		100	–	0.2		
			30–90	0.14		
Blood solution + tsoliklon	Negative agglutination reaction	2	–	0.07 (Fig. 6e)	0	–
			50	0.8 (Fig. 6f)	2.5	0.47
	Positive agglutination reaction		–	6 (Fig. 6b)	2.3	–
			50	14 (Fig.6c)	7	9.22

Note that in the presence of a supernatant – sediment interface, the blood sedimentation rate was determined as the rate of the displacement of this boundary $v = \Delta Y/\Delta t$ using the results of photo processing (Fig. 3; Fig. 6 (b, e, f). In this case, the value of Δt was taken as the time interval from the moment of the beginning of the boundary motion up to the moment of time when blood sedimentation process is almost complete, the sedimentation rate is close to zero. As noted in Section 4.3 and it can be seen from Fig. 6f and Fig. 6c, the sedimentation may start even before the ultrasound is turned off, if sufficiently large erythrocyte associates are formed under the action of the ultrasound wave and the condition for their levitation is violated.

If there is no supernatant – sediment interface (a positive agglutination reaction in the presence of ultrasound, Fig. 5c and Fig. 6c), in the Section 4.4 the concept of an equivalent blood sedimentation rate was v_{eq} introduced. Table 2 shows the values of real blood sedimentation rate v but in the case of a positive reaction in the presence of ultrasound the value of v_{eq} is given (Fig. 6c).

It should be noted that the sedimentation rates in Table 2 give a qualitative, comparative idea about the order of these values only. This is due to the fact that the values of the velocities depend on many experimental factors, as well as on the approach to make such estimations. In the last column of Table 2 the references to the figures show on what basis the blood sedimentation rates were calculated.

Table 2 shows the following.

– In the absence of monoclonal substances (tsoliklon) RBC associates sedimentation rate v rather weakly depends on the presence or absence of ultrasound and the duration of its action. Indeed, this rate is determined by the initial erythrocytes concentration of in the suspension to a greater extent. The minimum speed $v \approx 0.03$ mm/min corresponds to a blood concentration in the suspension of 30–50(%). A decrease in concentration, like an increase in it, increases the speed value; explained in Section 3.

– For a negative agglutination reaction, the role of ultrasound increases significantly. Thus, the sedimentation rate of RB associates increases by more than an order (from 0.07 to 0.8 mm/min) due to the action of an ultrasonic standing wave. It seems quite natural that the erythrocytes grouping in the nodes of the standing ultrasound wave increases the probability of their aggregation (not agglutination).

– For a positive agglutination reaction, the blood sedimentation rate in the presence of ultrasound is more than twice higher the same rate but without ultrasonic action. However, we note that from the point of view of the development of acousto–optical method for blood typing, it is more important to compare the rates of its sedimentation at positive and negative agglutination reactions.

– In the presence of ultrasound, the blood sedimentation rate for a positive agglutination reaction v_{eq+} is significantly higher than the speed for a negative one v_{-} (v_{eq+}/v_{-}) ≈ 18;

– To more precisely comparison of sedimentation process two more speed parameters v_1 and v_2 were calculated:

v_1 – speed that was calculated on time range from start of sedimentation to the end of this process for positive agglutination reaction (Fig. 6c).

v_2 – speed parameter for cases with US sonication. Time range: from US switching off till the end of sedimentation for positive agglutination reaction (Fig. 6c).

These parameters (v_1 and v_2) are more suitable for comparison of sedimentation rates for cases which illustrated on Fig. 6. The difference between v_1 and v_2 for cases with US sonication shows that during sonication sedimentation goes faster for negative reaction, and slower for positive one than after US switching off. It is caused by RBC aggregation and agglutination: sonication increases process of RBC associates forming. After US switching off most of RBC aggregates are destructed and became a separate RBC or smaller aggregates unlike RBC agglutinates that still formed. This determines the sedimentation character after US switching off: for negative reaction it is slow and closer to the case for negative reaction without US sonication; for positive reaction it is rapid process caused by large RBC agglutinates sedimentation.

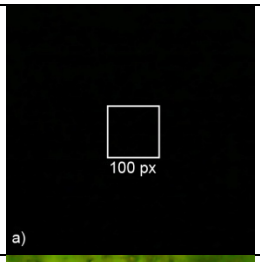
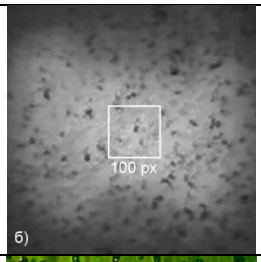
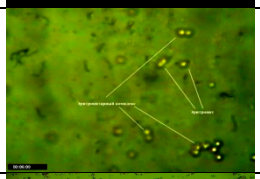
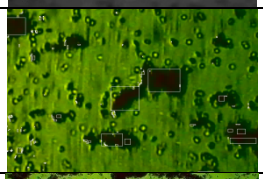
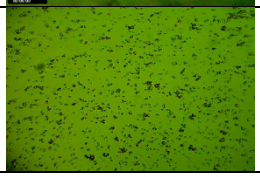
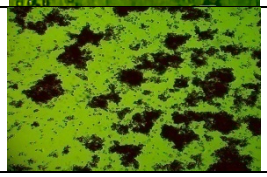
The latter circumstance determines a high level of the resolving power of the acousto-optical method for blood typing (Section 6) and, consequently, the reliability of its results.

6 Resolution of the acousto–optical method to determine blood group type according to the AB0 system

Such a significant difference in the sedimentation rate of erythrocyte agglutinates (positive reaction) from the sedimentation rate of free erythrocytes and their aggregates (negative reaction) at the ultrasonic action on the blood sample under study makes it possible to obtain a high level of resolution R in blood group determination. It may be considered that this parameter is responsible for the reliability of the blood group typing. There are different ways to introduce this parameter, for example, [18, 23–25, 28–31]. At any rate R shows how strongly the physical quantity measured by the device in the case of a positive agglutination reaction differs from the same value, but with a negative one. Naturally, the reliability of blood group determination increases with the increase of R.

Some examples of the experimentally obtained resolution values of the acousto–optical method for blood group determination are given in Table 3. It should be understood that the resolution R depends not only on the peculiarities of "blood solution – hemagglutinating serum (monoclonal substance)" interaction, but on the method of recording the result of the reaction also, as well

Table 3 – Comparison of optical methods resolution power.

№	Optical method of investigation	Method of resolution power form (R)	Negative reaction	Positive reaction	R, literary reference
	1	2	3	4	5
A	RBC sedimentation	Photometry: $R_{mean} = B_{+,mean}/B_{-,mean}$			150 [28]
		Statistics: $R_D = D_+/D_-$			328 [28]
		Discrete analysis $R_\Sigma = B_{+,\Sigma} / B_{-,\Sigma}$			2 400 [28]
B	Flow cytometry	Area: R $=S_{+\ mean}/S_{-,mean}$			500–10000 [24]
C	Digital microscopy	Area: R $=S_{+,\ mean}/S_{-,mean}$			1500–3000 [23]

as the method of processing the resulting photographic images.

Comments to the Table 3.

– The column 1 demonstrates the optical approach to register the presence or absence of the erythrocyte agglutination (the corresponding photo images are given in the columns 3 and 4). So, for example, the cell A–1 corresponds to the photographing of erythrocytes for a positive and negative reactions during blood sedimentation; the values measured were the magnitudes of photographic images brightness $B_{+,mean}$ and $B_{-,mean}$ – averaged over the area W of the image – photometry. During the statistic processing of the same photographs, the distributions of pixels' brightness of photographs obtained were determined and compared: D_+ and D_- are the values of the corresponding variances. The discrete analysis suggested:

1) either the calculation of the number of pixels with brightness above (or below) a given threshold of brightness value;

2) either the calculation of the total brightness values of all the pixels of the same photographic images, both for positive and negative agglutination reactions.

In Table 3, in particular, $B_{+,\Sigma}$ and $B_{-,\Sigma}$ are entered – the values of the total brightness of the pixels of the photographic images for positive and negative reactions, respectively.

– Flow cytometry (line B) allows to obtain and to compare the photographic images of two types of suspensions (positive and negative reactions) when they flow through a glass capillary of a small internal size: $S_{+,mean}$ and $S_{-,mean}$ are the mean values of the agglutinates areas or erythrocyte aggregates (and artifacts) in the corresponding photographs (the cells B–3 and B–4 of Table 3, respectively).

– Digital microscopy – photo registration of agglutinates (the cell B–3) and free erythrocytes and their aggregates (the cell B–4). Here $S_{+,mean}$ and $S_{-,mean}$ are the mean values of the agglutinates areas and of erythrocytes (aggregates), respectively.

The Column 5 lists the corresponding values of the resolutions R, as well as the corresponding literature references to the experimental works.

7 Conclusion

In accordance with the purpose of the work, an experimental study of the sedimentation of erythrocytes and their associates (aggregates or agglutinates) after ultrasonic irradiation was carried out in comparison with a similar experiment, but without acoustic action. The magnitudes of blood sedimentation rates were experimentally determined for the cases:

– blood solutions of various dilution levels in saline (with / without ultrasound);

– blood solutions containing naturally formed RBC aggregates, as well as erythrocyte aggregates formed by ultrasound standing wave for a negative agglutination reaction;

– erythrocyte agglutinates formed with / without the participation of an ultrasonic wave.

It is shown that, in the absence of a standing ultrasonic wave, the blood sedimentation rate in the case of a positive agglutination reaction is almost two orders of magnitude higher than for a negative reaction. At the same time, ultrasonic action additionally more than doubles the blood sedimentation rate for a positive agglutination reaction. What is important for the development of an acousto–optical method to determine the blood group type: when the solution of blood sample under test is exposed by a standing ultrasound wave, the rate of blood sedimentation for a positive agglutination reaction is approximately 18 times higher than for a negative one.

Such a high difference in blood sedimentation rates at positive and negative agglutination reactions leads to a significant difference in the optical energetic characteristics of the samples under study. It is shown that the brightness of blood sample photo image or another measured parameter for a positive agglutination reaction may be some orders of magnitude higher than the same parameter of the sample for a negative reaction. This principle is the base of acousto–optical method for instrumental determination of the blood sample group.

The studies carried out are useful to understand the physical fundamentals of the acousto-optical method for the blood typing and the reasons for the high level of its resolution achieved. From a practical point of view, the experiments, which describe the sedimentation kinetic of RBC and their associates are of most interest, especially for the cases of positive and negative agglutination reactions under the ultrasonic action. These experiments make it possible to estimate the required duration of ultrasonic action upon the blood tested, as well as the time duration of its incubation - the time interval from the moment of the end of the ultrasound irradiation to the moment of reading the result. This is all the more important if the proposed acousto-optical method will be used as the basis to create the automatic device for blood typing.

Disclosures

All authors declare that there is no conflict of interests in this paper.

References

1. W. L. Nyborg, Ultrasound: Its application in medicine and biology, Elsevier, New York (1978).
2. G. Whitworth, M. A. Grundy, and W. T. Coakley, "Transport and harvesting of suspended particles using ultrasound," Ultrasonics 29(6), 439–444 (1991).
3. C. J. Schram, "Manipulation of particles in an acoustic field," Adv. Sonochem, 2, 293 (1991).
4. W. T. Coakley, G. Whitworth, M. A. Grundy, R. K. Gould, and R. Allman, "Ultrasonic manipulation of particles and cells," Bioseparations 4(2), 73–83 (1994).
5. W. T. Coakley, D. W. Bardsley, M. A. Grundy, F. Zamani, and D. J. Clarke, "Cell manipulation in ultrasonic standing wave field," Journal of Chemical Technology & Biotechnology 44(1), 43–62 (1989).
6. M. S. Limaye, J. J. Hawkes, and W. T. Coakley, "Ultrasonic standing wave removal of microorganisms from suspension in batch systems," Journal of microbiological methods 27(2-3), 211–220 (1996).
7. W. T. Coakley, D. W. Bardsley, "Enhanced sedimentation of mammalian cells following acoustic aggregation," Biotechnology and bioengineering 34(4), 559–562 (1989).
8. O. Doblhoff–Dier, T. Gaida, H. Katinger, W. Burger, M. Groschl, and E. Benes, "A novel ultrasonic resonance field device for the retention of animal cells," Biotechnology Progress 10(4), 428–432 (1994).
9. J. J. Hawkes, W. Coakley, "A continuous flow ultrasonic cell filtering method," Enzyme and Microbial Technology 19(1), 57–62 (1996).
10. J. J. Hawkes, M. S. Limaye, and W. T. Coakley, "Filtration of bacteria and yeast by ultrasound–enhenced sedimentation," Journal of Applied Microbiology 82(1), 39–47 (1997).
11. F. Trampler, S. A. Sonderhoff, P. W. S. Pui, D. G. Kilburn, and J. M. Piret, "Acoustic cell filter for high density perfusion of culture of hybridoma cells," Bio/technology 12(3), 281–284 (1994).
12. C. A. Miles, M. J. Morley, W. R. Hudson, and B. M. Mackey, "Principles of separating microorganisms from suspensions using ultrasound," Journal of Applied Bacteriology 78(1), 47–54 (1995).
13. A. N. Alipov, V. Z. Vaninskiy, L. B. Denisov, S. I. Donskov, V. A. Dubrovskiy, E. N. Zav'yalov, and N. N. Knyazkov, "Method for determining the agglutination reaction," Inventor's Certificate of the invention №1683760, 04.06.1987. [in Russian].
14. M. A. Grundy, W. E. Bolek, W. T. Coakley, and E. Benes, "Rapid agglutination testing in an ultrasonic standing wave field," Journal of Immunological Methods 165(1), 47–57 (1993).
15. M. A. Grundy, K. Moore, and W. T. Coakley, "Increased sensitivity of diagnostic latex agglutination tests in an ultrasonic standing wave field," Journal of Immunological Methods 176(2), 169–177 (1994).
16. E. E. Pohl, E. H. Rosenfeld, P. Pohl, and R. Millner, "Effects of ultrasound on agglutination and aggregation of human erythrocytes in vitro," Ultrasound in Medicine & Biology 21(5), 711–719 (1995).
17. E. T. Nerys, W. T. Coakley, "Measurement of antigen concentration by an ultrasound–enhanced latex immunoagglutination assay," Ultrasound in Medicine & Biology 22(9), 1277–1284 (1996).

18. V. A. Doubrovski, K. N. Dvoretski, "Ultrasonic wave action upon the red blood cell agglutination in vitro," Ultrasound in Medicine & Biology 26(4), 655–659 (2000).
19. V. A. Doubrovski, K. N. Dvoretski, and A. E. Balaev, "Mechanism of erythrocyte aggregation enhancement by ultrasonic field," Acoustic Journal 50(2), 146–153 (2004).
20. K. N. Dvoretski, Increasing the resolution of the photometric method for recording agglutination of human erythrocytes in vitro, PhD Thesis, Saratov State University, Saratov (2004).
21. V. A. Doubrovski, A. A. Dolmashkin, "Human blood group typing based on digital photographs of RBC agglutination process," Journal of Optics and Spectroscopy 109(2), 236–267 (2010).
22. V. A. Doubrovski, A. A. Dolmashkin, "Blood group typing based on digital imaging of sedimentation of erythrocytes and their agglutinates," Biomedical Engineering 46(2), 65–70 (2012).
23. Yu. A. Ganilova, V. A. Doubrovski, and I. V. Zabenkov, "The resolving power of the flowing method to register the process of human erythrocytes agglutination in vitro on the base of correlation analysis of microphotographs," Proceedings of SPIE 7999, 799903 (2011).
24. V. A. Doubrovski, Yu. A. Ganilova, and I. V. Zabenkov, "Application of a spectrally filtered probing light beam and rgb decomposition of microphotographs for flow registration of ultrasonically enhanced agglutination of erythrocytes," Optics and Spectroscopy 115(2), 218–227 (2013).
25. V. A. Doubrovski, I. V. Zabenkov, and S. O. Torbin, "Blood group typing in the ab0 system using digital microscopy," Biomedical Engineering 47(3), 126–129 (2013).
26. Yu. A. Ganilova, V. A. Doubrovski, and I. V. Zabenkov, "R and G color components competition of RGB image decomposition as a criterion to register RBC agglutinates for blood group typing," Journal of Biomedical Optics 19(3), 036012 (2014).
27. V. A. Doubrovski, M. F. Medvedeva, "The acousto-optical method for blood typing (part 1). photometric and statistical methods for image processing," Biomedical Engineering 50(1), 10–14 (2016).
28. V. A. Doubrovski, M. F. Medvedeva, "The acousto-optical method for blood typing based on discrete processing of photographic images," Biomedical Engineering 50(2), 78–83 (2016).
29. V. A. Doubrovski, M. F. Medvedeva, S. O. Torbin, and K. N. Dvoretskiy, "Visualization of RBC grouping by ultrasonic standing wave in vitro," in Problems of Optics and Biophotonics, 20–28 (2014) [in Russian].
30. V. A. Doubrovski, C. N. Dvoretski, S. V. Markov, E. P. Karpocheva, and V. V. Tuchin, "Optical Digital Registration of Erythrocyte Sedimentation and Its Modeling in the Form of the Collective Process," Optics and Spectroscopy 126(5), 595–606 (2019).
31. R. A. Steven, A Simplified Visible/Near–Infrared Spectrophotometric Approach to Blood Typing for Automated Transfusion Safety, North Carolina State University, Raleigh (2005).
32. J. B. Lambert, A miniaturized device for blood typing using a simplified spectrophotometric approach, North Carolina State University, Raleigh (2006).

Visualization and Spectral Analysis of Pubic Periosteum Atrophy

Vladimir I. Belokonev[1], Valery P. Zakharov[2*], Sergey Y. Pushkin[1], Zinaida V. Kovaleva[1], Andrey V. Zharov[1], Natalya S. Burnaeva[1], Elizaveta V. Zakharova[1], and Yulia A. Khristoforova[2]

[1] Samara State Medical University, 89 Chapayevskaya str., Samara 443099, Russia

[2] Samara National Research University, 34 Moskovskoe shosse, Samara 443086, Russia

*** e-mail:** zakharov@ssau.ru

Abstract. The atrophy of the pubic periosteum is developing in patients with a long history of femoral hernia. The traditional plastic surgery methods are efficient only in patients with femoral hernia when the Cooper ligament of the pubic periosteum is preserved. The aim of this study is to determine the thinning and atrophy degree of the pubic periosteum in patients with femoral hernia using computer tomography and Raman spectroscopy analysis. It was shown that thinning of the periosteum due to atrophy is accompanied by a significant change in the hydroxyapatite ν_1PO_4 and Amide I (959/1660 cm^{-1}) Raman peaks ratio and decrease in the 1070/959 cm^{-1} peaks. It was found that Raman spectroscopy is able to confirm the preservation and atrophy degree of the pubic periosteum during surgical resection with an 83% accuracy. © 2021 Journal of Biomedical Photonics & Engineering.

Keywords: periosteum; visualization; X-ray method; computer tomography; ultrasound; Raman spectroscopy.

Paper #3439 received 21 Jun 2021; revised manuscript received 7 Sep 2021; accepted for publication 7 Sep 2021; published online 2 Nov 2021. doi: 10.18287/JBPE21.07.040502.

1 Introduction

Almost all bone structures, with the exception of their intra-articular surfaces, are covered with periosteum, a membrane consisting of the outer fibrous layer and the inner layer (cambium) [1]. Periosteum is important for blood supply to the bone and its regeneration after injury. The periosteal thickening and elevation over the bone may be caused by the development of inflammation or tumor that can be detected by the X-ray method [2]. Periosteum can be detected using magnetic resonance imaging (MRI) but in adults it is not normally visualized separately from the cortical bone layer due to its very low signal [3]. Moreover, it is practically impossible to detect pubic periosteum using computer tomography (CT) if there are no inflammatory changes in the bone. Although the ultrasound method has limitations for bone disease detection it allows imaging the periosteal reaction earlier than by means of conventional radiography. In children, the normal periosteum is visualized as a thin hypoechoic band located above the bone cortex, but in healthy adults it is barely visible on ultrasound scan [4–6].

In 2020, we detected a case [7] of a patient's pubic periosteum completely atrophied due to long-term hernia. The traditional plastic surgery for patients with femoral hernia is only applicable when the Cooper ligament of the pubic periosteum is preserved. Further clinical observations showed the similar periosteum changes in 11 patients. Taking into account the registered clinical data for patients with long-term femoral hernia it was necessary to diagnose pubic periosteum atrophy before and during surgical operation. Ultrasonography is one of the most effective instruments for examining inguinal areas because it is able to confirm the diagnosis of femoral hernia as well as to determine the tactics and the scope of the surgical operation. At the same time, it is problematic to obtain the effective imaging of pubic periosteum by ultrasound even in combination with X- ray, MRI, and CT when there is no inflammation or no periosteum peeling from the bone. The main problem is the thinning and destruction of periosteum. As a result, only the cortical bone plate is visualized using the ultrasound method while periosteum becomes completely invisible, though this does not mean it is not present. Therefore, other approaches are required for imaging and determination of atrophy and degradation of the periosteum.

Currently, fluorescence spectroscopy is widely used to study biological tissues including bone tissue [8]. Taking into account the four vascular systems that supply the periosteum (the intrinsic periosteal system located between the fibrous layer and the proliferative layer; the periosteocortical system comprising the nutritional arteries of the periosteum; the musculoperiosteal system responsible for the callus formation after fractures; and the fascioperiosteal system) [9], the periosteum degradation should be accompanied by changes in the endosteal and the periosteal blood flows, as well as in oxidative metabolism. These processes can be detected by the changes in NADH fluorescence [10], but NADH emission spectra are partially overlapped with collagen fluorescence. Moreover, periosteal atrophy causes a decrease in collagen production. These facts make it difficult to analyze periosteum degradation by means of fluorescence spectra. Raman spectroscopy has been reported as an effective method to study biological tissue of different origins including bone tissues, their mineralization, ageing and composition [11, 12]. The Raman shifts are important contrast indicators of tissue composition, for example, to assess carbonate substitutions for phosphate positions in bone [13, 14]. The bone extracellular matrix includes protein-rich vibrational modes corresponding mainly to collagen properties such as amide backbone, a secondary structure of the protein. However, the absolute Raman intensity is rarely used to analyze tissue properties because they are influenced by the efficiency of Raman scattering and various optical effects (refractive index, specimen surface roughness, etc.). Therefore, many studies apply Raman analysis for the ratios of the maximum peak intensities and the areas under the peaks, for instance, the bone mineralization degree can be defined as the ratio of the hydroxyapatite band ν_1PO_4 (959 cm^{-1}) and Amide I (1640–1720 cm^{-1}) intensities [15]. The other techniques include relative indexes that determine the B-type carbonate substitution (CO_3 / ν_1PO_4); overlapping peaks of the ν_3PO_4 carbonate vibration and the ν_1CO_3 vibrations within the 1070 cm^{-1} region; bending CH_2 vibrations within the 1450 cm^{-1} region; collagen crosslinking (the ratio of the Amide I sub-bands at 1670 cm^{-1} and 1690 cm^{-1}) [16], helical collagen status (the ratio of Amide I sub-bands at 1670 cm^{-1} and 1640 cm^{-1}) are assessed [13]. In general, it is arguable that the whole set of Raman peaks in the 800–1800 cm^{-1} "fingerprint" region gives a detailed picture of the test tissue, its changes during the disease growth [17, 18], ageing [17], and drug therapy [18]. However, the possibility of Raman spectroscopy to assess the periosteal atrophy degree requires a special study. Therefore, the aim of this work is to establish a possibility of visualization and determination of thinning and atrophy of the pubic periosteum all the way until its complete degradation in patients with femoral hernia.

2 Materials and Methods

X-ray, CT, and ultrasonographic methods as well as the Raman spectroscopy were carried out for imaging and detecting pubic periosteum in patients with femoral hernia. The X-ray, ultrasound, and CT data of the Lonny bones in patients with femoral and groin hernias were compared with the opposite side without hernia.

Raman spectroscopy was applied for the *ex vivo* bone samples taken during autopsies to identify preservation or atrophy of the femoral canal pubic periosteum. The periosteum was removed from a part of the pubic bone samples by an edge-tool, and then the *ex vivo* samples were delivered to the laboratory for spectral analysis. To ensure the objectivity of the study, the researcher of the optical laboratory did not know on what bone samples the periosteum was preserved.

The *ex vivo* study of the bone samples was performed using spectroscopic system that allows for simultaneous Raman and fluorescence signal registration in the near-infrared region [19]. The experimental setup included a thermally stabilized LML-785.0RB-04 laser diode module (785 ± 0.1 nm central wavelength, NECSEL, USA), a QE65Pro portable spectrometer (Ocean Optics Inc., USA) with a matrix CCD detector cooled down to 15 °C, an optical Raman probe (inPhotonics, USA). Laser radiation was delivered to the optical probe using the exciting fiber (100 μm diameter, 0.22 NA) and a collimating lens. The band-pass filter cuts out noise and fiber illumination. The dichroic mirror transmits the 785 nm radiation on the lens that focuses the excitation wavelength on the bone surface. The same lens collects the backscattering light that includes the Raman and the fluorescence signals from the irradiated bone area. The dichroic mirror directs the signal to the recording channel, that includes a long-wavelength filter for filtering the exciting 785 nm radiation and then to the corresponding lenses and the collecting optical fiber (200 μm diameter, 0.22 NA) connected to the spectrometer. A detailed description of the experimental setup is given in Ref. [19]. The bone and the periosteum fluorescence spectra were registered within the 800–914 nm spectral region at the acquisition time of 10 sec with triple accumulation. The laser power on the distal fiber of the optical probe was 150 mW.

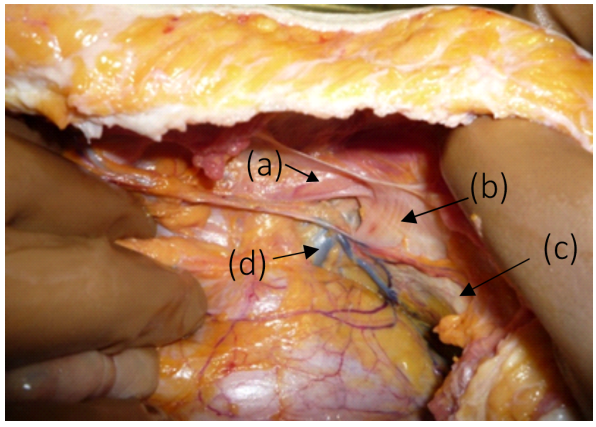


Fig. 1 The left femoral canal area from the abdominal cavity side: (a) Poupart ligament; (b) lunar (Zhimbernatov) ligament; (c) pubic bone covered with periosteum; (d) femoral vein.

3 Results and Discussion

Normally, the femoral canal is absent, but from the side of the abdominal cavity, a slit-like space between the medial wall of the femoral vein, the Poupart and the semilunar ligaments, and the pubic bone covered with the periosteum is clearly observed (Fig. 1). The slit-like space expands and a hernial sac exits through it during the femoral canal formation, which can cause atrophy of the pubic periosteum during a prolonged asymptomatic disease due to permanent friction of the hernial sac on the periosteum. The use of traditional plastic surgery methods is not possible for the femoral canal because of atrophy and thinning of the pubic periosteum.

The X-ray (Fig. 2) and the CT (Fig. 3) images of the pelvis of adult patients in the pubic articulation area clearly show a compact bone plate, but the periosteum is not distinctly visualized even in the case of a traumatic lesion. A compact substance can be clearly defined along the fracture line in the pubic articulation area in Fig. 3 but the periosteum is not observed.

The ultrasound study (Fig. 4 (a, b)) of 18–20-year-old patients revealed that the periosteum is determined as a hypoechoic band covering the anterior iliac cortex. The ultrasound scan of the spoke-bone in a 35-year-old patient shows the same result (Fig. 4 (c)), whereas for a 40-year-old patient the ultrasound transverse section clearly shows (Fig. 4 (d)) the superior pubic bone (asterisk) and an unchanged cortical layer of the bone is observed as a normal hyperechoic line (arrow) with a posterior acoustic shielding.



Fig. 2 X-ray image of the patient pelvis after the surgical resection of the hernia on the right. The compact bone substance is clearly visualized in the pubic articulation area.

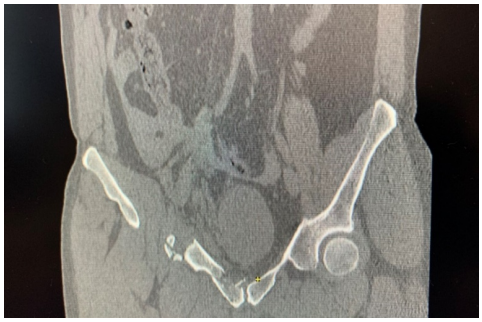
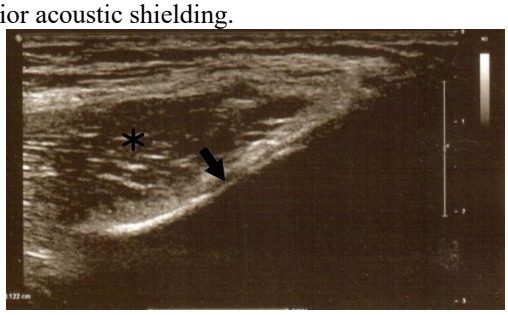
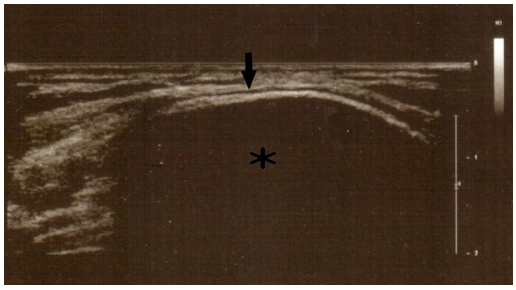


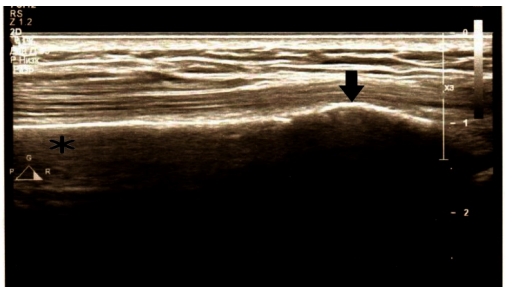
Fig. 3 CT image in the frontal plane of the pelvis with a pubic bone fracture.



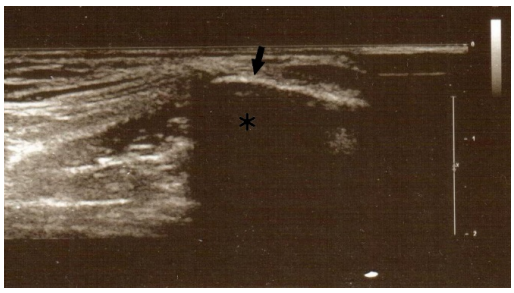
(a) 18-year-old patient



(b) 20-year-old patient



(c) 35-year-old patient



(d) 40-year-old patient

Fig. 4 The ultrasound scanning of the pubic bone: (a) on the longitudinal sonogram, the periosteum (arrow) is visualized as a hypoechoic strip covering the anterior part of the iliac cortex (asterisk); (b) the longitudinal section of the sonogram shows the anterior superior iliac spine (asterisk), thin periosteum is visualized as a hypoechoic strip (arrow); (c) the sonogram shows a longitudinal section of the upper third of the radius (asterisk), the hyperechoic line (arrow) corresponds to the cortical layer of the bone; (d) the transverse section of the anterior iliac spine (asterisk). On the ultrasound scanning, the unaltered cortical layer of the bone is observed as a normal hyperechoic line (arrow) with posterior acoustic dimming and some reverberation (artifacts).

The ultrasound scanning of a femoral hernia is shown in Fig. 5, where the arrow indicates the cortical layer of the bone (hyperechoic continuous line) and the rhombus marks the hernia area. The Doppler signal is not recorded, but the artery feeding the bone is visible.

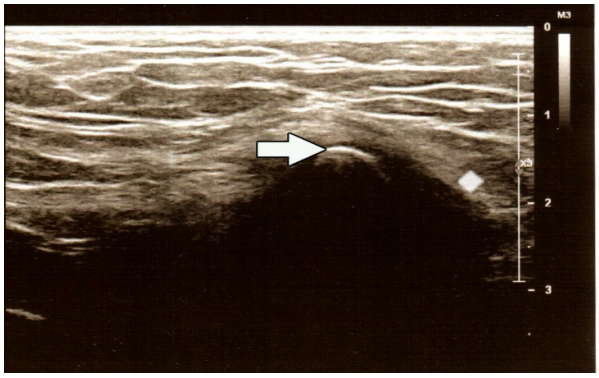


Fig. 5 The echogram of a longitudinal section of the superior iliac spine. The hyperechoic continuous line corresponds to the cortical bone (arrow). The rhombus indicates the femoral hernia.

The obtained results correlate with the study by A. D. Moraux et al. [6] stating that periosteum is reliably indicated on ultrasound images only for children, while in older age persons its determination is difficult. Other studies [4, 6] revealed that ultrasound scanning demonstrates a periosteal response indicating bone disease earlier than conventional X-rays. Considering that femoral hernia mainly affects the elderly, it is practically impossible to determine the atrophy degree, thinning or complete degradation of the pubic periosteum before surgery. Therefore, it is necessary to develop some intra-operative techniques for express analysis of the state of the periosteum pubic bone for which Raman spectroscopy seems to be one of the most promising methods.

Four pubic bone samples were studied *ex vivo* using spectral analysis. The fluorescence and the Raman spectra in the 800–914 nm band were measured from the random points at the central area of the bone and the periosteum surfaces (see Fig. 6) to avoid possible distortions associated with edge effects (residual mechanical tension or exfoliation of surface layers).

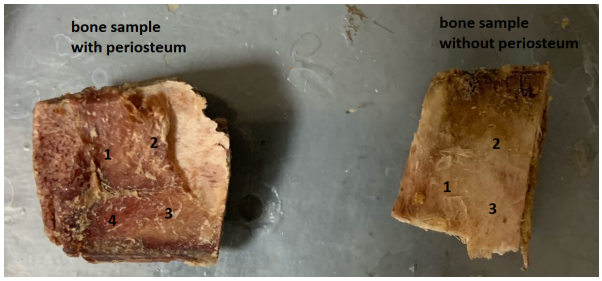


Fig. 6 Photo of the studied bone samples.

Fig. 7 shows the periosteum (blue) and bones (red) fluorescence spectra smoothed by the Savitzky-Golay filter and normalized to the standard deviation. The fluorescence spectrum is the falling curve with maximal value at the 800–810 nm initial region without highlighted spectral signatures. The fluorescence curve and its first derivative do not include any significant spectral differences, which could be associated with the presence or absence of the periosteum in the studied samples. Apparently, it can be a result of a large contribution of the bone substrate to the fluorescence signal that masks the fluorescence changes associated with the presence of a periosteum thin layer (less than 1 mm).

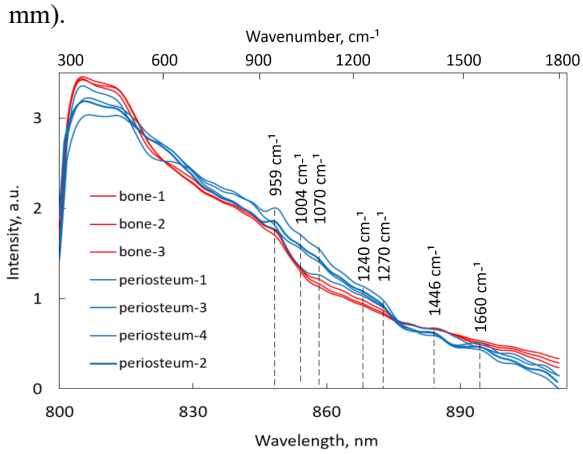
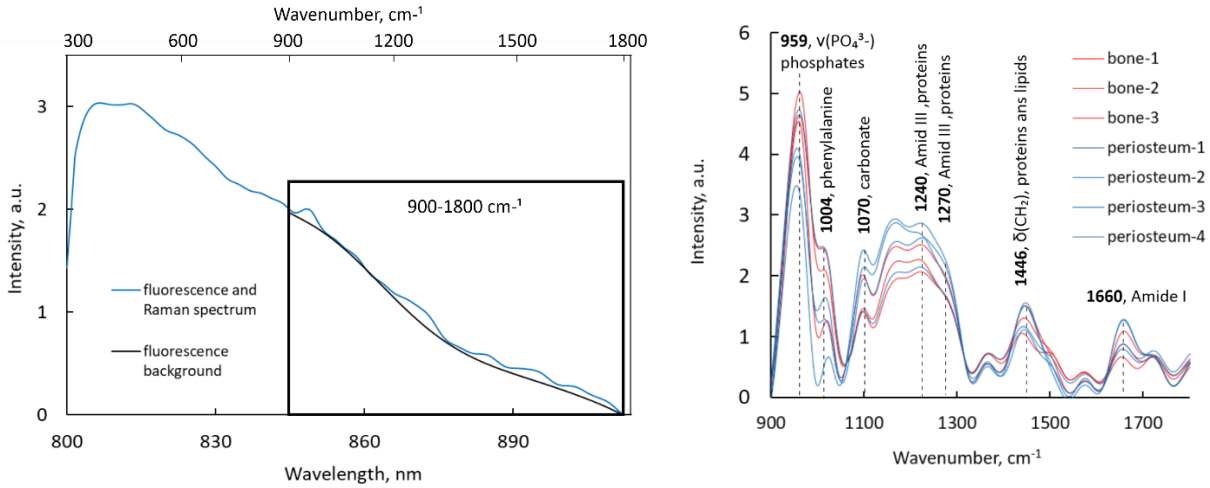


Fig. 7 The fluorescence spectra of periosteum and bone.

The bone Raman features are observed in the 900–1800 cm^{-1} wavenumber region. Therefore, to analyze the bone Raman spectrum, the fluorescence background is mathematically subtracted from the registered spectrum in 844–914 nm spectral region by a 5^{th} order polynomial approximation (Fig. 8a) [20, 21]. Fig. 8b demonstrates the Raman spectra of the bone and the periosteum samples normalized to the standard deviation after fluorescence removal.

The most prominent Raman band in both the periosteum and the bone spectra is observed at the 959 cm^{-1} (symmetric stretching PO_4^{3-} vibrations), which is associated with the contribution of the phosphate mineral. The narrow Raman band at 1004 cm^{-1} (phenylalanine) is merging with the 959 cm^{-1} band forming its shoulder peak. The highlighted Raman peak of the B-type carbonate at 1070 cm^{-1} ($\nu_1 CO_3^{2-}$) is expanded due to overlapping with a weaker peak at the 1076 cm^{-1} ($\nu_3 PO_4^{3-}$) caused by phosphate vibrations. The subtraction of the fluorescence background is able to detect the weak wide Raman peaks with the central maxima: a double 1240–1280 cm^{-1} band (Amide III), within the 1440–1450 cm^{-1} area (with the maximum at 1446 cm^{-1} associated with scissoring vibrations of the CH_2 in lipids), at 1640–1678 cm^{-1} (Amide I, with the maximum at the 1665 cm^{-1} corresponding to the polarized stretching vibrations C = O). Localization of the sub-peaks in the Amide I and Amide III bands was determined by the local minima of the second derivative of the spectrum therefore it was fractionally varied for



(a) (b)

Fig. 8 (a) fluorescence background in the analyzed 900–1800 cm^{-1} Raman area; (b) the normalized Raman spectra of the periosteum and bone after background removal.

Table 1 Raman indexes of the bone and periosteum samples.

Indexes*	Mean value (Standard deviation) Scatter		ROC AUC
	Bone (n=3)	Periosteum (n=4)	
A_{1070}/A_{959}	0.35 (0.08) 0.16	0.48 (0.17) 0.22	0.75
A_{1070}/A_{1660}	1.32 (0.13) 0.26	1.35 (0.23) 0.52	0.50
$A_{959}/A1_{660}$	3.86 (0.82) 1.63	2.98 (0.94) 2.2	0.75
I_{1070}/I_{959}	0.37 (0.07) 0.13	0.51 (0.13) 0.31	0.83
I_{1070}/I_{1660}	1.6 (0.15) 0.29	1.65 (0.24) 0.54	0.50
I_{959}/I_{1660}	4.39 (0.67) 1.32	3.4 (0.85) 1.9	0.83
I_{1240}/I_{1446}	1.64 (0.21) 0.38	1.7 (0.19) 0.46	0.75
I_{1660}/I_{1240}	0.50 (0.01) 0.016	0.47 (0.046) 0.09	0.67

* I – ratio of the maximum intensities of the Raman peaks;
A – integral indexes of the area under the peaks;
subscript indicates the peak position (cm^{-1})

different samples. It should be noted that the Raman peaks at the 959 cm^{-1} correspond to the mineral contribution (phosphate) while the peaks at 1240–1280, 1445, 1665 cm^{-1} correspond to the collagen contributions. Taking into account the small cohort of bone samples (3 spectra of the bone, 4 spectra of periosteum), to identify periosteum, spectral indexes of mineralization, carbonation, and the ratio of the organic and the mineral phases were calculated. The spectral index represents the ratio of the maximum intensities (I) or the areas under the peaks (A) at the Raman bands in question for each spectrum. Table 1 and Fig. 9 demonstrate the calculated Raman indexes and their graphical comparison for bones and periosteum samples.

Comparison of the Raman indexes has proved that for bone tissue analysis, the most informative is the ratio of the $\nu_1PO_4^{3-}$ / Amide I (I_{959}/I_{1660}) and $\nu_1CO_3^{2}$ / $\nu_1PO_4^{3-}$ (I_{1070}/I_{959}): the mean values of these indexes significantly differ between the bone and the periosteum spectra, and their dispersions scarcely overlap. For differentiating the bone and the periosteum samples on the basis of the I_{959}/I_{1660} and I_{1070}/I_{959} indexes, the ROC AUC is equal to 0.83. The mean value of the I_{959}/I_{1660} mineralization indexes for the bone spectra is 1.3 times higher in comparison with the periosteum, and the I_{1070}/I_{959} carbonate-phosphate index is 1.4 times lower, respectively. Therefore, analysis of these indexes allows detecting the progressive degradation and atrophy of the

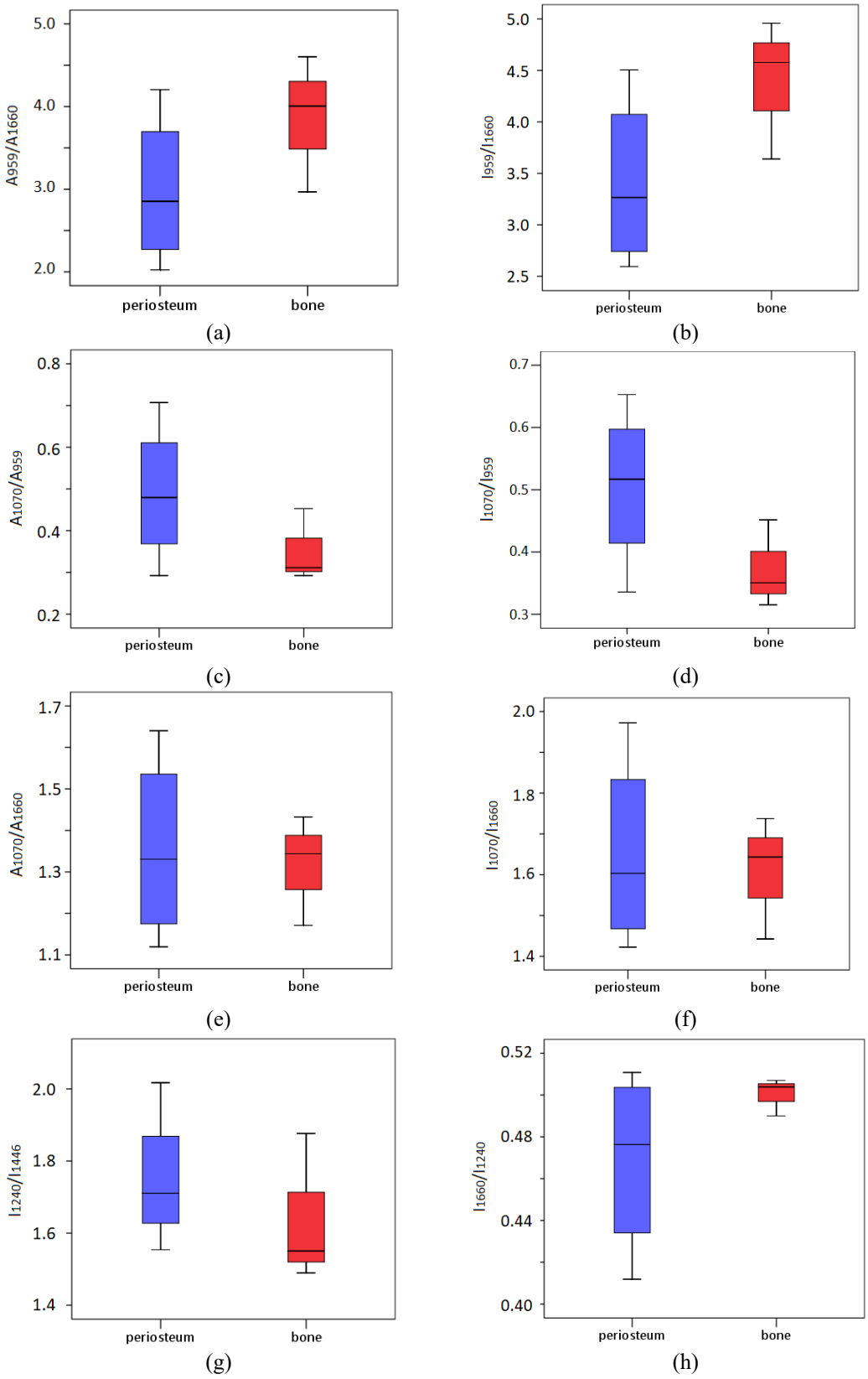


Fig. 9 Box plot diagrams with a mean value and standard deviation of the Raman indexes for periosteum (blue) and bone (red) samples, where (a) is the area ratio and (b) is the intensity ratio for the $\nu_1PO_4^{3-}$ (959 cm^{-1}) and Amid I (1660 cm^{-1}) peaks; (c) is the area ratio and (d) is the intensity ratio for the carbonate $\nu_1CO_3^{2-}$(1070 cm^{-1}) and phosphate $\nu_1PO_4^{3-}$ (959 cm^{-1}) peaks; (e) is the area ratio and (f) is the intensity ratio for the carbonate $\nu_1CO_3^{2-}$(1070 cm^{-1}) and Amide I (1660 cm^{-1}) peaks. For the Amide I (1660 cm^{-1}) and Amide III (1240 cm^{-1}) ratios as well as for the Amide III (1240 cm^{-1}) and $\nu(CH_2)$ ratio (1446 cm^{-1}) in lipids, only the intensity ratios are shown ((g) and (h) respectively).

periosteum and the manifestation of the bone spectral features in the Raman spectrum. Furthermore, it was observed that the indexes of the Amide I / Amide III (I_{1660}/I_{1240}) and I_{1240}/I_{1446} organic phases that characterize the ratio between the proteins and lipids concentrations are changing along with the change of mineralization and carbonization parameters. The changes of the organic parameters are less pronounced but in combination with the mineralization indexes they can be associated with a degree of periosteum atrophy. However, to prove this suggestion, it is necessary to perform clinical study with a large cohort of bone samples.

Comparison of the Raman indexes has proved that for bone tissue analysis, the most informative is the ratio of the $\nu_1PO_4^{3-}$ / Amide I (I_{959}/I_{1660}) and $\nu_1CO_3^{2}$ / $\nu_1PO_4^{3-}$ (I_{1070}/I_{959}): the mean values of these indexes significantly differ between the bone and the periosteum spectra, and their dispersions scarcely overlap. For differentiating the bone and the periosteum samples on the basis of the I_{959}/I_{1660} and I_{1070}/I_{959} indexes, the ROC AUC is equal to 0.83. The mean value of the I_{959}/I_{1660} mineralization indexes for the bone spectra is 1.3 times higher in comparison with the periosteum, and the I_{1070}/I_{959} carbonate-phosphate index is 1.4 times lower, respectively. Therefore, analysis of these indexes allows detecting the progressive degradation and atrophy of the periosteum and the manifestation of the bone spectral features in the Raman spectrum. Furthermore, it was observed that the indexes of the Amide I / Amide III (I_{1660}/I_{1240}) and I_{1240}/I_{1446} organic phases that characterize the ratio between the proteins and lipids concentrations are changing along with the change of mineralization and carbonization parameters. The changes of the organic parameters are less pronounced but in combination with the mineralization indexes they can be associated with a degree of periosteum atrophy. However, to prove this suggestion, it is necessary to perform clinical study with a large cohort of bone samples.

4 Conclusion

The periosteal atrophy was studied using X-ray, ultrasound, computer tomography, and optical spectroscopy. Using the X-ray method and CT before surgery is not sufficient to establish the preservation or atrophy of the pubic periosteum in the femoral canal area. With ultrasound scanning, visualization of the pubic periosteum is only possible for young patients. The spectroscopy method makes it possible to identify the degradation / atrophy of the pubic periosteum (with an accuracy of at least 83%) during intra-operative express analysis. The time of the spectral study (spectrum registration, mathematical processing of spectra and determination of Raman parameters) does not exceed 10–20 sec. However, additional clinical studies are needed to identify the peculiarities relations between Raman parameters and the age, gender, and the degree of periosteal atrophy.

Disclosures

All authors declare that there is no conflict of interests in this paper.

References

1. J. R. Dwek, "The periosteum: what is it, where is it, and what mimics it in its absence?" Skeletal radiology 39(4), 319–323 (2010).
2. D. Bisseret, R. Kaci, M. H. Lafage-Proust, M. Alison, C. Parlier-Cuau, J.-D. Laredo, and V. Bousson, "Periosteum: Characteristic imaging findings with emphasis on radiologic-pathologic comparisons," Skeletal radiology 44, 321–338 (2015).
3. I. L. Reichert, M. Benjamin, P. D. Gatehouse, K. E. Chappell, J. Holmes, T. He, and G. M. Bydder, "Magnetic Resonance Imaging of Periosteum With Ultrashort TE Pulse Sequences," Journal of Magnetic Resonance Imaging 19(1), 99–107 (2004).
4. R. S. Rana, J. S. Wu, and R. L. Eisenberg, "Periosteal reaction," American Journal of Roentgenology 193(4), W259–W272 (2009).
5. D. F. Hoffman, E. Adams, and S. Bianchi, "Ultrasonography of fractures in sports medicine," British Journal of Sports Medicine 49(3), 152–160 (2015).
6. A. D. Moraux, S. Gitto, and S. Bianchi, "Ultrasound Features of the Normal and Pathologic Periosteum," Journal of Ultrasound in Medicine 38(3), 775–784 (2019).
7. V. I. Belokonev, A. G. Zharov, "Features of Surgical Treatment of Patients with Uncomplicated Femoral Hernia," Novosti Khirurgii 27(2), 146–152 (2019) [in Russian].
8. D. Frikha-Benayed, J. Basta-Pljakic, R. J. Majeska, and M. B. Schaffler, "Regional differences in oxidative metabolism and mitochondrial activity among cortical bone osteocytes," Bone 90, 15–22 (2016).
9. C. H. M. F. Alencar, C. R. S. Silveira, M. M. Cavalcante, C. G. M. Vieira, M. J. D. Teixeira, F. A. Neto, A. de Abreu, and A. Chhabra, "Periosteum: An imaging review," European Journal of Radiology Open 7, 100249 (2020).
10. S. Jiang, J. T. Elliott, J. R. Gunn, C. Xu, A. J. Ruiz, B. W. Pogue, E. R. Henderson, and I. L. Gitajn, "Endosteal and periosteal blood flow quantified with dynamic contrast-enhanced fluorescence to guide open orthopaedic surgery," Proceedings of SPIE 11222, 112220F (2020).

11. V. P. Zakharov, I. A. Bratchenko, D. N. Artemyev, O. O. Myakinin, S. V. Kozlov, A. A. Moryatov, and A. E. Orlov, "Multimodal Optical Biopsy and Imaging of Skin Cancer," Chapter 17 in Neurophotonics and Biomedical Spectroscopy, R. R. Alfano, L. Shi (Eds.), Elsevier, 449–476 (2019). ISBN: 978-0-323-48067-3.
12. E. Brauchle, D. C. Berrio, M. Rieger, K. Schenke-Layland, S. Reinert, and D. Alexander, "Raman Spectroscopic Analyses of Jaw Periosteal Cell Mineralization," Stem Cells International 2017, 1651376 (2017).
13. M. Unal, S. Uppuganti, S. Timur, A. Mahadevan-Jansen, O. Akkus, and J. S. Nyman, "Assessing matrix quality by Raman spectroscopy helps predict fracture toughness of human cortical bone," Scientific Reports 9, 7195 (2019).
14. M. D Morris, G. S. Mandair, "Raman assessment of bone quality," Clinical Orthopaedics and Related Research 469(8), 2160–2169 (2011).
15. M. Fraulob, S. Pang, S. L. Cann, R. Vayron, M. Laurent-Brocq, S. Todatry, J. A. N. T. Soares, I. Jasiuk, and G. Haïat, "Multimodal characterization of the bone-implant interface using Raman spectroscopy and nanoindentation," Medical Engineering and Physics 84, 60–67 (2020).
16. E. Paschalis, K. Verdelis, S. B. Doty, A. L. Boskey, R. Mendelsohn, and M. I. Y. M. Yamauchi, "Spectroscopic Characterization of Collagen Cross-Links in Bone," Journal of Bone and Mineral Research 16(10), 1821–1828 (2001).
17. E. Paschalis, S. Gamsjaeger, and K. Klaushofer, "Vibrational spectroscopic techniques to assess bone quality," Osteoporosis International 28(8), 2275–2291 (2017).
18. G. S. Mandair, M. D. Morris, "Contributions of Raman spectroscopy to the understanding of bone strength," BoneKEy Reports 4, 620 (2015).
19. I. A. Bratchenko, L. A.Bratchenko, A. A. Moryatov, Y. A. Khristoforova, D. N. Artemyev, O. O. Myakinin, A. E. Orlov, S. V. Kozlov, and V. P. Zakharov, "In vivo diagnosis of skin cancer with a portable Raman spectroscopic device," Experimental Dermatology 30(5), 652–663 (2021).
20. H. Zeng, H. Lui, D. I. McLean, and H. Zeng, "Automated autofluorescence background subtraction algorithm for biomedical Raman spectroscopy," Applied spectroscopy 61(11), 1225–1232 (2007).
21. L. Shamina, I. Bratchenko, D. Artemyev, O. Myakinin, A. Moryatov, O. Kaganov, A. Orlov, S. Kozlov, and V. Zakharov, "Raman and autofluorescence analysis of human body fluids from patients with malignant tumors," Journal of Biomedical Photonics & Engineering 3(2), 020308 (2017).